Photochemical Design of Polymer Functional Nanodiamonds

Zur Erlangung des akademischen Grades eines

DOKTORS DER NATURWISSENSCHAFTEN

(Dr. rer. nat.)

von der KIT-Fakultät für Chemie und Biowissenschaften

des Karlsruher Instituts für Technologie (KIT)

genehmigte

DISSERTATION

von

Dipl.-Chem. Kilian Nikolaus Richard Wüst

aus

Bamberg, Deutschland

1. Referent: Prof. Dr. Christopher Barner-Kowollik

2. Referent: Prof. Dr. Hans-Achim Wagenknecht

Tag der mündlichen Prüfung: 11.12.2017

Abstract

The current thesis reports the application of light-induced ligation protocols to prepare well-defined polymeric structures on the surface of nanodiamonds (NDs). First, two light-triggered grafting-to strategies for the preparation of polymer coated ND are introduced. Subsequently, the photochemical synthesis of fluorescent glyco single-chain nanoparticles (SCNPs) and their application for ND coatings is described.

In the first part, the photoenol Diels-Alder ligation is introduced as a synthetic tool for the fabrication of polymer functional NDs (Chapter 3). Detonation NDs were modified with *o*-methyl benzaldehyde (photoenol) groups. The functionalization progress was monitored by ATR FTIR spectroscopy and X-ray photoelectron spectroscopy (XPS). Upon UV irradiation, maleimide terminal polymers were grafted to NDs. The polymer coated NDs were characterized in-depth using ATR FTIR spectroscopy, XPS and thermogravimetric analysis (TGA). The photo-grafting efficiency increased with decreasing molecular weight of the polymer. Importantly, the photo-grafting of mannose glycopolymers allowed for the generation of nanoparticles that bind to the lectin concanavalin A (ConA).

In the subsequent chapter (Chapter 4), the Diels-Alder reactivity of thermally annealed detonation NDs was exploited for the light-induced grafting of photoenol terminal polymers. A thermal annealing procedure in vacuum allowed for the generation of sp^2 carbon surface structures on NDs under retention of the diamond core as shown by XPS and X-ray diffraction (XRD) analysis. A novel photoenol functional chain transfer agent (CTA) was designed for the preparation of polymers with photoactive endgroups. Subsequent reversible addition fragmentation chain transfer (RAFT) polymerization afforded *o*-methyl benzaldehyde terminal polymers. Dienes generated by photoenolization of the polymeric endgroups were trapped by the surface of the graphitized NDs. In agreement with the results obtained in the previous chapter, a chain-length dependency of the grafting efficiency was observed.

Importantly, the co-grafting of different polymers allowed for the generation multi-functional surfaces on NDs.

The final part of the thesis highlights the controlled immobilization of glycopolymeric nanoparticles onto HPHT NDs (Chapter 5). Mannose based glycopolymers were synthesized *via* RAFT polymerization and modified with tetrazole and alkene groups. Glyco SCNPs were prepared by UV irradiation of highly diluted glycopolymer solutions that led to the formation of fluorescent crosslinks as a result of nitrile imine mediated tetrazole-ene cycloaddition (NITEC) reactions. A novel method to present size exclusion chromatography (SEC) data for SCNPs as hydrodynamic diameter plots was introduced. The obtained fluorescent glyco SCNPs were adsorbed onto HPHT NDs. The surface coverage could be adjusted by altering the SCNP concentration as shown in a photometric adsorption assay as well as with TGA. Importantly, the hybrid particles were non-toxic, fluorescent and bind to the lectin ConA. As a proof of concept, the hybrid particles were imaged in macrophages using confocal fluorescence microscopy.

In conclusion, the presented strategies for the modification of NDs with functional polymers expand the synthetic possibilities to generate polymeric surface structures with novel light-induced grafting-to protocols. Furthermore, novel surface morphologies, such as co-grafted polymer systems and SCNP decorated NDs, were introduced.

Zusammenfassung

Die vorliegende Dissertation befasst sich mit lichtinduzierten Reaktionen für die Darstellung von polymeren Oberflächenstrukturen auf Nanodiamanten. Zuerst werden zwei photochemische Aufpfropfverfahren zur Oberflächenfunktionalisierung von Nanodiamanten mit Polymeren vorgestellt. Anschließend wird die photochemische Darstellung von Einzelketten-Nanopartikeln und deren Adsorption auf Nanodiamanten beschrieben.

Im ersten Teil wurde mit der Photoenol-Diels-Alder-Reaktion für die Herstellung von polymerbeschichteten Nanodiamanten gearbeitet. Zunächst wurden Detonations-Nanodiamanten mit *o*-Methylbenzaldehyd-Gruppen modifiziert und mittels IR-Spektroskopie und Röntgenphotoelektronenspektroskopie (XPS) untersucht. Polymere mit Maleimid-Endgruppen wurden unter UV-Bestrahlung auf die Nanodiamanten gepfropft. Die polymerbeschichteten Nanodiamanten wurden mittels IR-Spektroskopie, XPS und Thermogravimetrie (TGA) untersucht. Die Anzahl gepfropfter Polymere nahm mit abnehmender Polymer-Kettenlänge zu. Zusätzlich wurde die photochemische Beschichtung mit Mannose-Glykopolymeren und die Bindung der resultierenden Nanopartikel mit dem Lektin Concanavalin A (ConA) gezeigt.

Anschließend wurde die Diels-Alder Reaktivität von getemperten Nanodiamanten für das lichtinduzierte Pfropfen von Polymeren untersucht. Das Tempern ($900\,°C$) von Detonations-Nanodiamanten unter vermindertem Druck generierte sp^2-Kohlenstoffstrukturen auf der Oberfläche. Polymere mit *o*-Methylbenzaldehyd-Endruppen wurden mittels reversibler Additions-Fragmentierungs Kettenübertragungs (RAFT)-Polymerisation hergestellt und unter UV-Bestrahlung auf die graphitisierten Nanodiamanten gepfropft. Wie im vorigen Projekt wurde eine Kettenlängenabhängigkeit der Effizienz der Aufpfropfreaktionen beobachtet. Außerdem wurde das Co-Pfropfen verschiedener Polymere zur Darstellung multifunktionaler Oberflächen untersucht.

Im letzten Projekt dieser Dissertation wurde die kontrollierte Immobilisierung von Glykopolymer-Nanopartikeln auf HPHT-Nanodiamanten unter-

sucht. Mannose-Glykopolymere wurden mittels RAFT-Polymerisation herge-
stellt und anschließend mit Tetrazol- und Alken-Gruppen modifiziert. Fluo-
reszente Glyko-Einzelketten-Nanopartikel wurden mittels lichtinduzierter
Nitrilimin-vermittelter Tetrazol-En Cycloadditionen (NITEC) hergestellt. Die
Nanopartikel wurden unter anderem mit Größenausschluss-Chromatographie
untersucht wobei eine Analysemethode zur Bestimmung von hydrodynamis-
chen Durchmessern vorgestellt wurde. Die Glyko-Einzelketten-Nanopartikel
wurden anschließend durch Adsorption auf die Oberfläche von HPHT-Nano-
diamanten aufgebracht. Die Oberflächenbedeckung konnte gezielt eingestellt
werden, wie mit UV/VIS-Spektroskopie und TGA nachgewiesen wurde. Die
Hybridpartikel waren nicht toxisch und konnten mittels Fluoreszenzmikro-
skopie in zellulärer Umgebung lokalisiert werden.

Die hier vorgestellten Strategien erweitern die synthetischen Möglichkei-
ten polymere Oberflächenstrukturen auf Nanodiamanten zu generieren mit
zwei photochemischen Aufpfropfansätzen. Außerdem wurden neuartige
Oberflächenstrukturen, wie co-gepropfte Polymere und Glyko-Einzelketten-
Nanopartikel-Strukturen auf Nanodiamanten erzeugt.

Contents

1

Introduction

Diamonds are renowned for their appealing appearance in gemstones and outstanding physical properties that led to many technological applications. The rigidity of the diamond lattice, which consists as tetrahedrally bonded carbon atoms, is the key to outstanding hardness and high thermal conductivity that is exploited for modern cutting and polishing applications.[1] The genesis of natural diamond is deep below the earth's surface (≥ 150 km) where high temperatures and pressures are found.[2] Due to the rareness of natural diamond, its technical synthesis was highly desirable for a long time. In 1955, *General Electric* developed the high pressure high temperature (HPHT) process, which allowed for the preparation of diamonds from graphite at 3000 °C and pressures of a few 10 kbar.[3] Nowadays, around 200 tonnes of diamonds are produced per year, which is more than ten times the amount of diamond obtained from natural sources.[3]

In the realm of nanotechnology, nanodiamonds (NDs) have emerged as a nano-sized version of bulk diamond. NDs are diamond nanoparticles that occur naturally in meteorites.[4] In the early 1960s, pioneering work in the synthesis of NDs was conducted in the former USSR.[5] In 1963, the so-called detonation synthesis of NDs was discovered,[5] which is still of great commercial importance since high quantities can be prepared at moderate costs.
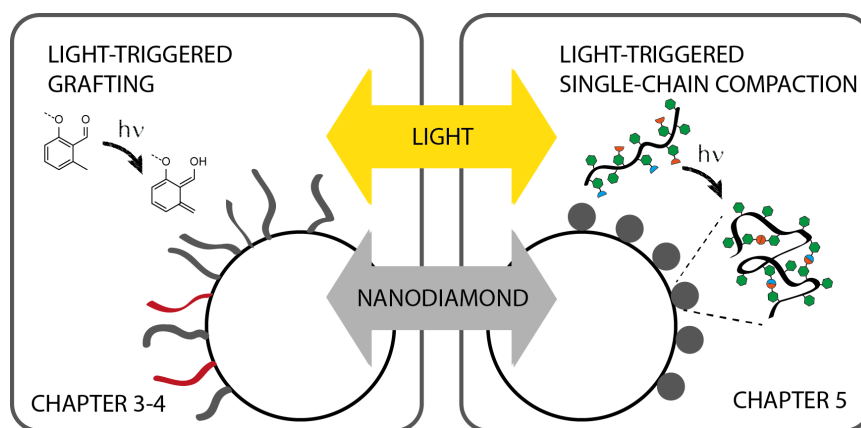
Figure 1.1. Graphical illustration of the projects described in the current thesis. Two light-triggered grafting-to approaches for the modification of NDs are introduced in Chapter 3-4. In Chapter 5 the photochemical synthesis of single-chain nanoparticles and their immobilization onto NDs is described.

In modern material design, the use of NDs in hybrid materials, such as ND enforced polymeric networks[6] and polymer coated nanodiamonds for biomedical applications,[7] has gained increasing interest. The development of efficient and versatile surface modification strategies is crucial for the fabrication of polymer ND hybrid materials. In general, light-induced ligation strategies have proven to be efficient for the modification of surfaces.[8] Key characteristics are high spatial and temporal control as well as mild reaction conditions, *e.g.* ambient temperature and catalyst-free. Thus, photochemical ligations are often employed for the modification of surfaces with sensitive materials, such as biomacromolecules. In the current thesis, the photochemical design of polymer coated NDs is explored (Figure 1.1).

In Chapter 3 and 4 light-induced ligation methods to modify NDs with polymers are introduced (Figure 1.1). Two synthetic approaches, one based on photoactive NDs and the other on photoactive polymers, are investigated in-depth. The light-triggered grafting-to protocols were studied in terms of efficiency, functionality and modularity. Importantly, glycopolymer functional NDs with interesting lectin binding behaviour were prepared (Chapter 3). Furthermore, the co-grafting of different polymers to prepare multifunctional surfaces is highlighted in Chapter 4.

In the final part of the current thesis, light-induced ligations are applied to

prepare fluorescent glyco single-chain nanoparticles (SCNPs) for the modification of HPHT NDs (Figure 1.1). The detailed investigation of experimental conditions and resulting properties allowed for the preparation of hybrid nanoparticles with structural motifs inspired by viruses. Furthermore, the potential of the novel glyco-ND structures for biomedical applications is discussed.

2

Theoretical background

The current chapter covers the theoretical background relevant to the thesis as well as a review of relevant literature. An introduction to nanodiamonds (NDs), their structure and properties as well as the preparation of polymer coated NDs is given in Section 2.1. In the following section, the concept of reversible deactivation radical polymerization (RDRP) is introduced and reversible addition fragmentation chain transfer (RAFT) polymerization is described in detail (Section 2.2). Photochemical ligation methods with emphasis on applications in polymer science are described in Section 2.3. In Section 2.4, the synthesis of mannose glycopolymers as well as their outstanding properties are highlighted. Finally, the field of single-chain nanoparticles (SCNPs) is introduced, including current advances in SCNP preparation and characterization (Section 2.5).

2.1. Nanodiamonds

Nanodiamonds (ND) are nanoparticles with extraordinary properties, such as high biocompatibility, stable fluorescence and surface properties that allow their facile modification. They occur naturally, however synthetic approaches have been developed that have led to large scale availability (Section 2.1.1).[9]

In general, the word *nanodiamond* describes all carbon nanoparticles with a diamond lattice structure. Due to different natural as well as synthetic origins, ND material can differ in particle size and shape, elemental composition, defect centres and surface functionalities.

2.1.1. Synthesis of nanodiamonds

A variety of ND synthesis methods have been developed.[10–16] However, NDs derived from the high pressure high temperature (HPHT) and detonation synthesis are the most commonly investigated ND materials.[17] In Chapter 3 and 4, detonation NDs were employed, whereas in Chapter 5 an application of HPHT NDs is described. Thus, detailed descriptions of the synthesis of detonation NDs and HPHT NDs are given in the following two sections.

Detonation nanodiamonds

The detonation synthesis of NDs is based on the following:[18]

  i) An explosion generates a shock wave that forms high temperatures and pressures.

  ii) An atmosphere of negative oxygen balance (C/O > 1) prevents full oxidation of the explosives and allows for the segregation of carbon.

  iii) The diamond crystals are formed by self-assembly of carbon atoms stemming from the explosives.

A typical explosive used for detonation synthesis is a mixture of hexogen and trinitrotoluene (Scheme 2.1). The detonation is performed in an enclosed chamber leading to high temperatures and pressures that allow the formation of diamond. After the explosion, pressure and temperature drop rapidly into the region where diamond is thermodynamically unstable. If the temperature is sufficiently high to allow a high mobility of carbon atoms, a diamond-graphite phase transition occurs, generating graphitic structures on the surface of the diamond nanocrystals. Thus, to minimize non-diamond carbon in the detonation soot, rapid cooling of the detonation mixture is crucial.[18]

Scheme 2.1. ND synthesis *via* the detonation process. During the detonation of explosives (*e.g.*TNT and hexogen) in an enclosed chamber diamond nanoparticles are formed.

Different non-oxidizing media, such as inert gas, water and dry ice, have been employed for the detonation synthesis. The amount of diamond carbon in the detonation soot (material resulting from detonation process) depends on the heat capacity of the medium with the following order: gas (40 wt.%) < water (63 wt.%) < ice (75 wt.%). However, the water synthesis is the most attractive economic approach and thus is commonly used for the commercial production of NDs.[19]

The resulting detonation soot contains the desired NDs as well as graphite micro- and nanoparticles and contamination from erosion processes of the reactor wall, such as iron oxides and silicon dioxide. To remove non-diamond carbon and metallic contamination, the detonation soot is treated with acid, *e.g.* nitric acid (50-67 %).[18] Detonation NDs are usually around 5 nm in diameter and form strong aggregates of up to a few hundred nanometres, which are difficult to break down.[20] Typically, a disaggregation procedure is applied prior to usage. Different disaggregation methods have been developed, with ultrasound assisted disaggregation being the most commmonly employed technique. Upon high power sonication, large aggregates can be broken down to smaller core aggregates of close to 100 nm in diameter.[20] However, complete disaggregation is not achievable, which indicates that besides non-covalent interactions covalent bonds bridge primary particles in core aggregates. In order to completely disintegrate the ND aggregates, harsher disaggregation methods need to be applied. For example, stirred media milling with micron-sized ceramic beads allows the formation of single-digit NDs.[20]

High pressure high temperature (HPHT) nanodiamonds

HPHT NDs are prepared by milling diamond microcrystals obtained from HPHT synthesis into nanometre sized particles. The HPHT synthesis of diamond is traditionally employed for the synthesis of macroscopic diamond crystals.[21] The synthesis of diamond from graphite starting material is performed in a hydraulic press in the presence of metal catalysts at high pressures (7-10 GPa) and high temperatures (1500-2200 °C).[17] Milling of the diamond microcrystals allows for the preparation of nanodiamonds of different sizes. Density gradient ultracentrifugation can be employed to separate nanodiamonds by size and obtain nanodiamond samples with uniform size distributions.[22] Furthermore, high energy ball milling of HPHT NDs allowed the preparation of ultrasmall nanodiamonds (≤ 10 nm).[23]

2.1.2. Fluorescence properties of nanodiamonds

The presence of vacancy centres in the diamond lattice leads to stable fluorescence.[24] The most common vacancy centre is the nitrogen vacancy (NV) centre (Figure 2.1). The typical process to introduce NV centres entails high energy irradiation with *e.g.* electrons,[24,25] or helium atoms,[26] followed by vacuum annealing at high temperatures (600-900 °C). High energy irradiation induces the formation of vacancy centres, whereas the annealing process leads to their migration until they are trapped by a nitrogen atom.[9] The NV centre exists in a neutral (NV^0) and negatively charged (NV^-) state with a
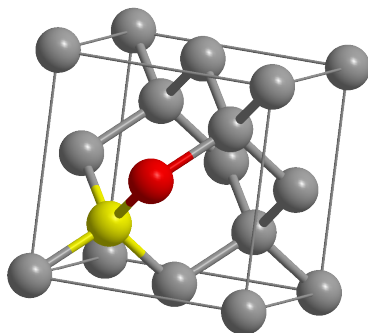
Figure 2.1. Diamond unit cell with a NV center (grey: carbon, red: nitrogen, yellow: vacancy center).

zero-phonon emmision at 575 nm and 637 nm, respectively.[27] The vacancy centres in NDs are highly interesting for imaging applications[28] as well as magnetic sensing[29,30] and quantum computing.[31] An alternative to the irradiation/annealing treatment is the attachment of a fluorophore to the ND's surface. Covalent attachment of a fluorophore to the surface leads to fluorescent particles that can be imaged by confocal fluorescence microscopy.[32–34] Detonation NDs show intrinsic fluorescence, which is much weaker than the fluorescence of treated HPHT NDs, yet sufficient to be used for confocal fluorescence imaging.[7,35,36]

2.1.3. Biocompatibility of nanodiamonds

For biomedical applications, such as drug delivery and imaging, the absence of any cytotoxic effects of the employed material is crucial. Several *in vitro* and *in vivo* studies demonstrated the biocompatibility of NDs and thus showed the high potential of ND material for biomedical applications.[37]

In 2007, Schrand *et al.* investigated the cytotoxicity of 2-10 nm large NDs *in vitro*. Cell viability assays showed that NDs are not toxic to a wide variety of cell lines (neuroblastoma, macrophage, keratinocyte and PC-12 cells) and cells could be cultured on ND-coated substrates without influencing the cell morphology.[38] In a further study by Schrand *et al.*, the order of biocompatibility of different nano-carbon materials was established (in neuroblastoma cells and macrophages): ND > carbon black > multi-walled carbon nanotubes > single-walled carbon nanotubes.[39] Similar results were obtained in a study from Liu *et al.* where the cytotoxicity of carboxylated NDs (5 nm or 100 nm) and carbon nanotubes on human lung A549 epithelial cells and HFL-1 normal fibroblast cells was investigated. The investigated NDs did not reduce cell viability or alter the protein expression profile, whereas carbon nanotubes were found to be cytotoxic.[40] Furthermore, Li *et al.* investigated the cytotoxicity of detonation NDs on HeLa cells, reporting no cytotoxicity in complete cell culture medium and cytotoxic effect when serum-free medium was used.[41] Studies investigating the genotoxicity of NDs have shown that the investigated NDs showed no genotoxic effects.[42,43]

In addition to *in vitro* experiments, *in vivo* experiments provided further information about effects of ND administration to animal models. For instance, Puzir *et al.* reported that subcutaneous injection of ND hydrosols in mice showed no inflammatory effect after 3 months. Subsequent transmission electron microscopy (TEM) experiments showed that ND aggregates were formed, however adjacent cells were not damaged.[44] The biodistribution of NDs was investigated by Zhang *et al.* using radiotracer techniques. [188]Re labelled NDs were administered by intratracheal instillation to mice. After variable time periods, the mice were sacrificed and the radioactivity of the organs was measured. NDs were mainly distributed in the lung, followed by the spleen, liver, bone and heart. Furthermore, signs for a dose-dependent toxicity to lung, liver, kidney and blood were reported.[45]

Overall, toxicity studies have shown that ND administration does not lead to apparent toxicity effects and thus NDs are a promising material for biomedical applications. However, a large variety of NDs with different sizes and compositions have been prepared and thus continued studies are required to ensure the safety of modern ND materials.

2.1.4. Surface chemistry of nanodiamonds

The fabrication method influences the morphology, structure and composition of the resulting NDs. For instance, the surface structure of detonation NDs depends on the condensation medium used.[46] However, due to oxidative purification protocols most available ND material possesses an oxidized surface, which is covered with a variety of functional groups (Figure 2.2). Carboxylic acids, lactones, esters, ethers and alcohols are the most common surface-expressed functionalities.[18]
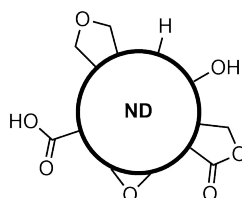
Figure 2.2. Schematic representation of typical surface functionalities on NDs.

2.1.4.1. General surface modification strategies

The modification of ND surfaces is of utmost importance for many applications. For instance, surface groups can enhance the colloidal stability and introduce bioactive molecules for biomedical applications. Several synthetic strategies have been developed to modify ND materials.

As mentioned above, most NDs are initially purified from contaminations using an oxidative treatment. However, to increase carboxylic acid groups and to homogenize the surface for further modification, often an additional oxidation step using oxidizing acids or thermal air oxidation is performed. Common oxidation mixtures include different combinations of concentrated sulfuric acid, nitric acid and perchloric acid,[47,48] piranha solution,[27] hydrogen peroxide,[48] and a combination of hydrofluoric and nitric acid.[49] An alternative to wet chemical approaches is the thermal oxidation with air/oxygen at elevated temperatures (above 400 °C).[50,51] The oxidation procedure removes amorphous and sp^2 carbon and generates an oxidized surface predominantly consisting of carboxylic acid groups.[49,50] The oxidation process is often accompanied with a size reduction of the NDs since surface layers are removed when oxidized.[52] Oxidized NDs are highly hydrophilic nanoparticles with a negative zeta-potential and are the most common applied starting material for further modifications.

A common approach to modify oxidized NDs is *via* esterification and amidation reactions to attach alcohols and amines, respectively (Scheme 2.2).[33,53] Coupling agents such as *N,N'*-dicyclohexylcarbodiimide (DCC) are typically employed or alternatively, the carboxylic acid groups can be transformed into acid chlorides to allow the ligation.[54]

a) R-OH
b) R-NH$_2$

X: O for a); NH for b)
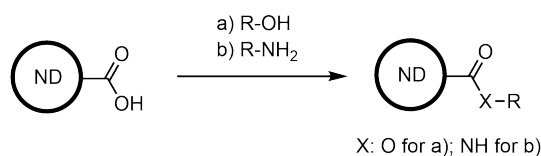
Scheme 2.2. Schematic representation of the esterification/amidation of oxidized NDs.

The reduction of ND surface groups is another common method applied prior to further modification. Reducing agents such as BH_3 and $LiAlH_4$ are used to obtain mostly hydroxy functional surfaces. Subsequently, the reduced surface can be esterified with carboxyl functional molecules,[55,56] an ether linkage can be formed,[57,58] or a silanization reaction can be performed (Scheme 2.3).[59–61] (3-Aminopropyl)trimethoxysilane is a commonly used silanization reagent to obtain amine functional NDs *e.g.* for subsequent coupling with amino acids.[59] The hydroxy groups on NDs can also be exploited to attach dopamine derivatives.[62]

Furthermore, the controlled generation of graphitic structures on the surface of NDs provides interesting conjugation sites for covalent C-C bond formation. Thermal annealing of NDs in the absence of oxygen (vacuum or inert atmosphere) leads to the desorption of surface functional groups followed by a shell to core, sp^3 to sp^2 phase transition. Controlling reaction parameters, such as temperature and annealing time, allows for the preparation of surface graphitized NDs.[63] The sp^2 carbon structures can then be employed to graft organic molecules to the surface. For instance, the functionalization of annealed NDs with aromatic diazonium salts was introduced from Krueger and coworkers.[54,64] Furthermore, Diels-Alder reactions with a thermally generated *ortho*-quinodimethane was shown to be an efficient surface modification
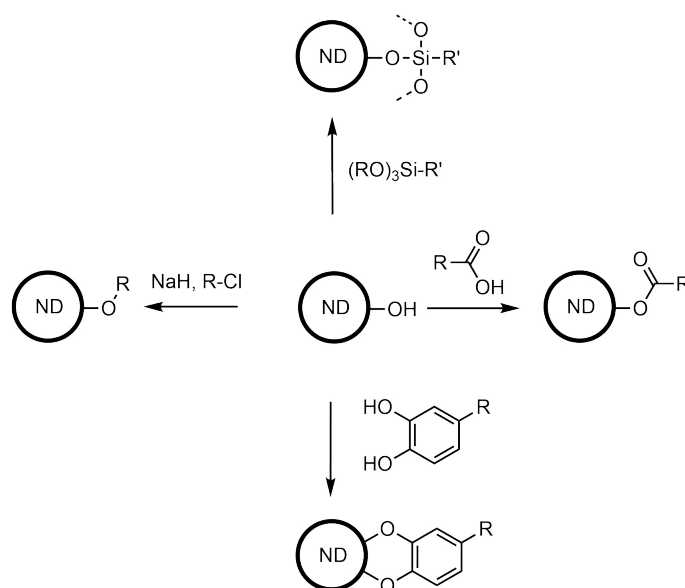
Scheme 2.3. Functionalization strategies to modify hydroxy functional NDs.

method.[65] In the current thesis (Chapter 4), a photochemical approach for the Diels-Alder grafting of polymers to annealed NDs is introduced.

2.1.4.2. Polymer functional nanodiamonds

The modification of NDs with polymers is an important area of research, since it allows to significantly alter the ND properties for a variety of applications. Polymers can be covalently attached to NDs or simply adsorbed to the surface (Scheme 2.4). Covalent attachment yields highly stable coatings, whereas non-covalent coatings might suffer from poor coating stability. In general, polymer grafting can be categorized in three main approaches:

1. **Grafting-from**: monomers are polymerized starting from the surface

2. **Grafting-to**: polymer chains are attached to the surface *via* chemical ligation methods

3. **Adsorption**: polymer chains are attached to the surface *via* non-covalent, site-unspecific interactions
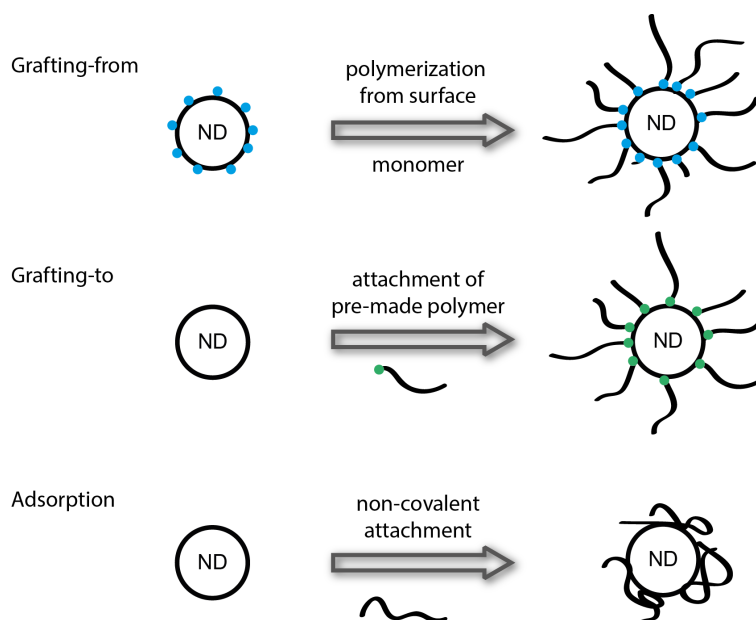
Scheme 2.4. Overview of different modification approaches to obtain polymer coated NDs.

In grafting-from protocols, the polymer is grown from the ND surface. Typically, an initiator that allows for the site-specific polymerization of monomers is first attached to the surface followed by the polymerization step. The grafting-from approach is applicable to different polymerization techniques. For instance, ring opening polymerization (ROP) has been performed from ND surfaces, *e.g.* to prepare poly(caprolactone) (PCL)[66] and poly(glycerol)[67–69] coated NDs. Furthermore, atom transfer radical polymerization (ATRP) initiators as well as chain transfer agents (CTAs) for reversible addition fragmentation chain transfer (RAFT) polymerizations have been attached to NDs for grafting-from experiments.[7,70] High grafting densities are typically achieved, however, the characterization of the polymeric structure is challenging.

In the grafting-to approach, a pre-made polymer is attached to the surface. Compared to grafting-from protocols, the polymer can be easily characterized prior to grafting. Moreover, the modular nature of the grafting-to process allows for the facile preparation of polymer libraries allowing ready access to a variety of coatings on the same ND material. However, compared to the grafting-from approach, lower grafting densities are usually obtained. The grafting-to approach has been applied for a variety of polymers and ligation methods. For example, hydroxy terminal poly(ethylene glycol) (PEG) has been grafted to oxidized NDs *via* esterification reactions.[70] Cha *et al.* grafted a PEG azo initiator *via* radical coupling reaction to NDs.[71] Azide functional NDs have been used to attach dibenzocyclooctyne terminal RAFT polymers *via* copper free click chemistry.[72] Barras *et al.* modified hydroxy functional NDs with dopamine terminal poly(*N*-isopropylacrylamide) (PNIPAM).[62] Two novel photochemical grafting-to approaches are described in Chapter 3 and Chapter 4.

Polymer coatings on NDs can also be achieved by simple surface adsorption. Non-covalent interactions, such as hydrogen bonds and electrostatic interactions, are typically the driving force for the adsorption process. Compared to covalent grafting approaches, non-covalent coating procedures are simpler and faster to perform and often yield particles with similar properties. However, since the adsorption process is not site-specific and polymers can adhere to multiple ND particles, aggregation can occur. For instance, poly(ethylene imine) was adsorbed onto oxidized NDs to obtain nanoparticles for gene

delivery.[73] In another study, Lee *et al.* coated NDs *via* physical adsorption of block copolymers and proteins for enhanced cellular uptake.[74] The controlled adsorption of polymeric single-chain nanoparticles (SCNPs) is introduced in Chapter 5.

2.2. Reversible deactivation radical polymerization

2.2.1. Overview

Reversible deactivation radical polymerization (RDRP), previously also often referred to as controlled/living radical polymerization,[a] is a class of radical polymerization techniques that allows for the synthesis of well-defined polymers with narrow molecular weight distributions (MWDs) and good control over molecular weight, endgroups and architecture.[76] Typical features of RDRP are a linear increase of molecular weight with conversion, low molecular weight dispersities and "living" character that allows for chain extension experiments. During the last 20 years, RDRP has developed into one of the most significant synthetic approaches in soft matter material design due to its versatility and ease of operation.[77] The most common RDRP techniques are atom transfer radical polymerization (ATRP), nitroxide mediated polymerization (NMP) and reversible addition fragmentation chain transfer (RAFT) polymerization.[78]

ATRP and NMP are based on the formation of dormant species that reduce radical concentration and the number of termination events. In NMP a nitroxide radical is used to reversibly trap radicals into dormant alkoxyamine species, whereas in ATRP the activation/deactivation process is based on organohalides that reversibly transfer halogen atoms usually to transition metal complexes. The reader is here referred to extensive review articles about ATRP[79–83] and NMP.[84–86] RAFT polymerization was employed in the current thesis to prepare a variety of functional polymers and is thus described in detail in the following sections.

---

[a]   In 2010, IUPAC recommended the term reversible deactivation radical polymerization and discouraged the use of the term controlled/living radical polymerization.[75]

2.2.2. Reversible addition fragmentation chain transfer polymerization

RAFT polymerization is one of the most commonly used RDRP techniques and was first described by CSIRO chemists in 1998.[87] At the same time, French scientists patented an equivalent technique using xanthates, which was referred to as macromolecular design via the interchange of xanthates (MADIX).[88]

The main experimental difference of RAFT to free radical polymerization (FRP) is the addition of a specific CTA, often referred to as a RAFT agent. The currently accepted mechanism for RAFT polymerization is depicted in Scheme 2.5. The formation of radicals is triggered by conventional radical initiators. The most commonly employed initiator is 2,2'-azoisobutyronitrile (AIBN). However, a variety of thermal and photo-initiators are available. Once a radical I$^{\cdot}$ is formed, propagation with monomer M occurs to form a growing chain radical P$_n^{\cdot}$, which can enter the pre-equilibrium. P$_n^{\cdot}$ adds to the CTA forming an intermediate radical which can fragment back to the starting compounds or forward to form radical R$^{\cdot}$. Ideally, the forward fragmentation is
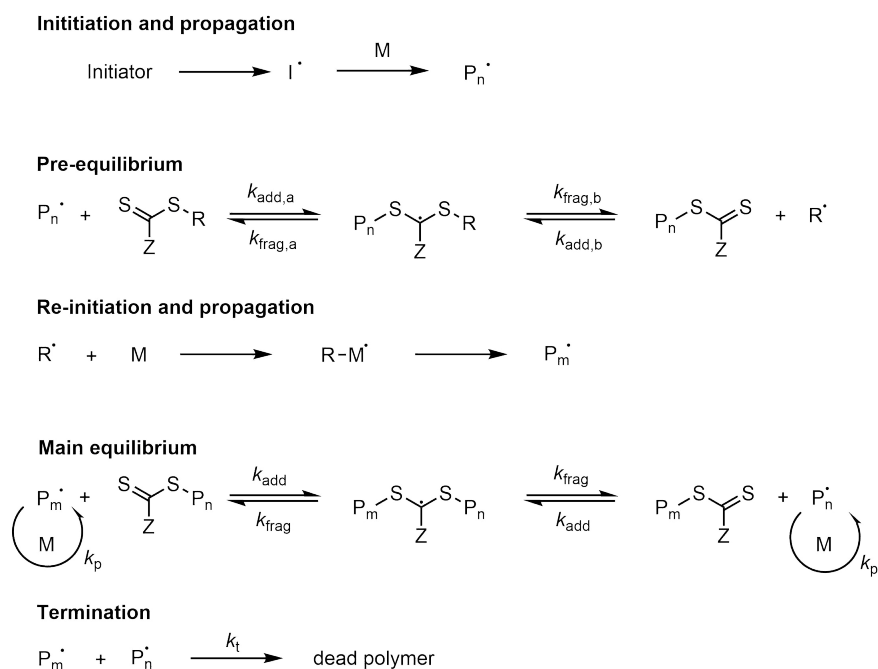
Scheme 2.5. Mechanism of RAFT polymerization with thiocarbonylthio CTAs.[89]

favoured, which occurs when R is a better leaving group than P_n. Subsequently, radical R· reinitiates polymerization and propagates. The hereby formed macro radical P_m· enters the main equilibrium by addition to a macro RAFT agent, where a macro radical P_n· or P_m· is released by fragmentation. This process is repeated until termination occurs. The degenerative chain transfer drastically increases the lifetime of propagating chains and provides equal possibilities for chain growth leading to polymers with narrow MWDs.[90]

A variety of monomers can be polymerized *via* RAFT polymerization providing a suited CTA is used. One limitation in RAFT polymerization is the use of monomers with nucleophilic groups, such as primary and secondary amines that can cleave the thiocarbonylthio group.[91] However, careful adjustment of polymerization conditions allows for the controlled polymerization of amine monomers in their protonated form.[92] The selection of an adequate CTA depends on the monomer reactivity and is crucial for an efficient RAFT process. In general, monomers can be classified according to their reactivity into more activated monomers (MAMs), including (meth)acrylates, (meth)acrylamides, styrenes, acrylonitrile, and less activated monomers (LAMs) including 1-alkenes, vinyl acetate and *N*-vinylpyrolidone.[91] In an efficient RAFT process, the addition of a radical to the C=S bond is favoured over the addition to the monomeric C=C bond. The Z-group influences the stability of the intermediate radical and thus affects addition and fragmentation rates.[91] For the RAFT polymerization of MAMs, trithiocarbonates or dithiobenzoates are typically employed, whereas xanthates and dithiocarbamates are used for LAMs (Figure 2.3).[91] On the other hand, the R-group of a CTA has to be a good leaving group and the formed radical R· has to be capable of re-initiating polymerization.[91]

Z-group

SR': trithiocarbonate
alkyl, aryl: dithioester
OR': xanthate
NR'R": dithiocarbamate
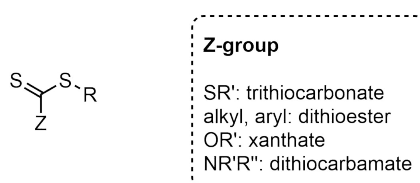
Figure 2.3. Typical structure of thiocarbonylthio CTAs for RAFT polymerization.

In an ideal RAFT process, the polymerization rate does not differ from FRP and can be described with the following equation:

$$R_p(t) = k_p[M]\sqrt{\frac{f k_d [I]_0 e^{-k_d t}}{k_t}} \tag{2.1}$$

where k_p and k_t are the propagation and termination rate coefficients, respectively, t the polymerizaton time, $[M]$ and $[I]$ the monomer and initiator concentration, respectively, and f is the initiator efficiency.[91] Consequently, high monomer and radical concentrations lead to fast polymerization kinetics.

The endgroups of RAFT polymers

RAFT polymerization allows for the preparation of polymers with well-defined endgroups. In Chapter 3 and 4, grafting-to experiments with endgroup functional RAFT polymers were conducted. Thus, a detailed discussion of the structure of RAFT polymers and how to influence endgroup functionalities is given here.

During RAFT polymerization monomer units are inserted between the thiocarbonylthio moiety and the R group yielding α,ω-functional polymers (Scheme 2.6). However, not all polymer chains posses this endgroup combination. The polymerization is initiated by a radical initiator and thus endgroups derived from the initiator can also be found in the polymerization product. In addition, bimolecular termination reactions occur between (macro)radicals leading to polymers with different combinations of R and initiator endgroups. In the case of disproportionation termination, unsaturated endgroups are formed. Importantly, the number of terminated chains without RAFT endgroups corresponds to the number of radicals introduced during polymerization.[91]
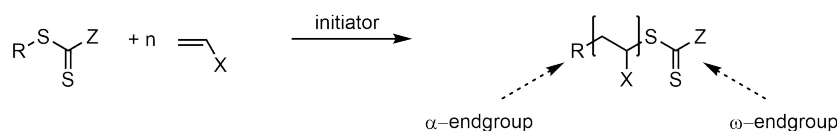
Scheme 2.6. RAFT polymerization and common terminology for polymer endgroups. Adapted from reference [93] with permission of The Royal Society of Chemistry.

Perrier described the number fraction of living chains (polymer chains with RAFT endgroups), termed as "livingness" L, as:

$$L = \frac{[CTA]_0}{[CTA]_0 + 2f[I]_0(1 - e^{-k_d t})(1 - \frac{f_c}{2})}$$

(2.2)

where $[I]_0$ and $[CTA]_0$ are initial concentrations of initiator and CTA, respectively, the term $2f$ means that one initiator molecule forms 2 primary radicals with the efficiency f, f_c is the radical-radical coupling factor where a value of 1 represents bimolecular termination and 0 disproportionation.[91] In a typical RAFT polymerization, an excess of CTA compared to initiator is used (typically around 1:10, [I]:[M]) allowing for a good control over polymer structure and endgroups . Thus, the majority of chains possess endgroups derived from the CTA (high number of living chains according to Equation 2.2), which is crucial for chain extension to form block copolymers or for further modification reactions (see below).[91]

There are two general approaches to adjust the endgroups of RAFT polymers: 1) the modification of the R-group of a CTA to obtain α-functional polymers and 2) the functionalization of the thiocarbonylthio endgroup to obtain ω-functional polymers.

On the one hand, post-polymerization modification of the thiocarbonylthio endgroups can be performed to obtain ω-functional polymers. One of the most common approaches is the reduction of the thiocarbonylthio endgroups to thiols, which can be exploited for subsequent modification steps.[94–97] For instance, Bulmus and coworkers performed the one-pot aminolysis (nucleophilic reaction of amines with thiocarbonyl moiety) of the ω-endgroups of RAFT polymers and thiol-ene modification with a (meth)acrylate functional mannose and maleimide functional biotin.[95] Another synthetic approach to modify the ω-terminus of RAFT polymers is to conduct radical induced endgroup coupling reactions. For example, Maynard and coworkers performed a radical cross-coupling reaction with a furan capped maleimide functional azo-initiator to prepare maleimide terminal polymers for the subsequent attachment to bovine serum albumin (BSA).[98] In addition, the Barner-Kowollik

team has introduced a method to convert RAFT polymers into hydroxy terminal polymers *via* a radical process.[99] Dithioester endgroups formed hydroxy-peroxy groups in the presence of an azo initiator at elevated temperature in tetrahydrofuran (THF) and in the presence of oxygen, which were reduced in a one-pot procedure with triphenlyphosphine to yield hydroxy endgroups. Another approach to modify RAFT endgroups is by hetero Diels-Alder reactions with the thiocarbonyl endgroup.[100–104] For instance, the ultrafast conjugation of cyclopentadienyl capped polymers with electron-deficient dithioester RAFT polymers presents a powerful synthetic tool to modify RAFT endgroups.[102]

On the other hand, R-group functional RAFT agents can be employed, which lead to α-functional polymers. CTAs with reactive R-groups, such as azides,[105] alkynes,[106] or activated esters,[107] are often employed for post-polymerization endgroup modifications. For instance, Geest and coworkers compared the performance of different protein reactive CTAs for polymer-protein conjugation.[107] Pentafluorophenylester and pyridyl disulfide-functionalized CTAs were found to be more efficient than a NHS-ester functional CTA. A contribution of Xiao and coworkers showed the successful application of a dibenzocyclooctyne functional CTA for RAFT polymerization and subsequent grafting onto nanodiamonds.[72] In the current thesis (Chapter 3 and 4), R-group functional CTAs were designed and employed for grafting-to experiments on nanodiamonds.

2.3. Photochemical ligations in polymer chemistry

In polymer science, a photochemical reaction or a photochemically induced reaction sequence that leads to a direct conjugation of a polymer to another entity (*e.g.* small molecule, another polymer, surface group) is referred to as a photochemical ligation. The advantage of light induced ligations compared to thermal reactions is a high spatial and temporal control. Photochemical ligations are mainly employed to couple polymer chains to form block-copolymers, to crosslink polymers intra- or intermolecularly and to attach polymers onto surfaces.

When a sample is irradiated with light, the intensity decreases exponentially on the way through the sample. A quantitative description of light absorption is given by the Beer-Lambert's law (Equation 2.3). The absorbance (A), which is calculated from the initial intensity (I_0) and transmitted intensity (I_1), is proportional to the concentration of absorbing molecules (c) and to the thickness of the sample (path length l), where ϵ is the molar extinction coefficient.[108]

$$A = log(\frac{I_0}{I_1}) = \epsilon \cdot c \cdot l \qquad (2.3)$$

The electronic states and transitions involved in photochemical processes can be depicted in a Jablonski diagram (Scheme 2.7).[109] Photon absorption leads to a transition from the singlet ground state (S_0) to an excited singlet state (S_n). Subsequently, non-radiative or radiative deactivation can occur. Vibrational relaxation (VR) is a non-radiative process from a higher vibrational state to the lowest vibrational state of one electronic state, whereas internal conversion (IC) is a spin-allowed relaxation from an excited electronic state to a lower electronic state of the same multiplicity (also non-radiative). Intersystem crossing (ISC) describes a non-radiative, spin-forbidden transition between two electronic states of different multiplicities. Excited states can also be deactivated by radiative transitions. Fluorescence is a transition from an excited singlet state to its ground state under emission of light. Phosphorescence
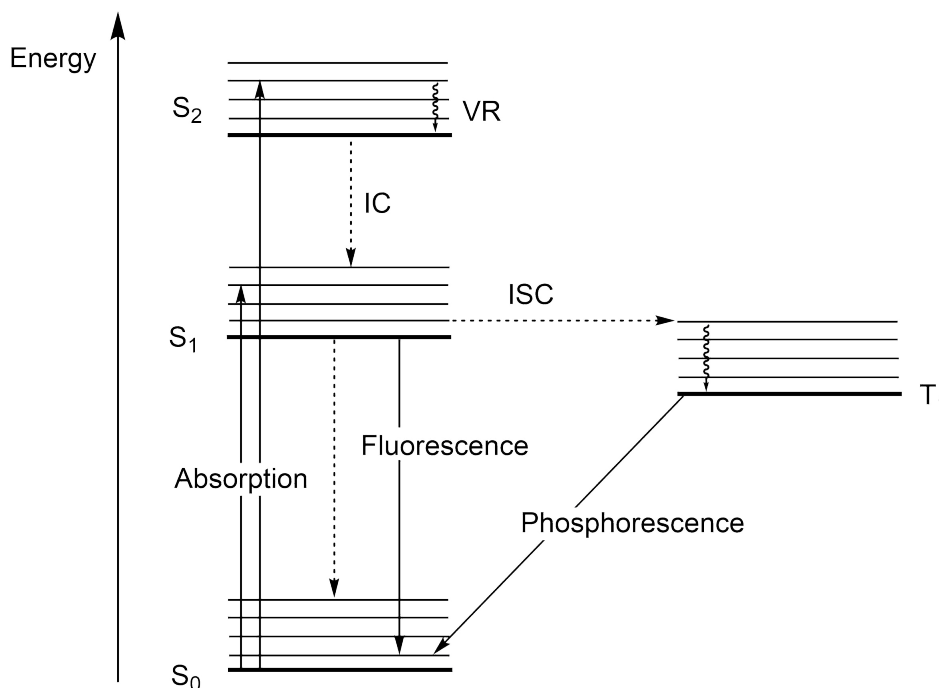
Scheme 2.7. Jablonski diagram. Radiative and non-radiative transitions are depicted with plain and dashed arrows, respectively.

describes the radiative transition from a triplet to a singlet state. Phosphorescence lifetimes are relatively long (up to hours) compared to fluorescence lifetimes (0.5-20 ns).[108]

Apart from the above described deactivation mechanisms, an excited state can also lead to a photochemical reaction. Typical reaction pathways arising from excited states are isomerization, dissociation, addition/insertion, abstraction/fragmentation and dissociative excitation.[108]

A variety of photochemical ligations have been employed in polymer science, including acyl sulfide ligation,[110,111] anthracene dimerization,[112,113] photoinitiated thiol-ene reacion[114] and alkyne-azide cycloaddition,[115] thiol-quinone methide reaction,[116] and azirine ligation.[117] The photoenol and tetrazole ligation are employed in Chapter 3-4 and Chapter 5, respectively, and thus are introduced in detail in the following two sections.

2.3.1. Photoenol chemistry

The photochemical enolization of *ortho*-substituted benzophenones was first described in 1961 by Yang and Rivas.[119] They reported the UV induced enolization of *o*-methyl benzophenone and the trapping of the diene intermediate with a dienophile (dimethyl acetylenedicarboxylate) in a [4+2]-cycloaddition. The currently accepted mechanism for the photoenol ligation was established from Porter and Tchir using flash photolysis experiments and is depicted in Scheme 2.8.[118,120] The light excitation of 2,4-dimethyl benzophenone leads to a n $\rightarrow$ π^* transition of the carbonyl group, followed by ISC forming an excited triplet state. Internal H-abstraction leads to the formation of a biradical, which upon rearrangement forms two enol isomers with relatively long lifetimes (4 s and 250 s).[118] The presence of two isomers suggests free rotation around the central carbon atom in the triplet state. The *E*-isomer can react in a Diels-Alder reaction with electron deficient dienophiles, which is
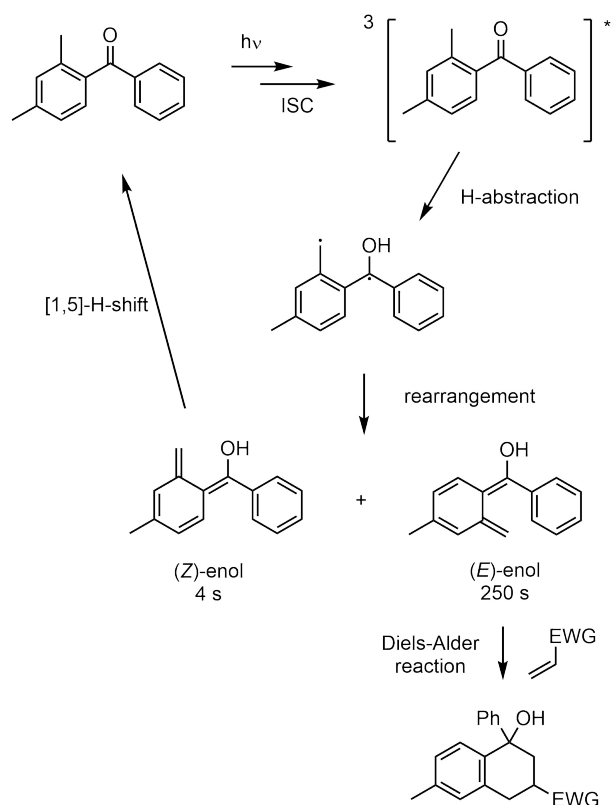
Scheme 2.8. Mechanism of the photoenolization of 2,4-dimethyl benzophenone and subsequent Diels-Alder trapping.[118]

24

nowadays known as the photoenol ligation. The reaction is irreversible due to the rearomatization of the phenyl ring.

The photochemical generation of Diels-Alder reactive dienes *via* the photoenolization process was rediscoverd by polymer scientists in the last decade. The photoenol ligation was applied for the synthesis of block copolymers,[121–123] cyclic polymers,[124] polymeric networks,[125,126] nanoparticles,[127,128] and for the grafting of polymers to planar[129–132] and non-planar[121,133] surfaces.

The application of photoenol chemistry for modular polymer-polymer ligation was demonstrated by Langer *et al*. A dual functional CTA including an *o*-methyl benzaldehyde moiety was prepared and employed to synthesize an $\alpha,\omega-$functional RAFT polymer. Subsequently, a hetero Diels-Alder ligation followed by a photoenol ligation to form a diblock and an amphiphilic triblock polymer, respectively, was performed. This modular ligation sequence demonstrated the potential of photoenol chemistry to generate complex polymeric structures.[123]

The application of photoenol chemistry for the crosslinking of single polymer chains to form single-chain nanoparticles (SCNPs)[127,128] and intermolecular crosslinking to prepare polymeric networks[125,126] was demonstrated in several studies. Light-triggered SCNP formation is described in detail in Section 2.5. Spatially resolved network formation was achieved with *e.g.* direct laser writing (DLW). Quick *et al*. crosslinked maleimide multifunctional poly(methyl methacrylate) (PMMA) with a tetra-functional *o*-methyl benzaldehyde crosslinker using a DLW setup with excitation at $\lambda = 700\,\mathrm{nm}$.[125] Two-photon absorption induced photoenolization of the *o*-methyl benzaldehyde groups was followed by Diels-Alder crosslinking reactions. 3D microstructures with a resolution down to 500 nm were fabricated. Residual *o*-methyl benzaldehyde groups were used to modify the written 3D structures in a spatially resolved fashion.

The spatially resolved surface modification *via* the photoenol ligation is a versatile approach to obtain well-defined, functional surfaces.[129–132] For instance, Pauloehrl *et al*. prepared an *o*-methyl benzaldehyde functional silane, which was immobilized onto silicon wafers. Spatially resolved modification of

the surface with a maleimide functional ATRP initiator, PEG and a peptide was achieved using a shadow mask.[129]

Furthermore, photoenol chemistry was employed for the modification of micro- and nanoparticles.[121,133] Kaupp *et al*. prepared an *o*-methylbenzaldehyde functional CTA for RAFT polymerization. The obtained photoactive polymers were photografted to porous poly(glycidyl methacrylate) microspheres. The advantage of spatial resolution in light-induced grafting protocols was demonstrated by preparing Janus microspheres using a pickering emulsion approach.[121] In another study, Stolzer *et al*. modified silver nanoparticles with *o*-methylbenzaldehyde groups using a benzotriazole linker. Maleimide terminal PEG and poly(carboxybetaine methacrylate) were successfully photografted to the surface of the silver nanoparticles.[133]

The photoenol ligation was also used for nanoparticle functionalization in the current thesis. Two novel approaches for the grafting of polymers to nanodiamonds *via* the photoenol ligation are described in Chapter 3 and Chapter 4.

2.3.2. Tetrazole chemistry

In 1959, the thermal decomposition of 2,5-disubstituted tetrazoles under release of nitrogen and formation of nitrile imine intermediates was introduced.[134] In 1967, Sustmann and coworkers reported the use of light to trigger the tetrazole cycloreversion reaction, which laid the foundation for modern tetrazole photochemistry.[135] Upon UV irradiation, tetrazoles release nitrogen and form nitrile imines, which are 1,3 dipoles (Scheme 2.9). Subsequently, the highly reactive nitrile imine intermediate can be trapped in a 1,3-dipolar cycloaddition with a dipolarophile to form a fluorescent pyrazoline link. The photo-induced reaction sequence is also known as the nitrile imine mediated tetrazole-ene cycloaddition (NITEC) reaction. The reaction yields a fluorescent product from non-fluorescent starting materials (profluorescent reaction), which can be exploited for the monitoring of the reaction progress *via* fluorescence spectroscopy. The generation of a fluorescent cycloadduct is also highly interesting for imaging applications, as demonstrated in Chapter 5.
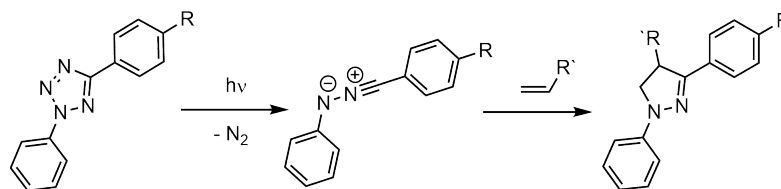
Scheme 2.9. Mechanism of NITEC reaction. Irradiation of a diphenyl tetrazole leads to a cycloreversion reaction forming a nitrile imine intermediate that can be trapped with an alkene in a subsequent 1,3-dipolar cycloaddition.

The reaction of nitrile imines generated by photolysis of tetrazoles with alkenes was employed in several studies. However, it was shown that nitrile imines can also react with a variety of nucleophiles, including carboxylic acids and thiols.[136–138] Thus, the NITEC reaction does not classify as a bioorthogonal reaction. Nevertheless, it is a powerful tool for fast and efficient ligations with the benefit of producing a fluorescent product.

In polymer science, the NITEC ligation was employed for step-growth polymerization,[139,140] block-copolymer synthesis,[141–143] crosslinking[144–147] and surface grafting.[148,149] The application of photo-triggered tetrazole reactions for SCNPs is discussed in section 2.5.

For instance, a diphenyl tetrazole functional trithiocarbonate CTA was prepared and employed for the statistical RAFT copolymerization of acrylonitrile and 1,3-butadiene. The tetrazole capped nitrile-butadiene rubber (NBR) polymers were selectively coupled with a bismaleimide linker. Interestingly, no side reactions with the double bonds from the NBR backbone were observed.[141] However, in another study, 1,2-polybutadienes were crosslinked with a tetrazole dilinker. It was shown that also non-activated double bonds are addressable with NITEC reactions.[144] The results obtained from the two studies indicate that in the presence of activated and non-activated double bonds, nitrile imines selectively react with the activated double bonds. However, non-activated double bonds are also feasible to undergo NITEC reactions, especially when large excess or high local concentrations (in the case of networks) are employed.

The application of NITEC chemistry for spatially resolved surface encoding was demonstrated in several studies.[148–151] For example, cellulose (filter paper) was functionalized with tetrazole groups. A shadow mask allowed for the
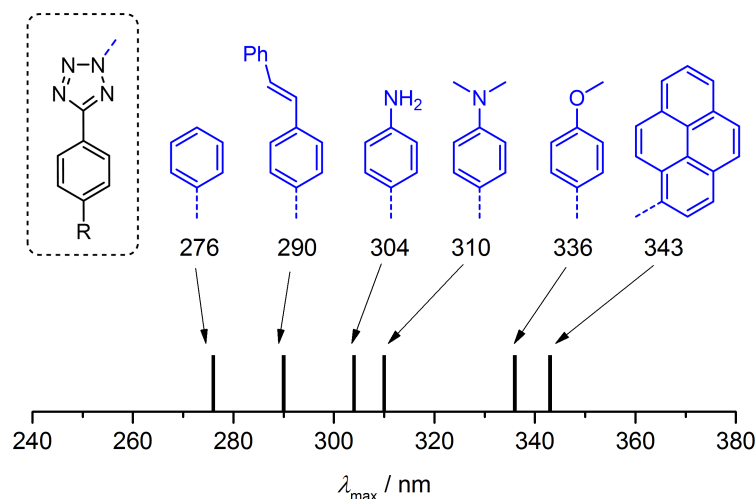
Figure 2.4. *N*-substituted phenyl tetrazoles in order of their absorption maximum λ_{max}.

spatially resolved functionalization of the cellulose surface with a maleimide functional tertiary bromine compound *via* NITEC reactions. Subsequently, carboxybetaine acrylamide was polymerized from the patterned surface *via* an ATRP process to obtain a non-fouling polymer layer.[149]

The red-shifting (bathochromic shifting) of photochemical ligation reactions is of great importance for many applications. For instance, many biomolecules absorb UV light and high energy irradiation can cause cell damage. Thus, low-energy (long wavelength) triggered photochemical ligations are highly desirable. In order to red-shift the absorption, a variety of tetrazole derivatives have been prepared. As shown by Lin and coworkers, the introduction of auxochromic or conjugative substituents in *para*-position of the *N*-phenyl moiety leads to a bathochromic shift in absorbance (Figure 2.4).[152,153] Barner-Kowollik and coworkers showed that the introduction of a *N*-pyrenyl substituent on the tetrazole ring could shift the absorption maximum even further (343 nm, Figure 2.4).[142] Importantly, the pyrene-tetrazole

group could be activated using visible light (blue LED, λ = 410-420 nm). Upon blue light irradiation, pyrene-tetrazole terminal PCL was reacted with maleimide capped PNIPAM and PEG to form well-defined block copolymers. Using upconversion nanoparticles, the reaction could be triggered with near infrared (NIR) light (λ = 974 nm).[143] Through-tissue irradiation and coupling of pyrene-tetrazole terminal PCL with a maleimide functional biotin derivative under retention of biotin activity were performed, demonstrating the suitability for biological applications.

2.4. Glycopolymers

Glycopolymers are biomimetic macromolecules that are inspired from natural carbohydrates and consist of a synthetic backbone with pendant carbohydrate units. Carbohydrates play an important role in many biological processes, such as inflammation, cancer cell metastasis and pathogen infection.[154] The motivation for the design of novel glycopolymeric materials is to mimic the activity of carbohydrate structures with synthetic systems in order to expand the knowledge about carbohydrate activity and generate novel materials for biomedical applications. The key process for the bioactivity of carbohydrate structures, such as natural glycoproteins or synthetic glycopolymers, is their interaction with lectins.[155]

Glycopolymers are either prepared by the polymerization of sugar containing monomers (glycomonomers) or the post-polymerization modification of functional polymers with carbohydrate units. The advantage of the first approach is the use of well-characterized monomers (in terms of *e.g.* stereochemistry) and polymers with high carbohydrate content are readily accessible. The post-polymerization functionalization approach allows for the facile preparation of glycopolymer libraries with different side group compositions starting from the same precursor for comparative studies. Using modern polymerization protocols, a variety of glycopolymer architectures are accessible, including linear polymers, star polymers and glycopolymer coated nanoparticles (Figure 2.5).[155–157]

Glycopolymers with different sugar epitopes have been reported, including glucose,[158–163] fructose,[164,165] galactose,[166,167] and lactose.[168–170] Extensive

| linear polymer | star polymer | polymer grafted nanoparticle |
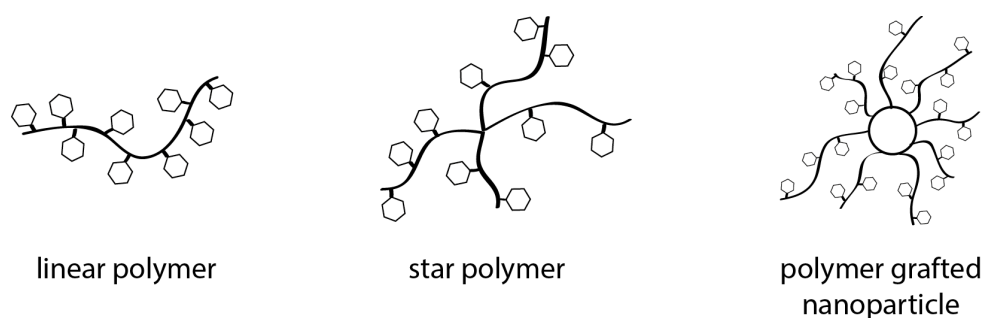
Figure 2.5. Schematic representation of important glycopolymer architectures.

reviews about glycopolymer syntheses and applications are reported in the literature.[154,155,157,171–178] The focus of the following sections is on mannose based glycopolymers prepared *via* radical polymerization due to the relevance in the current thesis (Chapter 3-5).

2.4.1. Synthesis of mannose monomers

Glycomonomers are not commercially available and thus a variety of synthetic protocols have been developed to prepare them.[155] Usually, a spacer is incorporated between the vinyl and the carbohydrate unit. Chemical glycosylations, which are coupling reactions of glycosyl donors and glycosyl acceptors forming a new glycosidic bond, are the most common synthetic methods to prepare glycomonomers (Scheme 2.10). The glycosyl donor is the carbohydrate unit containing the anomeric centre where the glycosylation occurs. A good leaving group (LG) on the anomeric centre is required for glycoslylations to occur. A hydroxy group can act as a leaving group (Fischer glycosylation), however more effective leaving groups have been developed, such as acetates, halides or imidates (Scheme 2.10). Typically, an activator (commonly a Lewis-acid) is used to cleave the leaving group off the glycosyl donor to form an oxocarbenium ion. Subsequently, the glycosyl acceptor reacts as a nucleophile with the activated glycosyl donor to form a glycosidic bond.[179] The glycosylation can be performed with vinyl containing glycosyl acceptors or a linker molecule, which is modified in a subsequent step with a polymerizable group.

BF$_3$-catalyzed glycosylation of peracetylated mannose

A common starting material for mannose glycomonomer syntheses is peracetylated mannose. The acetylation of mannose is typically performed with acetic anhydride and a catalytic amount of H$_2$SO$_4$. The reaction can be performed on large scales, proceeds with full conversion and no chromatographic purification steps are required.
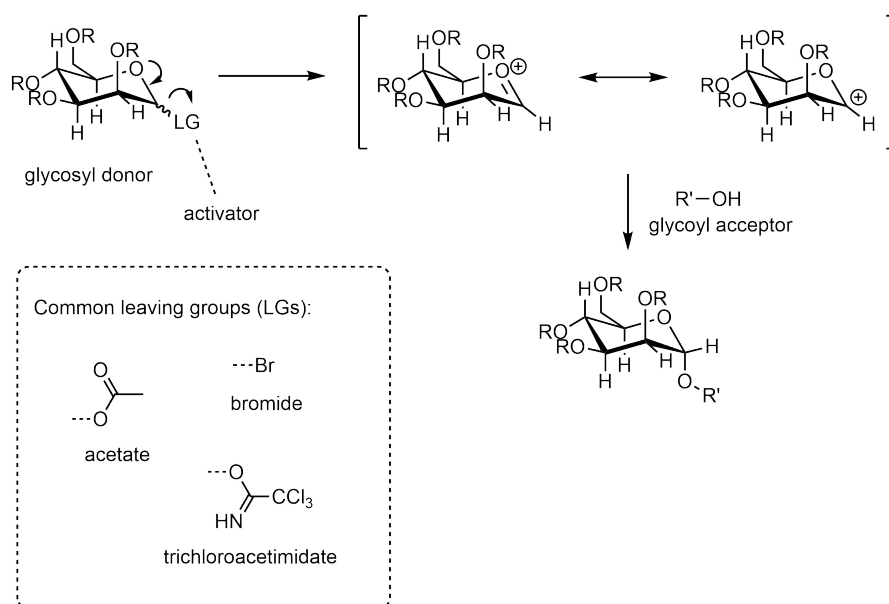
Scheme 2.10. Mechanism of chemical glycosylation and typical leaving groups of glycosyl acceptors.

The BF_3 catalysed glycosylation of peracetylated mannose is a key reaction employed for glycomonomer syntheses as well as for the preparation of reactive compounds for post-polymerization modifications. The mechanism is depicted in Scheme 2.11. The promoter BF_3 activates the acetyl leaving group to form an oxocarbenium intermediate. Subsequently, the acetyl group in the C-2 position forms a cyclic acyloxonium ion complex that shields, in the case of mannose, the β-position and allows the acceptor only to attack from one side. Consequently, only the α-anomer is formed.[179]

2-Hydroxy ethyl acrylates,[180,181] acrylamides,[182] or methacrylates[183–186] are commonly used as glycosyl acceptors (Figure 2.6). The deprotection of the acetate protecting groups is typically performed on the polymer since the deacetylation conditions (*e.g.* sodium methoxide in methanol) lead to the partial cleavage of (meth)acrylate ester bonds and further purification is required. However, deprotection on the polymer does not cleave the ester bond close to the backbone. Furthermore, the polymerization of protected sugars has the advantage of improved solubility in organic solvents, which is important for the synthesis of amphiphilic multiblock copolymers.
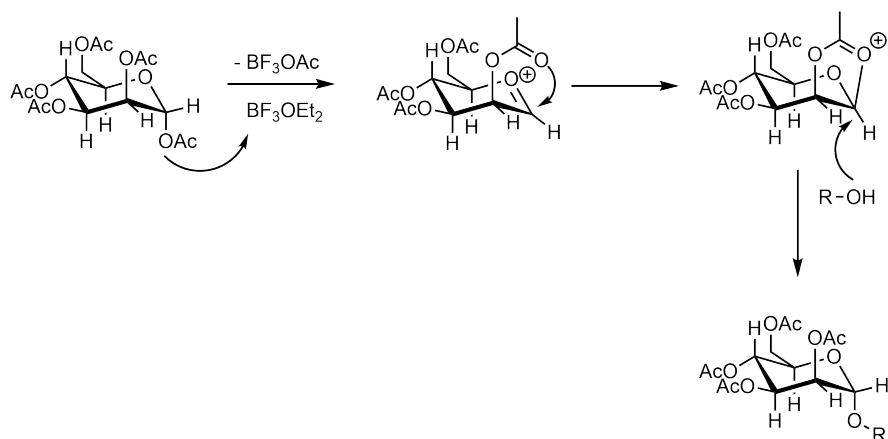
Scheme 2.11. Mechanism of BF$_3$-catalyzed glycosylation of peracetylated mannose.
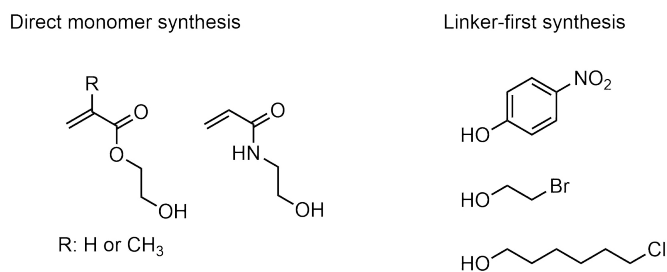
Figure 2.6. Common glycosyl acceptors used for the BF$_3$-catalyzed glycosylation of peracetylated mannose to prepare glycomonomers.

Furthermore, peracetylated mannose can be first glycosylated with a linker molecule that bears a functional group that is modified with a polymerizable functionality in a subsequent step. Typical linker molecules are depicted in Figure 2.6. For example, Miura and coworkers used *para*-nitrophenol as a linker. After glycosylation the nitro group was reduced to an amine and coupled to acryloyl chloride to form a mannose acrylamide monomer.[187] In another study, 2-bromoethanol was used as a glycosyl acceptor. The bromo group can be substituted with an azide group and subsequently coupled with an alkyne functional monomer in a copper catalyzed azide alkyne cycloaddition (CuAAC) reaction.[188,189] Matsuoka and coworkers glycosylated peracetylated mannose with 6-chloro-hexanol.[190] Subsequently, the chloro group was substituted with sodium azide, reduced to an amine and reacted with acryloyl chloride to form an acrylamide glycomonomer.

Mannose monomer synthesis *via* trichloroacetimidates
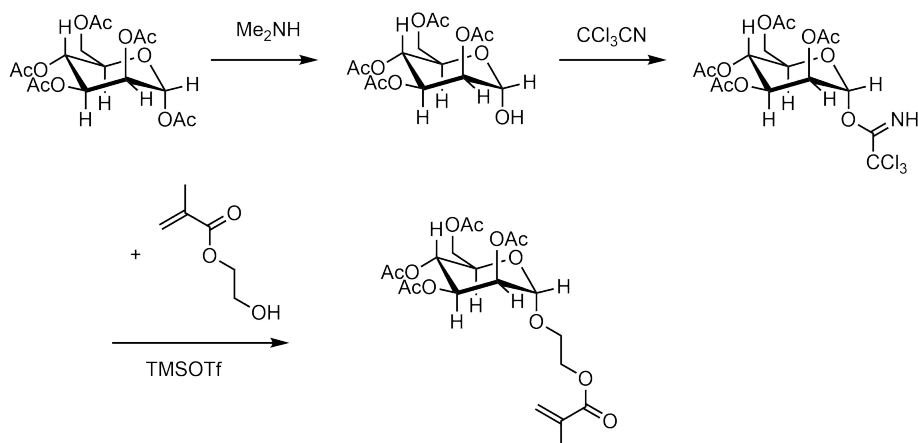
Scheme 2.12. Glycosylation of mannose trichloroacetimidate with 2-hydroxyethyl methacrylate.

Trichloroacetimidates were introduced by Schmidt and Michel in 1980 and are commonly used glycosyl donors for glycoside syntheses.[191] For instance, Song *et al.* prepared methacrylate monomers using trichloroacetimidate glycosyl donors.[192] Mannose *O*-glycosyl trichloroacetimidate was prepared from a reaction of trichloroacetonitrile with the free anomeric hydroxy group of mannose under basic conditions (Scheme 2.12). Subsequent glycosylation with 2-hydroxyethyl methacrylate in the presence of trimethylsilyl trifluoromethanesulfonate as a catalyst yielded a mannose monomer for radical polymerization.

Shoda activation

A protecting-group free synthetic approach to mannose monomers was introduced by Kimura and coworkers.[193] The one-pot synthesis from non-protected sugars is based on the so-called Shoda activation. 2-Chloro-1,3-dimethylimidazolinium chloride (DMC) promotes a dehydrative condensation reaction to form 1,6-anhydro mannose in aqueous media.[194] In the presence of aryl thiols, 1-thioglycosides are formed.[195] The use of 4-aminothiophenol as a nucleophile allowed the preparation of amine functional mannose that was subsequently reacted with acryloyl chloride to form an acrylamide mannose derivative.[193]
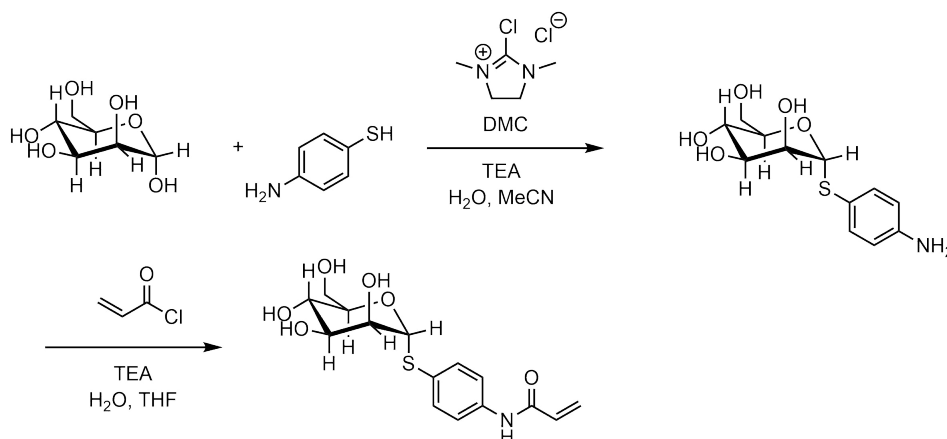
Scheme 2.13. Protecting-group free glycosylation of mannose *via* the Shoda activation and subsequent amidation reaction.

2.4.2. Radical polymerization of mannose monomers

Conventional FRP was initially used to prepare glycopolymers from vinyl functional mannose compounds and is still employed for applications where high control over polymer structure is not required.[183,187,189,190,196–201] An overview of mannose glycomonomers polymerized *via* FRP is depicted in Table 2.1. Protected glycomonomers are typically polymerized in organic solvents, such as *N,N*-dimethylformamide (DMF)[189] or dimethyl sulfoxide (DMSO).[199] The deprotection of the sugar residues is then performed on the polymer. Protecting-group free glycomonomers, deriving either from protecting-group free syntheses or the deprotection of protected glycomonomers are highly hydrophilic and thus polymerized in aqueous solutions,[197] polar organic solvents[187,196,201] or mixtures of both.[198]

For instance, Williams and coworkers prepared statistical copolymers consisting of 2-hydroxyethyl methacrylate (HEMA) and an acetyl protected mannose monomer using FRP in DMF with AIBN as the radical initiator. The copolymers were deprotected with sodium methoxide in DMF and showed mannose density dependent lectin binding properties (Table 2.1, entry 1).[189]

Table 2.1. Overview of mannose glycomonomers polymerized *via* FRP. I: Initiator; S: Solvent; C: Catalyst.

Entry / Ref.	Monomer	Polymerization conditions / polymer structure
1 / [189]		I: AIBN; S: DMF / statistical copolymer with HEMA
2 / [183]		I: AIBN; S: DMF / statistical copolymer with HEMA
3 / [190]		I: ammonium persulfate; C: TMEDA; S: water / statistical copolymer with acrylamide
4 / [199]		I: AIBN; S: DMSO / homopolymer
5 [187, 196, 201]		I: V-501; S: DMSO; surfactant: SDS / statistical copolymer with NIPAM, *N*-tert-butylacrylamide , acrylic acid, *N,N*-methylenebis(acrylamide);[187,201] statistical copolymer with acrylamide[196]
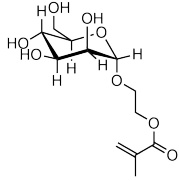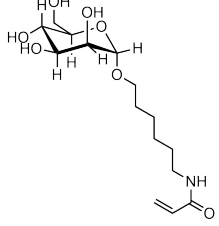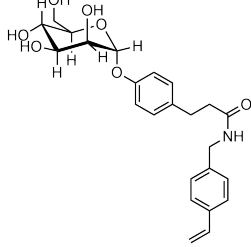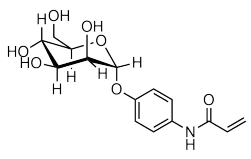
Table 2.1. Continued from previous page.

Entry / Ref.	Monomer	Polymerization conditions / polymer structure
6 / [197]		I: ammonium persulfate; C: TMEDA; S: water / statistical terpolymer with acrylamide and a β-lactosyl monomer
7 / [198]		I: DODA-501; S: water/methanol, 2:1, v:v / homopolymer
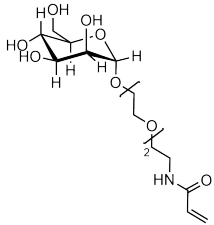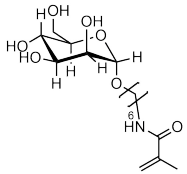
Reversible-deactivation radical polymerization (RDRP) techniques allow the preparation of well-defined and complex glycopolymer structures (Section 2.2). In this context, different mannose monomers have been polymerized using RAFT polymerization and ATRP (Table 2.2).

For instance, ABC triblock terpolymers have been prepared *via* RAFT polymerization of an acetyl-protected mannose acrylate with *n*-butyl acrylate and 4-vinylpyridine followed by a deacetylation step to obtain well-defined, amphiphilic and pH responsive polymers (Table 2.2, entry 1). The terpolymers were self-assembled into compartmentalized nanostructures with efficient cellular uptake into macrophage cells.[180]

Obata *et al.* employed aqueous AGET ATRP with 2-azidopropyl 2-bromo-2-methylpropanoate as an initiator. The obtained azide terminal mannose glycomonomers were coupled to alkyne terminal poly(L-lactide) in a CuAAC reaction. The block-copolymers self-assembled into complex aggregates as shown from dynamic light scattering (DLS) measurements.[185]

Table 2.2. Overview of mannose glycomonomers polymerized by RDRP techniques.

Entry / Ref.	Monomer	Polym. technique	Polymer structure
1 / [180, 181]		RAFT	ABC triblock terpolymer with n-butyl acrylate and 4-vinylpyridine;[180] 4-arm star polymer with diblock arms with HEA[181]
2 / [186]		RAFT	diblock copolymer with DMAEMA
3 / [202, 203]		RAFT	statistical copolymer with acrylamide
4 / [182]		RAFT	diblock copolymer with pentafluorophenyl acrylate
5 / [184, 185, 192]		RAFT,[184,185] ATRP[185]	statistical copolymer with pyridyl disulfide ethyl methacrylamide;[192] diblock and statistical copolymer with DMAEMA;[184] and diblock copolymer with PLLA[185]
6 / [188]		ATRP	statistical copolymer with rhodamine B methacrylate
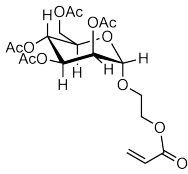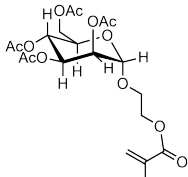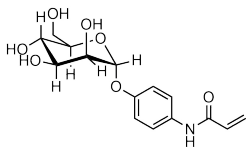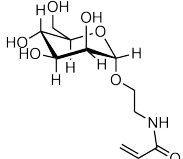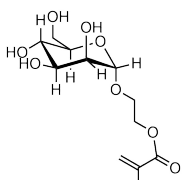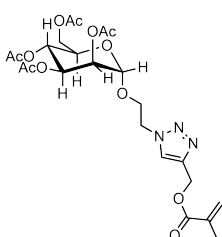
2.4.3. Mannose glycopolymers *via* post-polymerization modification protocols

An elegant alternative to the polymerization of glycomonomers is the post-polymerization modification of synthetic polymer scaffolds. A post-polymerization approach offers the possibility to prepare glycopolymer libraries with different sugars and the same polymer scaffold. Furthermore, glyco monomers often tend to self-polymerize and their syntheses contain tedious purification steps. Post-polymerization protocols often allow the facile purification of the reaction mixture using dialysis or precipitation.

The amidation reaction of a polymer with pendant carboxylic acid groups with an amine functional sugar is a highly efficient modification method (Scheme 2.14, A). Bertin *et al.* prepared a triblock terpolymer with a *N*-hydroxysuccinimide ester functional block that was converted into a glycopolymer block by an amidation reaction with an excess of D-glucosamine or D-mannosamine under basic conditions.[204] Full conversion was observed for the glucose derivative, whereas only 60 % conversion could be obtained with the mannose derivative. The limited conversion of D-mannosamine was explained with steric hindrance at the axial amine position. The prepared terpolymers were successfully employed for the preparation of micelles.
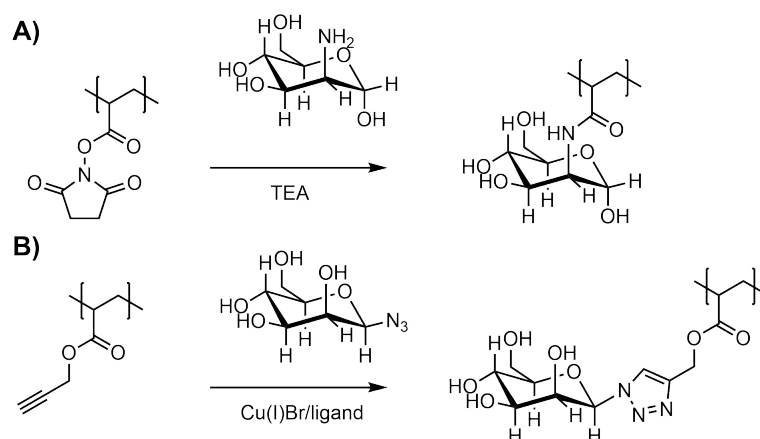
Scheme 2.14. Post-polymerization modification approaches for the preparation mannose glycopolymers. A: amidation[204]; B: CuAAC reaction.[205–207]

Another efficient post-polymerization modification approach to mannose gly-copolymers is the CuAAC functionalization of alkyne decorated polymers with azide mannose (Scheme 2.14, B).[205–207] α-Azido mannose can be prepa-red from free mannose using 2-chloro-1,3-dimethylimidazolinium chloride and sodium azide (Shoda activation). Gibson and coworkers optimized the reaction conditions of the CuAAC and found that tris[(1-benzyl-1H-1,2,3-triazol-4-yl)methyl]amine (TBTA) showed improved reaction kinetics.[205]

2.4.4. Applications of mannose glycopolymers

The increasing interest in glycopolymer based materials is due to their excep-tional lectin binding properties.[155] In addition to biomedical applications, the structure-activity correlation of glycopolymers is an important research field. The influence of polymer topography, sugar type, composition and density on lectin binding are key areas of interest. A variety of lectin binding assays has been developed to establish what polymer architecture and composition is optimal for efficient binding.[155] Cheap and easily available model lectins are normally used for binding assays. Concanavalin A (ConA) is a commonly used model lectin to investigate the bioactivity of mannose glycopolymers. It is a plant lectin that can be extracted from jack beans. ConA consists of 238 amino acid residues and exists as a tetramer with four saccharide binding pockets.[208]

Due to the tetrameric structure of ConA, it can bind to four mannose units. If the mannose units are attached to more than one polymer chain, crosslinking induced aggregation occurs (Scheme 2.15). The aggregation is accompanied
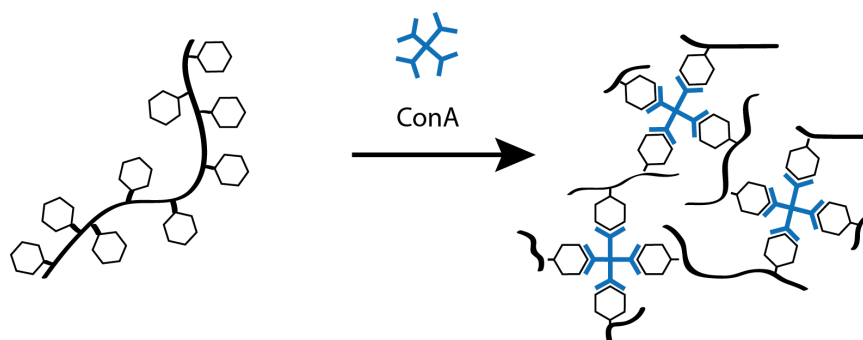
Scheme 2.15. Schematic representation of ConA-induced glycopolymer crosslinking.
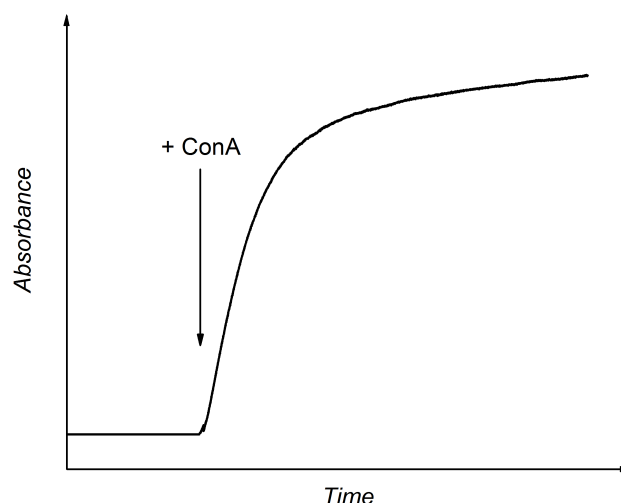
Figure 2.7. ConA turbidity assay to investigate the binding activity of glycopolymers to ConA.

with an increase in particle size, which is manifested in an observable turbidity. The turbidity is usually measured using UV-vis spectroscopy (Figure 2.7). The turbidity assay allows for the fast and facile qualitative investigation of ConA binding. Where quantitative information about lectin binding is required, other assays such as precipitation assay and surface plasmon resonance (SPR) are more suitable.[181]

The binding of single carbohydrate units to lectins is usually weak. However, if the lectin possesses multiple binding sites (*e.g.* ConA) more than one ligand of a multivalent system can bind (chelation). After the first ligand is bound, the binding of a second ligand is enhanced due to decreased translational and rotational entropy loss.[209] Binding enhancements are also observed with lectins that possess only one binding site due to several effects, such as statistical rebinding (proximity/statistical effects) and receptor clustering.[210] The enhancement of binding properties of multivalent glyco ligands is known as the *glycocluster effect*.[211]

Kiessling and coworkers reported an extensive study of multivalency on lectin binding.[210] Glycopolymers displayed up to 2000-fold more effective binding

to ConA than α-methyl mannose. The binding efficiency increased with increasing molecular weight and mannose density on the polymer backbone.[210]

Mannose glycopolymers as therapeutics

Glycopolymers have been investigated for therapeutics and drug delivery applications due to their interesting lectin binding properties. For instance, the use of glycopolymers for anti-viral therapeutics relies on the binding and blocking of specific cell receptors that viruses use for receptor-mediated endocytosis.[172]

For example, mannose glycopolymers have been investigated for the use as therapeutics for human immunodeficiency virus (HIV). The surface of HIV is decorated with the highly glycosylated protein gp120.[212] The mannosylated glycans on HIV bind to the lectin DC-SIGN on dendritic cells to escape the immune response and induce their internalization.[213] Haddleton and coworkers have prepared mannose glycopolymers that inhibit the interactions between gp120 glycoproteins on HIV and the lectin DC-SIGN for potential treatment of HIV infection.[214]

Mannose glycopolymers for drug delivery systems

Glycopolymers are highly promising building blocks for drug delivery systems.[180,183,215] In addition to their biocompatibility and high hydrophilicity, which are key properties for the development of drug carriers, they possess interesting targeting properties. Targeted drug delivery is the selective accumulation or release of a drug in a specific part of the body. The aim is to reduce the drug concentration and side effects in patients.[216] Importantly, the binding of glycopolymers to cell-specific lectins can induce receptor-mediated endocytosis leading to accumulation in the specific cell type. Mannose glycopolymers are typically investigated for targeting macrophages and dendritic cells, since mannose receptors are over-expressed on their cell surface.[155,175]

In this context, Giorgo and coworkers decorated azide functional micelles with mannose units to target the CD206 receptor on macrophages. The

self-assembled block copolymers consisted of a cationic PDMAEMA block that allowed for the encapsulation of siRNA.[217] Compared to mannose-free micelles, a four-fold improvement in the delivery of siRNA to macrophages was achieved. Furthermore, a 13 times higher cellular uptake in human macrophages was observed compared to model breast cancer cells.

The potential of mannose glycopolymers to target dendritic cells was shown in a study from de Geest and coworkers, where mannosylated nanogels were investigted.[182] Mannose receptors on dendritic cells allowed higher cellular uptake of mannosylated nanogels compared to galactosylated nanogels as shown by flow cytometry analysis.

Nanoparticles inspired by viruses

For the development of drug delivery systems, nature gives impressive examples that have inspired many scientists. Viruses are highly efficient in penetrating cell membranes and releasing their cargo in host cells. They bind to specific receptors on cells promoting cellular uptake and initiating productive infection.[218] Viruses are typically between 20-300 nm in size and exist in different shapes. Their well-defined surface structure and chemistry allow them to evade the body's defence system and promote efficient internalization into cells. In enveloped viruses, the outer membranes are typically decorated with envelope glycoproteins that often protrude in a spike-like manner from the surface. The viral surface topography including the so-called glycoprotein spikes, is believed to play an important role for their success in invading cells.[219–221] For instance, HIV with its highly glycosylated envelope glycoproteins, binds to mannose receptors on macrophages and dendritic cells.[219] Roux and coworkers have established the structure of envelope glycoprotein spikes on AIDS retroviruses *via* cryo electron microscopy tomography (Figure 2.16).[222] The envelope spikes on HIV consist of gp120 trimers and the transmembrane envelope glycoprotein gp41. The investigated virions had diameters close to 110 nm. The surface of simian immunodeficiency virus (SIV) was covered with 73 ± 25 spikes, whereas HIV possessed only 14 ± 7 spikes per particle. The glycoprotein spikes were 13.7 nm high with a head diameter of 10.5 nm and the tripod-like legs were between 1.9 to 3.7 nm in diameter.
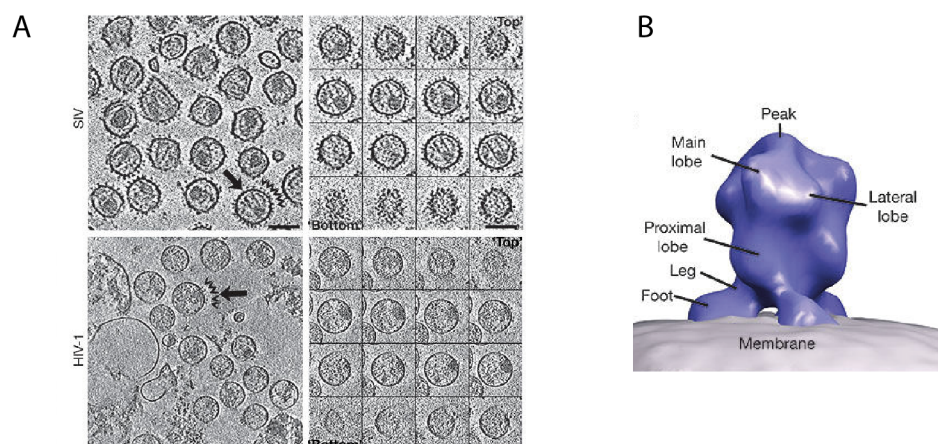
Scheme 2.16. A: Tomographic images of mutant SIV (top) and wild-type HIV-1 (bottom). Arrowheads are pointed onto glycoprotein spikes. Scale bars: 100 nm. B: Surface rendered model of SIV envelope glycoprotein spike. Adapted from reference [222] with permission from Nature Publishing Group.

The examples on mannosylated synthetic nanoparticles described in the previous section can be regarded as very simplistic virus mimics, where the targeting ligands are inspired by viruses. However, much more complex systems have been developed to mimic the structure of viruses with the intention to develop highly efficient drug delivery systems.

Viral glycoprotein structures have been mimicked using glycopolymer-protein conjugates.[188] A small library of glycopolymer-BSA conjugates was prepared by modifying poly(propargyl methacrylate) with galactopyranoside and mannopyranoside azides using the CuAAC reaction followed by its conjugation to BSA. The prepared glyco conjugates bound to recombinant rat mannose-binding lectin and were capable of activating the complement system *via* the lectin pathway.

The influence of nanoparticle surface roughness on cellular uptake was explored by Niu *et al*. Inspired by the surface topography of viruses, silica nanoparticles ($\sim$ 170 nm) were decorated with smaller silica nanoparticles ($\sim$ 6 nm) to generate a rough surface structures.[223] The nanoscale surface roughness enhanced the cellular uptake performance of the nanoparticles. Mimicking both the surface topography and the lectin binding ability of viruses has the potential of providing nanoparticles that are highly efficient in

invading specific cells.

Stenzel and coworkers described the controlled self-assembly of an ABC tri-block copolymer consisting of a mannose glycopolymer block, a poly(n-butyl acrylate) and a pH responsive poly(4-vinylpyridine) block.[180] Different morphologies resembling viruses were obtained by altering the pH value during self-assembly. Spherical as well as elongated patchy particles were obtained. The mannosylated nanoparticles were efficiently uptaken by RAW 264.7 macrophages. Flow cytometry experiments showed higher cellular uptake of worm-like structures compared to a spherical structure. However, no significant difference in cellular uptake between patchy and classical worm-like structures was observed.

Several studies have demonstrated the high potential of mannose glycopolymers for biomedical applications. In Chapter 5, a novel virus-inspired mannose glycopolymer nanostructure is introduced and its potential for nanomedicine is discussed.

2.5. Single-chain nanoparticles

Single-chain nanoparticles (SCNP) are polymeric nanoparticles consisting of single crosslinked polymer chains. The first description of SCNPs can be dated back to 1956, when Kuhn and coworkers described that the crosslinking of polymer solutions below a critical concentration leads to a decrease in viscosity.[224] However, until the development of modern polymerization techniques in the late 1990s,[225–227] which allowed the preparation of well-defined functional polymers, SCNPs remained unstudied. Due to structural similarities, SCNPs are often described as simple mimicries of folded protein structures. Comparable to proteins, SCNPs consist of polymer chains with intramolecular crosslinks that lead to a compact structure. However, the precision of proteins to fold into a defined secondary, tertiary and quaternary structure arising from the monomer sequence has not yet been achieved in SCNP systems. Polymeric nanoparticles of sizes below 10 nm in diameter are easily accessible using the SCNP approach, which cannot be obtained from conventional preparation methods, such as nanoprecipitation and emulsion polymerization.[228] The size of SCNPs can be fine-tuned by altering crosslinking density and polymer chain length.[229] Furthermore, properties and functionalities can be easily adjusted by varying the polymer composition. Several potential applications for SCNPs have been discussed, including catalysis,[230–232] sensors,[233] and drug drug delivery systems.[234]

2.5.1. Synthetic strategies

The crosslinking of polymers in concentrated solutions leads to the formation of networks due to intermolecular reactions. However, at concentrations below the overlapping concentration of single chains, predominantly intramolecular reactions occur and SCNPs are formed.

The intramolecular crosslinking of polymers can be performed either *via* the *selective point folding* or *repeating unit* approach. In the *selective point folding* approach, recognition units are placed at defined positions along the polymeric backbone.[235] Using this synthetically challenging approach, structures with defined folding points along the polymer chain can be prepared. Simple,

but defined architectures, such as cyclic,[236,237] and bicyclic structures,[238,239] have demonstrated the potential of this approach. The aim of this research field is to mimic the structure of proteins and prepare synthetic polymers with functions arising from their folded structure.[240] Synthetic tools that enable the defined positioning of multiple recognition units along the polymer backbone are required for the generation of protein-like structures. Recent advances in the synthesis of sequence defined polymers demonstrate the possibility to prepare polymers with a defined primary structure.[241–244] The introduction of selective point folding motifs in such systems will probably enable the preparation of folded synthetic polymeric structures of unprecedented precision.

Synthetic avenues to SCNPs typically follow the so-called *repeating unit* approach, where the crosslinking units are placed randomly along the polymeric backbone. The *repeating unit* approach is synthetically easier than the *selective point folding* approach, however, yield less defined structures.[235] Random, crosslinking groups containing copolymers with controlled molecular weight and low dispersities can be easily prepared using modern RDRP techniques (see Section 2.2). The *repeating unit* approach leads to single-chain architectures with randomly distributed crosslinks and globular structures. This approach was employed in Chapter 5 of the current thesis for the preparation of glyco SCNPs.
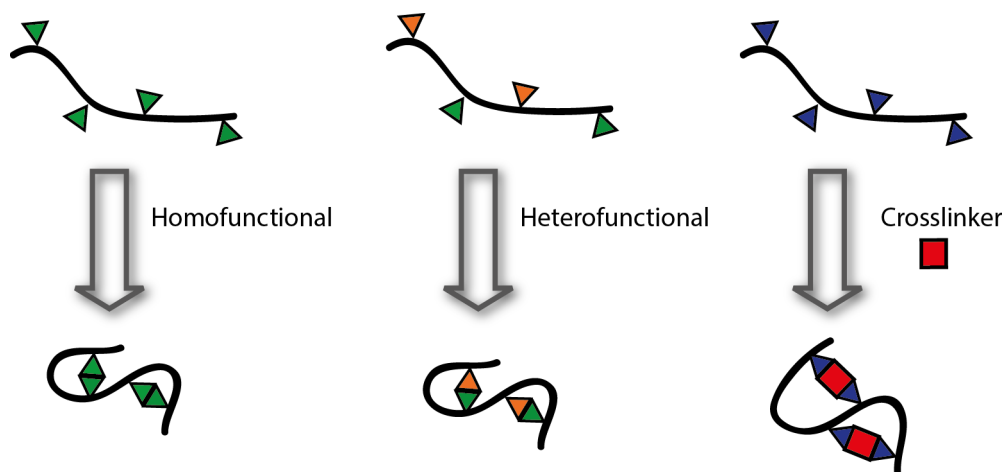
Scheme 2.17. Schematic representation of different crosslinking approaches for the preparation of SCNPs.

The preparation of SCNPs can be further categorized into three general cros-slinking strategies (Scheme 2.17). Firstly, a homofunctional crosslinker can induce the single chain collapse, *e.g.* through dimerization reactions. Secondly, a heterofunctional crosslinker can be employed and finally, the crosslinking of single polymer chains can be performed using an external crosslinker. Typically, highly diluted polymer solutions are used to prevent network formation. However, the continuous addition method allows for the preparation of SCNPs without the extensive use of solvent.[245,246] The slow addition of a concentrated polymer solution to a solution that triggers the crosslinking reaction provides a low non-crosslinked precursor concentration at any time and prevents intermolecular reactions.

Single polymer chains have been crosslinked *via* covalent,[127,146,147,233,246–248] dynamic covalent,[249–252] metal complexation,[232,253] and non-covalent cross-links.[254–257]

Due to the relevance for the current thesis (Chapter 5), the photochemically driven single-chain collapse is discussed in detail in the following paragraphs. Several studies have shown that the incorporation of photoactive groups, which allow for crosslinking upon light irradiation, is an efficient approach for the preparation of SCNPs.[257–260]

For instance, Berda *et al.* prepared a PMMA based polymer with *o*-nitrobenzyl protected 2-ureidopyrimidinone (UPy) side group functionalities. Upon UV irradiation the UPy groups were deprotected and the polymer chains collapsed due to UPy dimerization. The formation of SCNPs based on intra-chain hydrogen bonds was confirmed by size exclusion chromatography (SEC) and AFM experiments.[257]

He *et al.* prepared SCNPs *via* the photodimerization of coumarin. UV irradiation ($\lambda > 310\,\mathrm{nm}$) of coumarin functional polymers led to a chain size compaction as shown by SEC measurements. Interestingly, the crosslinking was reversible. UV irradiation at shorter wavelengths ($\lambda_{max} = 254\,\mathrm{nm}$) led to de-crosslinking and the formation of a free coil structure.[259]

Light induced ligations based on photoenols and tetrazoles were introduced in Section 2.3 and are efficient crosslinking methods for the preparation of SCNPs as shown in several reports.[128,138,146,147,260]

The application of photoenol chemistry for the preparation of SCNPs was first described by Altintas *et al.*[127] Polystyrene (PS) based polymers were functionalized with *o*-methyl benzophenone and maleimide groups. Upon UV irradiation (λ_{max} = 320 nm) in highly diluted solutions, light-triggered Diels-Alder reactions induced the formation of SCNPs. Blasco *et al.* transferred the photoenol approach to fluorescent polymers based on poly(thiophene). Interestingly, upon intramolecular crosslinking the fluorescence intensity was blue-shifted and decreased in intensity, probably due to changes in chain conformation.[260] In another study, phenacyl sulfide and photoenol chemistry were employed for the stepwise collapse of single polymer chains.[128] A methacrylate based polymer bearing lateral *o*-methyl benzaldehyde and phenacyl sulfide groups was first irradiated at λ_{max} = 355 nm where a thioaldehyde group was formed from the phenacyl moieties that reacted with a dithiol crosslinker. Chain compaction was shown *via* SEC measurements. Subsequent irradiation at λ_{max} = 320 nm in the presence of a diacrylate linker allowed further intramolecular crosslinking *via* photoenol Diels-Alder reactions that led to a second, less pronounced compaction.[128]

Recently, crosslinking reactions based on the photolysis of tetrazoles have gained increasing interest in the preparation of SCNPs.[138,146,147] Willenbacher *et al.* reported the light induced crosslinking of tetrazole and alkene functional PS polymers for the first time.[146] Importantly, they demonstrated that polymers that contain only tetrazole units and no alkene moieties can be crosslinked upon UV irradiation *via* dimerization reactions of photo-generated nitrile imines. The introduction of alkene groups to the system allowed for the preparation of fluorescent SCNPs *via* NITEC reactions.[146] Furthermore, photo-triggered tetrazole ligations were employed for the preparation of water soluble and degradable polymers.[138,147] In Chapter 5 of the current thesis, the preparation of NITEC SCNPs consisting of glycopolymers to obtain bioactive and fluorescent nanoparticles is described.

2.5.2. Characterization of single-chain nanoparticles

The intramolecular crosslinking of single polymer chains leads to a significant reduction in size (often termed as chain collapse). Analysis methods showing the size reduction (*e.g.* SEC, DLS, DOSY, TEM and AFM) in addition to characterization methods that elucidate the change in chemical structure (*e.g.* NMR, UV-vis, fluorescence, IR spectroscopy and mass spectrometry) are typically used to prove the formation of SCNPs.

Size exclusion chromatography (SEC) is the most commonly used characterization technique for following the collapse of single chains into SCNPs. SEC separates polymers by hydrodynamic volume, whereas large polymers elute first followed by smaller molecules.[261] Interchain crosslinking is manifested in broad distributions and shoulders at lower retention time whereas the successful formation of SCNPs leads to a signal shift towards higher retention time and often a decrease in dispersity. SEC is often used as a relative method showing the reduction in retention time, however, absolute size information can be extracted from SEC data, which is described in Chapter 5 of the current thesis.

Often apparent molecular weights, which are calculated from SEC calibration data, are discussed. As the name suggests, the apparent molecular weight does not represent the actual molecular weight. It serves as a measure of hydrodynamic size, where reductions in apparent molecular weight represent a decrease in hydrodynamic volume. Colmenero and coworkers derived an equation for the description of apparent SEC molecular weight M_{app} upon SCNP formation:[262]

$$M_{app} = c \cdot M^{\beta}$$
$$\beta = (1 + \alpha_F)/(1 + \alpha_{MHS})$$

$$(2.4)$$

The parameter α_{MHS} is the Mark-Howink-Sakurada (MHS) exponent for the linear precursor and α_F is a parameter related to the fractal degree of the SCNPs. For compact, uniform particles, β is estimated to be 0.56 and for nanoparticles with a fractal behaviour similar to flexible, swollen chains, it

is approximately one. The application of Equation 2.4 to values reported in literature showed that β lies in the expected range ($0.56 \leq \beta \leq 1$). Furthermore, the change in molecular weight dispersity ($Đ$) upon single chain collapse can be described with the following equation:[262]

$$Đ_{app} = Đ^{\beta^2} \tag{2.5}$$

Hence, single-chain collapse leads to a decrease in dispersity due to $\beta \leq 1$. In most cases, experimental data confirms this expectation, however, sometimes an increase in dispersity is observed, probably due to interchain crosslinking.[262]

Dynamic light scattering (DLS) is a powerful technique to determine absolute hydrodynamic diameter distributions of polymers or nanoparticles in solution. In a DLS experiment, the scattering intensity at a constant angle is measured over time. The collected data is analyzed using an autocorrelation function. An exponential fit allows the calculation of the diffusion coefficient (D) and using the Stokes-Einstein equation (Equation 2.6, T: temperature, k_b: Boltzmann constant, η: viscosity of solvent) the hydrodynamic diameters (D_h) of *e.g.* nanoparticles can be calculated.[263] DLS is often employed for monitoring the size compaction of the polymer chains upon SCNP formation.

$$D = \frac{k_b \cdot T}{3 \cdot \pi \cdot \eta \cdot D_h} \tag{2.6}$$

A recent article critically reviewed DLS values for SCNP systems reported in literature.[264] The diameters of SCNPs obtained from DLS measurements were plotted against the SEC determined apparent molecular weights of the polymeric precursors. Significant data scattering was observed. For one apparent molecular weight a range of different hydrodynamic diameters were reported, corresponding to a variety of densities. Varying amounts of crosslinks and different chemical structures lead to different SCNP densities. However, the magnitude of density scattering is remarkable and cannot exclusively be explained by structural differences.[264] Herein, another plot of literature values was performed to assess the accuracy of DLS measurements for the characterization of SCNP systems (Figure 2.8). SEC separates by size and
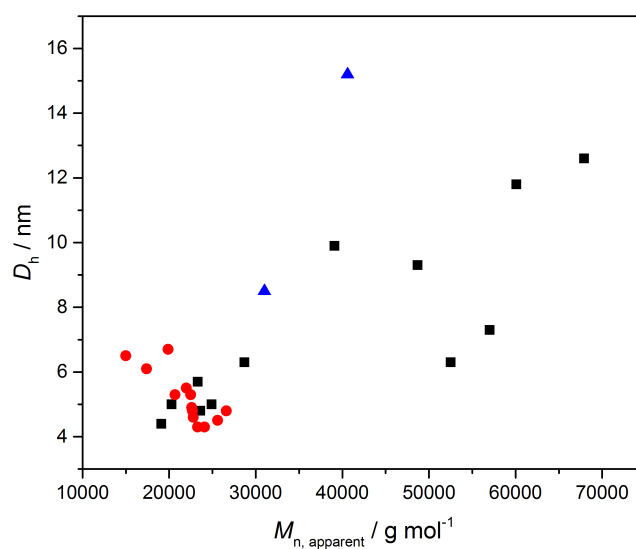
Figure 2.8. Hydrodynamic diameter of SCNPs and polymeric precursors determined
by DLS measurements in THF against the corresponding apparent mole-
cular weight determined by SEC in THF (black: T = n. a.;[255] red: T = 40
°C;[265] blue: T = 35 °C[232]). The plotted values are summarized in Table
A.1 (Appendix).

hence,[261] for the same measurement conditions (*i.e.* solvent and temperature)
one apparent molecular weight reflects one hydrodynamic volume. Thus,
an increase of hydrodynamic diameter with increasing apparent molecular
weight is expected for similar experimental conditions. However, the DLS
determined hydrodynamic diameters of literature reported values do not
strictly correlate with SEC determined apparent molecular weights as shown
in Figure 2.8. Even data obtained from the same instrument under the same
conditions do not reflect the expected correlation between SEC retention time
(or apparent molecular weight) and hydrodynamic diameter. Thus, the accu-
racy of hydrodynamic diameters from SCNP systems determined *via* DLS
needs to be reassessed.

Diffusion ordered NMR spectroscopy (DOSY) is a complimentary technique
to show the size reduction upon single-chain collapse.[147,232,246] Similar to
DLS analysis, diffusion coefficients are obtained and a hydrodynamic radius
can be calculated using the Stokes-Einstein equation (Equation 2.6). Careful
consideration is advised for the calculation of hydrodynamic sizes from DOSY

measurements, since information about the size distribution is not included in the diffusion coefficients. A SCNP sample consists of nanoparticles with varying sizes and can only be fully described with distributions data. However, an increase of the diffusion coefficient clearly indicates the reduction in size accompanied with SCNP formation.

The above described characterization methods are solution based and deliver information about the size of polymer particles in the solvated state. On the other hand, imaging techniques, such as atomic force microscopy (AFM) and TEM can be employed to investigate size and shape of SCNPs in the solid state. AFM and TEM experiments are usually performed after deposition of a SCNP solution on a surface and subsequent drying. It should be noted that the sample preparation step can influence the size and structure of the particles and might lead to aggregation.

AFM is typically used as a complimentary method to solution based characterization methods.[254,266–268] In AFM experiments, the specimen is scanned with a cantilever with a sharp tip. The force on the cantilever scanning the surface is measured to generate an image. In pioneering work from Coates and coworkers, the intramolecular olefin cross-metathesis crosslinking of vinyl functional polymers was studied using AFM.[266] Polymer solutions at different stages of crosslinking were spin-casted on mica for subsequent AFM visualization (Figure 2.9). The non-crosslinked polymer chains had extended
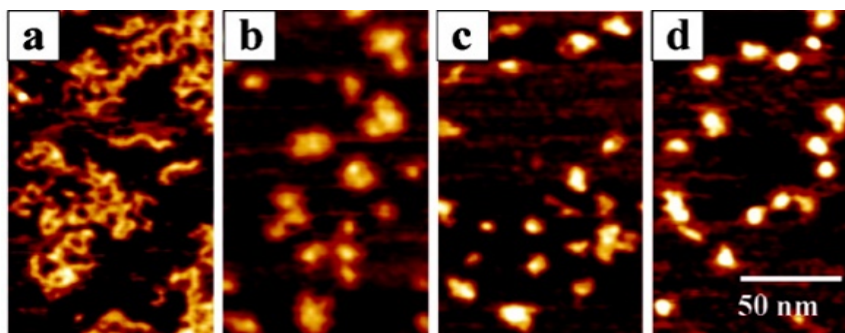
Figure 2.9. AFM height images visualizing the morphological changes accompanied by the intramolecular crosslinking process of linear polymer chains (a) to form SCNPs (b-d, increasing crosslinking density). Adapted with permission from reference [266]. Copyright (2007) American Chemical Society.

worm-like structures, whereas intramolecularly crosslinked polymer chains were spherical. Importantly, with increasing crosslinking progress the polymer surface extension decreased while the volume of the particles remained constant, clearly showing the transition from a random coil to a spherical structure.

Furthermore, transmission electron microscopy has been employed for imaging SCNP in the solid state.[229,253,259,268–272] Cryogenic TEM is an interesting alternative to standard TEM methods. It allows imaging of nanoparticles in solution and thus overcomes structural changes associated with sample preparation. For instance, Meijer and coworkers have employed cryogenic TEM to image the core of core-shell SCNPs in vitrified water.[273]

In addition to the size reduction, the elucidation of the crosslinking chemistry is of great importance. In addition to standard characterization methods, such as NMR, IR, UV-vis and fluorescence spectroscopy, recently high resolution electrospray ionization mass spectrometry (ESI MS) experiments were employed. A PMMA based polymer ($M_n = 13100\,\mathrm{g\cdot mol^{-1}}$) with statistically distributed glycidyl side group functionalities was crosslinked *via* intrachain cationic ROP using $B(C_6F_5)_3$ as a catalyst. ESI MS measurement revealed that crosslinking occurs predominantly through bimolecular coupling compared to propagation processes.[274]

In summary, an array of characterization methods are available for the characterization of SCNPs. However, critical evaluation of literature reported data indicated that most methods applied to determine SCNP sizes are only indicative and further development of accurate and reliable size characterization methods is required.[264]

3

Grafting of functional polymers to photoactive nanodiamonds
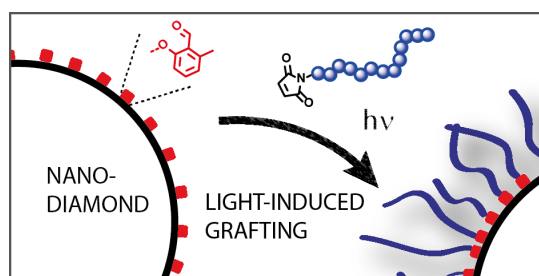
3.1. Motivation

Nanodiamonds (NDs) are non-toxic and versatile nanoparticles with high potential for biomedical applications (Section 2.1). The modification of NDs with polymers can improve colloidal stability and introduce (biological) functions. Grafting-from and grafting-to strategies have been applied to coat NDs with

polymers (Section 2.1.4.2). The light-triggered grafting of polymers to surfaces has developed into an efficient and mild conjugation strategy that allows for the preparation of defined surface structures,[8] and is investigated in the current chapter for the modification of NDs. The photoenol ligation is introduced for the light-triggered Diels-Alder grafting of polymers to NDs, which is a catalyst-free reaction that proceeds at ambient temperature. Photoactive NDs were prepared by modification of the ND's surface with *o*-methyl benzaldehyde groups. Subsequent UV irradiation in the presence of maleimide terminal polymers allowed for the surface functionalization *via* the photoenol ligation. Mannose functional NDs were prepared and a lectin binding assay demonstrated the potential of the introduced synthetic approach for the preparation of bioactive NDs.

3.2. Preparation of photoactive nanodiamonds
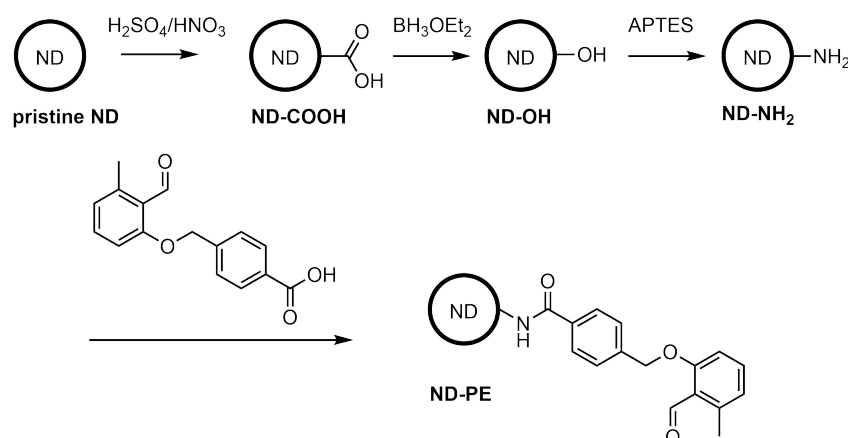
Scheme 3.1. Synthetic route from pristine NDs to photoenol functional NDs (ND-PE). Adapted with permission from reference [275]. Copyright (2016) American Chemical Society.

Detonation NDs (Section 2.1.1) were employed for the development of a light-triggered polymer grafting-to approach. The structure of detonation NDs consists of small primary particles (around 5 nm in diameter) that form larger aggregates of up to a few hundred nanometres. The NDs were ultrasonicated multiple times with a high power sonotrode to break large aggregates. However, full disintegration is not possible using ultrasound and is also not

always desired depending on the application. The surface of detonation NDs was functionalized with photoactive *o*-methyl benzaldehyde (photoenol, PE) groups in four synthetic steps (Scheme 3.1).

First, the surface was oxidized in a mixture of concentrated HNO_3/H_2SO_4 (9/1, v/v) at elevated temperature (90 °C). Acid treatment removes amorphous as well as sp^2 carbon structures and results in an oxidized, more homogeneous surface with an increased number of carboxylic acid groups.[54] ATR FTIR spectroscopy was employed to monitor the functionalization progress (Figure 3.1). After oxidation, a decrease of the absorption bands at $2920 \, \mathrm{cm}^{-1}$ and $2850 \, \mathrm{cm}^{-1}$ corresponding to C-H stretching vibrations was observed. In addition, the C=O stretching band at $1720 \, \mathrm{cm}^{-1}$ is present in the spectrum of the oxidized sample (ND-COOH) adjacent to an OH vibrational mode at $1624 \, \mathrm{cm}^{-1}$ arising from surface-bound water.[276] Next, the NDs were reduced using borane in THF, which led to a significant decrease of the C=O stretching band at $1720 \, \mathrm{cm}^{-1}$, indicating the successful reduction of carboxylic acid groups. Additionally, an absorption band at $1248 \, \mathrm{cm}^{-1}$ appeared, which could be assigned to the C-H deformation vibration of secondary alcohols. In a subsequent step the NDs were silanized with (3-aminopropyl)-triethoxysilane (APTES)
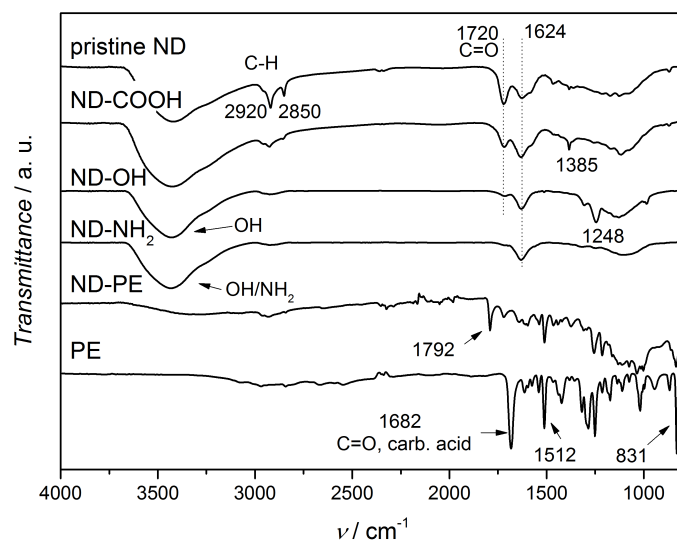
Figure 3.1. ATR FTIR spectra of samples from all synthetic steps to obtain photoenol functional NDs (ND-PE). Adapted with permission from reference [275]. Copyright (2016) American Chemical Society.

to obtain amine functional NDs (ND-NH$_2$). The surface expressed amino functionalities were used to attach photoactive *o*-methyl benzaldehyde groups *via* an EDC mediated amidation reaction. The successful decoration of the NDs with photoenol groups was shown by the presence of the characteristic photoenol IR bands at 1512 cm^{-1} and 831 cm^{-1} in the ATR FTIR spectrum. Furthermore, X-ray photoelectron spectroscopy (XPS) analysis of the photoenol functional NDs showed a strong Si 2p signal at 101.9 eV, confirming the successful silanization reaction (Figure 3.2).
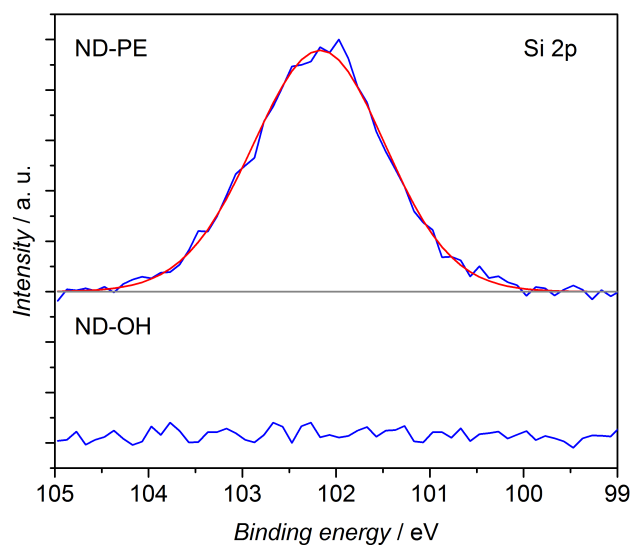
Figure 3.2. Si 2 p XP spectra of ND-OH and ND-PE. Adapted with permission from reference [275]. Copyright (2016) American Chemical Society.

3.3. Preparation of maleimide terminal polymers
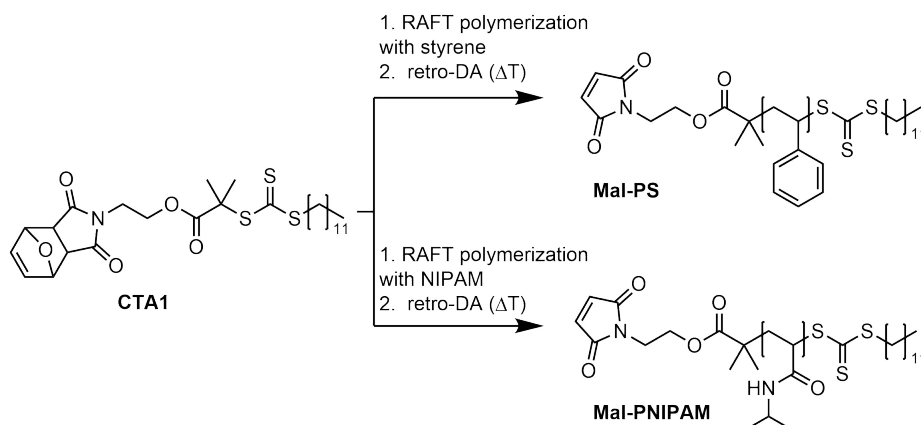
Scheme 3.2. Synthetic route to maleimide terminal PS and PNIPAM. Adapted with permission from reference [275]. Copyright (2016) American Chemical Society.

Activated double bonds, such as maleimides, are very efficient in trapping photo-generated *o*-quinodimethanes in Diels-Alder reactions, which was exploited in the current study for the grafting of polymers to ND-PE. Maleimide terminal polymers were prepared *via* reversible addition fragmentation chain transfer (RAFT) polymerization, which is a robust polymerization technique that allows for the preparation of well-defined, endgroup functional polymers (Section 2.2.2). First, a furan capped maleimide functional trithiocarbonate chain transfer agent (CTA) was synthesized, wherein the maleimide functionality was attached to the R-group of the RAFT agent (CTA1, Scheme 3.2). The RAFT polymerization of styrene and *N*-isopropylacrylamide (NIPAM) yielded well-defined endgroup functional polystyrene (PS) and poly(*N*-isopropylacrylamide) (PNIPAM), respectively. Subsequent *retro*-Diels-Alder deprotection of the furan capped endgroups at elevated temperatures (T ≥ 95 °C) led to maleimide terminal polymers. Size exclusion chromatography (SEC) results are depicted in Figure 3.3 showing well-defined polymers with low dispersities (Table 3.1). Furthermore, the *retro*-Diels-Alder deprotection procedure led to a small shift of the molecular weight distribution (MWD) to higher retention times without any change in its shape (Figure 3.3).

Table 3.1. SEC and NMR characterization data of prepared endgroup functional RAFT polymers.

Polymer	M_n^{SEC} / g·mol^{-1}	$Đ^{SEC}$	M_n^{NMR} / g·mol^{-1}	DP^{NMR}
PS	6200	1.16	6200	55
Mal-PS	5800	1.16	-	-
PNIPAM	6200	1.21	4700	37
Mal-PNIPAM	5800	1.21	-	-
PManAcEMA 1	23400	1.21	12900	27
Mal-PManAcEMA 1	24300	1.24	-	-
PManAcEMA 2	38000	1.30	20700	44
Mal-PManAcEMA 2	39000	1.30	-	-
PManAcEMA 3	56200	1.24	42000	90
Mal-PManAcEMA 3	58800	1.24	-	-
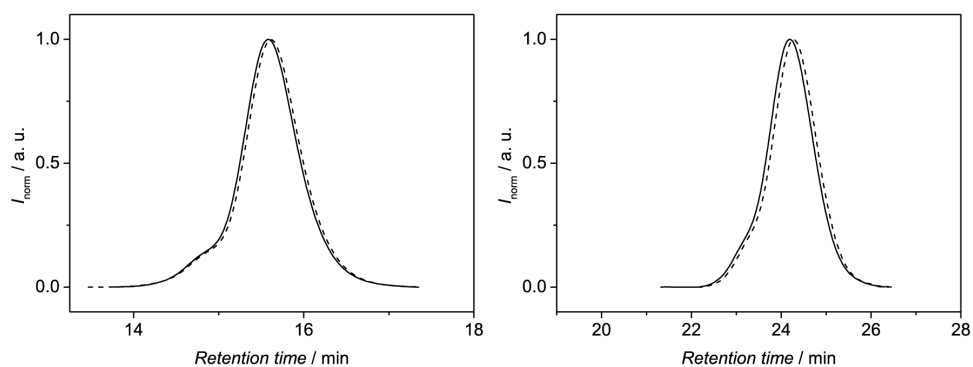
Figure 3.3. SEC results of PS (left, DMAC) and PNIPAM (right, THF) before (solid line) and after deprotection (dashed line), respectively. Adapted with permission from reference [275]. Copyright (2016) American Chemical Society.

^{1}H NMR spectroscopy was employed to verify the formation of maleimide end-groups. The thermal deprotection was accompanied with the disappearence of signals corresponding to the furan protecting group, *e.g.* the olefinic proton resonance at 6.52 ppm as well as the aliphatic proton signals at 5.25 ppm and 2.92 ppm (PNIPAM: Figure 3.4; PS: Figure B.7, Appendix). Furthermore, the appearance of resonances at 6.75 ppm can be assigned to olefinic protons of the newly formed maleimide moiety providing evidence of the successful *retro*-Diels-Alder reaction.

In addition to PS and PNIPAM, mannose based glycopolymers were prepared (Scheme 3.3). A fully acetylated mannose monomer was synthesized according to a modified literature procedure.[180] First, mannose was acetylated using acetic anhydride, followed by a BF$_3$ catalysed glycosylation reaction with 2-hydroxyethyl methacrylate (HEMA) yielding the mannose glycomonomer ManAcEMA (Scheme 3.3). A detailed description of the reaction mechanism is given in Section 2.4.1. Acetylated mannose is not bioactive as free hydroxy groups are required for the binding to lectins. Therefore, the mannose units need to be deprotected. However, deacetylation conditions may cleave the ester bond in CTA1 and lead to the cleavage of the polymer from the sur-
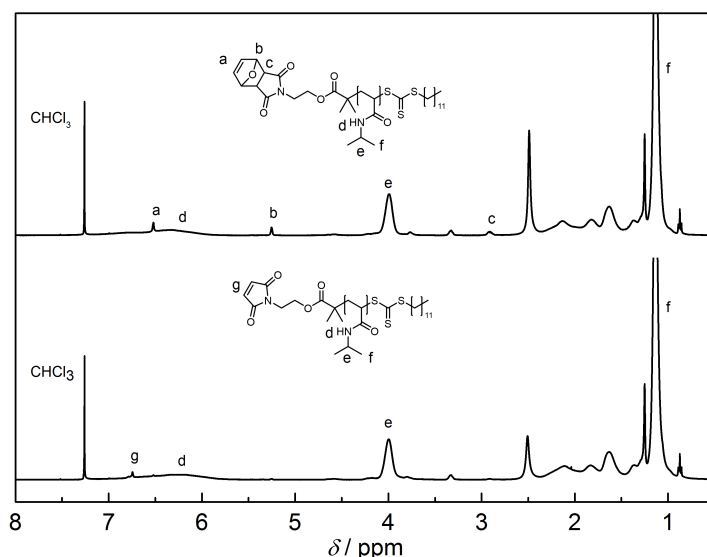
Figure 3.4. ^{1}H NMR spectra of PNIPAM polymer before (top) and after deprotection (bottom). Adapted with permission from reference [275]. Copyright (2016) American Chemical Society.
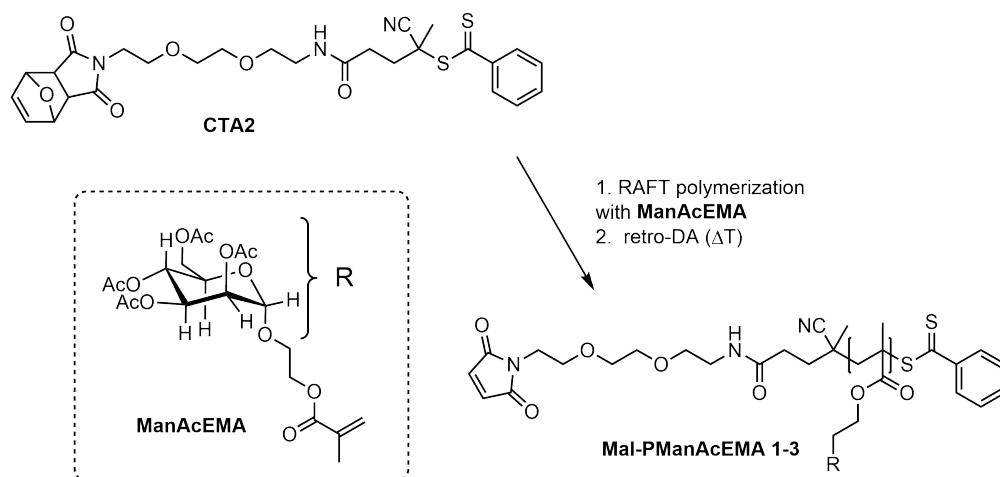
Scheme 3.3. Synthetic route to maleimide terminal PManAcEMA. Adapted with permission from reference [275]. Copyright (2016) American Chemical Society.

face. Hence, a novel RAFT agent with a more stable amide bond between the maleimide and dithioester group was designed (CTA2, Scheme 3.3). To obtain CTA2, an amine functional furan-capped maleimide compound was reacted with 4-cyanopentanoic acid dithiobenzoate (CPADP). Secondary and primary amines can cleave the dithiobenzoate group through a nucleophilic substitution (aminolysis). In order to minimize aminolysis side reactions, the amine was slowly added to mercaptothiazoline activated CPADP ensuring low amine concentrations and allowing for the formation of CTA2 (Figure B.5-B.6, Appendix).

The prepared chain transfer agent CTA2 controlled the polymerization of ManAcEMA successfully. Glycopolymers of three chain-lengths were prepared in order to investigate the effect of polymer chain length on resulting grafting density (M_n = 12900 g·mol^{-1}, 20700 g·mol^{-1} and 42000 g·mol^{-1}, Mal-PManAcEMA 1-3, Table 3.1). The *retro*-Diels-Alder deprotection of the furan capped endgroups was successful as shown by SEC (Figure 3.5) and ^{1}H NMR spectroscopy (Figure B.8-B.10, Appendix). It should be noted that the deacetylation of the mannose units on the glycopolymer was performed after the grafting reaction on the NDs and is discussed in detail later. An overview of all prepared polymers is depicted in Table 3.1.
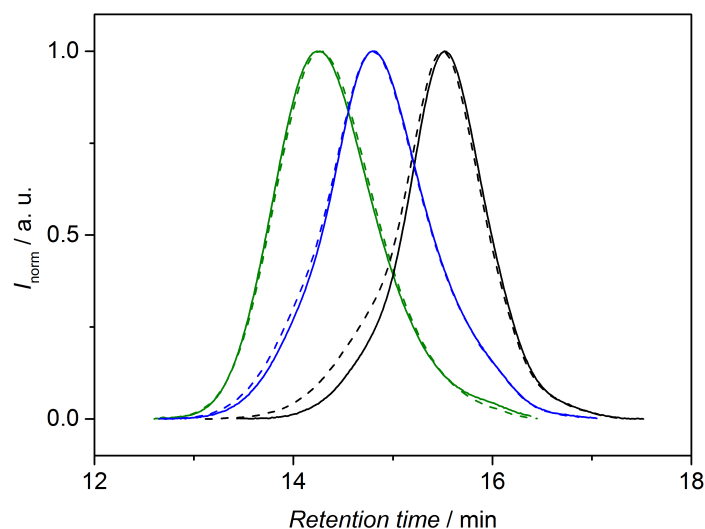
Figure 3.5. SEC results (THF) of PManAcEMA 1-3 (right to left) before (solid line) and after deprotection (dashed line). Adapted with permission from reference [275]. Copyright (2016) American Chemical Society.

3.4. Light-triggered polymer grafting
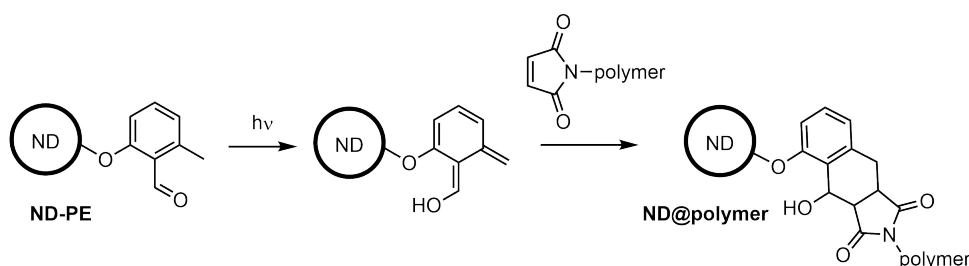
Scheme 3.4. Schematic representation of the photo-grafting process. Upon UV irradiation dienes are formed on ND-PE, which are trapped by maleimide terminal polymers.

Next, the light-induced grafting of the prepared maleimide terminal polymers to photoenol functional nanodiamonds (ND-PE) was investigated (Scheme 3.4). Photo-grafting experiments were performed in a custom built photoreactor equipped with a commercially available UV lamp (*Arimed B6*, λ_{max} = 320 nm). In a typical grafting experiment, ND-PE was dispersed in THF assisted by ultrasound, followed by addition of polymer and UV irradiation. Subsequently, the resulting NDs were centrifuged followed by several wa-

shing cycles to remove unreacted polymer (dispersion in suitable solvent, centrifugation, removal of supernatant).

In order to show successful photo-grafting, a control experiment was performed. A mixture of Mal-PS and ND-PE was divided into two samples. One sample was irradiated at λ_{max} = 320 nm whereas the control sample was stirred in the dark for the same time period. After purification, the grafting density was determined by thermogravimetric analysis (TGA) under oxidative conditions. At temperatures around 350 °C the polymer decomposes whereas the nanodiamonds are stable up to around 615 °C. The first decomposition step corresponding to the grafted polymer was used to calculate the grafting density in wt.% (mass polymer per mass sample). Importantly, only the irradiated sample contained polymer showing the success of the photo-grafting-reaction (Figure B.11, Appendix). Next, the kinetics of the photo-grafting process was investigated with Mal-PNIPAM and Mal-PManAcEMA 1 (Figure 3.6). An increase of grafting density with irradiation time was observed for both experiments, levelling out after 2 h and 5 h for Mal-PNIPAM and Mal-PManAcEMA 1, respectively. Further grafting experiments were performed overnight to ensure maximum grafting density.
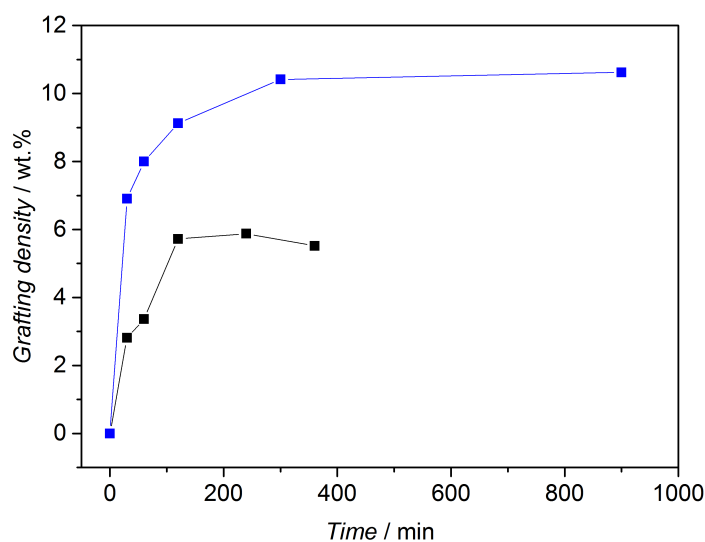
Figure 3.6. TGA determined grafting density against irradiation time. Black: Mal-PNIPAM; blue: Mal-PManAcEMA 1. Adapted with permission from reference [275]. Copyright (2016) American Chemical Society.

64
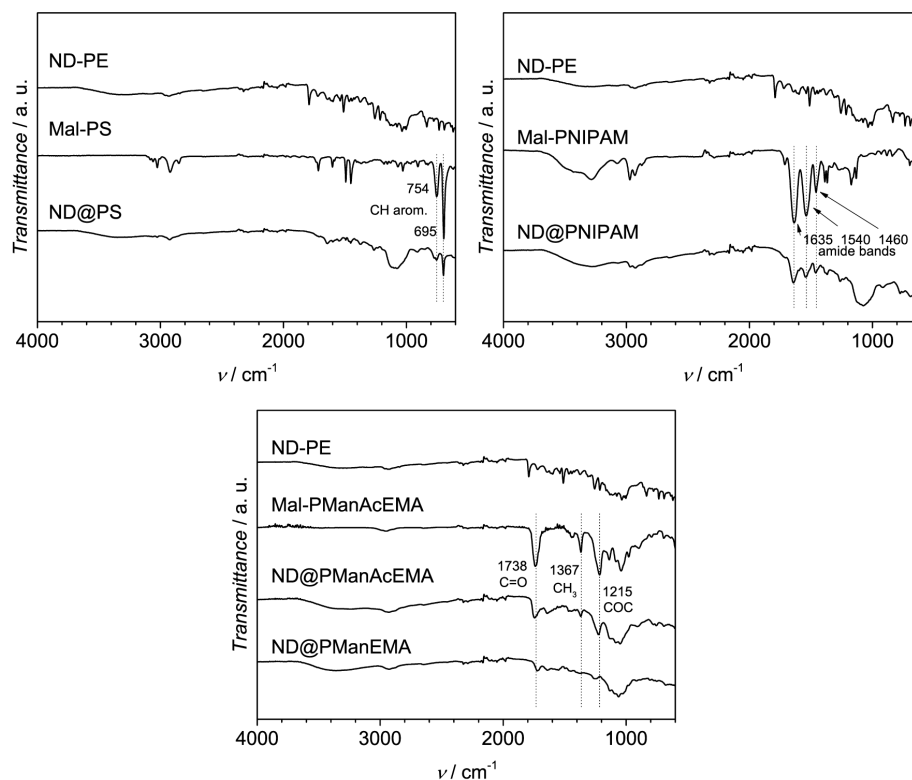
Figure 3.7. ATR FTIR spectra of ND-PE, polymers and polymer coated NDs. Adapted with permission from reference [275]. Copyright (2016) American Chemical Society.

Next, a series of ND-polymer core-shell particles was prepared by photo-grafting the maleimide terminal polymers (Mal-PS, Mal-PNIPAM and Mal-PManAcEMA 1-3, Table 3.1) to the photoactive NDs. ATR FTIR spectroscopy is a powerful technique to investigate surface functionalities and hence was employed to characterize the polymer grafted NDs. In the IR spectra of all polymer coated ND samples the characteristic IR bands of the parent polymer were present (Figure 3.7). For instance, the aromatic C-H vibration bands of Mal-PS at $754\,cm^{-1}$ and $695\,cm^{-1}$ are visible in the IR spectrum of ND@PS. The grafting of Mal-PNIPAM onto NDs led to the appearance of amide IR bands at $1635\,cm^{-1}$ and $1540\,cm^{-1}$ as well as a symmetric $-C(CH_3)_2$ deformation band at $1460\,cm^{-1}$.[277] The photo-grafting of Mal-PManAcEMA 1-3 yielded glycopolymer coated NDs where all hydroxy groups were acetylated. Since the hydroxy groups are crucial for the bioactivity of the glycopolymer, the mannose units on the PManAcEMA shell were deprotected using

sodium methoxide. The deprotecion was performed directly after the photo-grafting experiment without prior purification providing a simple synthetic approach. One acetylated sample was isolated for further characterization (ND@PManAcEMA 2). The glycopolymer photo-grafting was accompanied with the appearance of a carbonyl band at $1738\,\mathrm{cm^{-1}}$ corresponding to the acetate groups as well as the carbonyl group on the acrylate based backbone. Upon deprotection the carbonyl band at $1738\,\mathrm{cm^{-1}}$ decreased due to the loss of the acetate groups.

Furthermore, XPS gave valuable insight on the surface structure of the polymer coated NDs. XPS is a surface sensitive method, which provides information about the surface composition to a depth of around 10 nm. The grafting of Mal-PS did not lead to a significant change in the measured XP spectra due to similar elemental composition of the ND core and polymer shell (both consist mainly of carbon). However, the photo-grafting of hetero atom containing polymers could be readily monitored *via* XPS. The PNIPAM grafting led to a significant increase of the N 1s signal at 399.6 eV from 2.0 at.% to 3.0 at.% (Figure 3.8). It should be noted that the origin of the nitrogen in ND-PE is from nitrogen defects in the ND lattice as well as from the silanization reaction with APTES. However, the grafting of Mal-PNIPAM increased the nitrogen content on the surface. The photo-grafting of the glycopolymers (Mal-PManAcEMA) increased the oxygen content on the ND's surface, leading to a higher intensity ratio of the C-O, C-N (286.5 eV) and the C-H, C-C (285.0 eV) signals (Figure
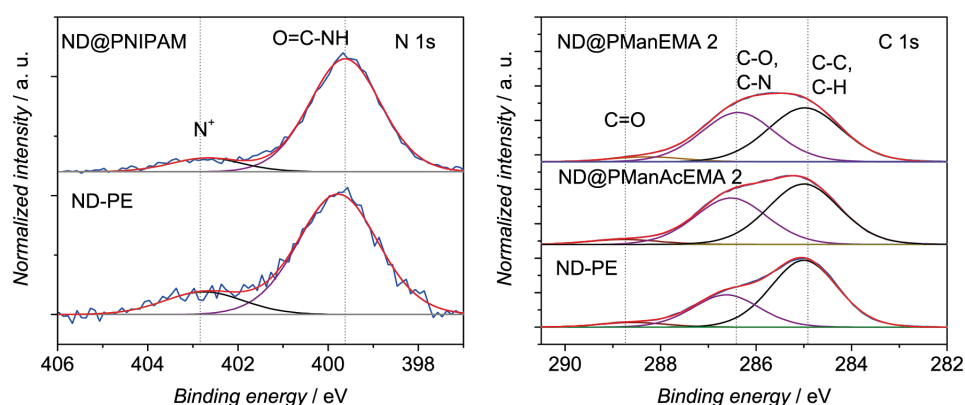
Figure 3.8. N 1s and C1s XP spectra of selected ND samples. Adapted with permission from reference [275]. Copyright (2016) American Chemical Society.

Table 3.2. Grafting densities of polymer coated NDs determined *via* TGA.

Sample	Grafting density /		Footprint /
	wt.%	μmol $\cdot$ g^{-1}	nm^2
ND@PS	3.8	6.4	2.7
ND@PNIPAM	5.0	11.1	1.5
ND@PManEMA 1	5.5	6.9	3.8
ND@PManAcEMA 2	10.9	5.9	3.1
ND@PManEMA 2	7.9	6.4	4.2
ND@PManEMA 3	9.3	3.8	7.9

3.8). The deacetylation led to a decrease in carbonyl groups and an increase in hydroxy groups which was in agreement with the deconvoluted C 1s signals.

Using TGA under oxidative conditions, the amount of grafted polymer (in wt.%) could be directly determined. Using size information from dynamic light scattering (DLS) and the molecular weight of the parent polymers, a molar grafting density was calculated. In addition, the polymer footprint (average surface area per polymer chain) was estimated using the surface area of ND-PE, which was calculated from the DLS determined hydrodynamic diameter of ND-PE assuming a spherical shape and the density of bulk diamond (3.52 g $\cdot$ cm^{-3}). It should be noted that due to the beforehand mentioned assumptions, the polymer footprint is a rough estimation, however, it delivers descriptive values that facilitates the comparison to other systems. The results are summarized in Table 3.2.

Grafting densities between 3.8 wt.% and 10.9 wt.% and molar grafting densities between 3.8 μmol $\cdot$ g^{-1} and 11.1 μmol $\cdot$ g^{-1} were obtained. Importantly, the grafting density in wt.% of ND@PManAcEMA 2 decreased from 10.9 wt.% to 7.9 wt.% upon deacetylation corresponding to the weight loss due to the cleavage of acetate groups. The polymer footprint was estimated to be between 1.5 nm^2 and 7.9 nm^2 and lies in the order of magnitude of literature reported values.[7,278]

Glycopolymers of three different chain lengths were photo-grafted to NDs. The determination of grafting densities by TGA revealed that the photo-grafting efficiency depends on the molecular weight of the grafted polymer
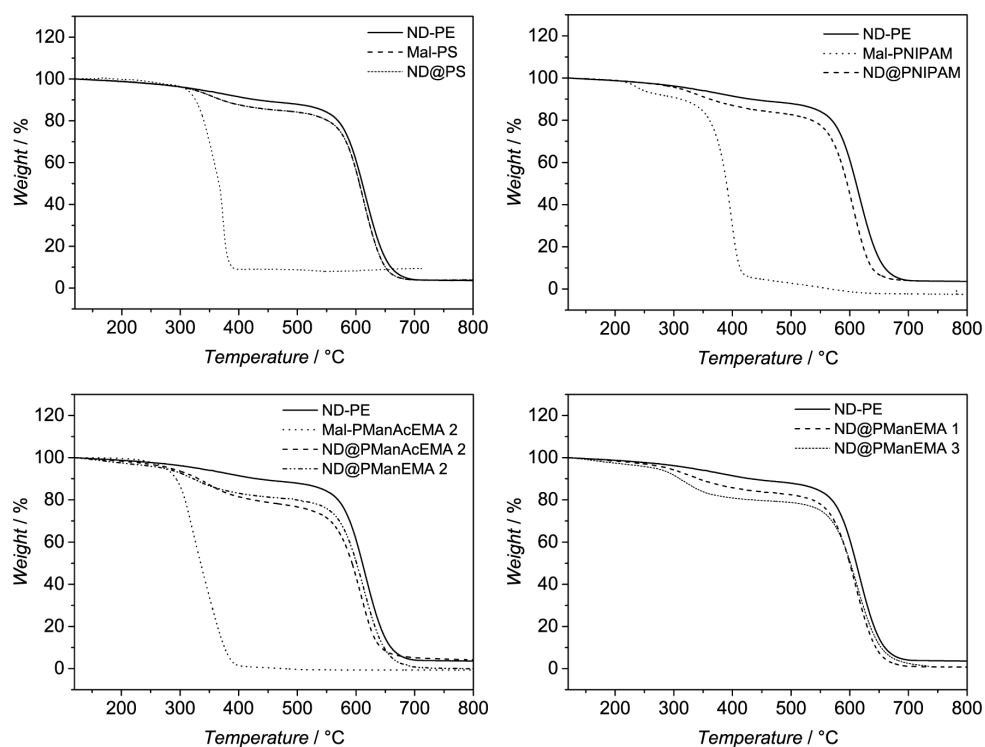
Figure 3.9. TGA results from polymers, ND-PE and polymer grafted NDs. Adapted with permission from reference [275]. Copyright (2016) American Chemical Society.
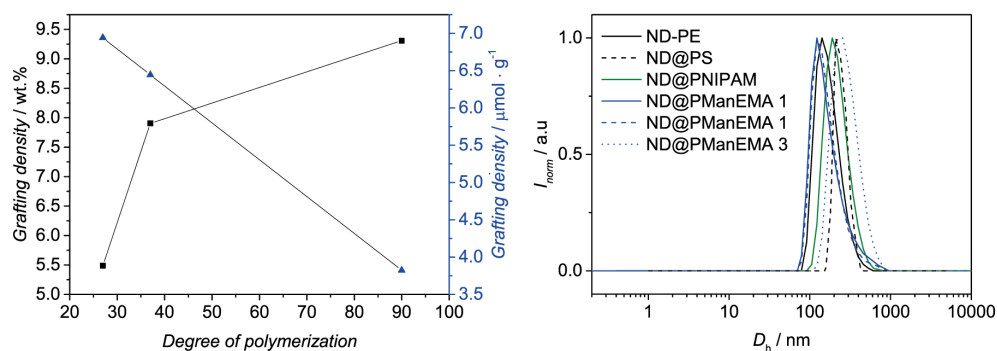
Figure 3.10. Left: Degree of polymerization vs. grafting density. Right: DLS result of prepared nanodiamonds (number distributions). Adapted with permission from reference [275]. Copyright (2016) American Chemical Society.

(Figure 3.10). The molar grafting density decreases with increasing polymer chain length. The chain-length dependency of the grafting process can be explained with steric effects. Larger polymers cover more space on the surface resulting in higher polymer footprints and lower molar grafting densities.

The hydrodynamic diameter distributions of the hybrid particles were determined *via* DLS experiments (Figure 3.10). The number average hydrodynamic diameters range between 170 nm and 290 nm. Upon photo-grafting, the hydrodynamic diameter increased with exemption of ND@PManEMA 1 and ND@PManEMA 2 that possessed a smaller hydrodynamic diameter than the precursor, probably due to better dispersibility.

3.5. Lectin binding

The specific binding of carbohydrates to lectins on cell surfaces can promote cellular uptake and thus glycopolymers are highly interesting for targeted drug delivery applications (Section 2.4.4). Concanavalin A (ConA) is a lectin that selectively binds to mannose and glucose units and serves in this study as a model protein to evaluate the bioactivity of the glycopolymer coated NDs. Since ConA has four binding pockets, the binding of glycopolymers to ConA is accompanied with a crosslinking induced turbidity, which can be monitored by UV-vis spectroscopy in a so-called turbidity assay. ConA was added to glycopolymer functional NDs (dispersion in HEPES buffer) and the binding was measured by the increase in absorbance at 420 nm. All glycopolymer functional NDs bind to ConA (Figure 3.11), whereas the hybrid particles with the smallest glycopolymer chains showed the steepest increase in turbidiy followed by a decrease probably due to sedimentation of large particles. No sedimentation of the particles with longer glycopolymer chains was observed. A potential explanation is that the possibility of ConA binding only to mannose units of one particle is higher when the glycopolymers are longer and thus less aggregation occurs.
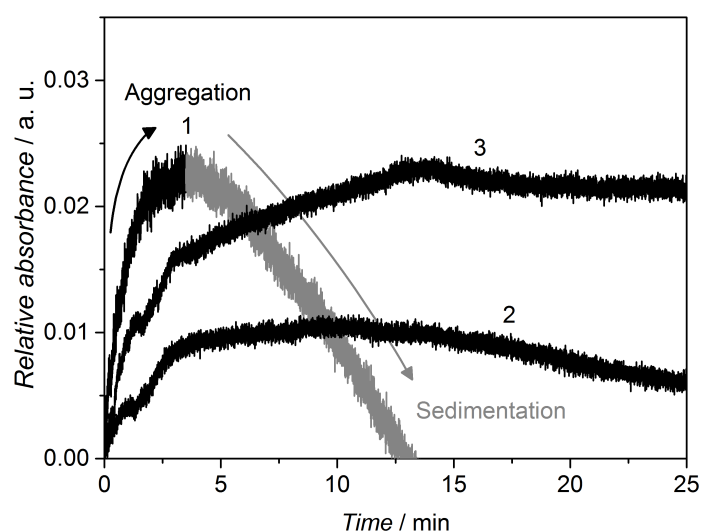
Figure 3.11. ConA turbidity assay. The absorbance at 420 nm was measured after the addition of ConA to a ND@PManEMA 1-3 dispersion. Adapted with permission from reference [275]. Copyright (2016) American Chemical Society.

3.6. Conclusion

In conclusion, a novel light-induced grafting-to protocol for the modification of NDs with functional polymers is introduced. The grafting-to protocol is based on the photoenolization of *o*-methyl benzaldehyde groups attached to NDs. The hereby formed dienes are trapped in Diels-Alder reactions with maleimide terminal polymers. The approach is modular as shown by the grafting of a variety of polymers (PS, PNIPAM and glycopolymers). Furthermore, a correlation between molecular weight of grafted polymer and resulting grafting density was observed. Higher molar grafting densities are achieved with lower molecular weight polymers due to steric hindrance. Importantly, glycopolymers with lateral mannose groups could be grafted to NDs and the binding activity towards the lectin ConA was demonstrated in a turbidity assay.

3.7. Experimental section

3.7.1. Materials

Methyl 4-((2-formyl-3-methylphenoxy)methyl)benzoic acid (PE),[131] 4-(2-hy-droxyethyl)-10-oxa-4-azatricyclo[5.2.1.02,6]dec-8-ene-3,5-dione,[279] 2-(((dode-cyl-thio)carbonothioyl)thio)-2-methylpropanoic acid[280] and 2-(2-(2-(2-amino-ethoxy)ethoxy)ethyl)-3a,4,7,7a-tetrahydro-1H-4,7-epoxyisoindole-1,3(2H)-di-one[281] were prepared according to literature procedures.

Detonation nanodiamonds ($< 10\,nm$ particle size by TEM, $> 97\,\%$ trace metals basis, Sigma-Aldrich), EDC$\cdot$HCl (99+ %, Roth), D(+)-mannose (99+ %, Acros), BF_3OEt_2 (98+ %, Alpha), acetic anhydride (99+ %, Acros), 4-cyano-4-((phe-nylcarbonothioyl)thio)pentanoic acid ($> 97\,\%$, Sigma-Aldrich), BH_3 in THF (1.0 M, Sigma-Aldrich), H_2SO_4 (96 %, Roth), HNO_3 (67 %, Roth), HCl (37 %, Roth), *N,N'*-dicyclohexylcarbodiimid (DCC, 99 %, Acros), 2,2'-azobis(isobuty-lonitrile) (AIBN, VWR), (3-aminopropyl) triethoxysilane (APTES, 98 %, abcr), 2-hydroxyethyl methacrylate (HEMA, 97 %, Sigma-Aldrich), 4-dimethylami-nopyridine (DMAP, 99 %, abcr), 2-thiazoline-2-thiol (98 %, Sigma-Aldrich), chloroform-d_1 ($CDCl_3$, 99.8 %, EURISO-TOP), dimethyl sulfoxide-d_6 (DMSO-d_6, 99.8 %, EURISO-TOP), 4-dimethylaminopyridine (DMAP, 99 %, Acros) were used as received. *N,N*-Dimethylformamid (DMF), tetrahydrofuran (THF), dichloromethane (DCM), diethyl ether, ethyl acetate and cyclohexane were purchased as analytical grade (Sigma-Aldrich) and used as received. Styrene (Sigma-Aldrich) was passed through a column of basic aluminium oxide (Acros). *N*-Isopropylacrylamide (NIPAM, TCI, 98 %) was recrystallized twice from hexane and stored at -20 °C prior to usage.

3.7.2. Instrumentation

Size exclusion chromatography (SEC)

THF system. A Polymer Laboratories PL - GPC 50 Plus Integrated System was used, comprising an autosampler, a PLgel 5 µm bead-size guard column (50$\cdot$7.5 mm) followed by three PLgel 5 µm Mixed-C and one PLgel 3 µm

Mixed-E column (300·7.5 mm) and a differential refractive index detector using THF as the eluent at 40 °C with a flow rate of 1 mL·min^{-1}. The SEC system was calibrated using linear poly(styrene) (PS) standards ranging from 474 to 2.5·10^6 g·mol^{-1}. Calculation of the molecular weight proceeded *via* the Mark-Houwink parameters for polystyrene, i.e. K = 14.1·10^{-5} dL·g^{-1}, α = 0.70.[282] The samples were filtered through polytetrafluorethylene (PTFE) membranes with a pore size of 0.2 µm prior to injection.

DMAc system. A Polymer Laboratories PL-GPC 50 Plus Integrated System was used, comprising an autosampler, a PLgel 5 µm bead-size guard column (50·7.5 mm) followed by three PLgel 5 × Mixed C columns (300·7.5 mm), and a differential refractive index detector with a flow rate of 1.0 mL·min^{-1}. *N,N*-dimethylacetamide (DMAC) containing 0.03 wt.% LiBr was used as an eluent and the system was operated at 50 °C. The SEC system was calibrated against linear poly(methyl methacrylate) standards with molecular weights ranging from 700 to 2·10^6 g·mol^{-1}. The samples were filtered through polytetrafluorethylene (PTFE) membranes with a pore size of 0.2 µm prior to injection.

UV-vis spectroscopy

UV-vis measurements were performed in a Varian Cary 100 Bio spectrometer including a temperature control unit. All measurements were carried out in quartz cuvettes.

Ultrasound systems

For the dispersion of NDs, a Branson Sonifier W450 (400 Watt) with a micro tip was employed (referred to as high power sonotrode). A Bandelin Sonorex Digitec ultrasound bath with temperature control was employed for mild ultrasound treatments.

Thermogravimetric analysis (TGA)

TGA was performed on a TGA Q5000 from TA Instruments. Pre-dried samples were measured in air atmosphere (oxidative conditions) with the following heating sequence:

1. Ambient temperature to $100\,°C$, $10\,°C \cdot min^{-1}$

2. Isothermal at $100\,°C$ for $10\,min$

3. $100\,°C$ - $800\,°C$, $10\,°C \cdot min^{-1}$

Electrospray ionization mass spectrometry (ESI MS)

ESI MS spectra were recorded on a Q Exactive mass spectrometer (Orbitrap) equipped with a HESI II probe (ThermoFisher Scientific, San Jose, CA, USA). The instrument was calibrated in the m/z range of 74-1822 by using a S2 premixed standard containing caffeine, Met-Arg-Phe-Ala acetate (MRFA) and a mixture of fluorinated phosphazenes (Ultramark 1621). A dimensionless sweep gas flow rate of 5 and a constant spray voltage of $4.6\,kV$ were applied. The capillary temperature was set to $320\,°C$. The S-lens RF level was set to 62.0. The samples were dissolved in a mixture of THF and MeOH (3:1), filtered through polytetrafluorethylene (PTFE) membranes with a pore size of $0.2\,\mu m$ and injected with a flow rate of $5\,\mu L \cdot min^{-1}$.

Nuclear magnetic resonance (NMR) spectroscopy

The synthesized compounds were analyzed *via* ^{1}H and ^{13}C NMR spectroscopy using a Bruker Avance 400 (^{1}H, 400 MHz; ^{13}C, 101 MHz) spectrometer. Samples were dissolved in deuterated solvents. The δ-scale was referenced against the residual solvent signal. Abbreviations used in the description of the materials synthesis include singlet (s), broad singlet (bs), doublet (d), triplet (t), quartet (q), and multiplet (m).

3.7.3. Synthetic procedures

Oxidation of nanodiamonds (ND-COOH)

According to a literature procedure,[283] detonation NDs (500 mg) were dispersed in 10 mL of a 9/1 (v/v) mixture of H_2SO_4 (96 %) and HNO_3 (67 %). The reaction mixture was stirred at 90 °C for three days. Subsequently, the NDs were washed with water and ultrasonicated with a high power sonotrode for 1 h. This procedure was repeated one more time before the treatment with 20 mL NaOH (0.5 M) at 90 °C for 1 h. After centrifugation, the NDs were redispersed in 20 mL aqueous HCl (0.1 M) and stirred at 90 °C for 1 h. Subsequently, the NDs were centrifuged and redispersed in 20 mL water and sonicated with a high power sonotrode for 2 h. After centrifugation and drying under reduced pressure oxidized NDs (ND-COOH), were obtained as a grey powder.

Reduction of nanodiamonds (ND-OH)

ND-COOH (400 mg) were dispersed in 20 mL anhydrous THF using an ultrasound bath. 5 mL BH_3 in THF (1 M) was added and stirred at 70 °C for 24 h. Subsequently, the reaction mixture was quenched with 5 mL HCl (2 M) and washed with a 1/1 (v/v) mixture of acetone/water until neutral. After centrifugation and drying under reduced pressure ND-OH were obtained.

Silanization of nanodiamonds (ND-NH$_2$)

ND-OH (235 mg) were dispersed in 40 mL anhydrous THF. APTES (2.10 mL) was added and stirred at ambient temperature for 48 h. The NDs were centrifuged, washed with acetone and dried under reduced pressure to obtain amine functional NDs (ND$-NH_2$).

Amidation of nanodiamonds (ND-PE)

$ND-NH_2$ (150 mg) were dispersed in 50 mL THF and sonicated in an ultrasound bath for 1 h. Next, methyl 4-((2-formyl-3-methylphenoxy)- methyl) benzoic acid (91.2 mg, 0.337 mmol, 1.00 eq), $EDC \cdot HCl$ (77.6 mg, 0.405 mmol, 1.20 eq) and DMAP (16.5 mg, 0.135 mg, 0.400 eq) were added. The reaction mixture was stirred at ambient temperature for 65 h. After centrifugation, the NDs were washed twice with water and twice with THF to obtain photoenol-functional NDs (ND-PE).

Synthesis of ManAcEMA
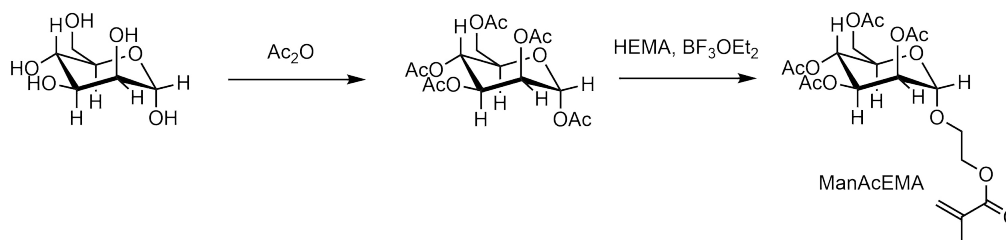
Acetylation of mannose. According to a literature procedure,[180] two drops sulfuric acid (96 %) were added to a suspension of mannose (5.00 g, 27.8 mmol, 1.00 eq) in acetic anhydride (26.2 mL, 28.3 g, 278 mmol, 10.0 eq) at 0 °C. The reaction mixture was stirred at ambient temperature for 18 h. 100 mL water was added and extracted with DCM. The organic phase was washed consecutively with saturated $NaHCO_3$ and water until the aqueous phase was neutral and the organic phase was dried over Na_2SO_4. After removal of solvent under reduced pressure peracetylated mannose (10.44 g, 26.7 mmol, 96 %) was obtained.

^{1}H NMR (400 MHz, CDCl$_3$), δ (ppm) = 6.08 (s, 1 H, CH, anomeric center), 5.49-5.38 (m, 1H), 5.28-5.24 (m, 1 H), 5.37-5.33 (m, 2 H), 4.33-4.24 (m, 1 H), 4.16-4.01 (m, 2 H), 2.17, 2.16, 2.08, 2.04, 2.00 (5 s, each 3 H, acetyl groups).

Glycosylation with HEMA. According to a literature procedure,[180] peracetylated mannose (3.00 g, 7.69 mmol, 1.00 eq) and HEMA (1.12 mL, 1.20 g, 9.22 mmol, 1.20 eq) were dissolved in 30 mL anhydrous DCM and cooled with

an ice bath. Subsequently, BF_3OEt_2 (4.74 mL, 5.45 g, 38.4 mmol, 5.00 eq) was added dropwise and stirred at ambient temperature for 20 h. 20 mL water was added and the resulting mixture was extracted with DCM, washed consecutively with water, saturated $NaHCO_3$ solution, water and dried over Na_2SO_4. The solvent was removed under reduced pressure and the crude product was purified by column chromatography (cyclohexane/ethyl acetate, 7/3, v/v) yielding ManAcEMA as a white solid (1.97 g, 4.28 mmol, 56 %).

^{1}H NMR (400 MHz, $CDCl_3$, Figure B.1), δ (ppm) = 6.17-6.08 (m, 1 H, C=C*H*), 5.61-5.58 (m, 1 H, C=C*H*), 5.34 (dd, J = 10.0, 3.4 Hz, 1 H, C*H*), 5.31-5.23 (m, 2 H, C*H*), 4.87 (d, J = 1.8 Hz, 1 H, C*H*, anomeric center), 4.38-4.31 (m, 2 H, C*H*$_2$), 4.26 (dd, J = 12.2, 5.4 Hz, 1 H, C*H*−OAc), 4.08 (dd, J = 12.2, 2.4 Hz, 1 H, C*H*−OAc), 4.01 (ddd, J = 9.9, 5.4, 2.4 Hz, 1 H, C*H*), 3.96âĽŠ 3.71 (m, 2 H, C*H*$_2$), 2.15, 2.09, 2.03, 1.98 (4 s, each 3 H, acetyl groups), 1.95 (dd, J = 1.3 Hz, J = 1.3 Hz, 3 H, C*H*$_3$).

^{13}C NMR (101 MHz, $CDCl_3$, Figure B.2), δ (ppm) = 170.75, 170.13, 169.98, 169.82, 167.23, 136.09, 126.18, 97.66, 69.56, 69.08, 68.75, 66.24, 66.04, 63.26, 62.54, 21.00, 20.84, 20.81, 18.41.

ESI-MS: $[M + Na]^+$,$[C_{20}H_{28}O_{12}Na]^+$, theoretical: 483.147; experimental: 483.148

Synthesis of CTA1
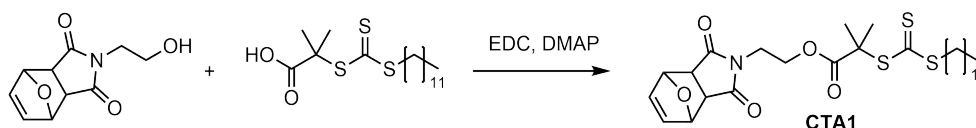
According to a literature procedure,[284] 2-(((dodecyl-thio)carbonothioyl)thio)-2-methylpropanoic acid (1.50 g, 4.12 mmol, 1.00 eq), 4-(2-hydroxyethyl)-10-oxa-4-azatricyclo[5.2.1.02,6]dec-8-ene-3,5-dione (1.29 g, 6.18 mmol, 1.50 eq) and DMAP (0.101 g, 0.823 mmol, 0.200 eq) were dissolved at 0 °C in 75 mL anhydrous THF. Subsequently, EDC·HCl (2.37 g, 12.4 mmol, 3.00 eq) was added and the reaction mixture was stirred at ambient temperature for 18 h. The solvent was removed under reduced pressure and the residue was dissolved in DCM. The solution was washed with saturated $NaHCO_3$ solution,

brine and water, and dried over Na_2SO_4. The solvent was removed under reduced pressure and the residue was purified by column chromatography (cyclohexane/ethyl acetate, 1/1, v/v) yielding CTA1 as a yellow solid (897 mg, 1.61 mmol, 39 %).

^{1}H NMR (400 MHz, $CDCl_3$, Figure B.3), δ (ppm) = 6.50 (s, 2H, C*H*=C*H*), 5.25 (s, 2 H, C*H*-O), 4.24 (t, J = 5.4 Hz, 2 H, CO_2–C*H*$_2$), 3.77 (t, J = 5.4 Hz, 2 H, N–C*H*$_2$), 3.24 (t, J = 7.4 Hz, 2 H, S–C*H*$_2$), 2.86 (s, 2 H, C*H*-CON), 1.68-1.50 (m, 8 H, C*H*$_3$ and C*H*$_2$), 1.38-1.05 (m, 18H, C*H*$_2$), 0.88 (t, J = 6.8 Hz, 3 H, CH_2–C*H*$_3$).

^{13}C NMR (101 MHz, $CDCl_3$, Figure B.4), δ (ppm) = 221.80, 175.91, 172.83, 136.67, 80.99, 62.31, 56.08, 47.67, 37.70, 37.17, 32.04, 29.76, 29.68, 29.58, 29.47, 29.23, 29.10, 27.94, 25.26, 22.82, 14.26.

ESI-MS: $[M + Na]^+$,$[C_{27}H_{41}NO_5S_3Na]^+$, theoretical: 578.204; experimental: 578.205; $[2M + Na]^+$,$[C_{54}H_{82}N_2O_{10}S_6Na]^+$, theoretical: 1133.419; experimental: 1133.422.

Synthesis of CTA2
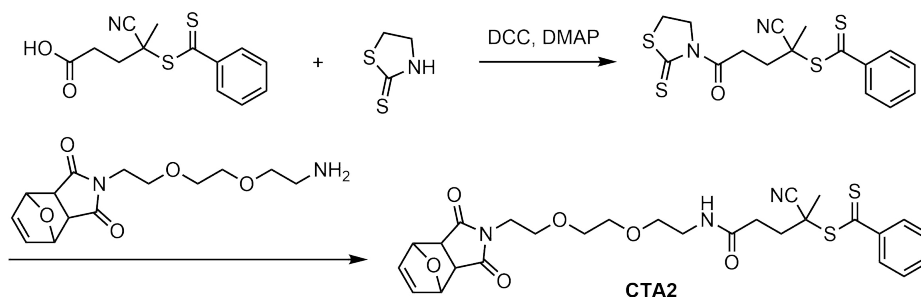
4-Cyano-4-((phenylcarbonothioyl)thio) pentanoic acid (650 mg, 2.33 mmol, 1.00 eq), mercaptothiazoline (277 mg, 2.33 mmol, 1.00 eq), DMAP (28.0 mg, 0.233 mmol, 0.100 eq) and DCC (577 mg, 2.80 mmol, 1.20 eq) were dissolved in 10 mL anhydrous DCM and stirred at ambient temperature for 14 h. Subsequently, 2-(2-(2-(2-aminoethoxy)ethoxy)ethyl)-3a,4,7,7a-tetrahydro-1H-4,7-epoxyisoindole-1,3(2H)-dione (655 mg, 2.13 mmol, 0.95 eq) in 4 mL anhydrous DCM was added dropwise (over 1 h to minimize aminolysis of the dithiobenzoate group) and stirred at ambient temperature for 5 h. The precipitate was

filtered off, and the solvent was removed under reduced pressure. The residue was purified by column chromatography (ethyl acetate/cyclohexane, 1/4, v/v, gradient to pure ethyl acetate) yielding CTA2 (205 mg, 0.368 mmol, 16 %).

^{1}H NMR (400 MHz, CDCl$_3$, Figure B.5), δ (ppm) = 7.90 (dd, J = 8.5, 1.3 Hz, 2 H, Ph), 7.59-7.53 (m, 1 H, Ph), 7.39 (dd, J = 8.4, 7.4 Hz, 2 H, Ph), 6.62 (s, 1H, N*H*), 6.50 (s, 2 H, C*H*=C*H*), 5.25 (s, 2 H, C*H*-O), 3.86-3.41 (m, 10 H, CH$_2$), 2.86 (s, 2 H, C*H*), 2.78-2.36 (m, 4 H, CH$_2$), 1.95 (s, 2 H, N−C*H*$_2$), 1.25 (s, 3 H C*H*$_3$).

^{13}C NMR (101 MHz, CDCl$_3$, Figure B.6), δ (ppm) = 222.81, 176.53, 170.80, 144.72, 136.70, 133.10, 128.69, 126.81, 118.90, 81.09, 70.49, 70.16, 69.78, 67.53, 47.64, 46.30, 39.54, 38.69, 34.33, 31.73, 29.83, 24.29.

ESI-MS: [M + Na]$^+$,[C$_{27}$H$_{31}$N$_3$O$_6$S$_2$Na]$^+$, theoretical: 580.155; experimental: 580.156.

RAFT polymerizations

Preparation of PS. CTA1 and AIBN were dissolved in styrene ([M]:[CTA]:[I], 1000:10:1), degassed by four freeze-pump-thaw cycles and stirred at 60 °C for 14 h. The polymerization was stopped by cooling with liquid nitrogen and exposing to air. Subsequently, the polymerization mixture was precipitated twice in methanol and the resulting polymer was dried under reduced pressure.

Preparation of PNIPAM. NIPAM, CTA1 and AIBN ([M]:[CTA]:[I], 1000:10:1) were dissolved in 5 mL DMF ([M] = 1.77 mol·L^{-1}) and degassed by four freeze-pump-thaw cycles and the polymerization mixture was stirred at 60 °C for 8 h. The polymerization was stopped by cooling with liquid nitrogen and exposing to oxygen. Finally, the crude product was precipitated twice in diethyl ether and dried under reduced pressure.

Preparation of PManAcEMA 1. ManAcEMA, CTA2 and AIBN ([M]:[CTA]:[I], 250:5:1) were dissolved in 1 mL DMF. The polymerization mixture was degassed by four freeze-pump-thaw cycles and polymerized at 60 °C for 14 h.

The crude product was precipitated twice in cold diethyl ether and dried under reduced pressure.

Preparation of PManAcEMA 2. ManAcEMA, CTA2 and AIBN ([M]:[CTA]:[I], 250:5:1) were dissolved in 1 mL DMF. The polymerization mixture was degassed by four freeze-pump-thaw cycles and polymerized at 60 °C for 22 h. The crude product was precipitated twice in cold diethyl ether and dried under reduced pressure.

Preparation of PManAcEMA 3. ManAcEMA, CTA2 and AIBN ([M]:[CTA]:[I], 500:5:1) were dissolved in 1 mL DMF. The polymerization mixture was degassed by four freeze-pump-thaw cycles and polymerized at 60 °C for 16 h. The crude product was precipitated twice in cold diethyl ether and dried under reduced pressure.

Retro-Diels-Alder deprotection of polymer endgroups. The deprotection reactions were performed in bulk and under reduced pressure (PS: 110 °C for 6 h, PNIPAM: 95 °C for 10 h, PManAcEMA 1-3: 110 °C for 15 h).

Photo-grafting

General procedure. ND-PE was dispersed in THF ($1\,\mathrm{g}\cdot\mathrm{L}^{-1}$) and ultrasonicated in an ultrasound bath for 1 h. Maleimide terminal polymer was added (final concentration = $1\,\mathrm{g}\cdot\mathrm{L}^{-1}$) and degassed by purging with nitrogen for 10 min. Subsequently, the reaction mixture was irradiated with UV light (Arimed B6 lamp, distance to lamp = 15 cm, $1.57\,\mathrm{mW}\cdot\mathrm{cm}^{-2}$) at ambient temperature. The NDs were centrifuged, washed four times with THF and dried under reduced pressure.

Kinetic Study for the photo-grafting of Mal-PNIPAM and Mal-PManAcEMA 1. ND-PE was dispersed in THF ($1\,\mathrm{g}\cdot\mathrm{L}^{-1}$) and ultrasonicated in an ultrasound bath for one hour. Polymer was added ($0.210\,\mathrm{mmol}\cdot\mathrm{L}^{-1}$) solution and the reaction mixture was degassed by purging with nitrogen for 10 min. The resulting dispersion was irradiated with UV light (Arimed B6 lamp, distance to lamp = 15 cm, $1.57\,\mathrm{mW}\cdot\mathrm{cm}^{-2}$) at ambient temperature for different time intervals (Mal-PNIPAM: 30 min, 60 min, 120 min, 240 min and 360 min; Mal-PManAcEMA 1: 30 min, 60 min, 120 min and 900 min). The NDs were

centrifuged, washed four times with THF, dried under reduced pressure and analyzed by TGA. The results are depicted in Figure 3.6.

Deacetylation of glycopolymer coated nanodiamonds

The deprotection of acetylated glycopolymers was performed after the grafting reaction without prior purification. A sodium methoxide solution in methanol (25 wt.%, 260 μL per 10 mg NDs) was added and stirred at ambient temperature for 2 h. Subsequently, the reaction mixture was washed twice with water and twice with THF and dried under reduced pressure.

ConA turbidity assay

The ConA turbidity assay was performed with ND@PManEMA 1-3. 150 μL ConA solution (2 mg·mL^{-1} in HEPES buffer, pH = 7) was added to 500 μL ND@PManEMA dispersion (0.1 mg·mL^{-1} in HEPES buffer) in a quartz cuvette, mixed thoroughly and added immediately to the UV-vis spectrometer. The absorbance at $\lambda = 420$ nm was measured over time. The starting point for data acquisition was set to 0 min.

4

Grafting of photoactive polymers to graphitic nanodiamonds
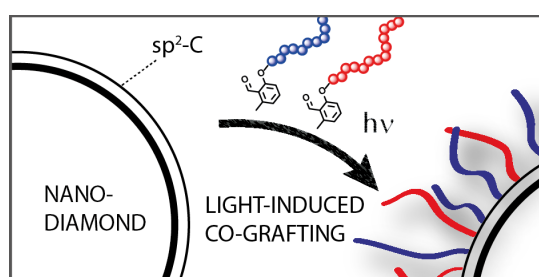
4.1. Motivation

The surface modification of nanodiamonds (NDs) is commonly performed in multi-step procedures involving initial oxidation or reduction followed by chemical reactions that lead to the attachment of the molecule of interest (Section

2.1.4 and Chapter 3). An elegant alternative is the generation of graphene-like carbon structures on NDs *via* thermal annealing. Typically, temperatures above 700 °C are employed that lead to the desorption of surface groups followed by a sp^3-sp^2 phase transition.[63] Importantly, the formation of sp^2 carbon structures starts at the surface and proceeds to the core. Hence, the preparation of surface graphitized nanoparticles with retention of the diamond core is possible. Coupling reactions with diazonium salts,[64,285] maleimides,[286] as well as thermally generated *o*-quinodimethanes[65] have been performed on surface graphitized NDs. The latter example is based on Diels-Alder reactions with surface-expressed graphene structures. Importantly, the curvature of sp^2 carbon structures increases the Diels-Alder reactivity.[287] The increased reactivity can be explained with strain relief due to sp^2-sp^3 rehybridization during Diels-Alder reactions.[288] Besides NDs,[65] other curved sp^2 hybridized carbon structures, such as fullerenes[289] and carbon nanotubes[290] have successfully been modified by Diels-Alder grafting. On the basis of the previous chapter, the photoenol ligation was employed herein, however, *o*-methyl benzaldehyde groups were attached to polymer endgroups that allowed for the light triggered Diels-Alder grafting onto graphitic NDs (grNDs). Furthermore, co-grafting on NDs is investigated for the generation of complex polymeric surface structures.

4.2. Annealing of nanodiamonds
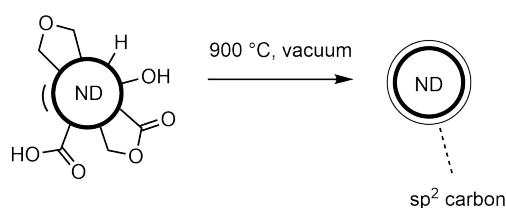
Scheme 4.1. Schematic representation of the thermal annealing of NDs. Adapted from Ref. [291] with permission from The Royal Society of Chemistry.

First, detonation NDs were thermally annealed to generate surface-expressed dienophiles for photoenol grafting (Scheme 4.1). The selective surface graphitization of detonation NDs was performed in vacuum at 900 °C for 2 h. X-ray diffraction (XRD) measurements of the sample before and after annealing
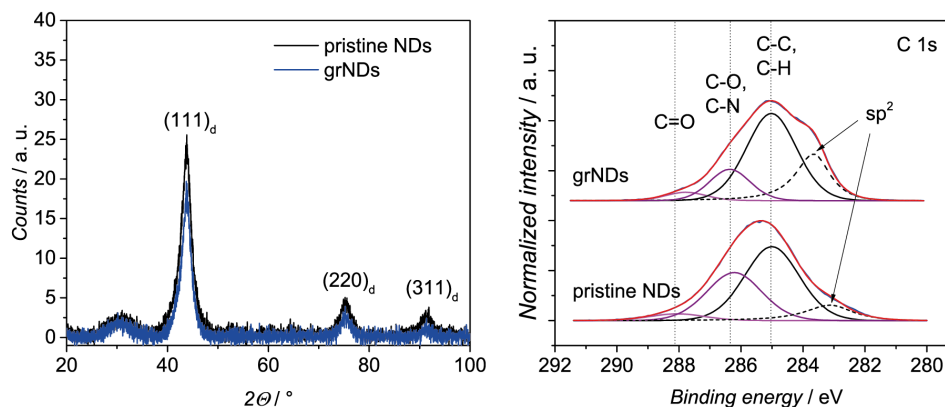
Figure 4.1. XRD patterns (left) and XP spectra (right) of NDs before and after thermal annealing. Adapted from Ref. [291] with permission from The Royal Society of Chemistry.

revealed the retention of the diamond diffraction pattern (Figure 4.1). X-ray photoelectron spectroscopy (XPS) was employed to investigate the degree of graphitization (Figure 4.1). The analysis of thin ND powder layers was conducted using charge compensation. However, probably due to the particulate properties of the sample, charge compensation was not completely successful. The spectra were referenced to the characteristic sp^3 component of NDs (C-C, C-H, 285 eV) leading to a shift of 1.2 eV towards lower binding energy. Consequently, graphitic carbon is graphically charge-overcompensated and appears at 283.3 ± 0.2 eV. Without energy corrections the sp^2 component appears at 284.4 ± 0.2 eV. According to the XP spectra, the annealing process leads to a significant increase in sp^2 carbon from 9.8 at.% to 21.8 at.%. Interestingly, the signals at 286.3 eV and 288.0 eV, which usually correspond to oxidized carbon species (C-O, C-N and C=O, respectively) do not align with the oxygen and nitrogen content of the sample. Hence, a further contribution to these signals has to be assumed. Structural defects might contribute to the signals.[292] However, further investigation is required in order to fully understand the origin of these signals.

4.3. Preparation of photoactive polymers
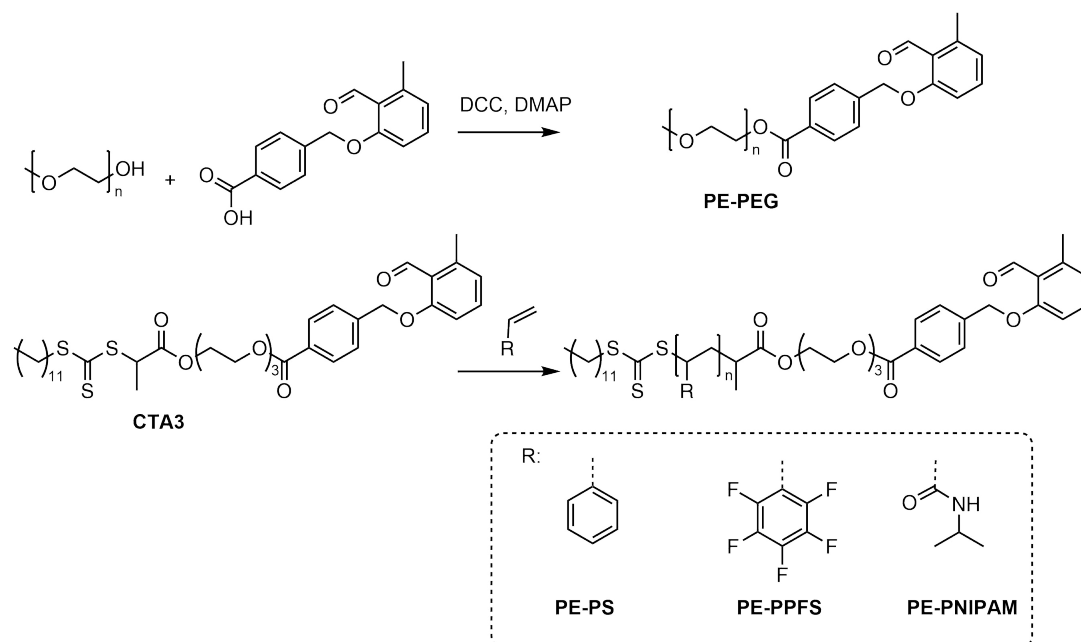
Scheme 4.2. Preparation of photoactive polymers. Adapted from Ref. [291] with permission from The Royal Society of Chemistry.

A small library of *o*-methyl benzaldehyde terminal polymers was prepared for the investigation of light-triggered Diels-Alder grafting on annealed NDs (Scheme 4.2). First, hydroxy terminal poly(ethylene glycol) (PEG) (M_n = 2000 g·mol^{-1}) was reacted with a fourfold excess of 4-((2-formyl-3-methyl-phenoxy)methyl)benzoic acid *via* a DCC mediated esterification reaction (Scheme 4.2). The ^{1}H NMR spectrum of the obtained photoenol functional PEG (PE-PEG) exhibits the proton signals corresponding to the introduced photoactive endgroups including the aldehyde proton resonance at 10.75 ppm (Figure C.12, Appendix). Additionally, the successful functionalization of PEG was confirmed *via* electrospray ionization mass spectrometry (ESI MS) (Figure 4.2). The main signals of the ESI MS spectra can be assigned to the product PE-PEG. Double-charged species corresponding to adducts of PE-PEG with two Na$^+$ ions, for instance at m/z 1068.080 (exp.) (1068.081 (th.)), were observed (Figure 4.2) and prove the success of the functionalization procedure.
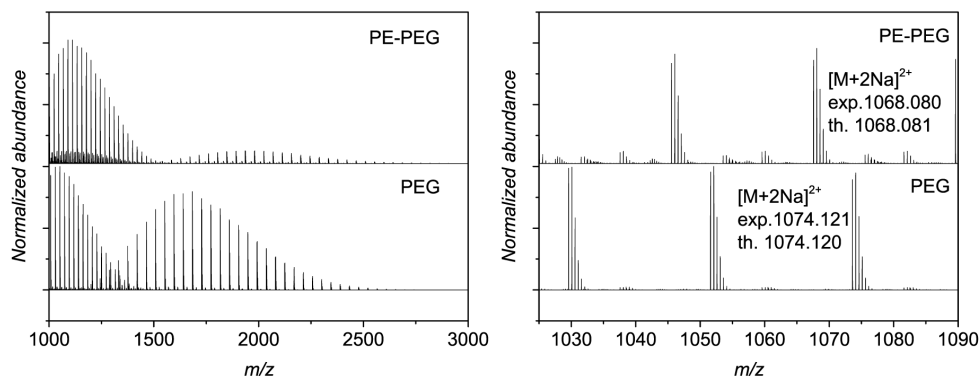
Figure 4.2. ESI MS results of the functionalization of PEG with photoenol groups. Adapted from Ref. [291] with permission from The Royal Society of Chemistry.

Furthermore, a novel photoenol functional chain transfer agent (CTA) for reversible addition fragmentation chain transfer (RAFT) polymerization was prepared (CTA3, Scheme 4.2). 2-(Dodecylthiocarbonothioylthio)propionic acid was reacted in two consecutive EDC mediated esterification reactions, first with triethylene glycol, which acts as a spacer, and then with 4-((2-formyl-3-methylphenoxy)methyl)benzoic acid. The successful formation of CTA3 was confirmed *via* NMR spectroscopy (Figure C.15-C.16). In detail, the proton resonances at 10.75 ppm and 2.59 ppm confirm the presence of the *o*-methyl benzaldehyde group whereas resonances at 3.90 ppm - 3.28 ppm and at 1.25 ppm can be assigned to the triethylene glycol spacer and the aliphatic proton signals of the dodecyl group, respectively. In addition, ESI MS experiments confirmed the successful formation of CTA3 with a signal at m/z 757.292 (exp) (757.287 (th.)) corresponding to the sodium adduct.

Subsequently, a small library of photoactive polymers was prepared *via* RAFT polymerization. First, styrene and pentafluorostyrene (PFS) were polymerized in bulk. Further, poly(*N*-isopropylacrylamide) (PNIPAM) polymers of three chain lengths were prepared in DMF. Size exclusion chromatography (SEC) of the photoenol terminal polymers revealed low dispersities ($Đ \leq 1.27$) and monomodal molecular weight distributions (MWDs) (Figure 4.3). The SEC results as well as NMR determined molecular weight and degree of polymerization (DP) are summarized in Table 4.1.
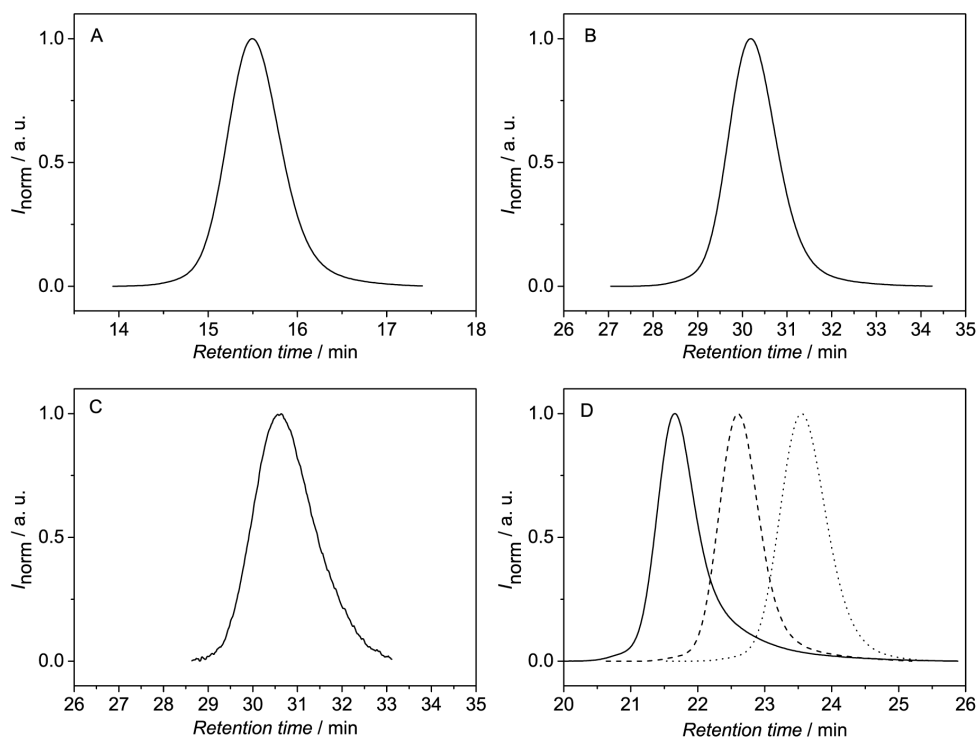
Figure 4.3. SEC results of the prepared polymers. A: PE-PEG in THF. B: PE-PS in THF. C: PE-PPFS in THF. D: PE-PNIPAM in DMAC (1-3, right to left). Adapted from Ref. [291] with permission from The Royal Society of Chemistry.

Table 4.1. SEC and NMR characterization data of photoenol terminal polymers.

Polymer	M_n^{SEC} / g·mol^{-1}	$Đ^{SEC}$	M_n^{NMR} / g·mol^{-1}	DP^{NMR}
PE-PEG	3300	1.03	2400	48
PE-PS	9400	1.09	11700	105
PE-PPFS	7500	1.11	12400	60
PE-PNIPAM 1	9300	1.10	7600	61
PE-PNIPAM 2	18600	1.11	17000	144
PE-PNIPAM 3	30500	1.27	34800	301

4.4. Photo-grafting
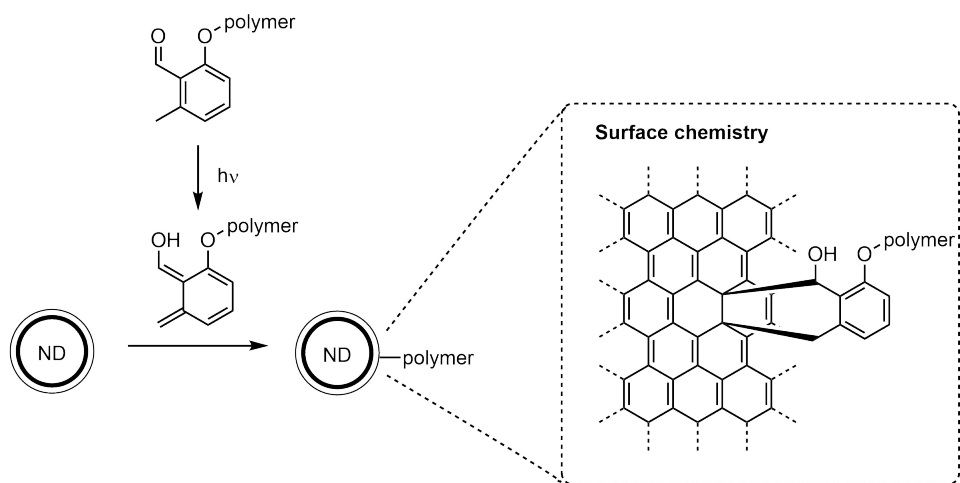
Scheme 4.3. Schematic representation of the photo-grafting of functional polymers to NDs and proposed surface chemistry. Adapted from Ref. [291] with permission from The Royal Society of Chemistry.

The annealing process described above led to the formation of sp^2 carbon on the ND's surface. The photoenol ligation is based on the light induced formation of *o*-quinodimethanes, which are dienes that can react in a subsequent Diels-Alder reaction with suitable double bonds. Thus, an increase of the available double bonds for the Diels-Alder reactions should increase the grafting density. To investigate the effect of thermal annealing on the Diels-Alder reactivity, non-treated as well as annealed NDs were irradiated at λ = 320 nm in the presence of PE-PS. Subsequently, the samples were freed from unreacted polymer and the grafting density was determined by thermogravimetric analysis (TGA). During a typical TGA experiment, the sample was heated at a constant rate of 10 °C·min^{-1} to 800 °C in the presence of oxygen (air atmosphere) while recording the mass. The NDs were completely oxidized at around 600 °C leading to full weight loss, whereas the polymers decomposed at lower temperatures. The difference in the decomposition temperature of ND and polymer allowed for the calculation of the amount of grafted polymer. Importantly, the annealing process led to a significant higher grafting density (13.7 wt.% compared to 3 wt.%, Figure 4.6 and Figure C.22, Appendix, respectively). Furthermore, with increasing irradiation time, the grafting density increases, clearly showing the success of the photo-grafting approach (Figure C.23, Appendix).
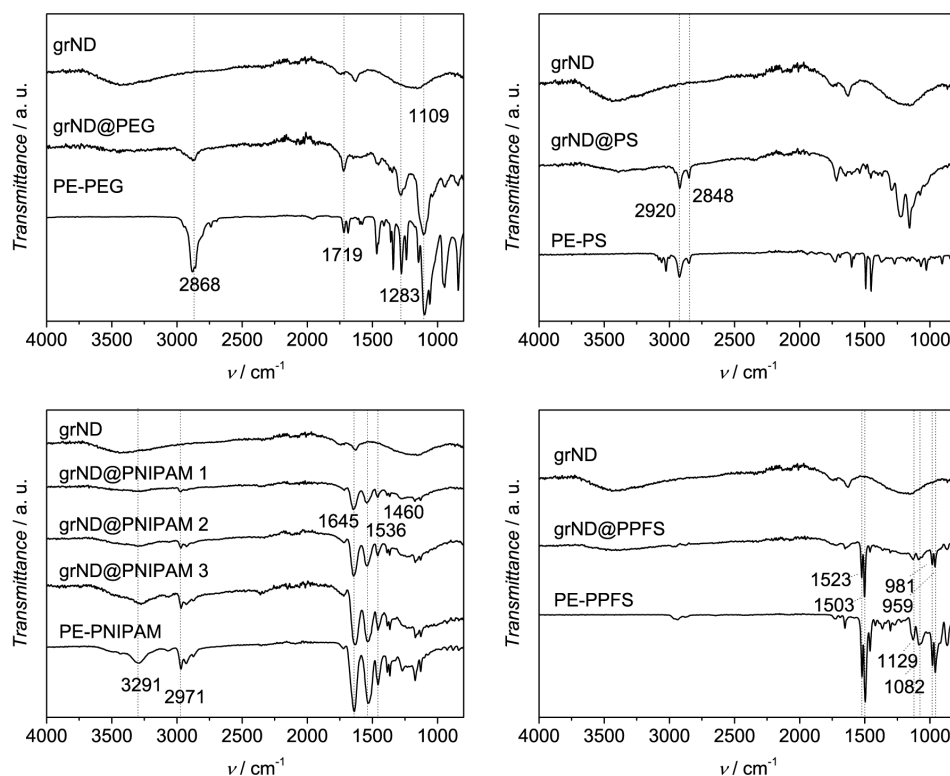
Figure 4.4. ATR FTIR spectra of the prepared samples. Adapted from Ref. [291] with permission from The Royal Society of Chemistry.

Next, the photoenol terminal polymers from Section 4.3 were photo-grafted to grNDs and characterized *via* ATR FTIR spectroscopy (Figure 4.4). Characteristic absorption bands of the corresponding polymers were found in the spectra of all polymer coated NDs. For instance, the symmetrical CH_2 stretching vibration at $2868\,cm^{-1}$ confirmed the successful grafting of PE-PEG. The photo-grafting of PE-PS was accompanied with the appearance of absorption bands at $2920\,cm^{-1}$ and $2848\,cm^{-1}$ that are characteristic for the CH_2 bands of PS.[293] The photo-grafting of PE-PPFS onto NDs led to characteristic PPFS absorption bands at $1503\,cm^{-1}$ and $959\,cm^{-1}$. Furthermore, the presence of PPFS on the NDs could be confirmed *via* XPS (Figure 4.5). A strong fluorine signal at $688.4\,eV$ appeared upon photo-grafting of PE-PPFS. The grafting of PE-PNIPAM to grND was accompanied with the appearance of characteristic amide bands at $1645\,cm^{-1}$, $1536\,cm^{-1}$ and a symmetric $-C(CH_3)_2$ deformation band at $1460\,cm^{-1}$.[277] In agreement with the ATR FTIR results, XPS confirmed the successful PNIPAM photo-grafting. The content of nitrogen correspon-
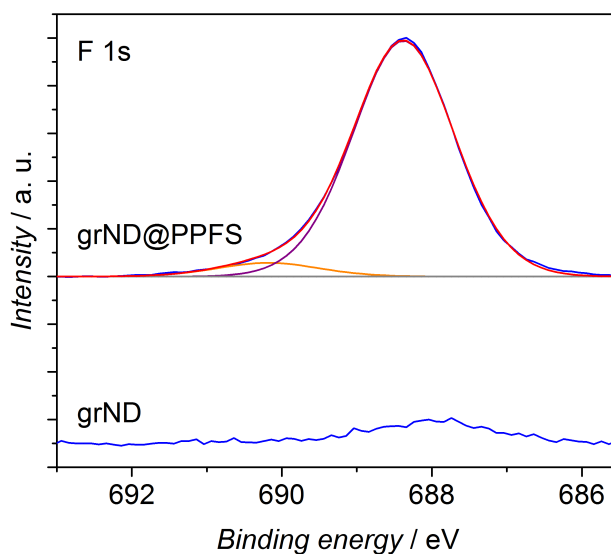
Figure 4.5. XP F 1s spectra of grNDs and grND@PPFS. Adapted from Ref. [291] with permission from The Royal Society of Chemistry.

ding to amide functionalities increased upon photo-grafting from 1.1 at.% to 4.1 at.%, 4.5 at.%, and 4.9 at.% for PE-PNIPAM 1-3, respectively.

As described above, TGA was employed to determine grafting densities in wt.% (mass of polymer per mass sample). Furthermore, the calculation of molar grafting densities as well as polymer footprints (surface area per polymer chain) was performed. The grafting densities are summarized in Table 4.2. Grafting densities up to 26.7 wt% and 21.7 μmol $\cdot$ g^{-1} were obtained. Compared to the grafting approach in Chapter 3, the direct grafting of photoenol functional polymers to graphitic NDs led to significantly higher grafting densities. The grafting densities for PE-PS and PE-PNIPAM were approximately twice as high. The high grafting densities achieved here can be explained with a higher densitiy of reactive groups on the NDs. Compared to the simple one step annealing approach to obtain grNDs, the immobilization of *o*-methyl benzaldehyde groups was a four step procedure leading to less reactive surface groups. It should be noted that the PE-PEG grafting density is unexpectedly high (five chains per nm^2). Additional adsorption could be the reason for the high grafting density.
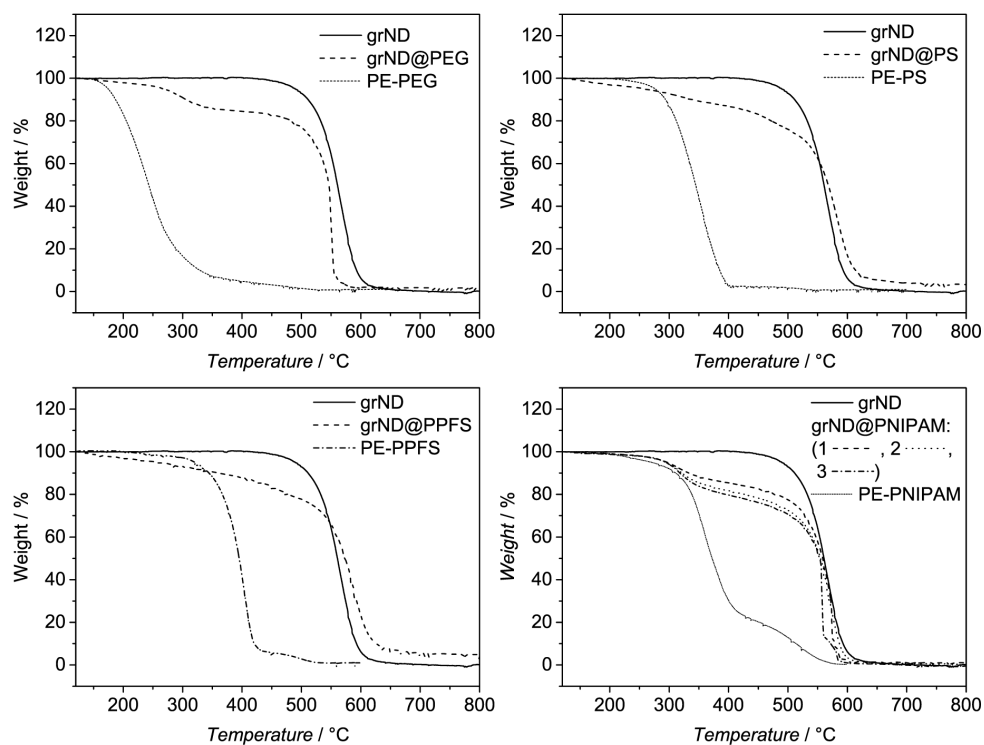
Figure 4.6. TGA results of the prepared samples. Adapted from Ref. [291] with permission from The Royal Society of Chemistry.

Similar to Chapter 3, a chain length dependency of the grafting process was observed (Figure 4.7). The grafting density of PE-PNIPAM correlated with its molecular weight. Longer polymer chains led to lower molar grafting densities. The decrease in molar grafting density is due to steric hindrance. Longer polymers cover a larger area on the ND's surface. However, the grafting density in wt.% increases with increasing molecular weight, which is in agreement with the nitrogen content determined *via* XPS (see above).

In the present study, detonation NDs were employed, which are aggregates consisting of small primary particles (close 5 nm). To obtain information about the size distributions of the respective ND samples, dynamic light scattering (DLS) experiments were performed (Table 4.2, Figure C.24, Appendix). The number average hydrodynamic diameter of grNDs was 166 nm. Further disintegration of the aggregates using high power ultrasonication was not possible. Covalent bonds are likely responsible for the close structure of ND aggregates. Although not investigated here, the grafting-process should be
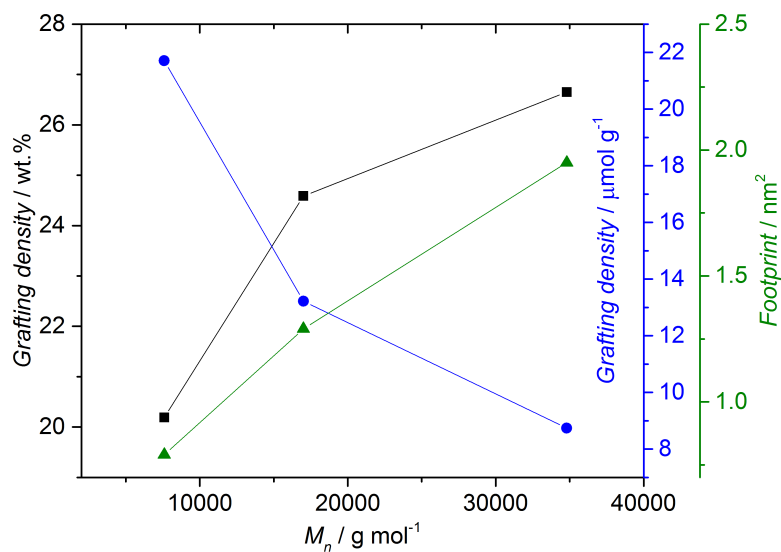
Figure 4.7. TGA results. Grafting densities of PE-PNIPAM polymers vs. molecular weight. The molar grafting densities (blue) as well as the polymer footprints (green) were calculated from the weight grafting densities (black). Adapted from Ref. [291] with permission from The Royal Society of Chemistry.

Table 4.2. Characterization data of prepared polymer coated NDs. Hydrodynamic diameters and grafting densities were determined *via* DLS and TGA measurements, respectively.

Sample	D_{h} / nm	Grafting density / wt.%	Grafting density / $\mu\mathrm{mol} \cdot \mathrm{g}^{-1}$	Footprint / nm^2
grND@PS	210	13.7	9.4	1.49
grND@PEG	347	16.4	82	0.21
grND@PPFS	192	9.9	6.5	2.64
grND@PNIPAM 1	201	20.2	21.7	0.79
grND@PNIPAM 2	219	24.6	13.2	1.29
grND@PNIPAM 3	205	26.7	8.7	1.95
grND@PNIPAM/PPFS 1	219	15.7	11.8	1.45
grND@PNIPAM/PPFS 2	210	13.5	10.8	1.58
grND@PNIPAM/PPFS 3	252	13.5	13.6	1.25

independent of aggregate size. In all experiments, the hydrodynamic diameter increased upon photo-grafting due to the formation of a polymeric shell.

4.5. Co-grafting

So far, only the grafting of one polymer type to NDs was described. However, the generation of multifunctional surfaces by grafting different polymer types to the same surface in a modular approach might allow for the facile generation of complex surface structures with fine-tuned properties. For instance, polymers with targeting properties and therapeutic polymers (*e.g.* drug containing polymers) could be co-grafted to prepare nanoparticles for targeted drug delivery. The ratio between the two polymers will probably influence the efficacy of the system. Thus, a synthetic co-grafting approach and an analytical method to characterize these structures is highly desirable.

As a proof of concept, the simultaneous co-grafting of PE-PNIPAM 1 and PE-PPFS was investigated. PE-PNIPAM 1 was selected from the prepared PNIPAM polymers due to the similar degree of polymerization ($DP \approx 60$). The polymer types were carefully chosen due to structural differences that allowed for the investigation of the co-grafting ratio by XPS and ATR FTIR spectroscopy. The exclusive presence of fluorine and nitrogen in PE-PPFS and PE-PNIPAM, respectively, allowed for the XPS characterization of the co-grafting ratio. Furthermore, the co-grafting ratio was quantified by comparing characteristic IR absorbance bands. PE-PNIPAM 1/PE-PPFS mixtures with 25 %, 50 % and 75 % PE-PNIPAM (molar fractions) were prepared and added to grND dispersions. Subsequent UV irradiation at $\lambda_{max} = 320\,\text{nm}$ and purification from unreacted polymer led to NDs with co-grafted surface structures. Similar grafting densities were obtained with values in between the homo-grafted systems (Table 4.2). The PNIPAM amide I vibration band at $1636\,\text{cm}^{-1}$ (A_1) and PPFS band at $981\,\text{cm}^{-1}$ (A_2) were integrated to obtain the ratio A_1/A_2, which was compared to a calibration curve established with PE-PNIPAM/PE-PPFS mixtures of known ratios (Figure C.25 and C.26, Appendix). Importantly, the employed feedstock ratio for the photo-grafting experiment correlated with the resulting co-grafting ratio on the ND's surface.

Increasing the PE-PNIPAM 1 content in the feedstock leads to an increase of grafted PE-PNIPAM 1 on the NDs (Figure 4.8). In agreement with the ATR FTIR experiments are the observations from XPS. The fluorine to nitrogen ratio of the co-grafted NDs increased with increasing PPFS content in the feedstock. However, quantification of the co-grafting ratio *via* XPS was not possible since the information depth is deeper than the polymeric coating and, thus, the measured signals are partially from the ND core and the origin of the signal cannot be distinguished.

The co-grafting of bioactive polymers, such as glycopolymers, is highly interesting for biomedical applications. Glycopolymers can be used as targeting ligands for targeted drug delivery and promote accumulation of nanoparticles in specific cell types (Section 2.4.4). The minimum amount of glycopolymer required for efficient lectin binding as well as the influence of polymer chain length ratio on bioactivity are key aspects for the development of co-grafted systems for biomedical applications. Thus, the above introduced co-grafting approach was investigated further for the generation of a polymeric shell consisting of PNIPAM and a mannose glycopolymer. PNIPAM was selected
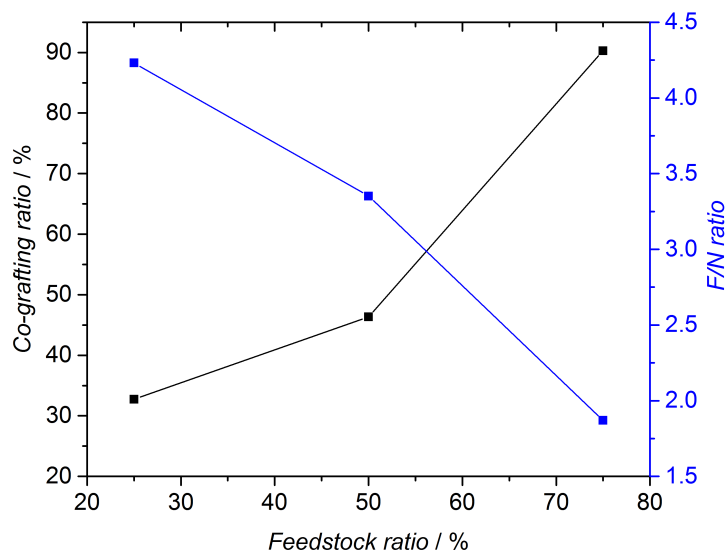
Figure 4.8. Feedstock ratio vs. co-grafting ratio (both molar fractions) and F/N ratio determined via IR and XPS analysis, respectively. Adapted from Ref. [291] with permission from The Royal Society of Chemistry.

93

for the co-grafting experiments since it is biocompatible and thermoresponsive. Above the lower critical solution temperature (LCST) PNIPAM collapses, which could be exploited to influence the surface structure by altering the amount of freely accessible carbohydrate units for lectin binding.

A novel CTA was designed for the preparation of photoenol terminal glycopolymers (CTA4, Scheme 4.4). CTA3 was not used in this study since the photoenol group is attached to the trithiocarbonate moiety *via* two ester groups, which might cleave during deprotection of the glycopolymer. CTA4 was prepared from 2-((4-(bromomethyl)benzyl)oxy)-6-methylbenzaldehyde and *in situ* formed dodecyltrithiocarbonate anions in a substitution reaction. ^{1}H NMR spectroscopy confirms the formation of the photoenol functional RAFT agent (Figure C.27, Appendix). Subsequent RAFT polymerization with CTA4 allowed for the preparation of photoenol terminal polymers. A glycopolymer (PE-PManAcEA, M_n= 39400 g·mol^{-1}) based on 2-(2',3',4',6'-tetra-*O*-acetyl-α-D-mannosyloxy)ethyl acrylate (ManAcEA) and three PNIPAM polymers differing in molecular weight (PE-PNIPAM A-C, M_n= 3800, 12400 and 33400 g·mol^{-1}, Scheme 4.4 and Table 4.3) were prepared. Whereas the molecular weight of the PE-PNIPAM polymers determined by SEC and NMR are similar, a threefold higher molecular weight was calculated from ^{1}H NMR spectra compared to the SEC determined value. The SEC molecular weight was calculated using PMMA as a standard and is not an absolute molecular weight determination. Thus, values determined via ^{1}H NMR spectroscopy were used for further calculations. Importantly, the prepared PNIPAM series
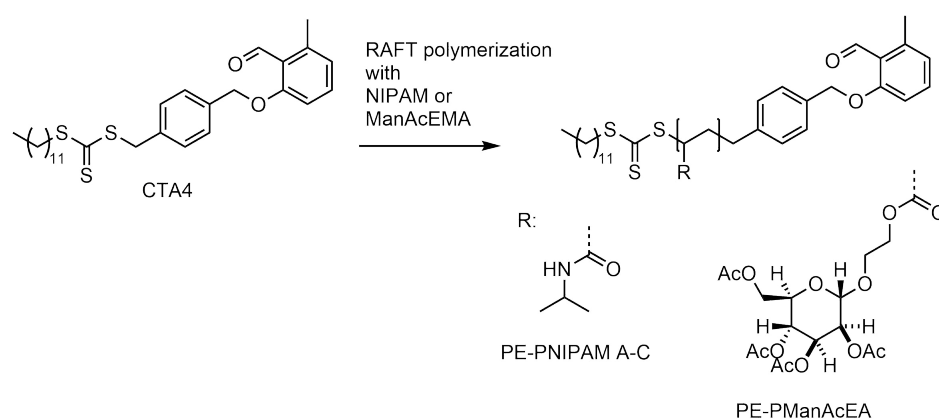
Scheme 4.4. RAFT polymerization of NIPAM and ManAcEA to obtain photoenol terminal polymers.
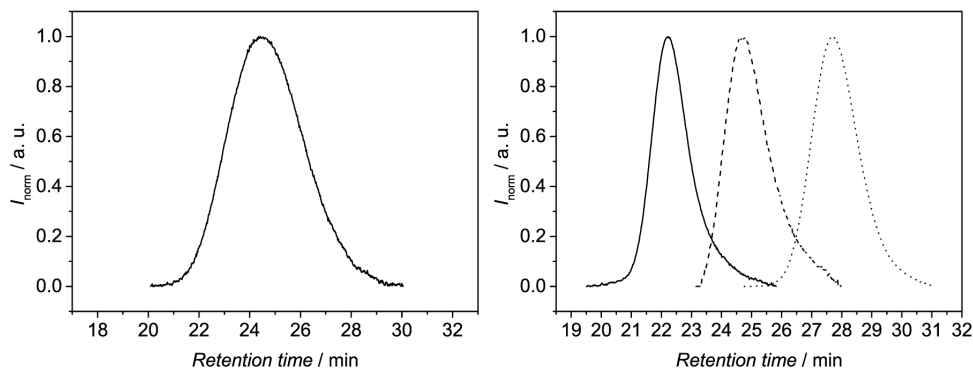
Figure 4.9. SEC results of the prepared polymers. Left: PE-PManAcEA. Right: PE-PNIPAM A-C (right to left)

Table 4.3. SEC and NMR characterization data of prepared polymers.

Polymer	M_n^{SEC} / g·mol^{-1}	$Đ^{SEC}$	M_n^{NMR} / g·mol^{-1}	DP^{NMR}
PE-PNIPAM A	4400	1.14	3800	29
PE-PNIPAM B	13000	1.08	12400	105
PE-PNIPAM C	30300	1.08	33400	291
PE-PManAcEA	13300	1.27	39400	87

consists of polymers of smaller, similar and a larger degree of polymerization compared to the glycopolymer allowing for the investigation of chain length ratio and resulting co-grafted structures.

To enable the quantification of the co-grafting ratio, a calibration curve using different mixtures of PE-PNIPAM C and PE-PManAcEA was determined by ATR FTIR spectroscopy (Figure C.32, Appendix). It should be noted that the calibration curve for PE-PNIPAM C was used for all co-grafting systems and the contribution of the endgroup to the IR spectra was assumed to be negligible. The feedstock and co-grafting ratios are reported here as a weight fraction.
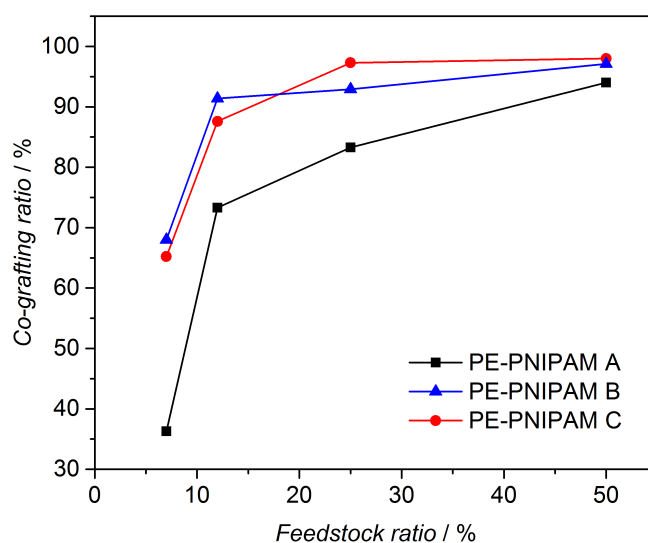
Figure 4.10. PNIPAM feedstock ratio *vs* co-grafting ratio (weight fraction) determined *via* ATR FTIR spectroscopy analysis.

Different feedstock ratios of PE-PNIPAM A-C and PE-PManAcEA were co-grafted to grNDs and the co-grafting ratio was determined *via* ATR FTIR spectroscopy (Figure 4.10). PE-PNIPAM is preferentially photo-grafted to the ND's surface. A significant increase of glycopolymer feedstock ratio is required to obtain above 10 % glycopolymer content on the NDs.

TGA revealed grafting densities of 14.4, 15.7 and 18.5 wt.% for the co-grafting (50 % feedstock ratio) of PNIPAM A-C, respectively (Figure C.33, Appendix). The surface-expressed glycopolymers were deprotected using sodium methylate, which led to a mass decrease of the polymer layer between 5.5 and 7.0 wt.% (Figure C.34 - C.36, Appendix). However, the absolute grafting density of PE-PManAcEA in the co-grafting experiments with PNIPAM A-C (50 % feedstock ratio) was below 1 wt.% according to the IR analysis, which indicates that polymer chains were removed from the surface during deacetylation. TGA of the sample prepared from a 7 % PE-PNIPAM B feedstock ratio revealed a total grafting density of 18.1 wt.% corresponding to 12.3 wt.% PNIPAM, which is above the expected value (Figure C.37, Appendix). During the grafting procedure, NDs were first dispersed using ultrasound and sedimented particles were removed to obtain a homogeneous dispersion, which

decreased the final ND concentration and explains the high PNIPAM grafting densities. Even at a low PNIPAM feedstock ratio, PNIPAM is preferentially attached to the surface (Figure 4.10). The reason for the preferential co-grafting behaviour is not known yet and further investigation of the dependence of co-grafting ratio on polymer structure and grafting conditions is required.

4.6. Conclusion

The modular and light-induced modification of surface graphitized NDs (grNDs) is introduced. First, detonation NDs were annealed to generate graphitic surface structures. A variety of photoenol terminal polymers (PEG, PS, PPFS and PNIPAM) were prepared and grafted directly onto grNDs. Furthermore, the co-grafting of PNIPAM and PPFS was investigated. The feedstock ratio was directly reflected on the co-grafting ratio as shown by IR spectroscopy and XPS. A second set of photoenol polymers consisting of a glycopolymer and three PNIPAM polymers of varying chain lengths was prepared for further co-grafting experiments. The co-grafting of this system led to a significant higher amount of PNIPAM in the co-grafted sample compared to the employed feedstock ratio. In general, endgroup fidelity is important for an efficient grafting-to process and poor photoenol termination of the glycopolymer could have led to the preferential co-grafting behaviour. Furthermore, an additional spacer between polymeric backbone and photoactive group as employed in the first system (PNIPAM/PPFS) could increase glycopolymer grafting efficiency. In addition, the solvent might affect the co-grafting ratio since the accessibility of the polymer endgroup is influenced by the solubility of the polymer. Further studies on the effect of polymer structure and reaction conditions on co-grafting ratio are required to fully understand the co-grafting process.

4.7. Experimental section

4.7.1. Materials

Methyl 4-((2-formyl-3-methylphenoxy)methyl)benzoic acid[131] and 2-(2',3',4',6'-tetra-*O*-acetyl-*α*-D-mannosyloxy)ethyl acrylate (ManAcEA)[180] were prepared according to literature procedures. Detonation nanodiamonds (purified, grade G01) were purchased from PlasmaChem GmbH (Berlin) and used as received. 2-(Dodecylthiocarbonothioylthio)propionic acid (DOPAT) was provided from Lanxess. Methoxy polyethylene glycol (PEG, M_n = 2000 g·mol^{-1}, Sigma-Aldrich), triethylene glycol (TEG, Sigma-Aldrich), *N,N'*-dicyclohexylcarbodiimide (DCC, 99 %, Acros), 4-(dimethylamino)pyridine (DMAP, 99 %, abcr), 1-ethyl-3-(3-dimethylaminopropyl)carbodiimide (EDC) hydrochloride (EDC·HCl, 99+ %, Roth), 2,2'-azobis(isobutylonitrile) (AIBN, VWR), chloroform-d$_1$ (CDCl$_3$, 99.8 %, EURISO-TOP), dimethyl-d$_6$ sulfoxide (DMSO-d$_6$, 99.8 %, EURISO-TOP) were used as received. *N*-Isopropylacrylamide (NIPAM, TCI, 98 %) was recrystallized from hexane before usage. Styrene and pentafluorostyrene were passed through a column of basic alumina prior to polymerization. *N,N*-Dimethylformamide (DMF), tetrahydrofuran (THF), dichloromethane (DCM), acetonitrile, diethyl ether, ethyl acetate, and cyclohexane were purchased as analytical grade (Sigma-Aldrich) and used as received.

4.7.2. Instrumentation

The description of the TGA, NMR spectroscopy, ESI MS, XPS, the sonotrode and photoreactor including lamp can be found in Chapter 3, Section 3.7.

ATR FTIR spectroscopy.

IR spectra from polymer/ND powders were recorded on a Bruker Alpha ATR FTIR spectrometer.

4.7.3. Experimental procedures

Thermal annealing of NDs (grND)

The thermal annealing of pristine NDs (PlasmaChem, purified grade 01) was performed in a quartz tube under reduced pressure (approx. $2 \cdot 10^{-2}$ mbar, dynamic vacuum) at 900 °C for 2 h. The following heating protocol was applied:

1. Ambient temperature to 900 °C, heating over 2 h

2. Isothermal at 900 °C for 2 h

3. 900 °C - 500°C in 2 h inside the turned off tube furnace

4. 500 °C to ambient temperature in 1 h outside the tube furnace

Synthesis of *o*-methyl benzaldehyde terminal PEG (PE-PEG)
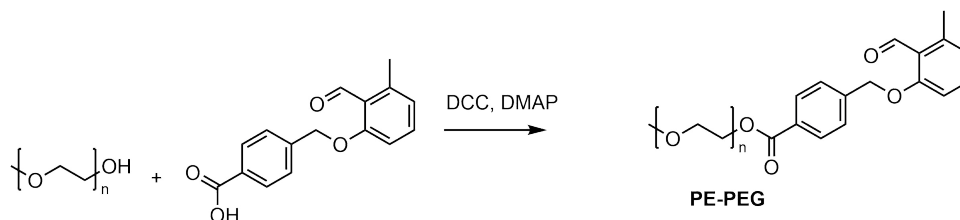
MeO-PEG-OH (2000 Da, 700 mg, 0.35 mmol, 1.00 eq), DCC (144 mg, 0.70 mmol, 2.00 equiv), 4-dimethylaminopyridine (DMAP) (32.1 mg, 0.26 mmol, 0.750 eq) and methyl 4-((2-formyl-3-methylphenoxy)methyl)benzoic acid (378 mg, 1.40 mmol, 4.00 eq) were dissolved in an anhydrous mixture of DMF/DCM (10/1, v/v, 11 mL) and stirred for 20 h. The precipitate was removed *via* filtration. Subsequently, the solvent was removed under reduced pressure and the residue was precipitated three times in 35 mL cold diethyl ether.

^{1}H NMR (400 MHz, CDCl$_3$), δ (ppm) = 10.75 (s, 1H, C*H*O), 8.08 (d, J = 8.3 Hz, 2H, Ph), 7.50 (d, J = 8.4 Hz, 2H, Ph), 7.36 (dd, J = 8.4, 7.6 Hz, 1H, Ph), 6.94

- 6.80 (m, 2H, Ph), 5.23 (s, 2H, PhCH_2O), 4.60 - 4.40 (m, 2H, COOCH_2), 3.92 - 3.79 (m, 2H, COOCH$_2$CH_2), 3.64 (s, (C$_2H_4$O)$_n$, 194 H), 2.59 (s, 3H, PhCH_3).

Synthesis of CTA3

DOPAT

DOPAT-OH

CTA3
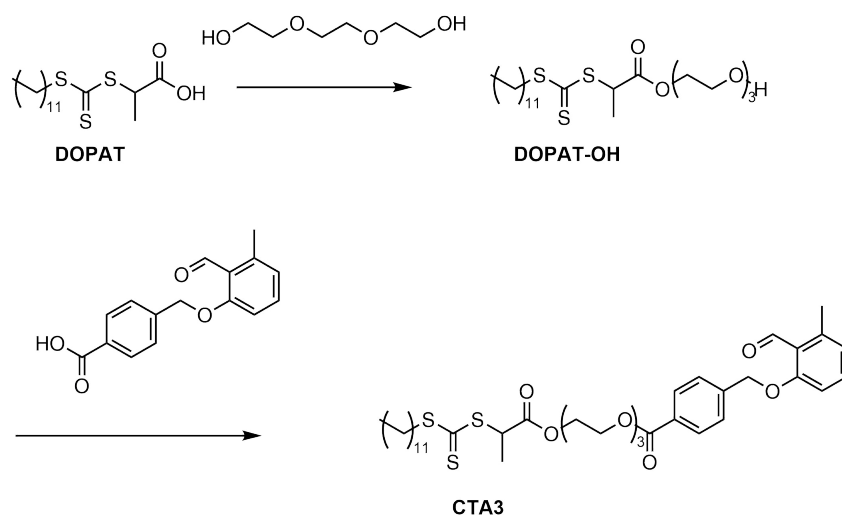
2-(Dodecylthiocarbonothioylthio)propionic acid (5.00 g, 14.3 mmol, 1.00 eq), EDC hydrochloride (4.10 g, 21.4 mmol, 1.50 eq), DMAP (174 mg, 1.43 mmol, 0.100 eq) and triethylene glycol (42.8 g, 285 mmol, 20.0 eq) were dissolved in 30 mL anhydrous DCM and stirred for 15 h. Subsequently, 150 mL saturated NaHCO$_3$ solution was added. The aqueous phase was extracted (3×) with DCM. The combined organic layers were washed consecutively with 1 N HCl, water and brine and dried over Na$_2$SO$_4$. The solvent was removed under reduced pressure to obtain 2-(2-(2-hydroxyethoxy)ethoxy)ethyl 2-(((dodecylthio)carbonothioyl)thio)propanoate (DoPAT-OH, 6.70 g, 13.9 mmol, 97 %).

^{1}H NMR (400 MHz, CDCl$_3$), δ (ppm) = 4.84 (q, J = 7.4 Hz, 1H, SCH), 4.39 - 4.26 (m, 2H, COOCH_2), 3.82 - 3.55 (m, 10H, triethylene glycol spacer), 3.45 - 3.26 (m, 2H, SCH2), 1.68 (m, 2H, CH_2CH$_3$), 1.61 (d, J = 7.4 Hz, 3H, CH_3CH), 1.48 - 1.15 (m, 18H, (CH_2)$_9$), 0.88 (t, J = 7.0 Hz, 3H, CH$_2$CH_3).

^{13}C NMR (101 MHz, CDCl$_3$), δ (ppm) = 222.2, 171.3, 72.6, 70.8, 70.6, 69.0, 64.9, 62.0, 48.1, 37.4, 32.1, 29.8, 29.8, 29.7, 29.6, 29.5, 29.2, 29.1, 28.0, 22.8, 17.0, 14.3.

ESI-MS: [M + Na]$^+$, [C$_{22}$H$_{42}$O$_5$S$_3$Na]$^+$, theoretical: 505.209; experimental: 505.211.

DoPAT-OH (1.00 g, 2.13 mmol, 1.00 eq), DMAP (122 mg, 26.1 mmol, 0.100 eq), EDC · HCl (613 mg, 3.20 mmol, 1.50 eq) and 4-((2-formyl-3-methylphenoxy)-methyl)benzoic acid (577 mg, 2.13 mmol, 1.00 eq) were dissolved in an anhydrous mixture of DCM/DMF (10/3, v/v, 13 mL) and stirred for 15 h. Subsequently, 150 mL saturated NaHCO$_3$ solution was added and the aqueous phase was extracted three times with DCM. The organic layers were combined and washed with 1 N HCl, water and brine. The organic phase was dried over Na$_2$SO$_4$ and the solvent was removed under reduced pressure. The crude product was purified by column chromatography (silica gel, ethyl acetate/cyclohexane, 1/1, v/v) to obtain of CTA3 (1.12 g, 1.55 mmol, 73 %).

^{1}H NMR (400 MHz, CDCl$_3$), δ (ppm) = 10.75 (s, 1H, C*H*O), 8.09 (d, J = 8.3 Hz, 2H, Ph), 7.50 (d, J = 8.0 Hz, 2H, Ph), 7.36 (t, J = 8.0 Hz, 1H, Ph), 6.85 (m, 2H, Ph), 5.23 (s, 2H), 4.82 (q, J = 7.4 Hz, 1H, SC*H*), 4.56 - 4.44 (m, 2H, SC*H*$_2$), 4.33 - 4.22 (m, 2H, PhCO$_2$C*H*$_2$), 3.90 - 3.81 (m, 2H, TEG), 3.78 - 3.62 (m, 6H, TEG), 3.39 - 3.28 (m, 2H, TEG), 2.59 (s, 3H, PhC*H*$_3$), 1.67 (m, 2H, C*H*$_2$CH$_3$), 1.59 (d, J = 7.4 Hz, 3H, C*H*3CH), 1.25 (m, 18H, (C*H*$_2$)$_9$), 0.87 (t, J = 6.8 Hz, 3H, CH$_2$C*H*$_3$).

^{13}C NMR (101 MHz, CDCl$_3$), δ (ppm) = 222.1, 192.1, 171.3, 166.3, 162.0, 142.4, 141.6, 134.5, 130.3, 130.1, 127.0, 124.8, 123.8, 110.5, 77.5, 77.4, 77.2, 76.8, 70.9, 70.9, 70.1, 69.4, 69.1, 65.0, 64.4, 48.1, 37.4, 32.1, 29.8, 29.8, 29.7, 29.6, 29.5, 29.2, 29.1, 28.0, 22.8, 21.6, 17.0, 14.3, 1.2.

ESI-MS: [M + Na]$^+$, [C$_{38}$H$_{54}$O$_8$S$_3$Na]$^+$, theoretical: 757.287; experimental: 757.292.

Synthesis of CTA4
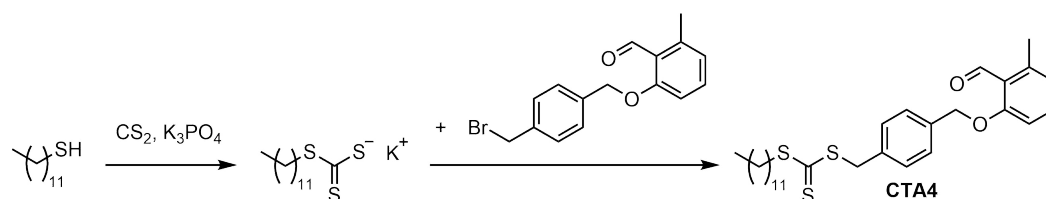
2-((4-(Bromomethyl)benzyl)oxy)-6-methylbenzaldehyde was prepared from 2-hydroxy-6-methylbenzaldehyde and 1,4-bis(bromomethyl)benzene according to a literature procedure.[145] The product contained residual 1,4-bis(bromo-methyl)benzene, which was used without further purification in the next step, where equivalents were calculated respective to bromo groups in the reaction mixture and the yield was calculated respective to the reactant 2-((4-(bromomethyl)benzyl)oxy)-6-methylbenzaldehyde.

Dodecane thiol (5.10 g, 25.2 mmol, 1.50 eq), K_3PO_4 (5.34 g, 25.2 mmol, 1.50 eq) were added to 20 mL THF and stirred for 20 min. Subsequently, carbon disulfide (5.76 g, 75.6 mmol, 4.50 eq) was added and stirred for 60 min before 2-((4-(bromomethyl)benzyl)oxy)-6-methylbenzaldehyde (2.46 g, 7.71 mmol contaminated with 9.09 mmol 1,4-bis(bromomethyl)benzene from previous synthetic step, in total 16.8 mmol bromo groups, 1.00 eq) were added and stirred over night. The reaction mixture was filtered and purified by column chromatography (silica gel, cyclohexane/ethyl acetate, 9/1, v/v). CTA4 was obtained as a yellow solid (3.20 g, 80 %).

^{1}H NMR (400 MHz, CDCl$_3$, Figure C.27), δ (ppm) = 10.72 (s, 1H, CO*H*), 7.40 - 7.33 (m, 5H, aromatic C*H*), 6.88 (d, J = 8.4 Hz, 1H, aromatic C*H*), 6.83 (d, J = 7.6 Hz, 1H, aromatic C*H*), 5.14 (s, 2H, O-C*H*$_2$), 4.63 (s, 2H, S-C*H*$_2$-Ph), 3.37 (d, J = 7.8 Hz, 2H, S-C*H*$_2$), 2.58 (s, 3H, Ph-C*H*$_3$), 1.80 - 1.63 (m, 2H, S-CH$_2$-C*H*$_2$), 1.44 - 1.36 (m, 2H, C*H*$_2$), 1.26 (s, 19H, C*H*$_2$), 0.88 (d, J = 6.8 Hz, 3H, C*H*$_3$).

RAFT polymerizations

Preparation of PE-PS. AIBN and CTA3 were dissolved in styrene (1.50 g, [AIBN]:[CTA]:[S], 1:10:3000) and degassed *via* four consecutive freeze-pump-

thaw cycles. Subsequently, the polymerization mixture was stirred at 60 °C for 21 h. The resulting polymer was purified by precipitation in cold methanol (3×).

Preparation of PE-PNIPAM 1. AIBN, CTA3 and *N*-isopropylacrylamide were dissolved in DMF ([M] = 3.50 mol·L^{-1}, [AIBN]:[CTA]:[NIPAM], 1: 1:7.5:525, 2: 1:7.5:1050, 3: 1:7.5:2100) and degassed *via* four consecutive freeze-pump-thaw cycles. Subsequently, the polymerization mixture was stirred at 60 °C for 1 h 45 min. The resulting polymer was purified by precipitation in cold diethyl ether (3×).

Preparation of PE-PNIPAM 2. AIBN, CTA3 and *N*-isopropylacrylamide were dissolved in DMF ([M] = 3.50 mol·L^{-1}, [AIBN]:[CTA]:[NIPAM], 1:7.5:1050) and degassed *via* four consecutive freeze-pump-thaw cycles. Subsequently, the polymerization mixture was stirred at 60 °C for 4 h. The resulting polymer was purified by precipitation in cold diethyl ether (3×).

Preparation of PE-PNIPAM 3. AIBN, CTA3 and *N*-isopropylacrylamide were dissolved in DMF ([M] = 3.50 mol·L^{-1}, [AIBN]:[CTA]:[NIPAM], 1:7.5:2100) and degassed *via* four consecutive freeze-pump-thaw cycles. Subsequently, the polymerization mixture was stirred at 60 °C for 6 h. The resulting polymer was purified by precipitation in cold diethyl ether (3×).

Preparation of PE-PPFS. AIBN and CTA3 were dissolved in pentafluorostyrene (750 mg, [AIBN]:[CTA]:[PFS], 1:7.5:1050) and degassed *via* four consecutive freeze-pump-thaw cycles. The polymerization mixture was stirred at 60 °C for 17 h. The resulting polymer was purified by precipitation in cold methanol (3×).

Preparation of PE-PManAcEA. AIBN and CTA4 and ManAcEA were dissolved in dioxane ([M] = 1.00 mol·L^{-1}, 1.50 g, [AIBN]:[CTA]:[ManAcEA], 1:7.5:750) and degassed *via* four consecutive freeze-pump-thaw cycles. The polymerization mixture was stirred at 70 °C for 6 h. The resulting polymer was purified by precipitation in diethyl ether (2×).

Preparation of PE-PNIPAM A. AIBN, CTA4 and *N*-isopropylacrylamide were dissolved in DMF ([M] = 3.50 mol·L^{-1}, [AIBN]:[CTA]:[NIPAM], 1:7.5:525) and degassed *via* four consecutive freeze-pump-thaw cycles. Subsequently, the

103

polymerization mixture was stirred at 60 °C for 2 h. The resulting polymer was purified by dialysis against water.

Preparation of PE-PNIPAM B. AIBN, CTA4 and *N*-isopropylacrylamide were dissolved in DMF ([M] = 3.50 mol·L^{-1}, [AIBN]:[CTA]:[NIPAM], 1:7.5:1050) and degassed *via* four consecutive freeze-pump-thaw cycles. Subsequently, the polymerization mixture was stirred at 60 °C for 4 h. The resulting polymer was purified by dialysis against water.

Preparation of PE-PNIPAM C. AIBN, CTA4 and *N*-isopropylacrylamide were dissolved in DMF ([M] = 3.50 mol·L^{-1}, [AIBN]:[CTA]:[NIPAM], 1:7.5:2100) and degassed *via* four consecutive freeze-pump-thaw cycles. Subsequently, the polymerization mixture was stirred at 60 °C for 6 h. The resulting polymer was purified by precipitation in cold diethyl ether (3×).

Photo-grafting

In a typical photo-grafting experiment, grNDs were dispersed in acetonitrile (1 mg·mL^{-1}) and treated with ultrasound using a high power sonotrode for 1 h. Non-dispersed NDs were rejected. The polymer was added to obtain a 1 mg·mL^{-1}solution and the reaction mixture was degassed by purging with nitrogen for 15 min. The reaction mixture was irradiated with the Arimed B6 lamp under stirring overnight. The resulting reaction mixture was washed with acetonitrile (4×) by consecutive centrifugation, ultrasound assisted (ultrasound bath) redispersion cycles and dried under reduced pressure. The grafting experiments with PE-PPFS and PE-PS were performed in tetrahydrofuran (THF).

Calibration curve for co-grafting of PE-PNIPAM 1 and PE-PPFS

Solutions of different ratios of PE-PNIPAM 1 and PE-PPFS (15 - 90 %, molar fraction) were prepared by mixing two stock solutions in THF (2 mg·mL^{-1}) in the desired ratio. The solvent was removed under reduced pressure and IR absorption spectra were recorded. The ratio of the integrals of the area from

1690.2 - 1585.4 cm^{-1} and from 998.2 - 971.6 cm^{-1} was used for calibration (Figure C.25 and C.26). The expirimental data was fitted with a linear fit:

$$y = -9.98 + 0.576x \qquad (4.1)$$

Co-grafting of PE-PNIPAM 1 and PE-PPFS

The co-grafting experiments were performed with PE-PNIPAM 1 and PE-PPFS (25, 50 and 75 %, molar fraction). The photo-grafting procedure and subsequent work-up was performed as described above for the homo-grafting experiments.

Calibration curve for co-grafting of PE-PNIPAM A-C and PE-PManAcEA

Solutions of different ratios of PE-PNIPAM C and PE-PManAcEA (10 - 90 %, weight fraction) were prepared by mixing two stock solutions in dichloromethane (2 mg·mL^{-1}) in the desired ratio. The solvent was removed under reduced pressure and IR absorption spectra were recorded. The ratio of the integrals of the area from 1780 -1700 cm^{-1} and from 1681 - 1595 cm^{-1} was used for calibration (Figure C.32). The expirimental data was fitted with an polynomial fit:

$$y = 0.951 - 0.00207x - 7.157x^2 \qquad (4.2)$$

Co-grafting of PE-PNIPAM A-C and PE-PManAcEA

The co-grafting experiments were performed with PE-PNIPAM A-C and PE-PManAcEA (7, 12.5, 25 and 50 %, weight fraction). The photo-grafting procedure and subsequent work-up was performed as described above for the homo-grafting experiments.

Deacetylation of PManAcEA shell on NDs

The deprotection of the acetate protecting groups of the glycopolymers was performed after the co-grafting experiments. In a typical procedure, 10 mg polymer coated NDs were dispersed in 10 mL anhydrous methanol and put in an ultrasound bath for 1 h. Subsequently, 300 µL sodium methoxide (25 % in methanol) were added and stirred for 1 h. The NDs were centrifuged and washed three times with water and one time with dichloromethane. The samples were dried under reduced pressure and analyzed via TGA (Figure C.34 - C.36, Appendix).

<div style="text-align: right">

5

</div>

Glyco single-chain nanoparticle modified nanodiamonds
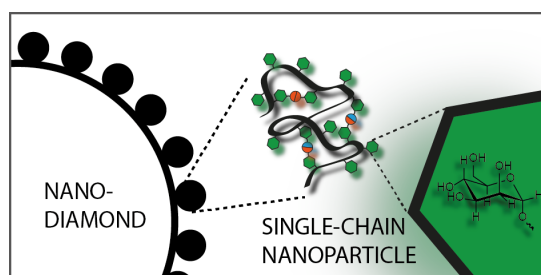
5.1. Motivation

The efficiency of viruses in entering cells and releasing their cargo has inspired synthetic chemists for many years (Section 2.4.4). Viruses are highly optimized systems that often possess glycosylated surfaces consisting of glycoprotein

spikes.[219–221] In order to improve the efficacy of synthetic drug delivery systems, biomimetic nanoparticles with surface structures resembling viruses are highly promising (Section 2.4.4). For example, one study showed the preparation of a virus-like surface morphology on silica nanoparticles resulting in an increased cellular uptake.[223]

Herein, the preparation of virus-like surface structures on nanodiamonds (NDs) was investigated. Glycoproteins were mimicked by synthetic glycopolymers. A crosslinked glycopolymer structure was generated using the single-chain nanoparticle (SCNP) technology. SCNPs are nanoparticles consisting of intramolecularly crosslinked polymer chains and possess a more compact, globular structure compared to their linear precursors (Section 2.5). Linear glycopolymer chains were collapsed into SCNPs using light-triggered, tetrazole based crosslinking reactions. The immobilization of the prepared glyco SCNPs onto NDs to generate virus-like structures was investigated using an adsorption assay and the bioactivity was examined *via* lectin binding experiments. The cytotoxicity of the nanoparticles was assessed and the cellular uptake in macrophages was investigated using confocal fluorescence microscopy.

5.2. Preparation of glycopolymers

In the current chapter, SCNPs based on mannose glycopolymers were prepared *via* light-triggered tetrazole based intramolecular crosslinking reactions. Upon UV irradiation, tetrazoles form nitrile imines, which react with suitable double bonds in a 1,3-dipolar cycloaddition, referred to as the nitrile imine mediated tetrazole-ene cycloaddition (NITEC) (Section 2.3.2). Importantly, fluorescent pyrazoline derivatives are formed during NITEC reactions, which provide instantaneous feedback of the reaction progress and constitute potential labels for fluorescence imaging.

First, mannose glycopolymers were prepared *via* RAFT polymerization of ManAcEMA (Scheme 5.1, see Chapter 3 for the monomer synthesis). 2-Cyano-2-propyl benzodithioate (CPDB) was used as chain transfer agent (CTA). The RAFT polymerization was conducted in DMF with AIBN as the initiator. A
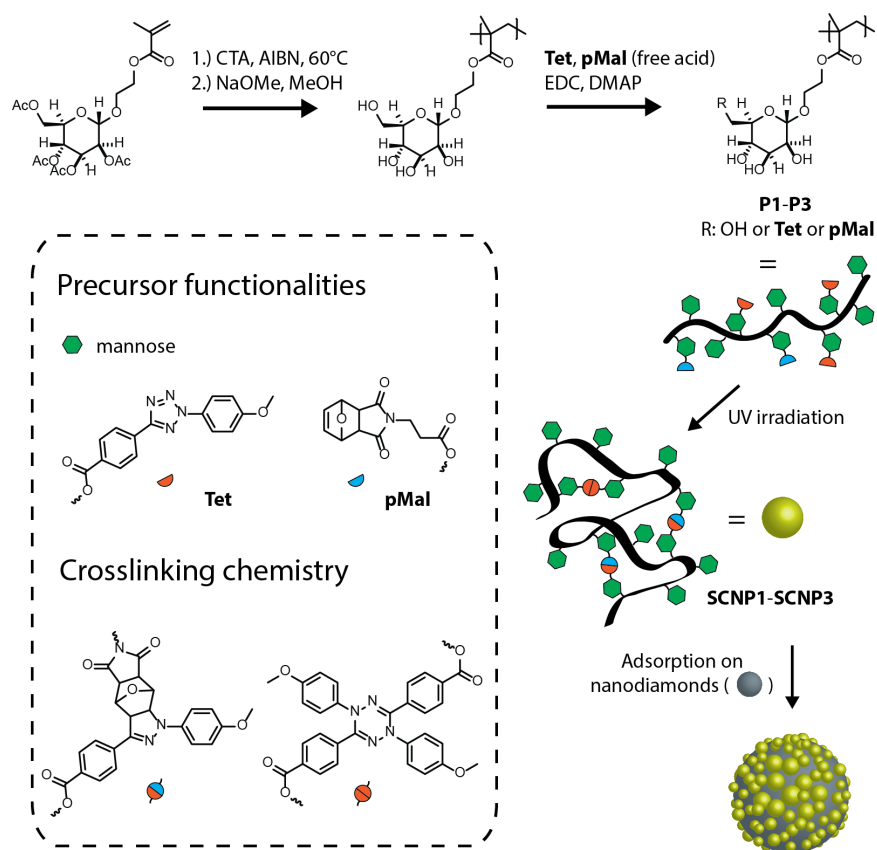
Scheme 5.1. Schematic overview of the synthetic route to glyco SCNP functional NDs. Glycopolymers were prepared *via* RAFT polymerization of ManAcEMA. Subsequently, the polymers P1-P3 were intramolecularly crosslinked to form fluorescent SCNPs. Finally, the SCNPs were decorated onto NDs. Reproduced with permission from reference [294]. Copyright (2017) American Chemical Society.

one-pot polymerization-deprotection procedure was employed, where the deacetylation agent (sodium methylate) was directly added to the reaction mixture after polymerization. Two well-defined glycopolymers (A1 and A2) with different molecular weights and low dispersities were prepared (M_n(A1) = 18100 g·mol^{-1} and M_n(A2) = 35800 g·mol^{-1}; Đ = 1.12, Figure 5.1).

^{1}H NMR spectroscopy confirmed full deacetylation (Figure 5.2). It should be noted that the deacetylation procedure leads to the cleavage of the RAFT end-group *via* a nucleophilic substitution reaction and subsequent thiol-Michael addition with residual ManAcEMA monomer to form mannose endgroups. Low molecular weight dispersities (Đ = 1.12) indicate that disulfide formation between intermediate thiol endgroups did not occur. Compared to the poly-
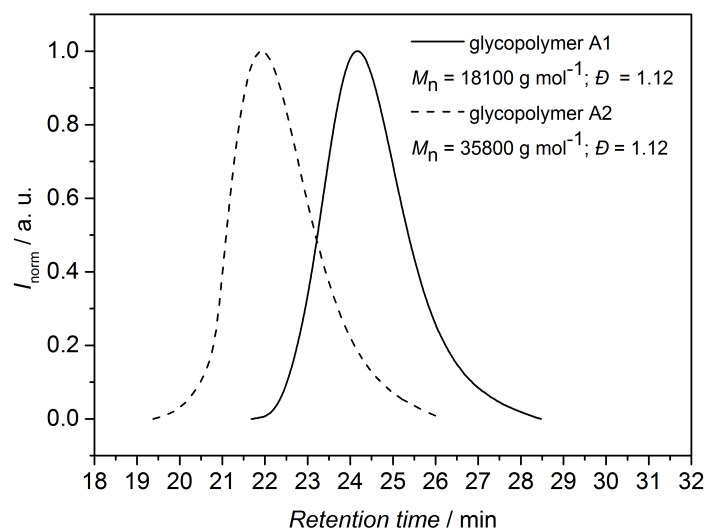
Figure 5.1. SEC results of glycopolymer A1 and A2. Adapted with permission from reference [294]. Copyright (2017) American Chemical Society.
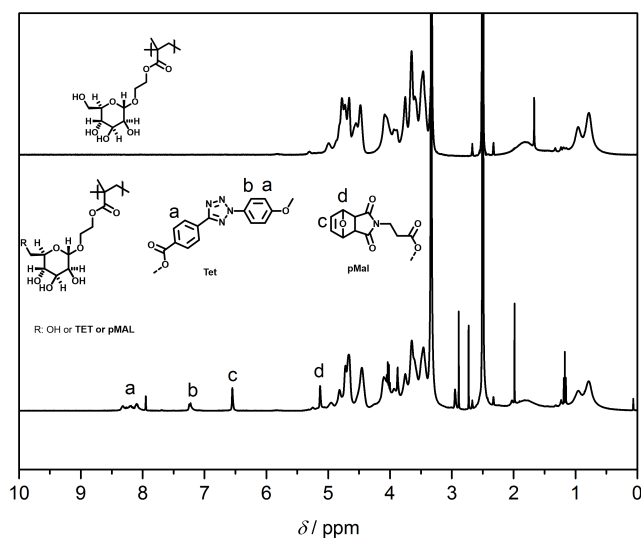
Figure 5.2. ^{1}H NMR spectra of glycopolymer A1 (top) and after functionalization with Tet and pMal (P1, bottom). Adapted with permission from reference [294]. Copyright (2017) American Chemical Society.

mers used in the previous chapters (Chapter 3-4), the polymer endgroup here is not critical, since the subsequent grafting process onto NDs does not rely on endgroups. The SCNPs were adsorbed onto NDs *via* non-covalent interactions of the polymer side group functionalities with the ND's surface (see below).

Next, crosslinking groups were attached to the glycopolymers A1 and A2 (Scheme 5.1). A carboxylic acid functional tetrazole derivative (Tet) as well as a carboxylic acid functional furan protected maleimide derivative (pMal) bearing a double bond for NITEC reactions were attached in an EDC mediated esterification reaction to hydroxy groups of the glycopolymers. The two esterification reactions were performed simultaneously in a one-pot fashion. The functionalization probably occurred predominantly at the primary hydroxy group of mannose due to its higher reactivity compared to secondary hydroxy groups. Three functional glycopolymers were prepared (Table 5.1). The degree of functionalization, herein referred to as %Mal and %Tet, corresponds to the molar ratio of functional groups per repeating unit and was determined *via* ^{1}H NMR spectroscopy (Figure 5.2). Resonances at 8.32–8.08 ppm and 7.21 ppm correspond to the aromatic protons of the tetrazole group, whereas resonances 6.54 ppm and 5.12 ppm can be assigned to the pMal units. Integration of these signals and the comparison to the proton signals of the polymeric backbone allowed for the calculation of the degree of functionalization. The functionalized glycopolymers P1 and P2 possess the same functionalization degrees (8 % Tet and 10 % pMal), yet differ in molecular weight. The EDC coupling reactions were performed with 0.1 equivalents of each compound (Tet and pMal, Scheme 5.1) resulting in quantitative yield for pMal and 80 % yield for the Tet carboxylic acid. Additionally, a glycopolymer with higher Tet content was prepared (P3, Table 5.1) in order to increase the crosslinking density.

Table 5.1. SEC and NMR characterization data of prepared glycopolymers P1-P3.

Polymer	M_n^{NMR} / g·mol^{-1}	DP^{NMR}	M_n^{SEC} / g·mol^{-1}	$Đ^{SEC}$	%Tet	%Mal
P1	32000	94	24400	1.20	8	10
P2	61000	180	45000	1.18	8	10
P3	66500	180	51500	1.25	20	8

5.3. Light-induced synthesis of single-chain nanoparticles

Glycopolymers P1-P3 were crosslinked *via* the photolysis of lateral tetrazole groups and subsequent intra-chain cycloaddition reactions. In order to prevent intermolecular reactions, highly diluted aqueous solutions ($16.7\,mg \cdot L^{-1}$) were prepared and subsequently irradiated at $\lambda_{max} = 320\,nm$. Size exclusion chromatography (SEC) was employed to monitor the SCNP collapse. Upon photo-crosslinking of all glycopolymers (P1-P3), an increase in retention time was observed clearly showing the reduction of hydrodynamic volume resulting from SCNP formation (Figure 5.3).
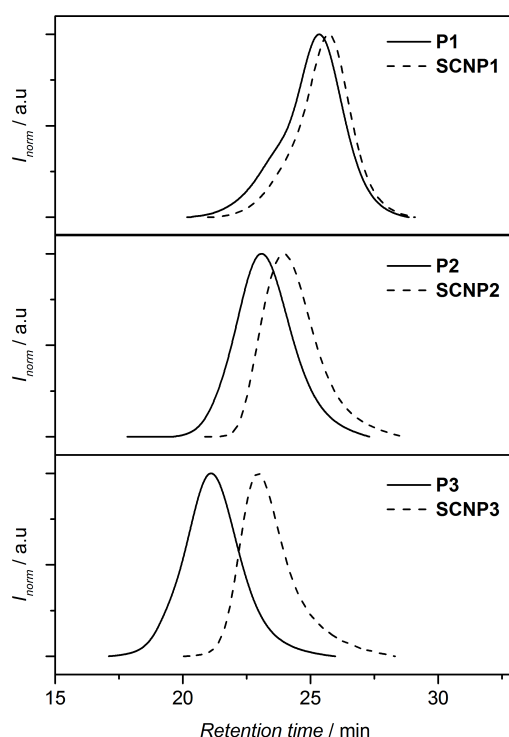
Figure 5.3. Size exclusion chromatograms from polymeric precursors P1-P3 and corresponding SCNPs. A shift of the SEC traces to higher retention times indicates SCNPs formation. Adapted with permission from reference [294]. Copyright (2017) American Chemical Society.

The shift of size exclusion chromatography (SEC) traces to higher retention times is clear evidence for SCNP formation, however absolute size information from SEC data would be highly desirable. Based on the hydrodynamic volume SEC analysis introduced by Gilbert and coworkers for the characterization of starch,[295] a facile method to obtain size distribution data from standard SEC measurements of SCNP systems is presented in the following paragraphs. The relation between hydrodynamic volume V_h and molecular weight M is given by following equation (N_a: Avogadro constant, $[\eta]$: intrinsic viscosity):[295]

$$V_h = \frac{2[\eta]M}{5N_a} \tag{5.1}$$

The Mark-Howink-Sakurada (MHS) equation describes the correlation between instrinsic viscosity and molecular weight (Equation 5.2). The empirically determined MHS parameters (α and K) have been determined for common SEC operation conditions (solvent, temperature) and are reported in the literature.

$$[\eta] = KM^\alpha \tag{5.2}$$

Combining Equation 5.1 and Equation 5.2 allows for the calculation of hydrodynamic diameter values (D_h) from molecular weights:

$$D_h = \left(\frac{12KM^{\alpha+1}}{5\pi N_A}\right)^{\frac{1}{3}} \tag{5.3}$$

In the current study, the SEC system was operated with DMF (0.1 M LiBr) at 50 °C and it was calibrated with linear PMMA standards. Thus, MHS parameters for PMMA at the above mentioned experimental conditions were used in Equation 5.3. In theory, the D_h calibration could be implemented into the SEC software, which is highly interesting considering hydrodynamic diameter distributions of polymers are frequently needed. Herein, Equation 5.3 was applied on apparent molecular weight distributions obtained from PMMA calibration. The resulting SEC hydrodynamic diameter plots from P1-P3 and
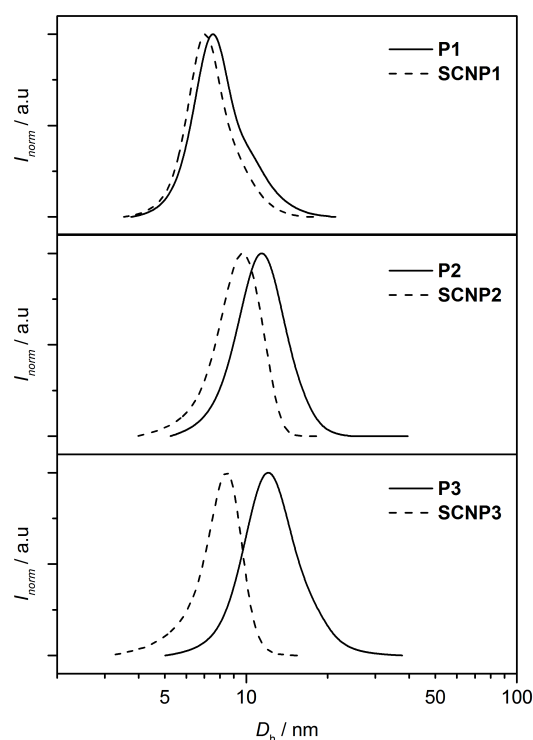
Figure 5.4. SEC hydrodynamic diameter distributions from polymeric precursors and SCNPs. Adapted with permission from reference [294]. Copyright (2017) American Chemical Society.

SCNP1-SCNP3 are displayed in Figure 5.4. The size distributions of all systems were shifted to lower diameters upon UV irradiation. Similar to average molecular weight calculations, average diameter values were calculated using Equation 5.4 (H_i: DRI detector signal).

$$D_h = \frac{\sum H_i}{\sum (H_i/D_i)} \tag{5.4}$$

The results from the SEC hydrodynamic diameter analysis are summarized in Table 5.2. SCNPs below 10 nm in diameter were obtained (7.1-8.8 nm). The decrease in diameter is more significant for larger polymeric precursors at the same functionalization degree (19 % compared to 7 % for P2-SCNP2 and P1-SCNP1, respectively). Furthermore, increasing the tetrazole content

114

Table 5.2. Summary of size information obtained from SEC and NMR experiments. Hydrodynamic diameters (D_h) values were obtained from SEC measurements in DMF and diffusion coefficients ($D_{diff.}$) were determined by DOSY experiments in D_2O.

Precursor	D_h^{SEC} / nm	$D_{diff.}^{DOSY}$ / $m^2 \cdot s^{-1}$	SCNP	D_h^{SEC} / nm	$D_{diff.}^{DOSY}$ / $m^2 \cdot s^{-1}$
P1	7.7	$6.98 \cdot 10^{-11}$	SCNP1	7.1	$1.00 \cdot 10^{-10}$
P2	10.8	$6.17 \cdot 10^{-11}$	SCNP2	8.8	$7.53 \cdot 10^{-11}$
P3	11.6	$6.92 \cdot 10^{-11}$	SCNP3	7.6	$1.05 \cdot 10^{-10}$

in the precursor polymer (P3 compared to P2) leads to a larger decrease in hydrodynamic diameter upon UV irradiation (35 %). Hence, SCNP size and density could be altered by the variation of the polymeric precursor in terms of molecular weight and crosslinker functionalization.

As a complimentary characterization method to SEC, diffusion ordered NMR spectroscopy (DOSY) measurements were performed in D_2O (Figure D.42, Appendix). Upon UV irradiation an increase of the diffusion coefficients correlating with a decrease in hydrodynamic volume was observed (Table 5.2). It should be noted that diffusion coefficients determined by DOSY measurements do not contain information about the distribution and therefore the assumption was made that the system was monodisperse.

The intra-chain crosslinking reactions are based on the photolysis of lateral tetrazole groups leading to the formation of nitrile imine intermediates (Section 2.3.2), which can react in a NITEC reaction with the pMal double bonds or dimerize (Section 2.5.1). Using ^{1}H NMR spectroscopy the degree of NITEC reactions was estimated (Figure 5.5). The olefinic proton resonances from pMal units decreased upon UV irradiation. A pMal conversion of 42 %, 63 % and 100 % was calculated for P1, P2 and P3, respectively. Full conversion of pMal could be obtained for the tetrazole rich polymer P3 since a 2.5-fold excess of Tet groups increases the possibility for NITEC reactions significantly.

Furthermore, UV-vis and fluorescence spectra of SCNP1-SCNP3 were recorded (Figure 5.6). The prepared SCNPs possess a strong absorbance band at λ_{max} = 412 nm and fluoresce at λ_{max} = 555 nm. The fluorescence arises from the pyrazoline crosslinks formed during the NITEC reactions. Importantly, the
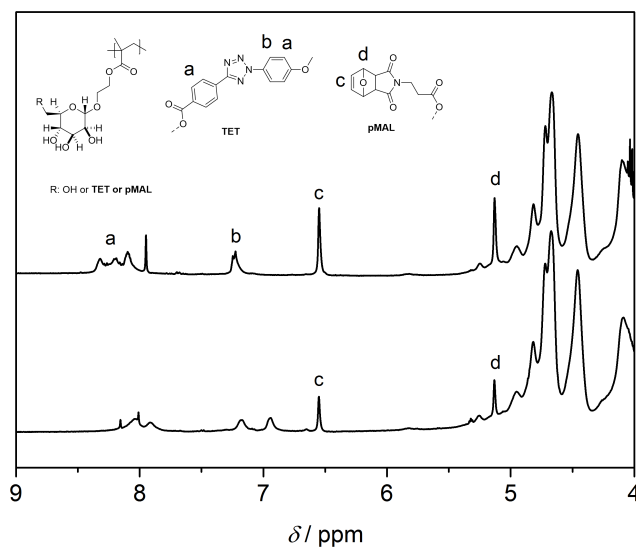
Figure 5.5. ^{1}H NMR spectra of polymeric precursors P1 before (top) and after UV irradiation (SCNP1, bottom). Adapted with permission from reference [294]. Copyright (2017) American Chemical Society.
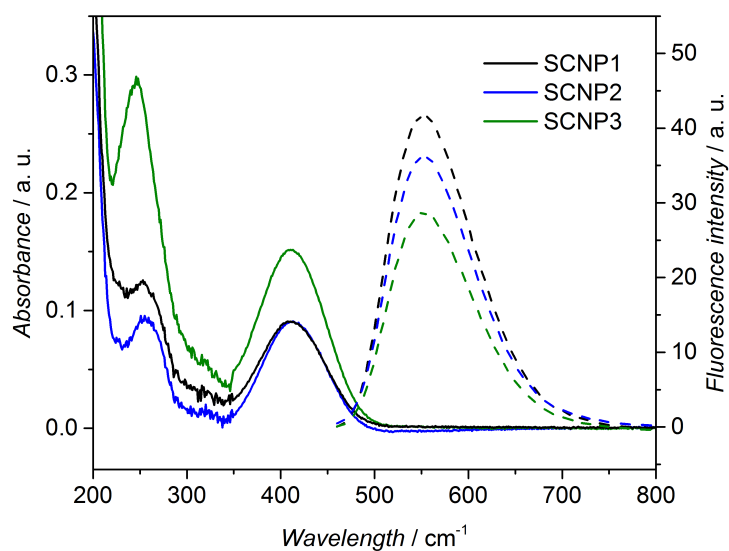
Figure 5.6. UV-vis (solid lines) and fluorescence (λ_{exc} = 440 nm, dashed lines) spectra from SCNP1-3. Adapted with permission from reference [294]. Copyright (2017) American Chemical Society.

fluorescence excitation and emission wavelengths are suitable for bio-imaging applications (see below).

The binding of the prepared nanoparticles to lectins is important for potential biomedical applications. Hence, a concanavalin A (ConA) turbidity assay was performed (Figure 5.7). In a similar assay as reported in Chapter 3, the aggregation of SCNPs in the presence of tetrameric ConA was monitored *via* UV-vis spectroscopy. After addition of SCNPs to a ConA solution, the absorbance at $\lambda = 550\,nm$ increased showing the successful binding of mannose functional SCNPs to ConA.
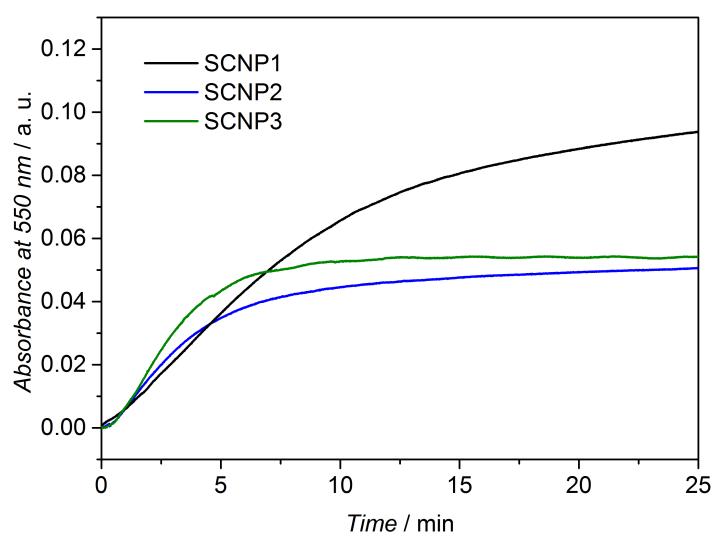
Figure 5.7. ConA turbidity assay of prepared SCNPs. At t = 0, ConA was added and the absorbance was monitored at $\lambda = 550\,nm$ using UV-vis spectroscopy. Adapted with permission from reference [294]. Copyright (2017) American Chemical Society.

5.4. SCNP decorated nanodiamonds

The prepared glyco SCNPs were used for the functionalization of NDs with the aim to mimic glycoprotein structures present on viruses. Compared to linear polymers, SCNPs are more compact with a fixed globular topology and thus, it

is proposed that their attachment to surfaces allows for the generation of spike-like structures, which could influence cellular uptake efficiency. Experimental studies have shown that morphology of nanoparticles (*e.g.* spherical, worm-like)[180,296] and their surface (*e.g.* smooth, rough)[223,297] plays an important role for their performance in biomedical applications. Herein, a simple synthetic approach to glyco SCNP decorated NDs is presented. Detonation NDs as used in the previous two chapters possess a nano-structured surface since they consist of small (close to 5 nm in diameter) aggregated primary particles. Thus, they are not suited for the generation and investigation of well-defined surface structures. Furthermore, the cellular uptake is size dependent and narrow size distributions are therefore important for the investigation of the effect of surface structure. Hence, high pressure high temperature (HPHT) NDs (Section 2.1.1) consisting of non-aggregated particles (~ 60 nm in diameter) were employed in the current study, which allow for the generation of defined surface morphologies using sub 10 nm SCNPs as building blocks.

First, HPHT NDs were oxidized using an acid treatment to obtain HPHT-ND-COOH with an oxidized surface. Subsequently, SCNP2 were adsorbed onto the NDs. To investigate the adsorption process, a small scale (100 µL) and high throughput assay was developed. HPHT-ND-COOH were dispersed in water and mixed with SCNP2 solutions to obtain mixtures of different SCNP2 concentrations while leaving the HPHT-ND-COOH concentration constant ($2 \, \text{mg} \cdot \text{mL}^{-1}$). The mixtures were shaken at ambient temperature for 3 h and centrifuged. Subsequently, the concentration of SCNP2 in the supernatant was measured and the amount of adsorbed polymer was calculated using a calibration curve (Figure D.43, Appendix). With increasing SCNP concentration the amount of adsorbed SCNPs increased and leveled out at around 11 wt.% (Figure 5.8).

Next, NDs were coated with SCNPs at a concentration of $1 \, \text{mg} \cdot \text{mL}^{-1}$ and washed several times with water to remove any free SCNPs. Thermogravimetric analysis (TGA) revealed a grafting density of 9.3 wt.% (Figure 5.9, sample is labelled as ND@SCNP-9%), which is slightly lower than the value obtained from the photometric assay above, yet shows the formation of a stable SCNP layer on the NDs. The mechanism of the interaction of glyco SCNPs with NDs was not studied in the current project. However, hydrogen bonds are
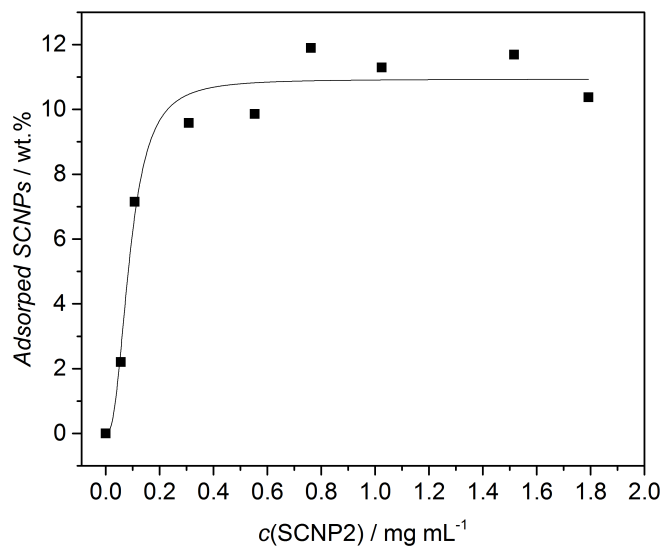
Figure 5.8. Uv-vis adsorption assay. The amount of adsorbed SCNPs was calculated from the SCNP2 concentration in the supernatant using calibration data (Figure D.43, Appendix). Adapted with permission from reference [294]. Copyright (2017) American Chemical Society.
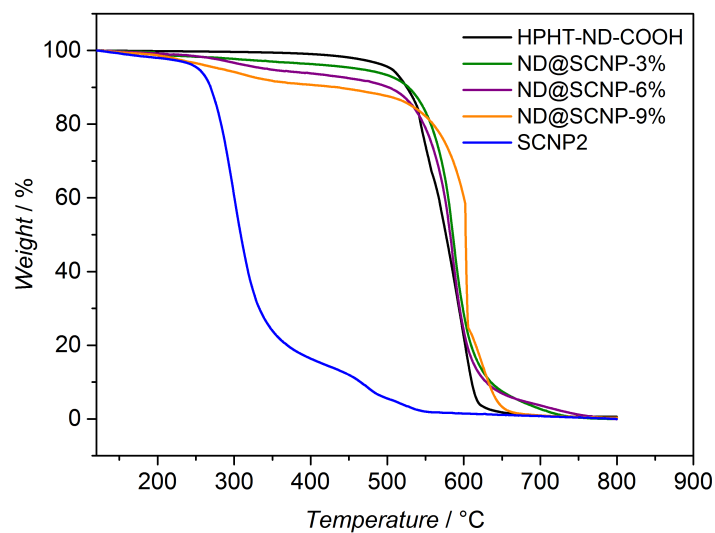
Figure 5.9. TGA results of SCNP2, NDs and prepared hybrid particles. Adapted with permission from reference [294]. Copyright (2017) American Chemical Society.

suggested to play an important role for the attachment of glyco SCNPs to oxidized NDs. Holt and coworkers reported the adsorption of ethanol on oxidized ND and provided experimental support *via* IR spectroscopic studies for hydrogen bonds between the hydroxy groups of ethanol and the oxidized surface of ND.[276]

In order to illustrate the NDs surface structure, following calculations were performed. The footprint *FP* of an individual SCNP on the ND's surface (ND surface area per SCNP) was estimated using Equation 5.5. The density ρ of bulk diamond, M_n of P2 (Table 5.2) and grafting density determined by TGA (GD in wt.%) was employed for the calculation.

$$FP = \frac{6 \cdot M_n}{D_h(ND) \cdot N_A \cdot \rho} \cdot \frac{(1 - GD)}{GD} \tag{5.5}$$

A SCNP footprint of 33 nm^2 was calculated for ND@SCNP-9% corresponding to a circle of 6.1 nm. Compared to the hydrodynamic diameter of SCNP2 (8.8 nm), the footprint is slightly smaller. However, the hydrodynamic diameter accounts for the solvation shell. Thus, full surface coverage is assumed, which is in agreement with the observation that higher SCNP concentration does not lead to a higher adsorption (Figure 5.8).

Next, the correlation between SCNP concentration and grafting density was exploited to prepare patchy surface structures. An initial SCNP concentration of 0.2 mg·mL^{-1} and 0.1 mg·mL^{-1} led to a grafting density of 6.0 wt.% and 2.8 wt.%, respectively (Table 5.3). In order to illustrate the surface structure, the surface coverage SC was estimated using Equation 5.6. 62 % and 28 % of the ND's surface on ND@SCNP-6% and ND@SCNP-3% is covered with SCNPs, clearly indicating patchy surface structures.

$$SC = \frac{FP_{max}}{FP_i} \tag{5.6}$$

dynamic light scattering (DLS) experiments were performed to obtain information about the size of the hybrid particles (Table 5.3). The number average hydrodynamic diameter of HPHT-ND-COOH is 57 nm. According to DLS measurements the SCNP surface layer of fully covered NDs (ND@SCNP-9%)

Table 5.3. Summary of characterization data for SCNP decorated NDs. Grafting densities were measured using TGA. Hydrodynamic diameters (D_h) values were obtained from DLS measurements in water.

Sample	GD / wt.%	FP / nm^2	SC / %	D_h^{number} / nm	$D_h^{intensity}$ / nm	PDI
HPHT-ND-COOH	-	-	-	57	97	0.108
ND@SCNP-3%	2.8	33	100	68	102	0.071
ND@SCNP-6%	6	50	65	72	111	0.083
ND@SCNP-9%	9.3	108	30	72	119	0.102
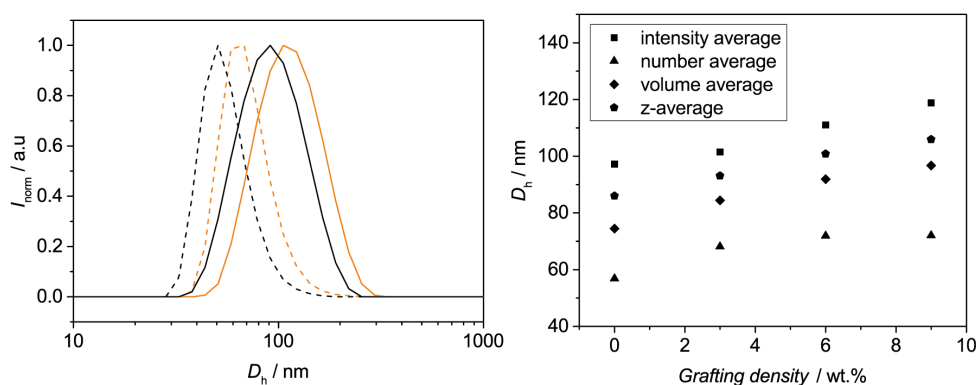
Figure 5.10. DLS results. Left: Number (dashed lines) and intensity weighted (solid lines) hydrodynamic diameter distributions of HPHT-ND-COOH (black) and ND@SCNP-9% (orange). Right: Overview of hydrodynamic diameters from all ND particles. Adapted with permission from reference [294]. Copyright (2017) American Chemical Society.

is 7.5 nm thick (Figure 5.10, Table 5.3), which is comparable to the SEC determined hydrodynamic diameter of SCNP2 (8.8 nm). The small discrepancy is due to different solvents and assumptions in the calculation of these values. In all three experiments, the hydrodynamic diameter of the NDs increased upon SCNP adsorption. Interestingly, the increase in hydrodynamic diameter directly correlated with the grafting density (Figure 5.10).

In order to investigate the lectin binding behaviour of the novel glycosylated ND structures, a DLS based ConA binding assay was performed. The binding of ConA to glycopolymers leads to aggregation, which was here monitored *via* DLS hydrodynamic diameter measurements. The addition of ConA to
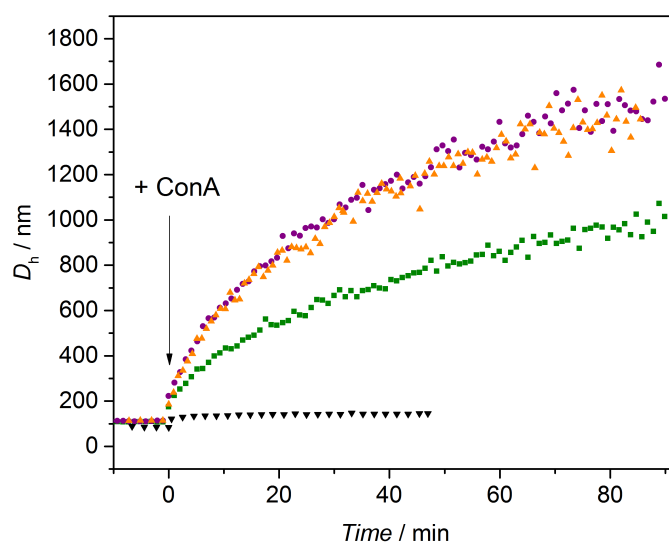
Figure 5.11. DLS based ConA binding assay. At t = O ConA was added and the hydrodynamic diameter (z-average is displayed) was measured over time. Green: ND@SCNP-3%. Purple: ND@SCNP-6%. Orange: ND@SCNP-9%. Adapted with permission from reference [294]. Copyright (2017) American Chemical Society.
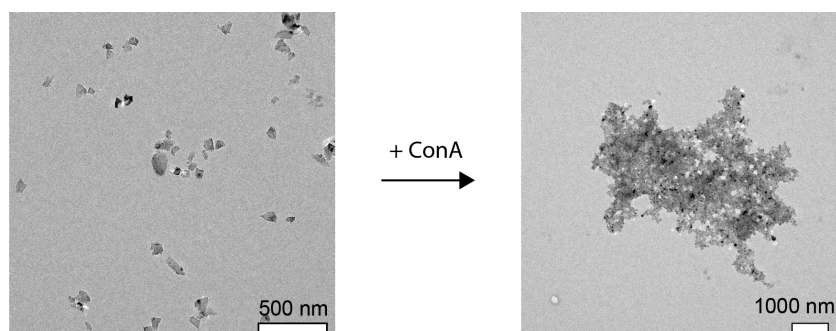
Figure 5.12. TEM of ND@SCNP-9% before (left) and after (right) the addition of ConA. Adapted with permission from reference [294]. Copyright (2017) American Chemical Society.

the glyco-ND dispersions led to an increase in hydrodynamic diameter (Figure 5.11). Interestingly, the rate of diameter increase is significantly lower for ND@SCNP-3% compared to ND@SCNP-6% and ND@SCNP-9%, which indicates that efficient binding is achieved above a certain surface coverage. However, full surface coverage is not required as shown by almost identical aggregation behaviour for ND@SCNP-6% and ND@SCNP-9%.

To further prove the binding to ConA, transmission electron microscopy (TEM) was performed (Figure 5.12). TEM images before the addition of ConA show individual particles, whereas large aggregates of several micrometres were observed after addition of ConA, which visualize the lectin binding induced crosslinking.

The biocompatibility of nanoparticles is crucial for biomedical applications. Macrophage cells were used to investigate the cytotoxicity of SCNP2 as well as the SCNP2 decorated NDs, since macrophages possess mannose receptors that can be exploited to target these cells. Mouse RAW 264.7 macrophage cells were incubated with the nanoparticles for two days and the cell viability was determined. The cell viability did not decrease upon addition of nanoparticles. In contrast, cell proliferation was observed in some cases. Thus, all nanoparticles are non-toxic against RAW 264.7 macrophage cells at a concentration of $100\,\mu g \cdot mL^{-1}$ (Figure 5.13).

The prepared SCNPs are fluorescent from the pyrazoline crosslinks formed during NITEC crosslinking reactions, which allows for the imaging of the SCNPs and SCNP modified NDs *via* confocal fluorescence microscopy. RAW 264.7 ma-
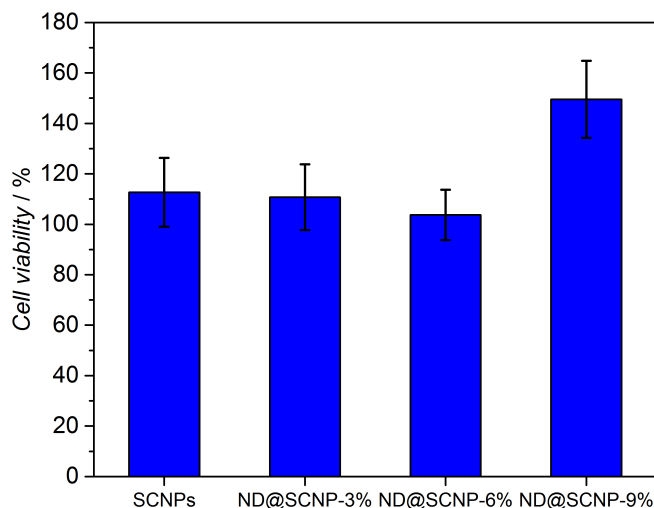
Figure 5.13. Cytotoxicity study of prepared nanoparticles in RAW 264.7 macrophage cells at a concentration of $100\,\mu g \cdot mL^{-1}$. Adapted with permission from reference [294]. Copyright (2017) American Chemical Society.

crophage cells were incubated with nanoparticle dispersions for one hour and imaged (Figure 5.14). The nanoparticles were distributed in the cytosol. The cellular uptake could not be quantified, since the nanoparticles possess different fluorescence intensities. Whereas fluorescence intensities of the SCNPs could be readily measured, the fluorescence of the hybrid particles could not be quantified *via* fluorescence spectroscopy. Thus, the fluorescence intensities from the microscopy experiments could not be compared. Nevertheless, the fluorescence images demonstrate the ability to image the nanoparticles in biological environments.
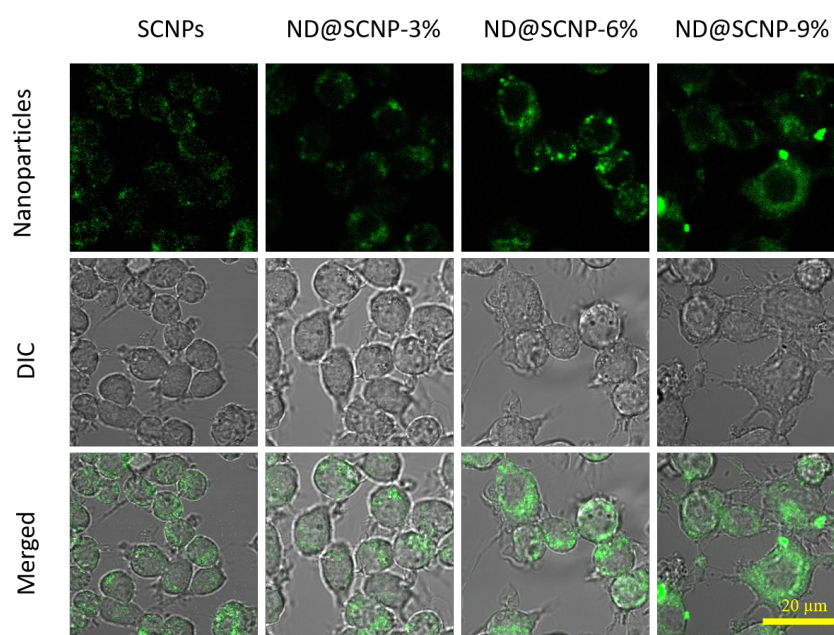
Figure 5.14. Confocal fluorescence microscopy images of macrophages incubated with prepared nanoparticles for 1 h. Scale bar: 20 μm. Top: fluorescence images (λ_{exc} = 488 nm). Center: differential interference contrast (DIC). Bottom: merged images. Adapted with permission from reference [294]. Copyright (2017) American Chemical Society.

5.5. Conclusion

In conclusion, a novel glycopolymer architecture consisting of intramolecularly crosslinked chains (glyco SCNPs) was introduced and employed for the controlled decoration of NDs. The SCNPs were prepared from tetrazole and

alkene functional mannose glycopolymers. Upon UV irradiation of aqueous glycopolymer solutions, intramolecular crosslinks including fluorescent pyrazoline bridges were formed. An SEC analysis method to obtain size distribution data from standard SEC measurements was introduced. The bioactive SCNPs were adsorbed onto NDs in a controlled fashion. Fully covered as well as patchy surface structures mimicking viral surfaces were prepared. Importantly, the hybrid nanostructures bind to the lectin ConA and are non-toxic. Furthermore, confocal fluorescence imaging of the intrinsic fluorescent nanoparticles was demonstrated.

5.6. Experimental section

5.6.1. Materials

3-(1,3-Dioxo-1,3,3a,4,7,7a-hexahydro-2H-4,7-epoxyisoindol-2-yl) propanoic acid (pMal)[298] and 4-(2-(4-Methoxyphenyl)-2H-tetrazol-5-yl)benzoic acid (Tet)[299] were prepared according to literature procedures. 2-(2',3',4',6'-Tetra-*O*-acetyl-β-D-mannosyloxy)ethyl methacrylate (ManAcEMA) was prepared as described in Chapter 3.

4-(Dimethylamino)pyridine (DMAP, 99 %, abcr), *N*-(3-dimethylaminopropyl)-*N'*-ethylcarbodiimide hydrochloride (EDC·HCl, 99+%, Roth), 2,2'-azobis(iso-butylonitrile) (AIBN, VWR), sodium methoxide (25 % in methanol, Sigma-Aldrich), 2-cyano-2-propyl benzodithioate (Sigma-Aldrich), *N,N*-dimethyl-formamide (DMF, anhydrous, Sigma-Aldrich), dimethyl sulfoxide-d_6 (DMSO-d_6, 99.8 %, EURISO-TOP), D_2O (Cambridge Isotope Laboratories), HPHT nanodiamonds (MSY 0-0.1, Microdiamant AG) were used as received.

5.6.2. Instrumentation

TGA, DLS, UV-vis spectroscopy and the photoreactor are described in Chapter 3, Section 3.7.

Fluorescence Spectroscopy

Fluorescence spectra were recorded in deionized water ($0.2\,\mathrm{mg\cdot mL^{-1}}$) on a Cary Eclipse spectrometer.

UV-vis microplate reader

A Benchmark Microplate Reader (Bio-Rad) was used at a wavelength of 315 nm with a reference wavelength of 655 nm.

Transmission electron microscopy (TEM)

Samples were prepared by depositing one drop of a $0.2\,mg\cdot mL^{-1}$ dispersion of nanodiamonds in water onto a carbon coated copper grid. The grids were dried overnight and measured on a FEI Tecnai G2 20 TEM at a voltage of $200\,kV$.

Size exclusion chromatography (SEC)

SEC was performed in DMF (0.1 M LiBr) on a Shimadzu modular system comprising an auto injector and a differential refractive index detector. The SEC system was equipped with three Phenomenex $5.0\,\mu m$ bead-size columns (10^4, 10^3 and $10^2\,nm$). All samples were filtered ($0.45\,\mu m$ PTFE) prior to injection. Molecular weights were estimated relative to narrow molecular weight distribution poly(methylmethacrylat) (100 to $1 \times 10^6\ g\cdot mol^{-1}$) calibration standards.

SEC retention times were converted into hydrodynamic diameters using the calibration data of the PMMA standards and the Mark-Houwink-Sakurada parameters for PMMA in DMF (0.1 M LiBr) at 50 °C (K = 0.0002094 dL g^{-1} ; $\alpha = 0.642$).[300] The calculations are described in detail in Section 5.3.

Nuclear magnetic resonance (NMR) spectroscopy

Standard NMR spectroscopy was performed as described in Chapter 3, Section 3.7.

Diffusion ordered spectroscopy (DOSY) was performed on a Bruker Avance III 600.13 MHz spectrometer, equipped with a 5 mm BBFO probe. Samples were dissolved in D_2O at a concentration of $5\,mg\cdot mL^{-1}$ and experiments were performed at 298 K. Diffusion experiments were performed using the stimulated echo pulse program with bipolar gradients for the suppression of eddy currents. The addition of the 3-9-19 or "Watergate" element was used to obtain water suppression.[301] A linear ramp consisting of 16 steps with gradient strengths from 2 % to 95 % was employed. Data was processed using *Topspin 3.5*.

5.6.3. Procedures

RAFT polymerizations

Glycopolymer A1. AIBN, 2-cyano-2-propyl benzodithioate and ManAcEMA ([I]:[CTA]:[M]; 1:7.5:900) were dissolved in DMF ([M] = $1.00\,\mathrm{mol\cdot L^{-1}}$) and degassed by purging with nitrogen for 20 min. Subsequently, the polymerization mixture was stirred at 60 °C for 15 h. The polymerization was quenched by cooling with an ice bath and exposing to air. The polymerization mixture was diluted threefold with DMF. Sodium methoxide (25 wt.% in methanol) was slowly added to the solution (1 equivalent per acetate group) and stirred at ambient temperature for 2 h. The reaction mixture was dialyzed against water and lyophilized.

Glycopolymer A2. AIBN, 2-cyano-2-propyl benzodithioate and ManAcEMA ([I]:[CTA]:[M]; 1 :10:2000) were dissolved in in DMF ([M] = $1.00\,\mathrm{mol\cdot L^{-1}}$) and degassed by purging with nitrogen for 20 min. Subsequently, the polymerization mixture was stirred at 65 °C for 20 h. The polymerization was quenched by cooling with an ice bath and exposing to air. The polymerization mixture was diluted threefold with DMF. Sodium methoxide (25 wt.% in methanol) was slowly added to the solution (1 equivalent per acetate group) and stirred at ambient temperature for 2 h. The reaction mixture was dialyzed against water and lyophilized.

Post-polymerization modification

In the following procedures the mannose repeating unit is defined as one equivalent (1 eq).

Glycopolymer P1. Glycopolymer A1 (80.0 mg, 0.274 mmol mannose units) was dissolved in 2 mL anhydrous DMF. Tet (8.11 mg, 0.0274 mmol, 0.1 eq), pMal (8.46 mg, 0.0274 mmol, 0.1 eq), EDC hydrochloride (31.5 mg, 0.164 mmol, 0.6 eq) and DMAP (2.01 mg, 0.0274 mmol, 0.06 eq) were added and stirred at ambient temperature for 2 d. Subsequently, the reaction mixture was dialyzed consecutively against DMF and water and lyophilized.

Glycopolymer P2. Glycopolymer A2 (80.0 mg, 0.274 mmol mannose units) was dissolved in 2 mL anhydrous DMF. Tet (8.11 mg, 0.0274 mmol, 0.1 eq), pMal (8.46 mg, 0.0274 mmol, 0.1 eq), EDC hydrochloride (31.5 mg, 0.164 mmol, 0.6 eq) and DMAP (2.01 mg, 0.0274 mmol, 0.06 eq) were added and stirred at ambient temperature for 2 d. Subsequently, the reaction mixture was dialyzed consecutively against DMF and water and lyophilized.

Glycopolymer P3. Glycopolymer A2 (80.0 mg, 0.274 mmol mannose units) was dissolved in 2 mL anhydrous DMF. Tet (20.3 mg, 0.0684 mmol, 0.25 eq), pMal (8.46 mg, 0.0274 mmol, 0.1 eq), EDC hydrochloride (36.7 mg, 0.192 mmol, 0.7 eq) and DMAP (2.34 mg, 0.0192 mmol, 0.07 eq) were added and stirred at ambient temperature for 2 d. Subsequently, the reaction mixture was dialyzed consecutively against DMF and water and lyophilized.

Preparation of single-chain nanoparticles

General procedure: The SCNP precursor (P1, P2 or P3) was dissolved in MilliQ water ($16.7 \, mg \cdot L^{-1}$) and stirred at ambient temperature in the dark for 2 h. Subsequently, the polymer solution was irradiated with UV light (Arimed B6 lamp) for 2 h. The water was removed under reduced pressure to obtain SCNPs (SCNP1, SCNP2 or SCNP3).

Oxidation of HPHT nanodiamonds (HPHT-ND-COOH)

According to literature,[283] HPHT NDs were oxidized in H_2SO_4/HNO_3 (9/1, v/v) at 90 °C for 3 d. Subsequently, the NDs were stirred in 0.5 M NaOH at 90 °C for 1 h, centrifuged and redispersed in 0.1 M HCl. The dispersion was stirred at 90 °C for 1 h. The NDs were centrifuged and washed multiple times with MilliQ water until the supernatant was neutral (pH = 7) and dried under reduced pressure.

Adsorption of SCNPs onto nanodiamonds

The adsorption assay and all following adsorption experiments were performed with SCNP2.

To allow a small scale (100 μL) and high throughput analysis, the adsorption assay was performed on a 96 spot well plate and analysed *via* a UV-vis absorbance reader. First, a calibration curve at $\lambda = 315\,\text{nm}$ was acquired for SCNP2 in MilliQ water (Figure D.43):

$$A = 0.6529 \cdot c_s \tag{5.7}$$

Oxidized HPHT NDs were dispersed in MilliQ water ($4\,\text{mg} \cdot \text{mL}^{-1}$) and sonicated in an ultrasound bath for 1 h. SCNP2 solutions of known concentrations were added to the ND dispersion and diluted with MilliQ water to obtain a final ND concentration of $2\,\text{mg} \cdot \text{mL}^{-1}$ and known initial SCNP2 concentration (c_0). The mixtures were shaken at ambient temperature for 3 h and centrifuged for 30 min (6000 rpm). The absorbance A of the supernatant ($\lambda = 315\,\text{nm}$) was measured to determine the SCNP2 concentration in solution c_s. The amount of adsorbed SCNPs in wt.% was calculated with following equation:

$$Grafting\ density = \frac{c_0 - c_s}{c_{ND}} \tag{5.8}$$

Further adsorption experiments were performed similar as described above, however on a larger scale (5 mL). The hybrid nanoparticles ND@SCNP-9%, ND@SCNP-6% and ND@SCNP-3% were prepared with a final SCNP2 concentration of $1\,\text{mg} \cdot \text{mL}^{-1}$, $0.2\,\text{mg} \cdot \text{mL}^{-1}$ and $0.1\,\text{mg} \cdot \text{mL}^{-1}$, respectively. The resulting NDs were purified from free SCNPs *via* four washing cycles with water and dried under reduced pressure.

ConA assay for glyco single-chain nanoparticles

The ConA turbidity assay was performed with SCNP1, SCNP2 and SCNP3. 50 μL of SCNP solution ($1\,\text{mg} \cdot \text{mL}^{-1}$ SCNPs in HBS buffer, pH = 7) was added to 500 μL ConA ($0.1\,\text{mg} \cdot \text{mL}^{-1}$ in HBS buffer) in a quartz cuvette, mixed thoroughly and added immediately to the UV-vis spectrometer. The absorbance at $\lambda = 550\,\text{nm}$ was measured over time. The starting point for data acquisition was set to 0 min.

ConA assay for glyco single-chain nanoparticle coated nanodiamonds

The ConA binding of the prepared glyco NDs was investigated using DLS. 50 µL ConA ($0.1\,\text{mg}\cdot\text{mL}^{-1}$ in PBS buffer, pH = 7) was added to 500 µL of a glyco ND dispersion ($0.2\,\text{mg}\cdot\text{mL}^{-1}$ in PBS buffer) and the hydrodynamic size was measured over time. Oxidized HPHT NDs (HPHT-ND-COOH) were used as a control sample. The starting point for data acquisition was set to 0 min.

Cell culture in vitro

Mouse RAW 264.7 macrophages were cultured in DMEM supplemented with 10 % fetal bovine serum and 2 mM Glutamax at 37 °C with 5 % CO_2. Once reached confluence, the cells were collected from cell culture flasks by trypsin/EDTA treatment. Trypsin/EDTA was removed by centrifugation and the cells were suspended in fresh medium and seeded into either 96 well cell culture plates for cytotoxicity test or 96 35 mm Fluoro-dishes for laser scanning confocal microscopy.

Cytotoxicity

Cells were seeded in 96 well plates (8000 cell per well) with 100 µL medium and cultured for 1 d before nanoparticle loading. The nanoparticles were dispersed in MilliQ water and sonicated in an ultrasound bath for 30 min. The suspension ($100\,\mu g\cdot\text{mL}^{-1}$) was sterilised with UV light for 10 min and added into the wells of the cell culture plate. Subsequently, the cells were cultured for another 2 d. The WST-1 assay was employed to evaluate the cell viability after nanoparticle treatment. The cells were washed with PBS twice and 100 µL of medium and 5 µL WST-1 reagent was added to the cells and incubated for 2 h at 37 °C. The supernatant (100 µL) was transferred into new 96 well plates and the absorbance was measured at $\lambda = 450\,\text{nm}$ ($\lambda_{reference} = 650\,\text{nm}$). Cells loaded with sterile MilliQ water were used as control samples.

Laser scanning confocal microscopy

Cells were seeded in 35 mm Fluoro-dishes ($1 \cdot 10^6$ cells per dish) and cultured for 2 d before nanoparticle loading. The nanoparticles were dispersed in MilliQ water, sonicated for 30 min in an ultrasound bath and sterilised with UV light for 10 min. Subsequently, the nanoparticles were added into the dishes at a concentration of $100\,\mu g \cdot \mathrm{mL}^{-1}$. After 1 h incubation, the cells were washed with PBS (3x) and imaged under a *LSM-780* (Carl Zeiss) laser scanning confocal microscope. The experiments were carried out with a 40x objective lens and emission was set from $\lambda = 493 - 634\,\mathrm{nm}$ ($\lambda_{excitation} = 488\,\mathrm{nm}$). The images were acquired using the *Zen 2012* software and analysed using *ImageJ* software.

6

Concluding remarks

Nanodiamonds (NDs) have emerged as a promising material for a variety of applications, especially in the field of nano-medicine. Several studies have shown their biocompatibility and potential for the delivery of drugs.[302] Furthermore, the cost-efficient synthesis of NDs has led to a large scale availability with exciting possibilities for commercial products.[17] The functionalization of NDs with polymers provides an elegant approach to equip the nanoparticles with properties and functions useful for drug carriers, such as colloidal stability and ligands for cellular recognition.[35] The present thesis addresses the development of novel functionalization strategies for the generation of complex surface structures with focus a on biomedical relevant systems. Light-induced ligation protocols were used to modify NDs as well as for the generation of glycopolymeric nanoparticles for the decoration of NDs. A range of different polymers have been investigated for ND coatings including bioactive mannose glycopolymers.

First, two light triggered grafting-to approaches for the modification of NDs with polymers — both based on Diels-Alder reactions of photoenols — were investigated. In the first part (Chapter 3) the photo-grafting of maleimide terminal polymers onto *o*-methyl benzaldehyde functional nanodiamonds was investigated. A variety of polymers were grafted onto the surface of NDs. Importantly, glycopolymer coated NDs were prepared and the binding to the

lectin concanavalin A (ConA) was shown. The second approach (Chapter 4) introduces the light-induced grafting of *o*-methyl benzaldehyde terminal polymers onto graphitic NDs. Compared to the first approach the generation of the reactive NDs consisted of a simple annealing step (compared to four synthetic modification steps) that yielded more reactive sites on the surface resulting in higher grafting densities. In addition, the simultaneous co-grafting of two polymers was investigated. Whereas the co-grafting of poly(pentafluorostyrene) (PPFS) and poly(*N*-isopropylacrylamide) (PNIPAM) yielded surface compositions tunable by the feedstock ratio, the co-grafting of a glycopolymer with PNIPAM was accompanied with a preferential attachment of PNIPAM.

In the last part of the current thesis (Chapter 5), light-induced ligations were employed to prepare small (below 10 nm in diameter) glycopolymeric nanoparticles for the decoration of NDs. The preparation of so-called single-chain nanoparticles (SCNPs) was based on the photolysis of lateral tetrazole groups and subsequent intrachain crosslinking reactions. The glyco SCNPs constitute a novel polymeric architecture for synthetic glycopolymers, with features resembling natural carbohydrate structures. The size of the glyco SCNPs could be adjusted and they possessed fluorescent properties useful for bio-imaging. Inspired by the surface structure of viruses, the controlled decoration of NDs with glyco SCNPs was investigated. An adsorption protocol was developed that allowed for the facile preparation of non-toxic and fluorescent hybrid structures. The fluorescence of the glyco SCNPs could be exploited to image the glyco SCNP decorated ND in macrophage cells.

Over the course of the present thesis, convergent approaches for the preparation of polymer functional NDs were employed, in which the polymers and ND precursors were synthesized independently and subsequently coupled. The modular strategies allowed for the preparation of nanoparticle libraries with varying functionalities. The synthetic basis for the generation of glycopolymeric surface structures on NDs with interesting lectin binding properties was established. The generation of mannosylated surfaces on NDs was inspired from viruses. Mannosylated glycoproteins are present on many viruses, for instance on HIV, dengue virus as well as ebola virus.[218] The glycoproteins protrude in a spike-like fashion from the surface and bind to cell surface

expressed lectins such as L-SIGN and DC-SIGN.[218] The binding of viruses to receptors on cell surfaces is crucial for cell entry. The nanoparticles prepared in the current thesis possess mannose ligands and their lectin binding behaviour was shown in binding assays with the model lectin ConA (Chapter 3 and 5). In addition, the hydrodynamic diameters of the prepared polymer functional NDs (68-72 nm, Chapter 5 and 170-347 nm, Chapter 3-4) are comparable to sizes of viruses. In Chapter 3-4 detonation NDs were employed, which consist of aggregated primary particles (close to 5 nm in diameter) and thus complicate the investigation of surface structure–property relations. However, co-grafting experiments (Chapter 4) demonstrated the ability to generate mixed surface compositions, which could be exploited for the generation of complex biomimetic surface structures. In Chapter 5, high pressure high temperature (HPHT) NDs were employed that constitute a better defined template, since aggregation does typically not occur. In contrast to the grafting-to protocols where polymers were attached *via* the endgroups to the NDs, here, the polymers were simply adsorbed onto the surface. Furthermore, SCNPs were employed that possess a fixed globular structure compared to linear polymers, which is closer to the morphology of glycoprotein spikes found on viruses.

The introduced synthetic approaches to (glyco-)polymer functional NDs should allow for the preparation of nanoparticle libraries for the investigation of the influence of surface structure on cellular uptake. In this context, the following points need to be considered. First of all, a suited template for the generation of different surface morphologies needs to be selected. HPHT NDs constitute a better defined template than detonation NDs since primary particle sizes of HPHT NDs are available that are relevant for virus mimics. Furthermore, a library of nanoparticles with different surface morphologies should be prepared. The co-grafting approach (Chapter 4) could be employed. However, the attachment of glyco SCNPs represents a more promising approach since surface immobilization of SCNPs will probably generate a different surface morphology than linear polymer chains. Its modular nature should allow for the preparation of nanoparticle libraries consisting of nanodiamonds coated with glycopolymers of varying sizes, epitopes and distance between "SCNP-spikes". Imaging techniques, such as electron microscopy, could be employed to confirm the proposed morphologies. In the current thesis, man-

nose ligands with a high potential for targeted cellular uptake were used. The assessment of the cellular uptake in a variety of cells, including macrophages and dendritic cells, which are known to possess mannose receptors, should provide additional information about their targeting properties. Such nanoparticle libraries should allow for the in-depth investigation of the influence of ND surface structure on cellular uptake.

High potential is seen for biomedical applications, however, the presented light-triggered grafting approaches might also be employed for the design of enforced networks. Light-triggered grafting protocols allow for a high temporal and spatial resolution, which could be exploited for the generation of 3D printed ND materials. The introduced functionalization strategies for the preparation of polymer–ND hybrid particles are envisioned to enable the development of exciting materials for a variety of applications.

Bibliography

(1) Field, J. E. *Reports on Progress in Physics* **2012**, *75*, 126505–126540.

(2) Shirey, S. B.; Cartigny, P.; Frost, D. J.; Keshav, S.; Nestola, F.; Nimis, P.; Pearson, D. G.; Sobolev, N. V.; Walter, M. J. *Reviews in Mineralogy and Geochemistry* **2013**, *75*, 355–421.

(3) Collin, G. *Mitteilungen - Gesellschaft Deutscher Chemiker, Fachgruppe Geschichte der Chemie* **2010**, *21*, 177–192.

(4) Dai, Z. R.; Bradley, J. P.; Joswiak, D. J.; Brownlee, D. E.; Hill, H. G. M.; Genge, M. J. *Nature* **2002**, *418*, 157–159.

(5) Danilenko, V. V. *Physics of the Solid State* **2004**, *46*, 595–599.

(6) Mochalin, V. N.; Neitzel, I.; Etzold, B. J. M.; Peterson, A.; Palmese, G.; Gogotsi, Y. *ACS Nano* **2011**, *5*, 7494–7502.

(7) Huynh, V. T.; Pearson, S.; Noy, J.-M.; Abboud, A.; Utama, R. H.; Lu, H.; Stenzel, M. H. *ACS Macro Letters* **2013**, *2*, 246–250.

(8) Delaittre, G.; Goldmann, A. S.; Mueller, J. O.; Barner-Kowollik, C. *Angewandte Chemie* **2015**, *54*, 11388–11403.

(9) Mochalin, V. N.; Shenderova, O.; Ho, D.; Gogotsi, Y. *Nature Nanotechnology* **2012**, *7*, 11–23.

(10) Frenklach, M.; Howard, W.; Huang, D.; Yuan, J.; Spear, K. E.; Koba, R. *Applied Physics Letters* **1991**, *59*, 546–548.

(11) Banhart, F.; Ajayan, P. M. *Nature* **1996**, *382*, 433–435.

(12) Yang, G.-W.; Wang, J.-B.; Liu, Q.-X. *Journal of Physics: Condensed Matter* **1999**, *10*, 7923–7927.

(13) Daulton, T.; Kirk, M.; Lewis, R.; Rehn, L. *Nuclear Instruments and Methods in Physics Research B* **2001**, 12–20.

(14) Welz, S.; Gogotsi, Y.; McNallan, M. J. *Journal of Applied Physics* **2003**, *93*, 4207–4214.

(15) Galimov, É. M.; Kudin, A. M.; Skorobogatskii, V. N.; Plotnichenko, V. G.; Bondarev, O. L.; Zarubin, B. G.; Strazdovskii, V. V.; Aronin, A. S.; Fisenko, A. V.; Bykov, I. V.; Barinov, A. Y. *Doklady Physics* **2004**, *49*, 150–153.

(16) Kumar, A.; Ann Lin, P.; Xue, A.; Hao, B.; Khin Yap, Y.; Sankaran, R. M. *Nature Communications* **2013**, *4*, 2618.

(17) Nunn, N.; Torelli, M.; McGuire, G.; Shenderova, O. *Current Opinion in Solid State and Materials Science* **2017**, *21*, 1–9.

(18) *Nanodiamond*; Williams, O. A., Ed.; RSC Nanoscience & Nanotechnology; Royal Society of Chemistry: Cambridge, 2014.

(19) Dolmatov, V. Y.; Veretennikova, M. V.; Marchukov, V. A.; Sushchev, V. G. *Physics of the Solid State* **2004**, *46*, 611–615.

(20) Krüger, A.; Kataoka, F.; Ozawa, M.; Fujino, T.; Suzuki, Y.; Aleksenskii, A. E.; Vul', A. Y.; Osawa, E. *Carbon* **2005**, *43*, 1722–1730.

(21) Shenderova, O. A.; Zhirnov, V. V.; Brenner, D. W. *Critical Reviews in Solid State and Materials Sciences* **2002**, *27*, 227–356.

(22) Mahfouz, R.; Floyd, D. L.; Peng, W.; Choy, J. T.; Loncar, M.; Bakr, O. M. *Nanoscale* **2013**, *5*, 11776–11782.

(23) Boudou, J.-P.; Curmi, P. A.; Jelezko, F.; Wrachtrup, J.; Aubert, P.; Mohamed Sennour; Balasubramanian, G.; Reuter, R.; Thorel, A.; Gaffet, E. *Nanotechnology* **2009**, *20*, 235602.

(24) Gruber, A. *Science* **1997**, *276*, 2012–2014.

(25) Treussart, F.; Jacques, V.; Wu, E.; Gacoin, T.; Grangier, P.; Roch, J. F. *Physica B: Condensed Matter* **2006**, *376-377*, 926–929.

(26) Chang, Y.-R.; Lee, H.-Y.; Chen, K.; Chang, C.-C.; Tsai, D.-S.; Fu, C.-C.; Lim, T.-S.; Tzeng, Y.-K.; Fang, C.-Y.; Han, C.-C.; Chang, H.-C.; Fann, W. *Nature Nanotechnology* **2008**, *3*, 284–288.

(27) Rondin, L.; Dantelle, G.; Slablab, A.; Grosshans, F.; Treussart, F.; Bergonzo, P.; Perruchas, S.; Gacoin, T.; Chaigneau, M.; Chang, H. C.; Jacques, V.; Roch, J. F. *Physical Review B - Condensed Matter and Materials Physics* **2010**, *82*, 1–5.

(28) Petrakova, V.; Benson, V.; Buncek, M.; Fiserova, A.; Ledvina, M.; Stursa, J.; Cigler, P.; Nesladek, M. *Nanoscale* **2016**, *8*, 12002–12012.

(29) Balasubramanian, G.; Chan, I. Y.; Kolesov, R.; Al-Hmoud, M.; Tisler, J.; Shin, C.; Kim, C.; Wojcik, A.; Hemmer, P. R.; Krueger, A.; Hanke, T.; Leitenstorfer, A.; Bratschitsch, R.; Jelezko, F.; Wrachtrup, J. *Nature* **2008**, *455*, 648–651.

(30) Maze, J. R.; Stanwix, P. L.; Hodges, J. S.; Hong, S; Taylor, J. M.; Cappellaro, P; Jiang, L; Dutt, M. V.; Togan, E; Zibrov, A. S.; Yacoby, A; Walsworth, R. L.; Lukin, M. D. *Nature* **2008**, *455*, 644–647.

(31) Neumann, P.; Beck, J.; Steiner, M.; Rempp, F.; Fedder, H.; Hemmer, P. R.; Wrachtrup, J.; Jelezko, F. *Science* **2010**, *329*, 542–544.

(32) Huang, L. C.; Chang, H. C. *Langmuir* **2004**, *20*, 5879–5884.

(33) Yan, J.; Guo, Y.; Altawashi, A.; Moosa, B.; Lecommandoux, S.; Khashab, N. M. *New J. Chem.* **2012**, *36*, 1479–1484.

(34) Lai, H.; Chen, F.; Lu, M.; Stenzel, M. H.; Xiao, P. *ACS Macro Letters* **2017**, 796–801.

(35) Zhao, J.; Lai, H.; Lu, H.; Barner-Kowollik, C.; Stenzel, M. H.; Xiao, P. *Biomacromolecules* **2016**, *17*, 2946–2955.

(36) Lu, M.; Wang, Y. K.; Zhao, J.; Lu, H.; Stenzel, M. H.; Xiao, P. *Macromolecular Rapid Communications* **2016**, *37*, 2023–2029.

(37) Zhu, Y.; Li, J.; Li, W.; Zhang, Y.; Yang, X.; Chen, N.; Sun, Y.; Zhao, Y.; Fan, C.; Huang, Q. *Theranostics* **2012**, *2*, 302–312.

(38) Schrand, A. M.; Huang, H.; Carlson, C.; Schlager, J. J.; Osawa, E.; Hussain, S. M.; Dai, L. *Journal of Physical Chemistry B* **2007**, *111*, 2–7.

(39) Schrand, A. M.; Dai, L.; Schlager, J. J.; Hussain, S. M.; Osawa, E. *Diamond and Related Materials* **2007**, *16*, 2118–2123.

(40) Liu, K.-K.; Cheng, C.-L.; Chang, C.-C.; Chao, J.-I. *Nanotechnology* **2007**, *18*, 325102–325112.

(41) Li, J.; Zhu, Y.; Li, W.; Zhang, X.; Peng, Y.; Huang, Q. *Biomaterials* **2010**, *31*, 8410–8418.

(42) Liu, K. K.; Wang, C. C.; Cheng, C. L.; Chao, J. I. *Biomaterials* **2009**, *30*, 4249–4259.

(43)   Huang, H.; Pierstorff, E.; Osawa, E.; Ho, D. *Nano Letters* **2007**, *7*, 3305–3314.

(44)   Puzyr, A. P.; Baron, A. V.; Purtov, K. V.; Bortnikov, E. V.; Skobelev, N. N.; Mogilnaya, O. A.; Bondar, V. S. *Diamond and Related Materials* **2007**, *16*, 2124–2128.

(45)   Zhang, X.; Yin, J.; Kang, C.; Li, J.; Zhu, Y.; Li, W.; Huang, Q.; Zhu, Z. *Toxicology Letters* **2010**, *198*, 237–243.

(46)   Kulakova, I. I. *Physics of the Solid State* **2004**, *46*, 636–643.

(47)   Butenko, Y. V.; Kuznetsov, V. L.; Paukshtis, E. a.; Stadnichenko, a. I.; Mazov, I. N.; Moseenkov, S. I.; Boronin, a. I.; Kosheev, S. V. *Fullerenes, Nanotubes and Carbon Nanostructures* **2006**, *14*, 557–564.

(48)   Mitev, D.; Dimitrova, R.; Spassova, M.; Minchev, C.; Stavrev, S. *Diamond and Related Materials* **2007**, *16*, 776–780.

(49)   Pichot, V.; Comet, M.; Fousson, E.; Baras, C.; Senger, a.; Le Normand, F.; Spitzer, D. *Diamond and Related Materials* **2008**, *17*, 13–22.

(50)   Osswald, S.; Yushin, G.; Mochalin, V.; Kucheyev, S. O.; Gogotsi, Y. *Synthesis* **2006**, 11635–11642.

(51)   Aramesh, M.; Shimoni, O.; Ostrikov, K.; Prawer, S.; Cervenka, J. *Nanoscale* **2015**, *7*, 5726–5736.

(52)   Turner, S.; Lebedev, O. I.; Shenderova, O.; Vlasov, I. I.; Verbeeck, J.; Van Tendeloo, G. *Advanced Functional Materials* **2009**, *19*, 2116–2124.

(53)   Mochalin, V. N.; Gogotsi, Y. *Journal of the American Chemical Society* **2009**, *131*, 4594–4595.

(54)   Krueger, A.; Lang, D. *Advanced Functional Materials* **2012**, *22*, 890–906.

(55)   Krueger, A.; Boedeker, T. *Diamond and Related Materials* **2008**, *17*, 1367–1370.

(56)   Shi, Y.; Liu, M.; Wang, K.; Huang, H.; Wan, Q.; Tao, L.; Fu, L.; Zhang, X.; Wei, Y. *Applied Surface Science* **2015**, *357*, 2147–2153.

(57)   Zheng, W.-W.; Hsieh, Y.-H.; Chiu, Y.-C.; Cai, S.-J.; Cheng, C.-L.; Chen, C. *Journal of Materials Chemistry* **2009**, *19*, 8432–8441.

(58)   Liu, K.-K.; Zheng, W.-W.; Wang, C.-C.; Chiu, Y.-C.; Cheng, C.-L.; Lo, Y.-S.; Chen, C.; Chao, J.-I. *Nanotechnology* **2010**, *21*, 315106–315120.

(59) Krüger, A.; Liang, Y.; Jarre, G.; Stegk, J.; Krueger, A.; Liang, Y.; Jarre, G.; Stegk, J. *Journal of Materials Chemistry* **2006**, *16*, 2322.

(60) Romanova, E. E.; Akiel, R.; Cho, F. H.; Takahashi, S. *The journal of physical chemistry. A* **2013**, *117*, 11933–9.

(61) Krueger, A.; Stegk, J.; Liang, Y.; Lu, L.; Jarre, G. *Langmuir* **2008**, *24*, 4200–4204.

(62) Barras, A.; Lyskawa, J.; Szunerits, S.; Woisel, P.; Boukherroub, R. *Langmuir* **2011**, *27*, 12451–12457.

(63) Zeiger, M.; Jäckel, N.; Mochalin, V.; Presser, V. *Journal of Materials Chemistry A* **2015**, *4*, 3172–3196.

(64) Liang, Y.; Ozawa, M.; Krueger, A. *ACS Nano* **2009**, *3*, 2288–2296.

(65) Jarre, G.; Liang, Y.; Betz, P.; Lang, D.; Krueger, A. *Chemical Communications* **2011**, *47*, 544–546.

(66) Ma, W.; Yu, X.; Qu, X.; Zhang, Q. *Diamond and Related Materials* **2016**, *62*, 14–21.

(67) Lukowiak, M. C.; Ziem, B.; Achazi, K.; Gunkel-Grabole, G.; Popeney, C. S.; Thota, B. N. S.; Böttcher, C.; Krueger, A.; Guan, Z.; Haag, R. *J. Mater. Chem. B* **2015**, *3*, 719–722.

(68) Zhao, L.; Takimoto, T.; Ito, M.; Kitagawa, N.; Kimura, T.; Komatsu, N. *Angewandte Chemie* **2011**, *50*, 1388–1392.

(69) Zhao, L.; Xu, Y.-H.; Akasaka, T.; Abe, S.; Komatsu, N.; Watari, F.; Chen, X. *Biomaterials* **2014**, *35*, 5393–5406.

(70) Zhang, X.; Fu, C.; Feng, L.; Ji, Y.; Tao, L.; Huang, Q.; Li, S.; Wei, Y. *Polymer* **2012**, *53*, 3178–3184.

(71) Cha, I.; Hashimoto, K.; Fujiki, K.; Yamauchi, T.; Tsubokawa, N. *Materials Chemistry and Physics* **2014**, *143*, 1131–1138.

(72) Lai, H.; Lu, M.; Lu, H.; Stenzel, M. H.; Xiao, P. *Polymer Chemistry* **2016**, *7*, 6220–6230.

(73) Zhang, X. Q.; Chen, M.; Lam, R.; Xu, X.; Osawa, E.; Ho, D. *ACS Nano* **2009**, *3*, 2609–2616.

(74) Lee, J. W.; Lee, S.; Jang, S.; Han, K. Y.; Kim, Y.; Hyun, J.; Kim, S. K.; Lee, Y. *Molecular BioSystems* **2013**, *9*, 1004–1011.

(75) Jenkins, A. D.; Jones, R. G.; Moad, G. *Pure and Applied Chemistry* **2009**, *82*, 483–491.

(76) Shipp, D. A. *Polymer Reviews* **2011**, *51*, 99–103.

(77) Stenzel, M. H.; Barner-Kowollik, C. *Material Horizons* **2016**, *3*, 471–477.

(78) Braunecker, W. A.; Matyjaszewski, K. *Progress in Polymer Science* **2007**, *32*, 93–146.

(79) Matyjaszewski, K.; Xia, J. *Chemical Reviews* **2001**, *101*, 2921–2990.

(80) Matyjaszewski, K. *Macromolecules* **2012**, *45*, 4015–4039.

(81) Matyjaszewski, K.; Tsarevsky, N. V. *Journal of the American Chemical Society* **2014**, *136*, 6513–6533.

(82) Sun, Y. L.; Zhu, B.; Zhou, S. S.; Chen, B. L.; Gao, J.; Li, Y. W. *Advanced Materials Research* **2014**, *1033-1034*, 978–986.

(83) Krys, P.; Matyjaszewski, K. *European Polymer Journal* **2017**, *89*, 482–523.

(84) Sciannamea, V.; Jérôme, R.; Detrembleur, C. *Chemical Reviews* **2008**, *108*, 1104–1126.

(85) Grubbs, R. B. *Polymer Reviews* **2011**, *51*, 104–137.

(86) Nicolas, J.; Guillaneuf, Y.; Bertin, D.; Gigmes, D.; Charleux, B. *Polymer Science: A Comprehensive Reference, 10 Volume Set* **2012**, *3*, 277–350.

(87) Chiefari, J.; Chong, Y. K. B.; Ercole, F.; Krstina, J.; Jeffery, J.; Le, T. P. T.; Mayadunne, R. T. A.; Meijs, G. F.; Moad, C. L.; Moad, G.; Rizzardo, E.; Thang, S. H. *Macromolecules* **1998**, *31*, 5559–5562.

(88) Corpart, P.; Charmot, D.; Biadatti, T.; Zard, S. Z.; Michelet, D. D. Int. Patent WO9858974., 1998.

(89) Moad, G.; Rizzardo, E.; Thang, S. H. *Australian Journal of Chemistry* **2012**, *65*, 985.

(90) Hill, M. R.; Carmean, R. N.; Sumerlin, B. S. *Macromolecules* **2015**, *48*, 5459–5469.

(91) Perrier, S. *Macromolecules* **2017**, *50*, 7433–7447.

(92) Yildirim, T.; Rinkenauer, A. C.; Weber, C.; Traeger, A.; Schubert, S.; Schubert, U. S. *Journal of Polymer Science, Part A: Polymer Chemistry* **2015**, *53*, 2711–2721.

(93) Willcock, H.; O'Reilly, R. K. *Polymer Chemistry* **2010**, *1*, 149–157.

(94) Scales, C. W.; Convertine, A. J.; McCormick, C. L. *Biomacromolecules* **2006**, *7*, 1389–1392.

(95) Boyer, C.; Granville, A.; Davis, T. P.; Bulmus, V. *Journal of Polymer Science Part A: Polymer Chemistry* **2009**, *47*, 3773–3794.

(96) Abel, B. A.; McCormick, C. L. *Macromolecules* **2016**, *49*, 6193–6202.

(97) Li, M.; De, P.; Li, H.; Sumerlin, B. S. *Polymer Chemistry* **2010**, *1*, 854–859.

(98) Heredia, K. L.; Grover, G. N.; Tao, L.; Maynard, H. D. *Macromolecules* **2009**, *42*, 2360–2367.

(99) Gruendling, T.; Dietrich, M.; Barner-Kowollik, C. *Australian Journal of Chemistry* **2009**, *62*, 806–812.

(100) Inglis, A. J.; Sinnwell, S.; Davis, T. P.; Barner-Kowollik, C.; Stenzel, M. H. *Macromolecules* **2008**, *41*, 4120–4126.

(101) Inglis, A. J.; Stenzel, M. H.; Barner-Kowollik, C. *Macromolecular Rapid Communications* **2009**, *30*, 1792–1798.

(102) Inglis, A. J.; Sinnwell, S.; Stenzel, M. H.; Barner-Kowollik, C. *Angewandte Chemie* **2009**, *48*, 2411–2414.

(103) Sinnwell, S.; Inglis, A. J.; Davis, T. P.; Stenzel, M. H.; Barner-Kowollik, C. *American Chemical Society, Polymer Preprints, Division of Polymer Chemistry* **2008**, *49*, 240–241.

(104) Oehlenschlaeger, K. K.; Mueller, J. O.; Heine, N. B.; Glassner, M.; Guimard, N. K.; Delaittre, G.; Schmidt, F. G.; Barner-Kowollik, C. *Angewandte Chemie* **2013**, *52*, 762–766.

(105) Gondi, S. R.; Vogt, A. P.; Sumerlin, B. S. *Macromolecules* **2007**, *40*, 474–481.

(106) Góis, J. R.; Costa, J. R. C.; Popov, A. V.; Serra, A. C.; Coelho, J. F. J. *RSC Advances* **2016**, *6*, 16996–17007.

(107) Vanparijs, N.; Maji, S.; Louage, B.; Voorhaar, L.; Laplace, D.; Zhang, Q.; Shi, Y.; Hennink, W. E.; Hoogenboom, R.; De Geest, B. G. *Polymer Chemistry* **2015**, *6*, 5602–5614.

(108) Atkins, P. W.; de Paula, J., *Physikalische Chemie*, 5th ed.; Wiley-VCH: Weinheim, 2013.

(109) Jablonski, A. *Nature* **1933**, 839–840.

(110) Glassner, M.; Oehlenschlaeger, K. K.; Welle, A.; Bruns, M.; Barner-Kowollik, C. *Chemical Communications* **2013**, *49*, 633–635.

(111) Tuten, B. T.; Menzel, J. P.; Pahnke, K.; Blinco, J. P.; Barner-Kowollik, C. *Chemical Communications* **2017**, *53*, 4501–4504.

(112) Claus, T. K. et al. *Chemical Communications* **2017**, *11*, 190–207.

(113) Telitel, S.; Blasco, E.; Bangert, L.; Schacher, F. H.; Goldmann, A. S.; Barner-Kowollik, C. *Polymer Chemistry* **2017**, 4038–4042.

(114) Campos, L. M.; Killops, K. L.; Sakai, R.; Paulusse, J. M. J.; Damiron, D.; Drockenmuller, E.; Messmore, B. W.; Hawker, C. J.; Lyon, C. B. *Macromolecules* **2008**, *41*, 7063–7070.

(115) Adzima, B. J.; Tao, Y.; Kloxin, C. J.; DeForest, C. A.; Anseth, K. S.; Bowman, C. N. *Nature Chemistry* **2011**, *3*, 258–261.

(116) Arumugam, S.; Popik, V. V. *Journal of the American Chemical Society* **2012**, *134*, 8408–8411.

(117) Mueller, J. O.; Schmidt, F. G.; Blinco, J. P.; Barner-Kowollik, C. *Angewandte Chemie* **2015**, *54*, 10284–10288.

(118) Porter, G.; Tchir, M. F. *Journal of the Chemical Society D: Chemical Communications* **1970**, *6*, 1372–1373.

(119) Yang, N. C.; Rivas, C. *Journal of the American Chemical Society* **1961**, *83*, 2213–2213.

(120) Porter, G.; Tchir, M. F. *Journal of the Chemical Society A: Inorganic, Physical, Theoretical* **1971**, 3772–3777.

(121) Kaupp, M.; Tischer, T.; Hirschbiel, A. F.; Vogt, A. P.; Geckle, U.; Trouillet, V.; Hofe, T.; Stenzel, M. H.; Barner-Kowollik, C. *Macromolecules* **2013**, *46*, 6858–6872.

(122) Hiltebrandt, K.; Elies, K.; D'hooge, D. R.; Blinco, J. P.; Barner-Kowollik, C. *Journal of the American Chemical Society* **2016**, *138*, 7048–7054.

(123) Langer, M.; Mueller, J. O.; Goldmann, A. S.; Schacher, F. H.; Barner-Kowollik, C. *ACS Macro Letters* **2016**, *5*, 597–601.

(124) Zhu, W.; Li, Z.; Zhao, Y.; Zhang, K. *Macromolecular Rapid Communications* **2015**, *36*, 1987–1993.

(125) Quick, A. S.; Rothfuss, H.; Welle, A.; Richter, B.; Fischer, J.; Wegener, M.; Barner-Kowollik, C. *Advanced Functional Materials* **2014**, *24*, 3571–3580.

(126) Mueller, P.; Zieger, M. M.; Richter, B.; Quick, A. S.; Fischer, J.; Mueller, J. B.; Zhou, L.; Nienhaus, G. U.; Bastmeyer, M.; Barner-Kowollik, C.; Wegener, M. *ACS Nano* **2017**, *11*, 6396–6403.

(127) Altintas, O.; Willenbacher, J.; Wuest, K. N. R.; Oehlenschlaeger, K. K.; Krolla-Sidenstein, P.; Gliemann, H.; Barner-Kowollik, C. *Macromolecules* **2013**, *46*, 8092–8101.

(128) Claus, T. K.; Zhang, J.; Martin, L.; Hartlieb, M.; Mutlu, H.; Perrier, S.; Delaittre, G.; Barner-Kowollik, C. *Macromolecular Rapid Communications* **2017**, *38*, 1700264.

(129) Pauloehrl, T.; Delaittre, G.; Winkler, V.; Welle, A.; Bruns, M.; Börner, H. G.; Greiner, A. M.; Bastmeyer, M.; Barner-Kowollik, C. *Angewandte Chemie* **2012**, *51*, 1071–1074.

(130) Tischer, T.; Claus, T. K.; Bruns, M.; Trouillet, V.; Linkert, K.; Rodriguez-Emmenegger, C.; Goldmann, A. S.; Perrier, S.; Börner, H. G.; Barner-Kowollik, C. *Biomacromolecules* **2013**, *14*, 4340–4350.

(131) Preuss, C. M.; Tischer, T.; Rodriguez-Emmenegger, C.; Zieger, M. M.; Bruns, M.; Goldmann, A. S.; Barner-Kowollik, C. *J. Mater. Chem. B* **2014**, *2*, 36–40.

(132) Vigovskaya, A.; Abt, D.; Ahmed, I.; Niemeyer, C. M.; Barner-Kowollik, C.; Fruk, L. *Journal of Materials Chemistry B* **2016**, *4*, 442–449.

(133) Stolzer, L.; Ahmed, I.; Rodriguez-Emmenegger, C.; Trouillet, V.; Bockstaller, P.; Barner-Kowollik, C.; Fruk, L. *Chemical Communications* **2014**, *50*, 4430–4433.

(134) Huisgen, R.; Seidel, M.; Sauer, J.; McFarland, J.; Wallbillich, G. *The Journal of Organic Chemistry* **1959**, *24*, 892–893.

(135) J. S. Clovis, A. Eckell, R. Huisgen, R. S. *Chem. Ber.* **1967**, *100*, 60–70.

(136) Feng, W.; Li, L.; Yang, C.; Welle, A.; Trapp, O.; Levkin, P. A. *Angewandte Chemie* **2015**, *54*, 8732–8735.

(137) Li, Z.; Qian, L.; Li, L.; Bernhammer, J. C.; Huynh, H. V.; Lee, J. S.; Yao, S. Q. *Angewandte Chemie* **2016**, *55*, 2002–2006.

(138) Heiler, C.; Offenloch, J. T.; Blasco, E.; Barner-Kowollik, C. *ACS Macro Letters* **2016**, *6*, 56–61.

(139) Mueller, J. O.; Voll, D.; Schmidt, F. G.; Delaittre, G.; Barner-Kowollik, C. *Chemical Communications* **2014**, *50*, 15681–15684.

(140) Estupiñán, D.; Gegenhuber, T.; Blinco, J. P.; Barner-Kowollik, C.; Barner, L. *ACS Macro Letters* **2017**, 229–234.

(141) Dürr, C. J.; Lederhose, P.; Hlalele, L.; Abt, D.; Kaiser, A.; Brandau, S.; Barner-Kowollik, C. *Macromolecules* **2013**, *46*, 5915–5923.

(142) Lederhose, P.; Wüst, K. N. R.; Barner-Kowollik, C.; Blinco, J. P. *Chemical Communications* **2016**, *52*, 5928–5931.

(143) Lederhose, P.; Chen, Z.; Müller, R.; Blinco, J. P.; Wu, S.; Barner-Kowollik, C. *Angewandte Chemie* **2016**, *55*, 12195–12199.

(144) Mueller, J. O.; Guimard, N. K.; Oehlenschlaeger, K. K.; Schmidt, F. G.; Barner-Kowollik, C. *Polymer Chemistry* **2014**, *5*, 1447–1456.

(145) Kaupp, M.; Hiltebrandt, K.; Trouillet, V.; Mueller, P.; Quick, A. S.; Wegener, M.; Barner-Kowollik, C. *Chemical Communications* **2016**, *52*, 1975–1978.

(146) Willenbacher, J.; Wuest, K. N. R.; Mueller, J. O.; Kaupp, M.; Wagenknecht, H. A.; Barner-Kowollik, C. *ACS Macro Letters* **2014**, *3*, 574–579.

(147) Offenloch, J. T.; Willenbacher, J.; Tzvetkova, P.; Heiler, C.; Mutlu, H.; Barner-Kowollik, C. *Chemical Communications* **2017**, *53*, 775–778.

(148) Dietrich, M.; Delaittre, G.; Blinco, J. P.; Inglis, A. J.; Bruns, M.; Barner-Kowollik, C. *Advanced Functional Materials* **2012**, *22*, 304–312.

(149) Tischer, T.; Rodriguez-Emmenegger, C.; Trouillet, V.; Welle, A.; Schueler, V.; Mueller, J. O.; Goldmann, A. S.; Brynda, E.; Barner-Kowollik, C. *Advanced Materials* **2014**, *26*, 4087–4092.

(150) Blasco, E.; Piñol, M.; Oriol, L.; Schmidt, B. V.K. J.; Welle, A.; Trouillet, V.; Bruns, M.; Barner-Kowollik, C. *Advanced Functional Materials* **2013**, *23*, 4011.

(151) Wedler-Jasinski, N.; Delbosc, N.; Virolleaud, M.-A.; Montarnal, D.; Welle, A.; Barner, L.; Walther, A.; Bernard, J.; Barner-Kowollik, C. *Chem. Commun.* **2016**, *52*, 8753–8756.

(152) Wang, Y.; Hu, W. J.; Song, W.; Lim, R. K. V.; Lin, Q. *Organic Letters* **2008**, *10*, 3725–3728.

(153) Wang, Y.; Song, W.; Hu, W. J.; Lin, Q. *Angewandte Chemie (International ed. in English)* **2009**, *48*, 5330.

(154) Sunasee, R.; Adokoh, C. K.; Darkwa, J.; Narain, R. *Expert Opinion on Drug Delivery* **2014**, *11*, 867–884.

(155) Ting, S. R. S.; Chen, G.; Stenzel, M. H. *Polymer Chemistry* **2010**, *1*, 1392–1412.

(156) Li, X.; Chen, G. *Polymer Chemistry* **2015**, *6*, 1417–1430.

(157) Miura, Y.; Hoshino, Y.; Seto, H. *Chemical Reviews* **2016**, *116*, 1673–1692.

(158) Pearson, S.; Scarano, W.; Stenzel, M. H. *Chemical Communications* **2012**, *48*, 4695–4697.

(159) Zhang, K.; Jia, Y. G.; Tsai, I. H.; Strandman, S.; Ren, L.; Hong, L.; Zhang, G.; Guan, Y.; Zhang, Y.; Zhu, X. X. *Biomacromolecules* **2017**, *18*, 778–786.

(160) Park, H.; Walta, S.; Rosencrantz, R. R.; Körner, A.; Schulte, C.; Elling, L.; Richtering, W.; Böker, A. *Polymer Chemistry* **2016**, *7*, 878–886.

(161) Kim, S. H.; Goto, M.; Cho, C. S.; Akaike, T. *Biotechnology Letters* **2000**, *22*, 1049–1057.

(162) Hu, Z.; Fan, X.; Zhang, G. *Carbohydrate Polymers* **2010**, *79*, 119–124.

(163) Chen, G.; Amajjahe, S.; Stenzel, M. H. *Chemical Communications* **2009**, 1198–1200.

(164) Ganda, S.; Jiang, Y.; Thomas, D. S.; Eliezar, J.; Stenzel, M. H. *Macromolecules* **2016**, *49*, 4136–4146.

(165) Zhao, J.; Babiuch, K.; Lu, H.; Dag, A.; Gottschaldt, M.; Stenzel, M. H. *Chem. Commun.* **2014**, *50*, 15928–15931.

(166) Pearson, S.; Vitucci, D.; Khine, Y. Y.; Dag, A.; Lu, H.; Save, M.; Billon, L.; Stenzel, M. H. *European Polymer Journal* **2015**, *69*, 616–627.

(167) Wang, Y.; Zhang, X.; Yu, P.; Li, C. *International Journal of Pharmaceutics* **2013**, *441*, 170–180.

(168) Chen, W.; Meng, F.; Cheng, R.; Deng, C.; Feijen, J.; Zhong, Z. *Journal of Materials Chemistry B: Materials for biology and medicine* **2015**, *3*, 2308–2317.

(169) Guo, T.-Y. Y.; Liu, P.; Zhu, J.-W. W.; Song, M.-D. D.; Zhang, B.-H. H. *Biomacromolecules* **2006**, *7*, 1196–1202.

(170) Sun, X. L.; Grande, D.; Baskaran, S.; Hanson, S. R.; Chaikof, E. L. *Biomacromolecules* **2002**, *3*, 1065–1070.

(171) Okada, M. *Progress in Polymer Science* **2001**, *26*, 67–104.

(172) Spain, S. G.; Cameron, N. R. *Polymer Chemistry* **2011**, *2*, 60–68.

(173) Ladmiral, V.; Melia, E.; Haddleton, D. M. *European Polymer Journal* **2004**, *40*, 431–449.

(174) Vázquez-Dorbatt, V.; Lee, J.; Lin, E. W.; Maynard, H. D. *ChemBioChem* **2012**, *13*, 2478–2487.

(175) Becer, C. R. *Macromolecular Rapid Communications* **2012**, *33*, 742–752.

(176) Zhang, Y.; Chan, J. W.; Moretti, A.; Uhrich, K. E. *Journal of Controlled Release* **2015**, *219*, 355–368.

(177) Ghadban, A.; Albertin, L. *Polymers* **2013**, *5*, 431–526.

(178) Yilmaz, G.; Becer, C. R. *Frontiers in Bioengineering and Biotechnology* **2014**, *2*, 1–18.

(179) Das, R.; Mukhopadhyay, B. *ChemistryOpen* **2016**, *5*, 401–433.

(180) Dag, A.; Zhao, J.; Stenzel, M. H. *ACS Macro Letters* **2015**, *4*, 579–583.

(181) Chen, Y.; Lord, M. S.; Piloni, A.; Stenzel, M. H. *Macromolecules* **2015**, *48*, 346–357.

(182) De Coen, R.; Vanparijs, N.; Risseeuw, M. D.; Lybaert, L.; Louage, B.; De Koker, S.; Kumar, V.; Grooten, J.; Taylor, L.; Ayres, N.; Van Calenbergh, S.; Nuhn, L.; De Geest, B. G. *Biomacromolecules* **2016**, *17*, 2479–2488.

(183) Obata, M.; Shimizu, M.; Ohta, T.; Matsushige, A.; Iwai, K.; Hirohara, S.; Tanihara, M. *Polymer Chemistry* **2011**, *2*, 651–658.

(184) Obata, M.; Kobori, T.; Hirohara, S.; Tanihara, M. *Polymer Chemistry* **2015**, *6*, 1793–1804.

(185) Obata, M.; Otobuchi, R.; Kuroyanagi, T.; Takahashi, M.; Hirohara, S. *Journal of Polymer Science Part A: Polymer Chemistry* **2017**, *55*, 395–403.

(186) Ting, S. R. S.; Min, E. H.; Lau, B. K. F.; Hutvagner, G. *Journal of Applied Polymer Science* **2017**, *134*, 1–11.

(187) Hoshino, Y.; Nakamoto, M.; Miura, Y. *Journal of the American Chemical Society* **2012**, *134*, 15209–15212.

(188) Geng, J.; Mantovani, G.; Tao, L.; Nicolas, J.; Chen, G.; Wallis, R.; Mitchell, D. A.; Johnson, B. R. G.; Evans, S. D.; Haddleton, D. M. *Journal of the American Chemical Society* **2007**, *129*, 15156–15163.

(189) Charville, H.; Jin, J.; Evans, C. W.; Brimble, M. A.; Williams, D. E. *RSC Advances* **2013**, *3*, 15435–15441.

(190) Diwan, D.; Shinkai, K.; Tetsuka, T.; Cao, B.; Arai, H.; Koyama, T.; Hatano, K.; Matsuoka, K. *Molecules* **2017**, *22*, 157.

(191) Schmidt, R. R.; Michel, J. *Angewandte Chemie* **1980**, *19*, 731–732.

(192) Song, E. H.; Manganiello, M. J.; Chow, Y. H.; Ghosn, B.; Convertine, A. J.; Stayton, P. S.; Schnapp, L. M.; Ratner, D. M. *Biomaterials* **2012**, *33*, 6889–6897.

(193) Tanaka, T.; Inoue, G.; Shoda, S.-I.; Kimura, Y. *Journal of Polymer Science Part A: Polymer Chemistry* **2014**, 3513–3520.

(194) Tanaka, T.; Huang, W. C.; Noguchi, M.; Kobayashi, A.; Shoda, S.-i. *Tetrahedron Letters* **2009**, *50*, 2154–2157.

(195) Tanaka, T.; Matsumoto, T.; Noguchi, M.; Kobayashi, A.; Shoda, S.-i. *Chemistry Letters* **2009**, *38*, 458–459.

(196) Pagé, D.; Zanini, D.; Roy, R. *Bioorganic and Medicinal Chemistry* **1996**, *4*, 1949–1961.

(197) Li, J; Zacharek, S; Chen, X; Wang, J; Zhang, W; Janczuk, A; Wang, P. G. *Bioorg Med Chem* **1999**, *7*, 1549–1558.

(198) Kitano, H.; Ishino, Y.; Yabe, K. *Langmuir* **2001**, *17*, 2312–2316.

(199) Akai, S.; Kajihara, Y.; Nagashima, Y.; Kamei, M.; Arai, J.; Bito, M.; Sato, K.-i. *Journal of Carbohydrate Chemistry* **2001**, *20*, 121–143.

(200) Jain, N. K.; Mishra, V.; Mehra, N. K. *Expert Opinion on Drug Delivery* **2013**, *10*, 353–367.

(201) Maley, A. M.; Terada, Y.; Onogi, S.; Shea, K. J.; Miura, Y.; Corn, R. M. *Journal of Physical Chemistry C* **2016**, *120*, 16843–16849.

(202) Toyoshima, M.; Miura, Y. *Journal of Polymer Science Part A: Polymer Chemistry* **2009**, *47*, 1412.

(203) Toyoshima, M.; Tomoyuki, O.; Fukuda, T.; Matsumoto, E.; Miura, Y. *Polymer Journal* **2010**, *42*, 172–178.

(204) Handke, N.; Lahaye, V.; Bertin, D.; Delair, T.; Verrier, B.; Gigmes, D.; Trimaille, T. *Macromolecular Bioscience* **2013**, *13*, 1213–1220.

(205) Vinson, N.; Gou, Y.; Becer, C. R.; Haddleton, D. M.; Gibson, M. I. *Polymer Chemistry* **2011**, *2*, 107–113.

(206) Gou, Y.; Geng, J.; Richards, S. J.; Burns, J.; Remzi Becer, C.; Haddleton, D. M. *Journal of Polymer Science, Part A: Polymer Chemistry* **2013**, *51*, 2588–2597.

(207) Nurmi, L.; Lindqvist, J.; Randev, R.; Syrett, J.; Haddleton, D. M. *Chemical Communications* **2009**, 2727.

(208) Edelman, G. M.; Cunningham, B. a.; Reeke, G. N.; Becker, J. W.; Waxdal, M. J.; Wang, J. L. *Proceedings of the National Academy of Sciences of the United States of America* **1972**, *69*, 2580–2584.

(209) Pieters, R. J. *Organic & Biomolecular Chemistry* **2009**, *7*, 2013–25.

(210) Gestwicki, J. E.; Cairo, C. W.; Strong, L. E.; Oetjen, K. A.; Kiessling, L. L. *Journal of the American Chemical Society* **2002**, *124*, 14922–14933.

(211) Lundquist, J. J.; Toone, E. J. *Chemical Reviews* **2002**, *102*, 555–578.

(212) Barin, F; McLane, M.; Allan, J.; Lee, T.; Groopman, J.; Essex, M *Science* **1985**, *228*, 1094–1096.

(213) Van Kooyk, Y; Geijtenbeek, T. B. H. *Nature Reviews Immunology* **2003**, *3*, 697–709.

(214) Becer, C. R.; Gibson, M. I.; Geng, J.; Ilyas, R.; Wallis, R.; Mitchell, D. A.; Haddleton, D. M. *Journal of the American Chemical Society* **2010**, *132*, 15130–15132.

(215) Kim, N.; Jiang, D.; Jacobi, A. M.; Lennox, K. A.; Rose, S. D.; Behlke, M. A.; Salem, A. K. *International Journal of Pharmaceutics* **2012**, *427*, 123–133.

(216) Singh, R.; Lillard, J. W. *Experimental and Molecular Pathology* **2009**, *86*, 215–223.

(217) Yu, S. S.; Lau, C. M.; Barham, W. J.; Onishko, H. M.; Nelson, C. E.; Li, H.; Smith, C. A.; Yull, F. E.; Duvall, C. L.; Giorgio, T. D. *Molecular Pharmaceutics* **2013**, *10*, 975–987.

(218) Kalia, M.; Jameel, S. *Amino Acids* **2011**, *41*, 1147–1157.

(219) Stansell, E.; Desrosiers, R. C. *Yale Journal of Biology and Medicine* **2010**, *83*, 201–208.

(220) Qian, Z.; Dominguez, S. R.; Holmes, K. V. *PLoS ONE* **2013**, *8*, 1–12.

(221) Cifuentes-Muñoz, N.; Salazar-Quiroz, N.; Tischler, N. D. *Viruses* **2014**, *6*, 1801–1822.

(222) Zhu, P.; Liu, J.; Bess, J.; Chertova, E.; Lifson, J. D.; Grisé, H.; Ofek, G. a.; Taylor, K. a.; Roux, K. H. *Nature* **2006**, *441*, 847–852.

(223) Niu, Y.; Yu, M.; Hartono, S. B.; Yang, J.; Xu, H.; Zhang, H.; Zhang, J.; Zou, J.; Dexter, A.; Gu, W.; Yu, C. *Advanced Materials* **2013**, *25*, 6233–6237.

(224) Kuhn, V. W.; Majer, H *Die Makromolekulare Chemie* **1956**, *18*, 239–253.

(225) Georges, M. K.; Veregin, R. P. N.; Kazmaier, P. M.; Hamer, G. K. *Macromolecules* **1993**, *26*, 2987–2988.

(226) Wang, J. S.; Matyjaszewski, K. *Journal of the American Chemical Society* **1995**, *117*, 5614–5615.

(227) Kato, M.; Kamigaito, M.; Sawamoto, M.; Higashimura, T. *Macromolecules* **1995**, *28*, 1721–1723.

(228) Rao, J. P.; Geckeler, K. E. *Progress in Polymer Science* **2011**, *36*, 887–913.

(229) Kröger, A. P. P.; Boonen, R. J.; Paulusse, J. M. *Polymer* **2017**, *120*, 119–128.

(230) Wulff, G.; Chong, B.-O.; Kolb, U. *Angewandte Chemie (International ed. in English)* **2006**, *45*, 2955–2958.

(231) Perez-Baena, I.; Barroso-Bujans, F.; Gasser, U.; Arbe, A.; Moreno, A. J.; Colmenero, J.; Pomposo, J. A. *ACS Macro Letters* **2013**, *2*, 775.

(232) Knöfel, N. D.; Rothfuss, H.; Willenbacher, J.; Barner-Kowollik, C.; Roesky, P. W. *Angewandte Chemie* **2017**, *56*, 4950–4954.

(233) Gillissen, M. A. J.; Voets, I. K.; Meijer, E. W.; Palmans, A. R. A. *Polymer Chemistry* **2012**, *3*, 3166.

(234) Sanchez-Sanchez, A.; Akbari, S.; Etxeberria, A.; Arbe, A.; Gasser, U.; Moreno, A. J.; Colmenero, J.; Pomposo, J. A. *ACS Macro Letters* **2013**, *2*, 491–495.

(235) Altintas, O.; Barner-Kowollik, C. *Macromolecular Rapid Communications* **2016**, *37*, 29–46.

(236) Willenbacher, J.; Schmidt, B. V.K. J.; Schulze-Suenninghausen, D.; Altintas, O.; Luy, B.; Delaittre, G.; Barner-Kowollik, C. *Chemical Communications* **2014**, *50*, 7056–7059.

(237) Altintas, O.; Gerstel, P.; Dingenouts, N.; Barner-Kowollik, C. *Chemical Communications* **2010**, *46*, 6291–6293.

(238) Altintas, O.; Lejeune, E.; Gerstel, P.; Barner-Kowollik, C. *Polymer Chemistry* **2012**, *3*, 640–651.

(239) Shishkan, O.; Zamfir, M.; Gauthier, M. A.; Börner, H. G.; Lutz, J.-F. *Chemical Communications* **2014**, *50*, 1570.

(240) Cole, J. P.; Hanlon, A. M.; Rodriguez, K. J.; Berda, E. B. *Journal of Polymer Science, Part A: Polymer Chemistry* **2017**, *55*, 191–206.

(241) Ponader, D.; Wojcik, F.; Beceren-Braun, F.; Dernedde, J.; Hartmann, L. *Biomacromolecules* **2012**, *13*, 1845–1852.

(242) Zydziak, N.; Konrad, W.; Feist, F.; Afonin, S.; Weidner, S.; Barner-Kowollik, C. *Nature Communications* **2016**, *7*, 13672.

(243) Espeel, P.; Carrette, L. L. G.; Bury, K.; Capenberghs, S.; Martins, J. C.; Duprez, F. E.; Madder, A. *Angewandte Chemie* **2013**, *52*, 13261–13264.

(244) Porel, M.; Alabi, C. A. *Journal of the American Chemical Society* **2014**, *136*, 13162–13165.

(245) Harth, E.; Van Horn, B.; Lee, V. Y.; Germack, D. S.; Gonzales, C. P.; Miller, R. D.; Hawker, C. J. *Journal of the American Chemical Society* **2002**, *124*, 8653–8660.

(246) Hanlon, A. M.; Chen, R.; Rodriguez, K. J.; Willis, C.; Dickinson, J. G.; Cashman, M.; Berda, E. B. *Macromolecules* **2017**, *50*, 2996–3003.

(247) Oria, L.; Aguado, R.; Pomposo, J. A.; Colmenero, J. *Advanced Materials* **2010**, *22*, 3038–3041.

(248) Sanchez-Sanchez, A.; Asenjo-Sanz, I.; Buruaga, L.; Pomposo, J. A. *Macromolecular Rapid Communications* **2012**, *33*, 1262.

(249) Murray, B. S.; Fulton, D. A. *Macromolecules* **2011**, *44*, 7242.

(250) Tuten, B. T.; Chao, D.; Lyon, K; Berda, E. B.; Lyon, C. K.; Berda, E. B.; Chem, P.; Tuten, B. T.; Chao, D.; Lyon, C. K.; Berda, E. B. *Polymer Chemistry* **2012**, *3*, 3068–3071.

(251) Whitaker, D. E.; Mahon, C. S.; Fulton, D. A. *Angewandte Chemie* **2013**, *52*, 956–959.

(252) Sanchez-Sanchez, A.; Fulton, D. A.; Pomposo, J. A. *Chemical Communications* **2014**, *50*, 1871–1874.

(253) Mavila, S.; Diesendruck, C. E.; Linde, S.; Amir, L.; Shikler, R.; Lemcoff, N. G. *Angewandte Chemie* **2013**, *52*, 5767–5770.

(254) Appel, E. A.; Dyson, J.; del Barrio, J.; Walsh, Z.; Scherman, O. A. *Angewandte Chemie* **2012**, *51*, 4185–4189.

(255) Stals, P. J. M.; Gillissen, M. A. J.; Nicolaÿ, R.; Palmans, A. R. A.; Meijer, E. W. *Polymer Chemistry* **2013**, *4*, 2584–2597.

(256) Song, C.; Li, L.; Dai, L.; Thayumanavan, S. *Polymer Chemistry* **2015**, *6*, 4828–4834.

(257) Berda, E. B.; Foster, E. J.; Meijer, E. W. *Macromolecules* **2010**, *43*, 1430–1437.

(258) Njikang, G.; Liu, G.; Curda, S. A. *Macromolecules* **2008**, *41*, 5697–5702.

(259) He, J.; Tremblay, L.; Lacelle, S.; Zhao, Y. *Soft Matter* **2011**, *7*, 2380–2386.

(260) Blasco, E.; Yameen, B.; Quick, A. S.; Krolla-Sidenstein, P.; Welle, A.; Wegener, M.; Barner-Kowollik, C. *Macromolecules* **2015**, *48*, 8718–8728.

(261) Grubisic, Z.; Rempp, P.; Benoit, H. *J. Polym. Sci. B Polym. Lett.* **1967**, *5*, 753–759.

(262) Pomposo, J. A.; Perez-Baena, I.; Buruaga, L.; Alegría, A.; Moreno, A. J.; Colmenero, J. *Macromolecules* **2011**, *44*, 8644–8649.

(263) Einstein, A. *Annalen der Physik* **1905**, *322*, 549–560.

(264) Blasco, E.; Tuten, B. T.; Frisch, H.; Lederer, A.; Barner-Kowollik, C. *Polymer Chemistry* **2017**, *8*, 5845–5851.

(265) Chao, D.; Jia, X.; Tuten, B.; Wang, C.; Berda, E. B. *Chemical Communications* **2013**, *49*, 4178–4180.

(266) Cherian, A. E.; Sun, F. C.; Sheiko, S. S.; Coates, G. W. *Journal of the American Chemical Society* **2007**, *129*, 11350–11351.

(267) Bartolini, A.; Tempesti, P.; Resta, C.; Berti, D.; Smets, J.; Aouad, Y. G.; Baglioni, P. *Phys. Chem. Chem. Phys.* **2017**, *19*, 4553–4559.

(268) Wen, J.; Yuan, L.; Yang, Y.; Liu, L.; Zhao, H. *ACS Macro Letters* **2013**, *2*, 100.

(269) Tuten, B. T.; Chao, D.; Lyon, K; Berda, E. B. *Polymer Chemistry* **2012**, *3*, 3068–3071.

(270) De Luzuriaga, A. R.; Ormategui, N.; Grande, H. J.; Odriozola, I.; Pomposo, J. A.; Loinaz, I. *Macromolecular Rapid Communications* **2008**, *29*, 1156–1160.

(271) Jiang, X.; Pu, H.; Wang, P. *Polymer* **2011**, *52*, 3597–3602.

(272) Frank, P.; Prasher, A.; Tuten, B.; Chao, D.; Berda, E. *Applied Petrochemical Research* **2015**, *5*, 9–17.

(273) Terashima, T.; Mes, T.; De Greef, T. F. A.; Gillissen, M. A. J.; Besenius, P.; Palmans, A. R. A.; Meijer, E. W. *Journal of the American Chemical Society* **2011**, *133*, 4742–4745.

(274) Steinkoenig, J.; Rothfuss, H.; Lauer, A.; Tuten, B. T.; Barner-Kowollik, C. *Journal of the American Chemical Society* **2017**, *139*, 51–54.

(275) Wuest, K. N. R.; Trouillet, V.; Goldmann, A. S.; Stenzel, M. H.; Barner-Kowollik, C. *Macromolecules* **2016**, *49*, 1712–1721.

(276) Inel, G. A.; Ungureau, E.-M.; Varley, T. S.; Hirani, M.; Holt, K. B. *Diamond and Related Materials* **2016**, *61*, 7–13.

(277) Maeda, Y.; Higuchi, T.; Ikeda, I. *Langmuir* **2000**, *16*, 7503–7509.

(278) Liang, M.; Lin, I.-C.; Whittaker, M. R.; Minchin, R. F.; Monteiro, M. J.; Toth, I. *ACS nano* **2010**, *4*, 403–413.

(279) Syrett, J. A.; Mantovani, G.; Barton, W. R. S.; Price, D.; Haddleton, D. M. *Polymer Chemistry* **2010**, *1*, 102–106.

(280) Skey, J.; O'Reilly, R. K. *Chemical Communications* **2008**, 4183–4185.

(281) Chen, B.; Sleiman, H. F. *Macromolecules* **2004**, *37*, 5866–5872.

(282) Straziellea, C.; Benoita, H.; Vogl, O. *Eur. Polym. J.* **1978**, *14*, 331–334.

(283) Bradac, C; Gaebel, T; Naidoo, N; Sellars, M. J.; Twamley, J; Brown, L. J.; Barnard, a. S.; Plakhotnik, T; Zvyagin, a. V.; Rabeau, J. R. *Nature nanotechnology* **2010**, *5*, 345–349.

(284) Hufendiek, A.; Barner-Kowollik, C.; Meier, M. A. R. *Polymer Chemistry* **2015**, *6*, 2188–2191.

(285) Meinhardt, T.; Lang, D.; Dill, H.; Krueger, A. *Advanced Functional Materials* **2011**, *21*, 494–500.

(286) El Tall, O.; Hou, Y.; Abou-Hamad, E.; Raja, I. U.; Hedhili, M. N.; Peng, W.; Mahfouz, R.; Bakr, O. M.; Beaujuge, P. M. *Chemistry of Materials* **2014**, *26*, 2766–2769.

(287) Willocq, B.; Lemaur, V.; El Garah, M.; Ciesielski, A.; Samorì, P.; Raquez, J.-M.; Dubois, P.; Cornil, J. *Chemical Communications* **2016**, *52*, 7608–7611.

(288) Haddon, R. C. *Science* **1993**, *261*, 1545–1550.

(289) Nebhani, L.; Barner-Kowollik, C. *Macromolecular Rapid Communications* **2010**, *31*, 1298–1305.

(290) Yameen, B.; Rodriguez-Emmenegger, C.; Ahmed, I.; Preuss, C. M.; Dürr, C. J.; Zydziak, N.; Trouillet, V.; Fruk, L.; Barner-Kowollik, C. *Chemical Communications* **2013**, *49*, 6734.

(291) Wuest, K. N. R.; Trouillet, V.; Köppe, R.; Roesky, P. W.; Goldmann, A. S.; Stenzel, M. H.; Barner-Kowollik, C. *Polym. Chem.* **2017**, *8*, 838–842.

(292) Petit, T.; Arnault, J.-C.; Girard, H. A.; Sennour, M.; Bergonzo, P. *Physical Review B* **2011**, *84*, 233407.

(293) Liang, C. Y.; Krimm, S *Journal of Polymer Science* **1958**, *27*, 241–254.

(294) Wuest, K. N. R.; Lu, H.; Thomas, D. S.; Goldmann, A. S.; Stenzel, M. H.; Barner-Kowollik, C. *ACS Macro Letters* **2017**, *6*, 1168–1174.

(295) Hernández, J. M.; Gaborieau, M.; Castignolles, P.; Gidley, M. J.; Myers, A. M.; Gilbert, R. G. *Biomacromolecules* **2008**, *9*, 954–965.

(296) Zhao, J.; Lu, H.; Wong, S.; Lu, M.; Xiao, P.; Stenzel, M. H. *Polymer Chemistry* **2017**, *8*, 3317–3326.

(297) Xu, C.; Niu, Y.; Popat, A.; Jambhrunkar, S.; Karmakar, S.; Yu, C. *Journal of Materials Chemistry B* **2014**, *2*, 253–256.

(298) Mantovani, G.; Lecolley, F.; Tao, L.; Haddleton, D. M.; Clerx, J.; Cornelissen, J. J.L. M.; Velonia, K. *Journal of the American Chemical Society* **2005**, *127*, 2966–73.

(299) Rodriguez-Emmenegger, C.; Preuss, C. M.; Yameen, B.; Pop-Georgievski, O.; Bachmann, M.; Mueller, J. O.; Bruns, M.; Goldmann, A. S.; Bastmeyer, M.; Barner-Kowollik, C. *Advanced Materials* **2013**, *25*, 6123–6127.

(300) http://www.ampolymer.com/Mark-Houwink.html, accessed 2017-07-10.

(301) Bax, A. *Journal of Magnetic Resonance (1969)* **1985**, *65*, 142–145.

(302) Chen, X.; Zhang, W. *Chemical Society Reviews* **2017**, *46*, 734–760.

Appendix

A. Supporting information for Chapter 2

Table A.1. Literature reported apparent molecular weights and hydrodynamic diameters of SCNP systems (precursors and nanoparticles). The data is plotted in Figure 2.8.

Reference	$M_\mathrm{n}^{\mathrm{SEC}}$ / g·mol^{-1}	$D_\mathrm{h}^{\mathrm{DLS}}$ / nm
[255]	24900	5.0
	67900	12.6
	48700	9.3
	23600	4.8
	28700	6.3
	57000	7.3
	20300	5.0
	60100	11.8
	39100	9.9
	19100	4.4
	23300	5.7
	52500	6.3
[232]	40600	15.2
	31000	8.5
[265]	15000	6.5
	17400	6.1
	19900	6.7
	22500	5.3
	26600	4.8

Table A.1. Continued from previous page.

Reference	M_n^{SEC} / g·mol^{-1}	D_h^{DLS} / nm
	20700	5.3
	22600	4.9
	22800	4.6
	24100	4.3
	22000	5.5
	22700	4.8
	25600	4.5
	23300	4.3

B. Supporting information for Chapter 3
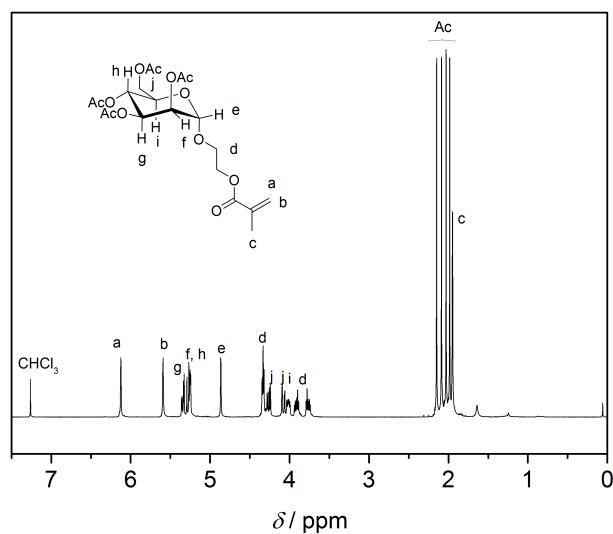
Figure B.1. ^{1}H NMR (400 MHz) spectrum of ManAcEMA in in CDCl$_3$. Adapted with permission from reference [275]. Copyright (2016) American Chemical Society.

Figure B.2. ^{13}C NMR (101 MHz) spectrum of ManAcEMA in CDCl$_3$. Adapted with permission from reference [275]. Copyright (2016) American Chemical Society.
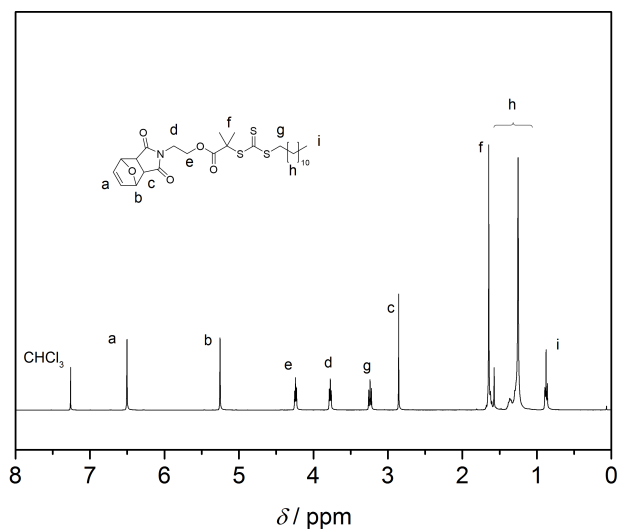
Figure B.3. ^{1}H NMR (400 MHz) spectrum of CTA1 in in CDCl$_3$. Adapted with permission from reference [275]. Copyright (2016) American Chemical Society.
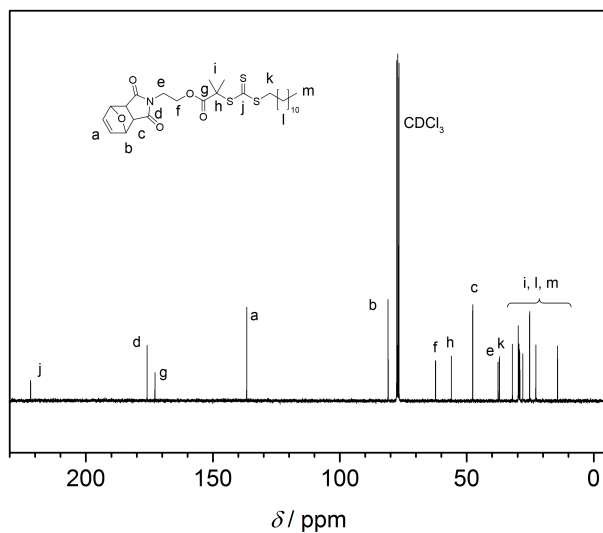
Figure B.4. ^{13}C NMR (101 MHz) spectrum of CTA1 in in CDCl$_3$. Adapted with permission from reference [275]. Copyright (2016) American Chemical Society.
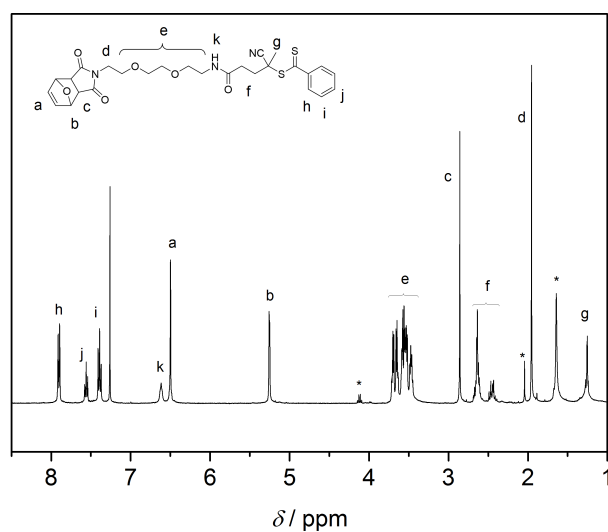
Figure B.5. ^{1}H NMR (400 MHz) spectrum of CTA2 in in CDCl$_3$. Adapted with permission from reference [275]. Copyright (2016) American Chemical Society.
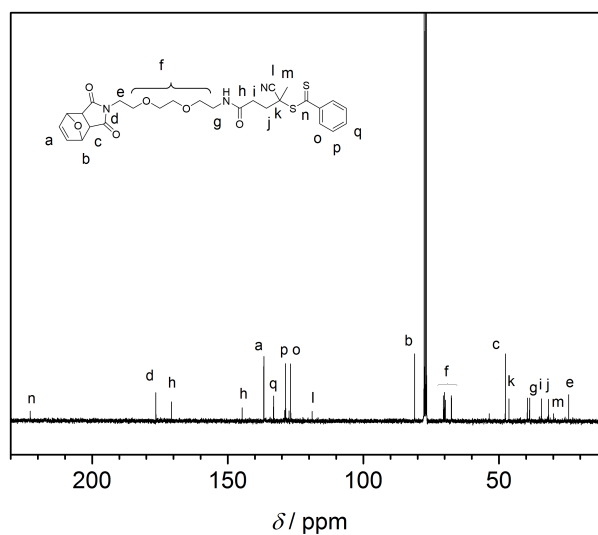
Figure B.6. ^{13}C NMR (101 MHz) spectrum of CTA2 in in CDCl$_3$. Adapted with permission from reference [275]. Copyright (2016) American Chemical Society.

161
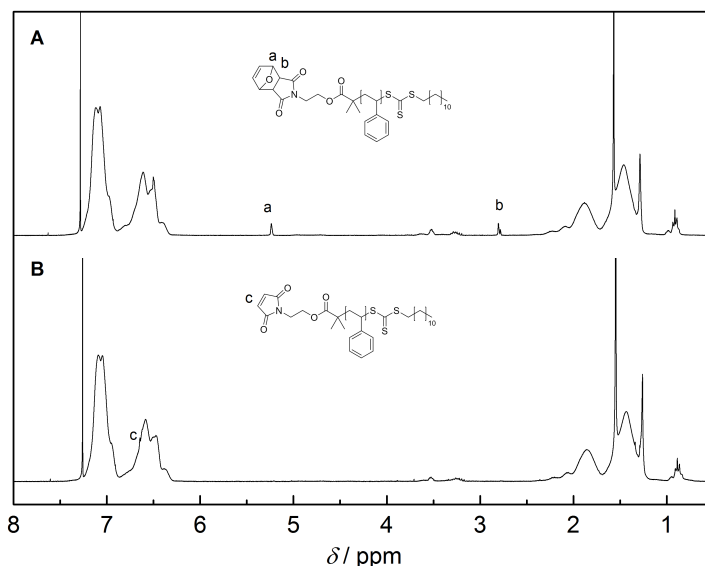
Figure B.7. ^{1}H NMR (400 MHz) spectrum of Mal-PS before (A) and after deprotection (B) in CDCl$_3$. Adapted with permission from reference [275]. Copyright (2016) American Chemical Society.
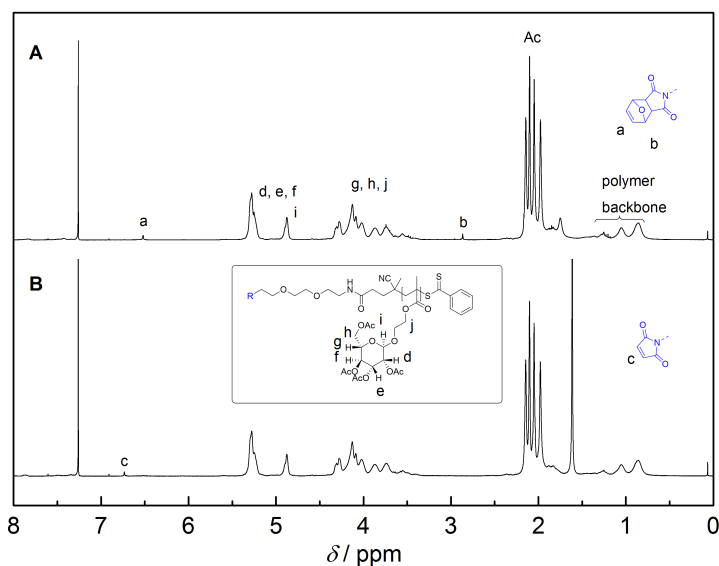
Figure B.8. ^{1}H NMR (400 MHz) spectrum of Mal-ManAcEMA 1 before (A) and after deprotection (B) in CDCl$_3$. Adapted with permission from reference [275]. Copyright (2016) American Chemical Society.
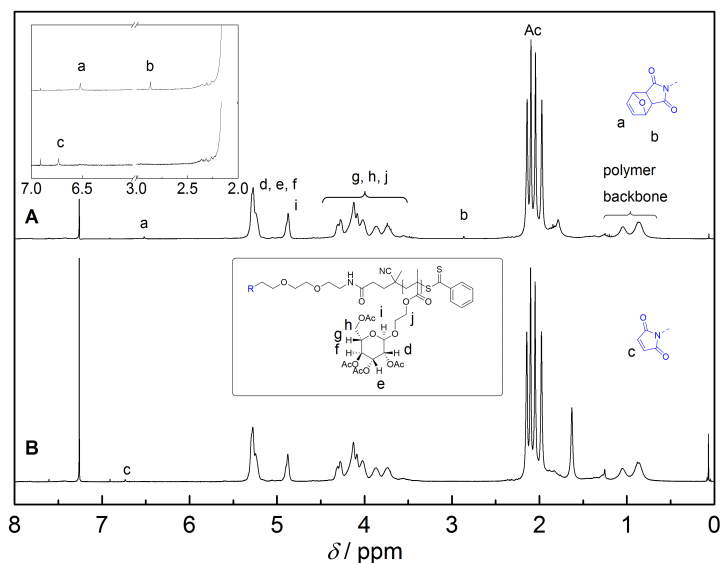
Figure B.9. ^{1}H NMR (400 MHz) spectrum of Mal-ManAcEMA 2 before (A) and after deprotection (B) in CDCl$_3$. Adapted with permission from reference [275]. Copyright (2016) American Chemical Society.
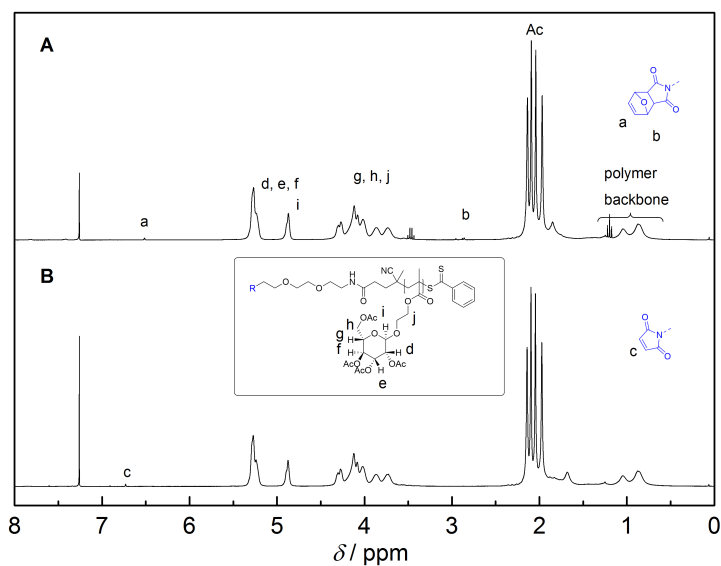
Figure B.10. ^{1}H NMR (400 MHz) spectrum of Mal-ManAcEMA 3 before (A) and after deprotection (B) in CDCl$_3$. Adapted with permission from reference [275]. Copyright (2016) American Chemical Society.
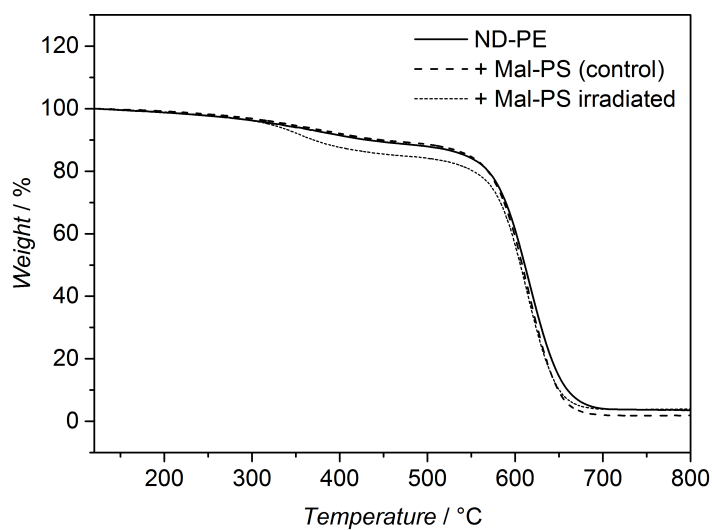
Figure B.11. TGA of ND-PE and control experiments, where a ND-PE/Mal-PS mixture was divided into two vials and one vial was irradiated with UV light at λ_{max} =320 nm whereas the other sample was stirred in the dark (control). The ND samples were purified and dried under reduced pressure before the thermogravimetric analysis. Adapted with permission from reference [275]. Copyright (2016) American Chemical Society.

C. Supporting information for chapter 4
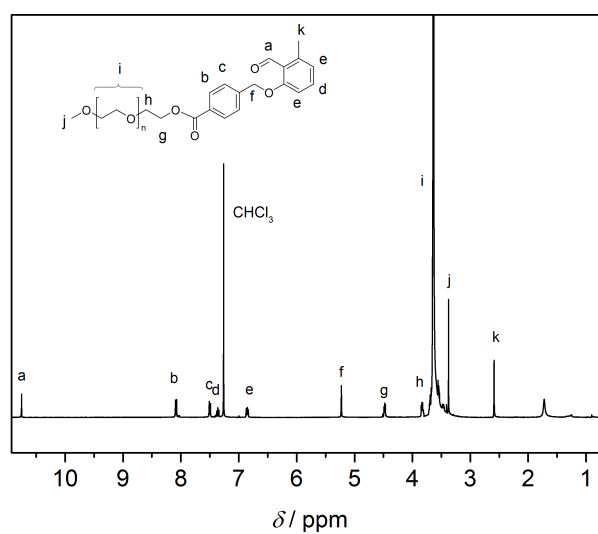
Figure C.12. ^{1}H NMR (400 MHz) spectrum of PE-PEG in CDCl$_3$. Adapted from Ref. [291] with permission from The Royal Society of Chemistry.
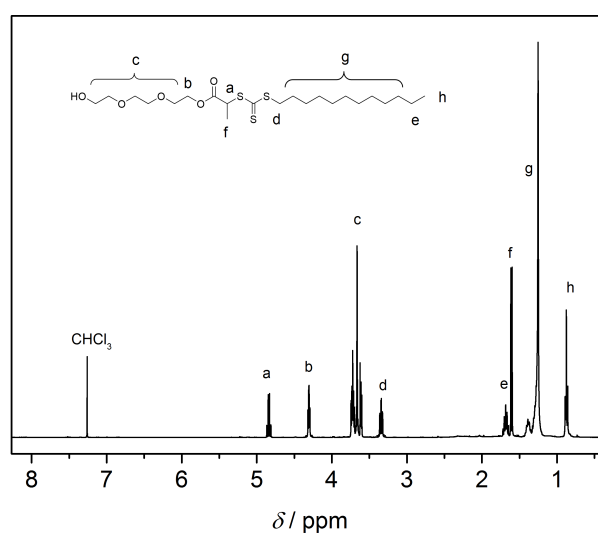
Figure C.13. ^{1}H NMR (400 MHz) spectrum of DOPAT-OH in CDCl$_3$. Adapted from Ref. [291] with permission from The Royal Society of Chemistry.
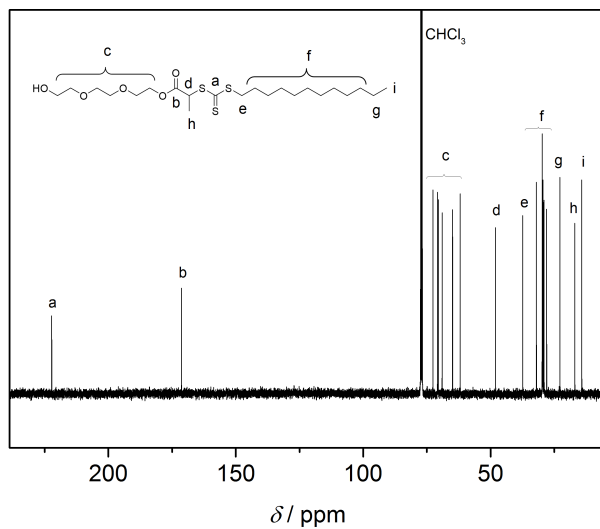
Figure C.14. ^{13}C NMR (101 MHz) spectrum of DOPAT-OH in CDCl$_3$. Adapted from Ref. [291] with permission from The Royal Society of Chemistry.
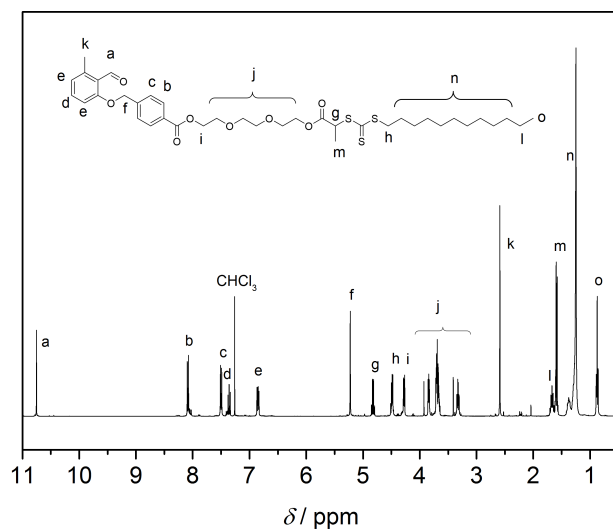
Figure C.15. ^{1}H NMR (400 MHz) spectrum of CTA3 in CDCl$_3$. Adapted from Ref. [291] with permission from The Royal Society of Chemistry.
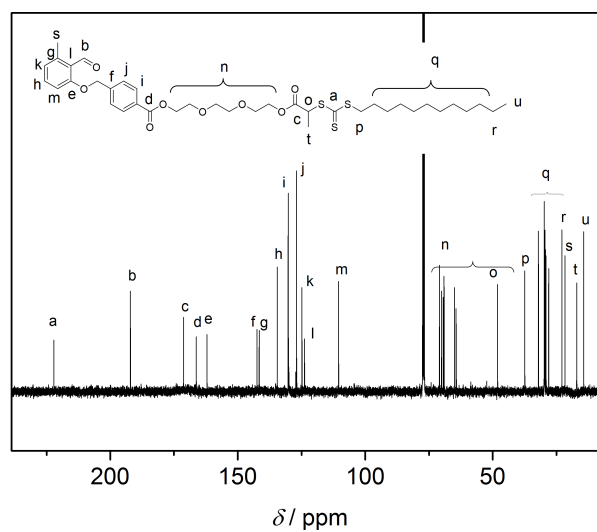
Figure C.16. ^{13}C NMR (101 MHz) spectrum of CTA3 in CDCl$_3$. Adapted from Ref. [291] with permission from The Royal Society of Chemistry.
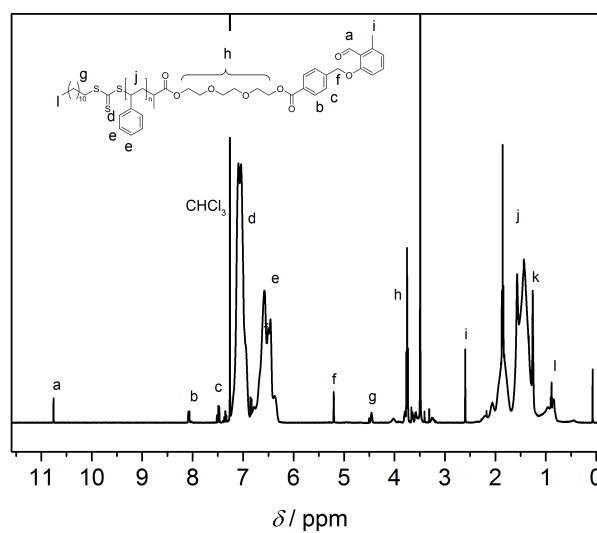
Figure C.17. ^{1}H NMR (400 MHz) spectrum of PE-PS in CDCl$_3$. Adapted from Ref. [291] with permission from The Royal Society of Chemistry.
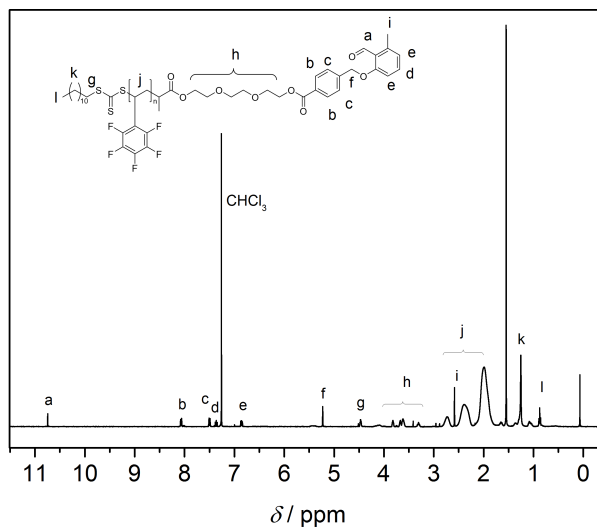
Figure C.18. ¹H NMR (400 MHz) spectrum of PE-PS in CDCl₃. Adapted from Ref. [291] with permission from The Royal Society of Chemistry.
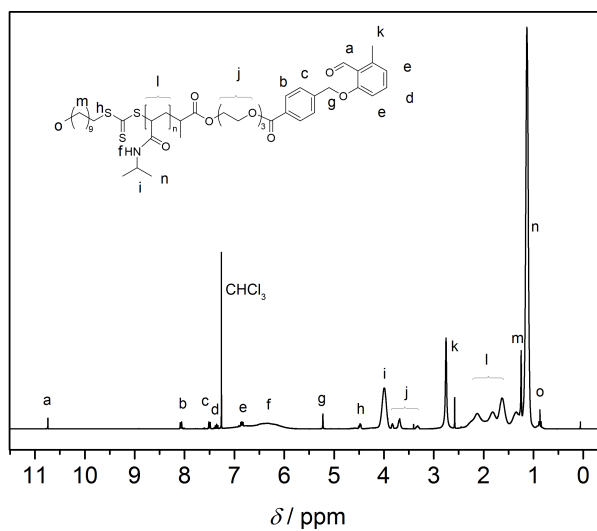
Figure C.19. ¹H NMR (400 MHz) spectrum of PE-PNIPAM 1 in CDCl₃. Adapted from Ref. [291] with permission from The Royal Society of Chemistry.
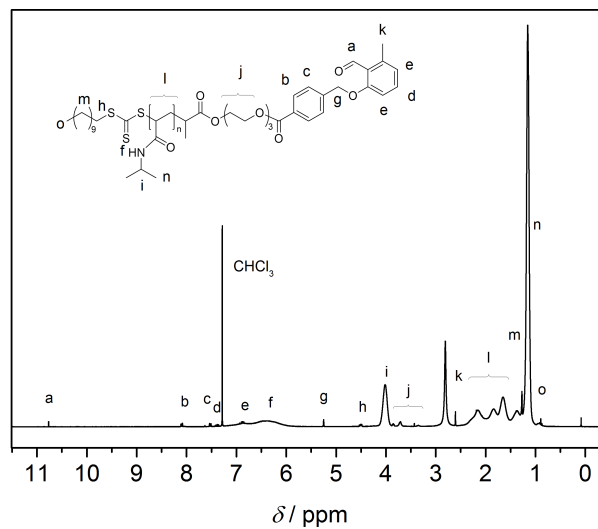
Figure C.20. ^{1}H NMR (400 MHz) spectrum of PE-PNIPAM 2 in CDCl$_3$. Adapted from Ref. [291] with permission from The Royal Society of Chemistry.
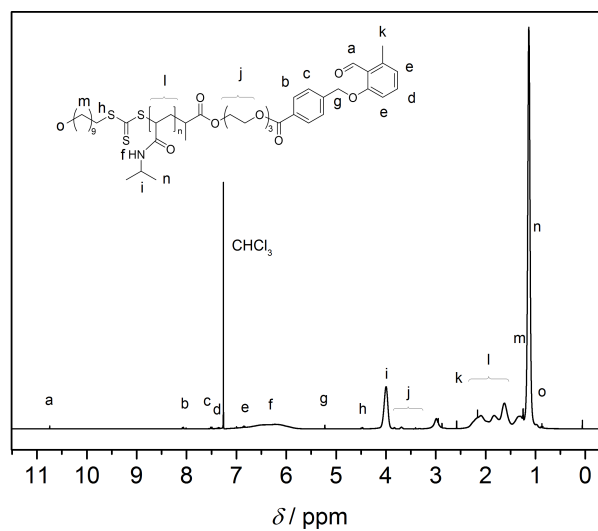
Figure C.21. ^{1}H NMR (400 MHz) spectrum of PE-PNIPAM 3 in CDCl$_3$. Adapted from Ref. [291] with permission from The Royal Society of Chemistry.
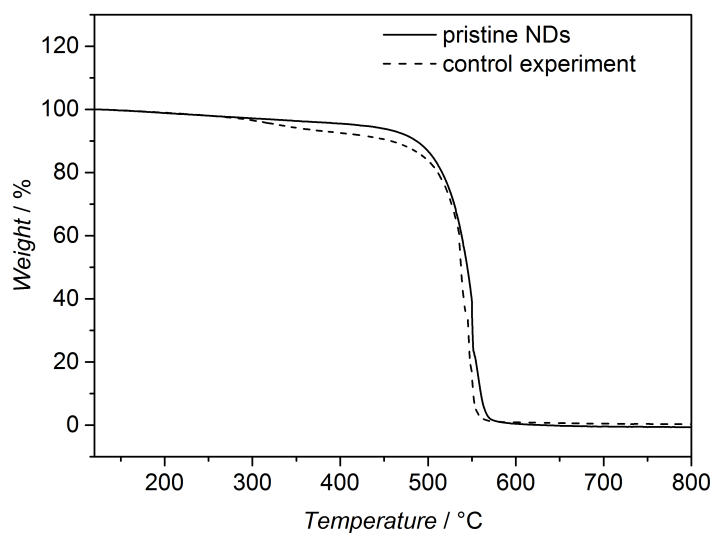
Figure C.22. TGA of pristine NDs and of a sample resulting from a photo-grafting experiment with PE-PS. Significant less polymer is on the surface of the NDs compared to the experiment where graphitic NDs were employed. Adapted from Ref. [291] with permission from The Royal Society of Chemistry.
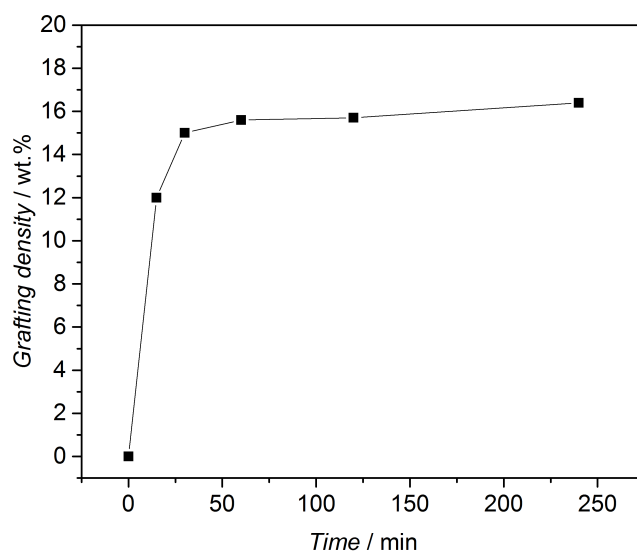
Figure C.23. Kinetic study of the photo-triggered grafting of PE-PEG to grNDs. Grafting densities were determined by TGA. Reproduced from Ref. [291] with permission from The Royal Society of Chemistry.
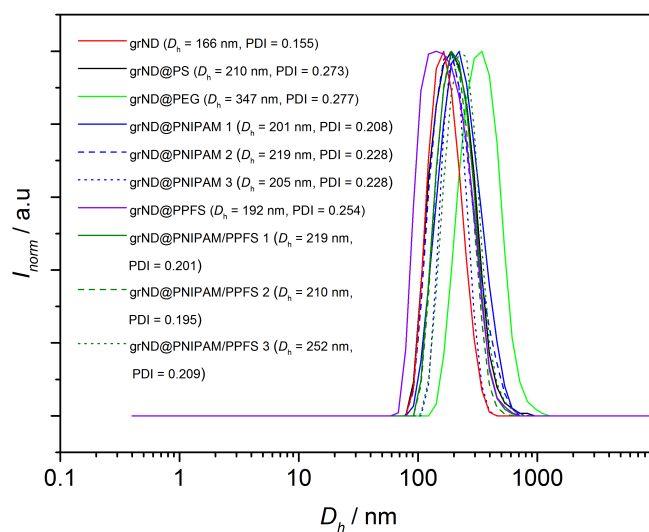
Figure C.24. DLS results from prepared NDs. Adapted from Ref. [291] with permission from The Royal Society of Chemistry.
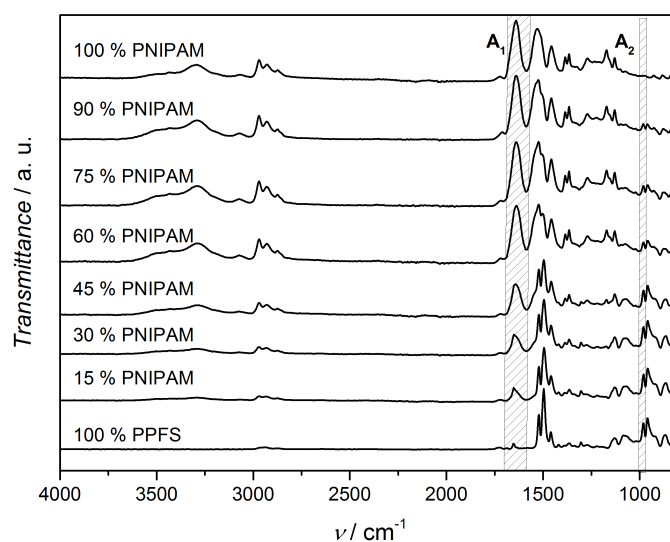
Figure C.25. ATR FTIR spectra of different ratios of PNIPAM 1 and PPFS and integation areas (A) for calibration. Adapted from Ref. [291] with permission from The Royal Society of Chemistry.
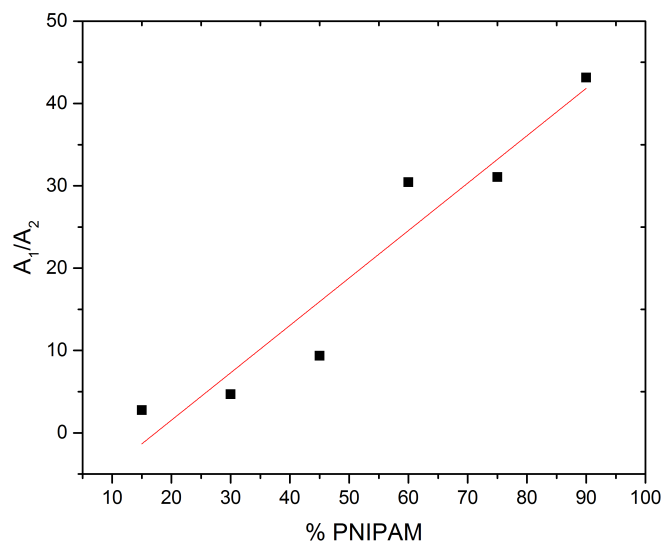
Figure C.26. Calibration plot used to determine the co-grafting ratio of PE-PPFS and PNIPAM 1. Adapted from Ref. [291] with permission from The Royal Society of Chemistry.
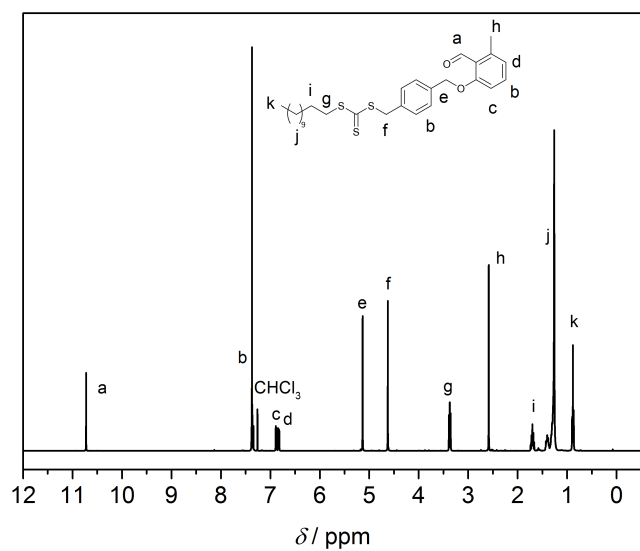
Figure C.27. ^{1}H NMR (400 MHz) spectrum of CTA4 in CDCl$_3$.
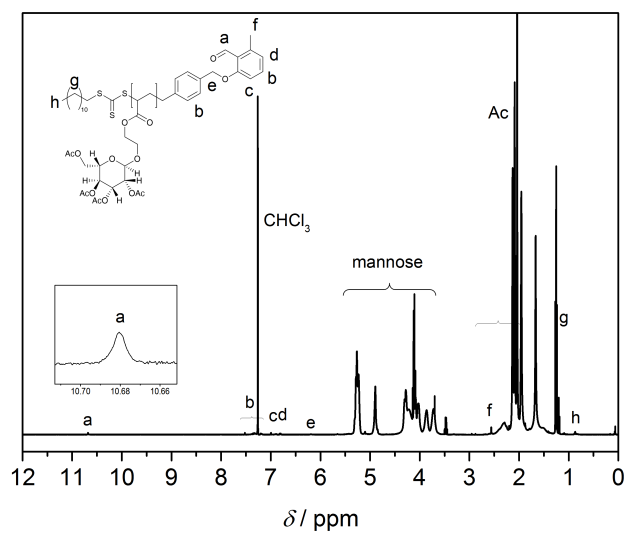
Figure C.28. [^1]H NMR (400 MHz) spectrum of PE-PManAcEMA in CDCl$_3$.
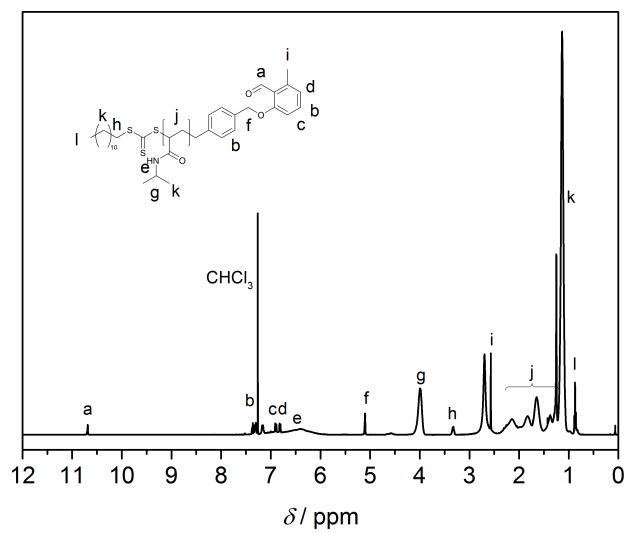
Figure C.29. [^1]H NMR (400 MHz) spectrum of PE-PNIPAM A in CDCl$_3$.
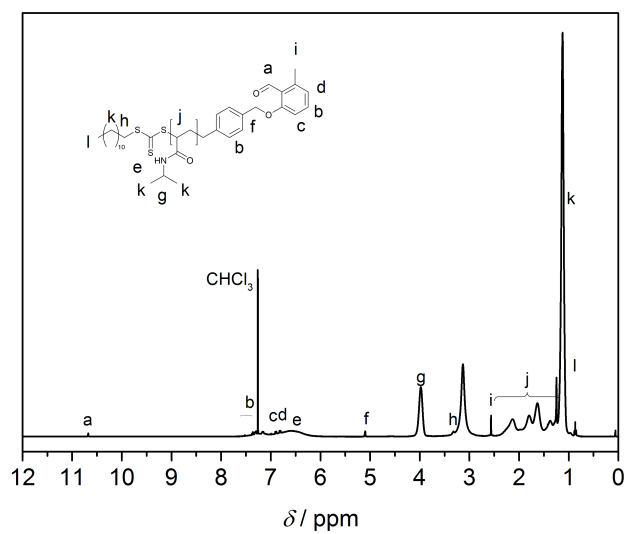
Figure C.30. ^{1}H NMR (400 MHz) spectrum of PE-PNIPAM B in CDCl$_3$.
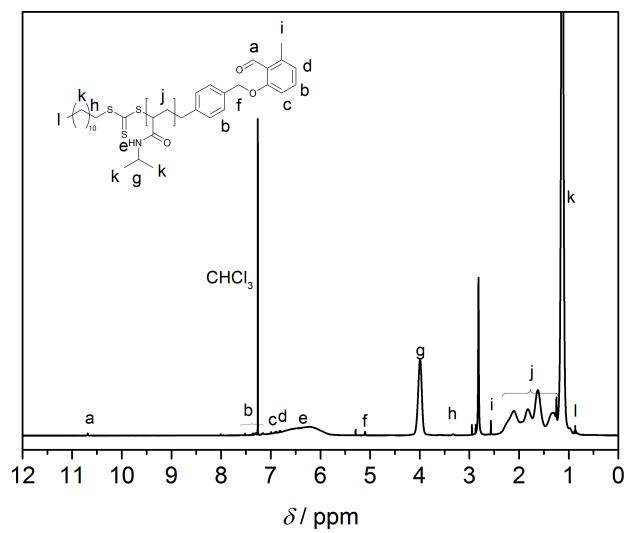
Figure C.31. ^{1}H NMR (400 MHz) spectrum of PE-PNIPAM C in CDCl$_3$.
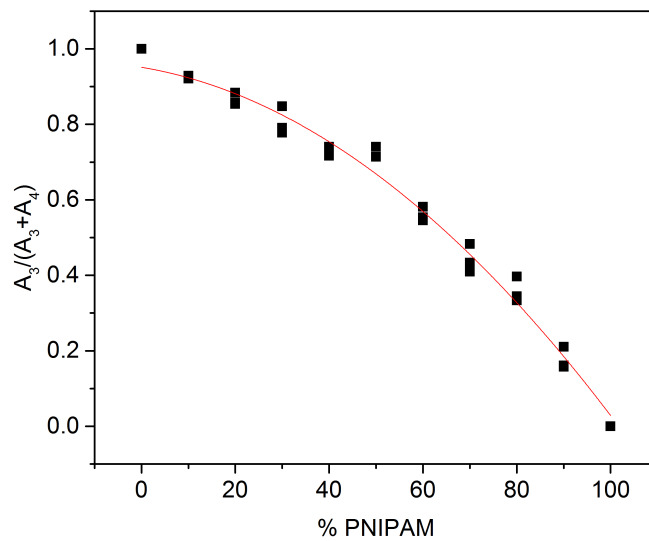
Figure C.32. Calibration plot used to determine the co-grafting ratio of PE-PManAcEMA and PNIPAM A-C.
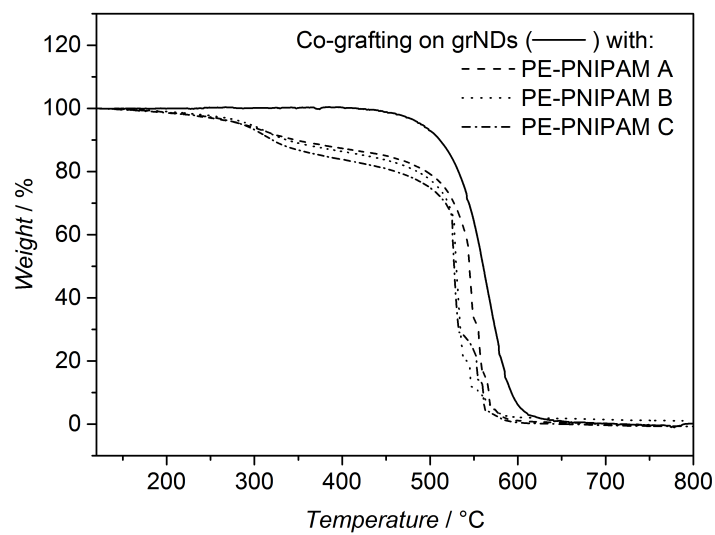
Figure C.33. TGA of the co-grafted samples (50 % feedstock ratio).
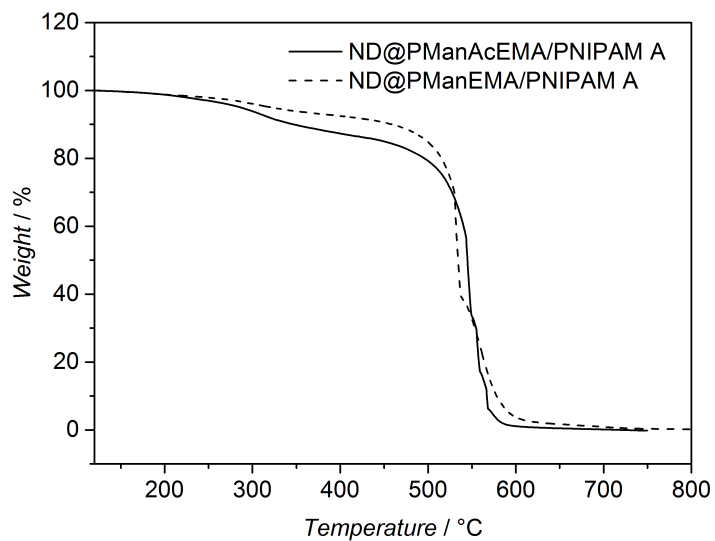
Figure C.34. TGA of the PE-PNIPAM A co-grafted sample (50 % feedstock ratio) before and after deacetylation with sodium methylate.
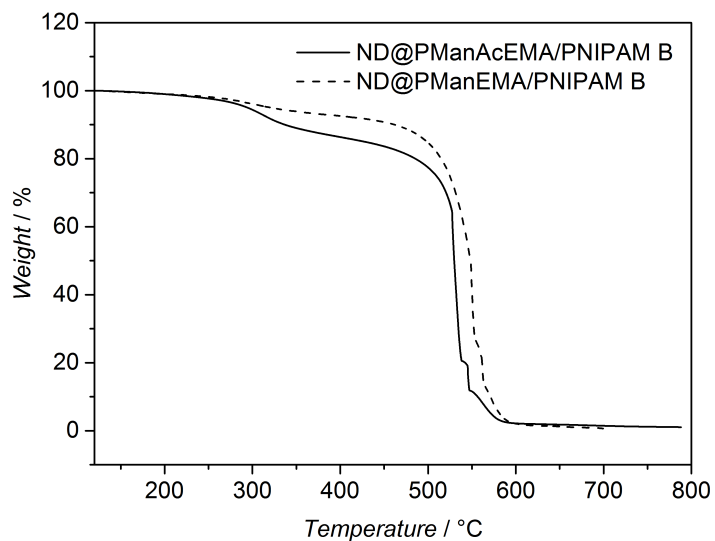
Figure C.35. TGA of the PE-PNIPAM B co-grafted sample (50 % feedstock ratio) before and after deacetylation with sodium methylate.
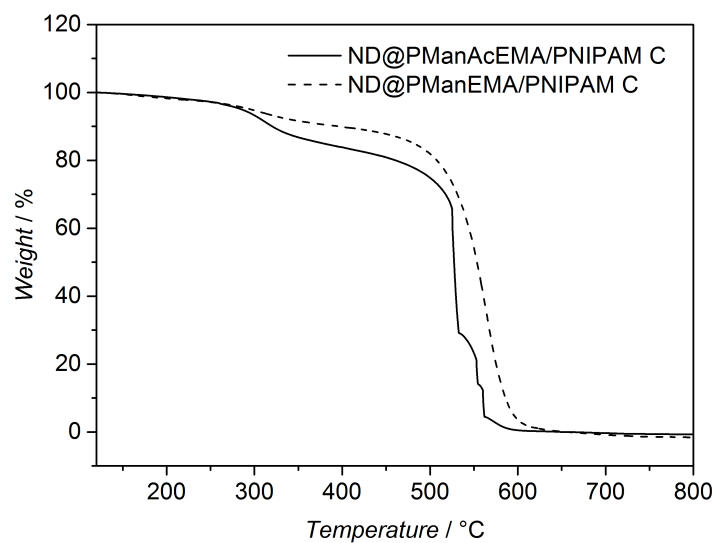
Figure C.36. TGA of the PE-PNIPAM C co-grafted sample (50 % feedstock ratio) before and after deacetylation with sodium methylate.
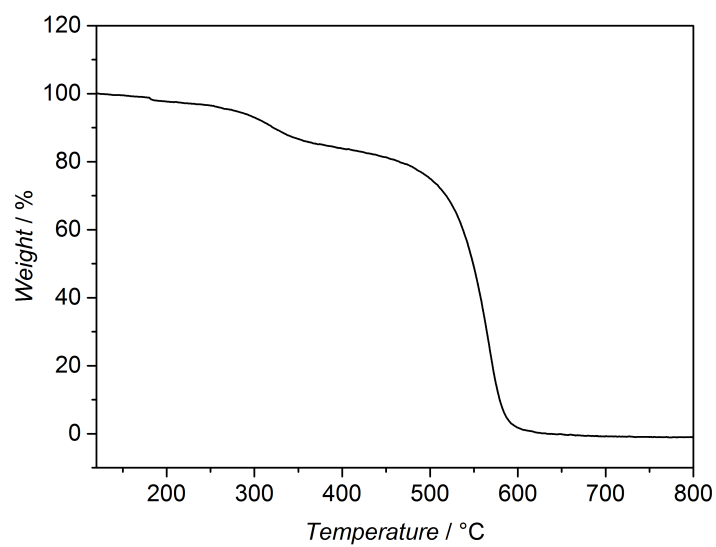
Figure C.37. TGA of the PE-PNIPAM B co-grafted sample (7 % feedstock ratio).

D. Supporting information for Chapter 5
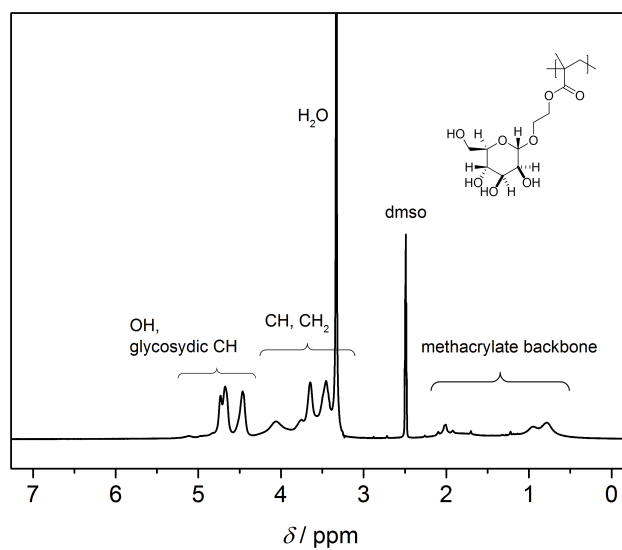
Figure D.38. ^{1}H NMR spectrum of glycopolymer A1 in DMSO-d$_6$. Adapted with permission from reference [294]. Copyright (2017) American Chemical Society.
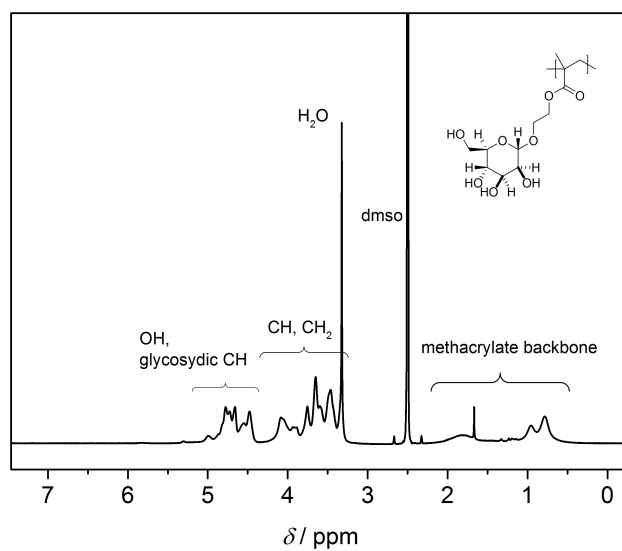
Figure D.39. ^{1}H NMR spectrum of glycopolymer A2 in DMSO-d$_6$. Adapted with permission from reference [294]. Copyright (2017) American Chemical Society.
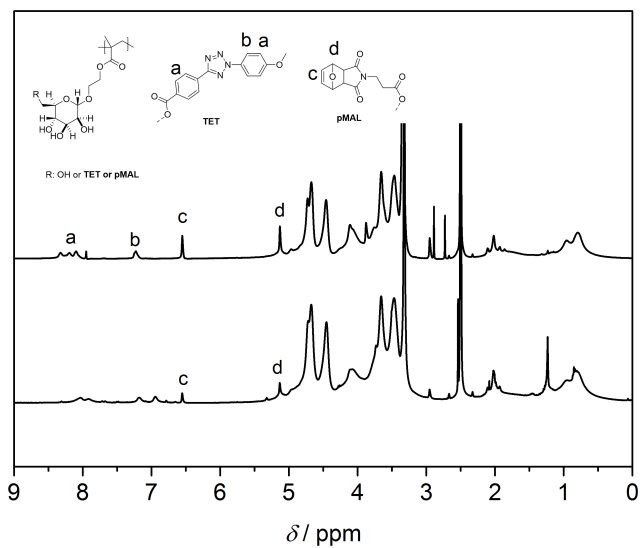
Figure D.40. ^{1}H NMR spectra of polymeric precursors P2 before (top) and after UV irradiation (SCNP2, bottom) in DMSO-d$_6$. Adapted with permission from reference [294]. Copyright (2017) American Chemical Society.
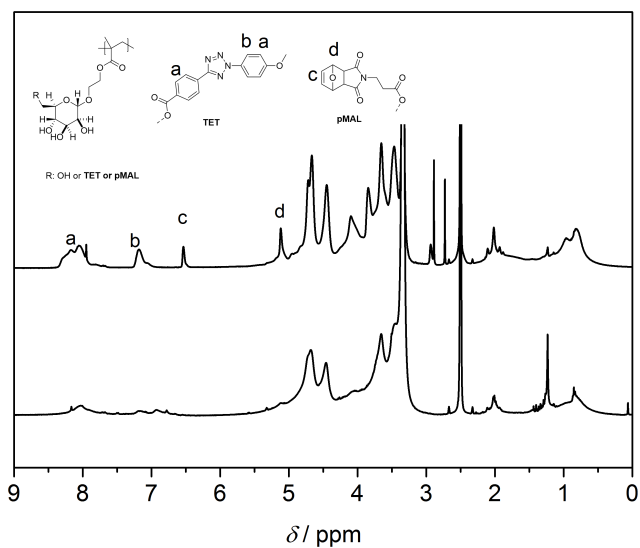
Figure D.41. ^{1}H NMR spectra of polymeric precursors P3 before (top) and after UV irradiation (SCNP3, bottom) in DMSO-d$_6$. Adapted with permission from reference [294]. Copyright (2017) American Chemical Society.
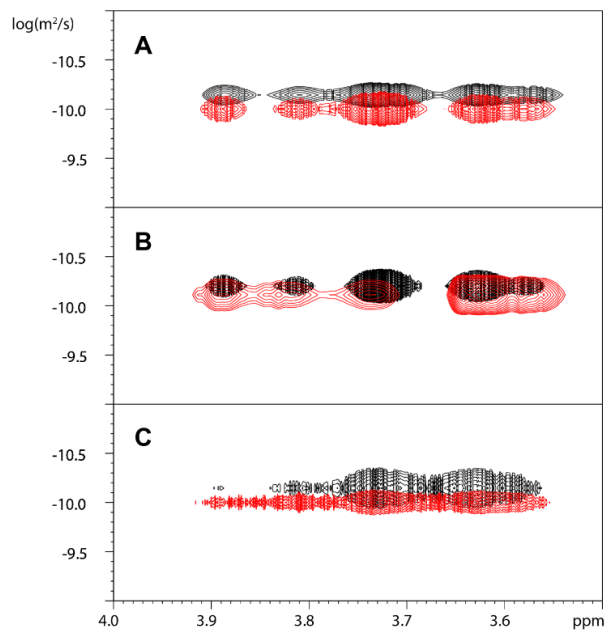
Figure D.42. DOSY results (600 MHz, D$_2$O): A: P1 (black) and SCNP1 (red); B: P2 (black) and SCNP2 (red); C: P3 (black) and SCNP3 (red). Reprinted with permission from reference [294]. Copyright (2017) American Chemical Society.
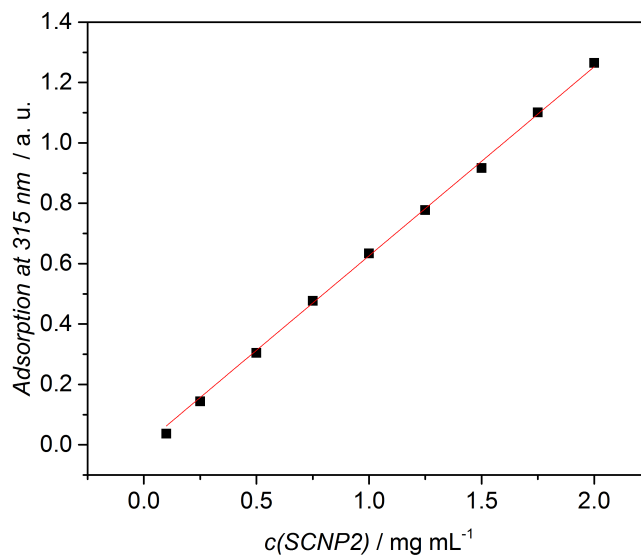
Figure D.43. Calibration curve for SCNP2. The absorbance at 315 nm was measured for different concentrations of SCNP2 in water and a linear fit was performed on the obtained data. Adapted with permission from reference [294]. Copyright (2017) American Chemical Society.
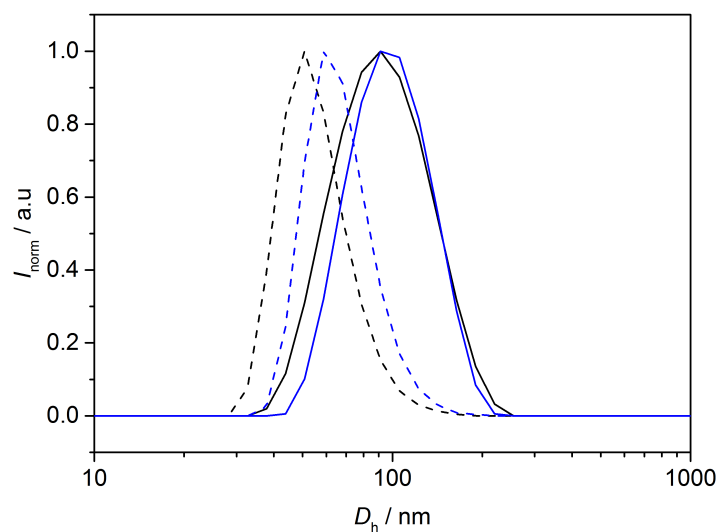
Figure D.44. DLS results of HPHT-ND-COOH (black) and ND@SCNP-3% (blue). The number (dashed line) and intensity weighted (solid lines) distributions are shown. Adapted with permission from reference [294]. Copyright (2017) American Chemical Society.
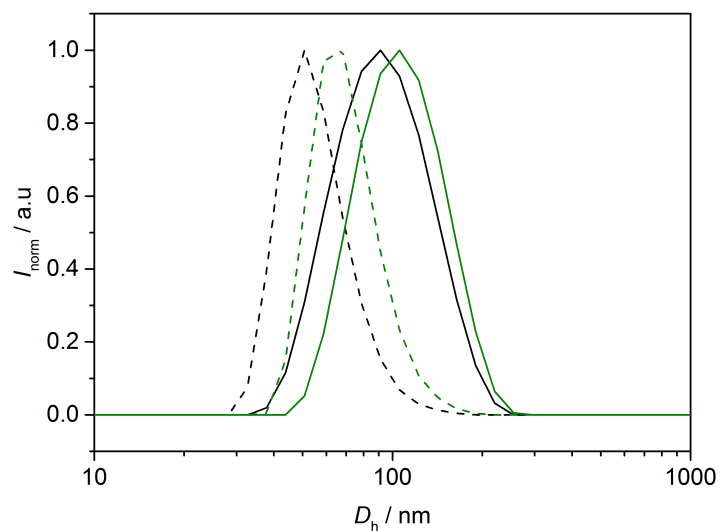
Figure D.45. DLS results of HPHT-ND-COOH (black) and ND@SCNP-6% (green). The number (dashed line) and intensity weighted (solid lines) distributions are shown. Adapted with permission from reference [294]. Copyright (2017) American Chemical Society.

Abbreviations

AFM	atomic force microscopy
AIBN	2,2'-azoisobutyronitrile
APTES	(3-aminopropyl)-triethoxysilane
ATRP	atom transfer radical polymerization
ATR FTIR	attenuated total reflectance fourier transform infrared
BSA	bovine serum albumin
CPADP	4-cyanopentanoic acid dithiobenzoate
ConA	concanavalin A
CPDB	2-cyano-2-propyl benzodithioate
CTA	chain transfer agent
CuAAC	copper catalyzed azide alkyne cycloaddition
DCM	dichloromethane
DCC	*N,N'*-dicyclohexylcarbodiimide
DC-SIGN	dendritic cell specific ICAM-3 grabbing nonintegrin
DLW	direct laser writing
DLS	dynamic light scattering
DMAEMA	2-(dimethylamino)ethyl methacrylate
DMAP	4-dimethylaminopyridine
DMF	*N,N*-dimethylformamide
DMSO	dimethyl sulfoxide
DOSY	diffusion ordered spectroscopy
EDC	1-ethyl-3-(3-dimethylaminopropyl)carbodiimide
ESI MS	electrospray ionization mass spectrometry
FRP	free radical polymerization
HEA	2-hydroxyethyl acrylate
HEMA	2-hydroxyethyl methacrylate
HIV	human immunodeficiency virus
HPHT	high pressure high temperature
IC	internal conversion
ISC	intersystem crossing

LAM	less activated monomer
LCST	lower critical solution temperature
LG	leaving group
MADIX	macromolecular design via the interchange of xanthates
MAM	more activated monomer
ManAcEMA	2-(2',3',4',6'-tetra-*O*-acetyl-α-D-mannosyloxy)ethyl methacrylate
ManAcEA	2-(2',3',4',6'-tetra-*O*-acetyl-α-D-mannosyloxy)ethyl acrylate
MHS	Mark-Howink-Sakurada
MWD	molecular weight distribution
NBR	nitrile-butadiene rubber
ND	nanodiamond
NHS	*N*-hydroxy succinimide
NITEC	nitrile imine mediated tetrazole-ene cycloaddition
NIPAM	*N*-isopropylacrylamide
NIR	near infrared
NMP	nitroxide mediated polymerization
NMR	nuclear magnetic resonance
NV	nitrogen vacancy
PCL	poly(caprolactone)
PDMAEMA	poly(2-(dimethylamino)ethyl methacrylate)
PEG	poly(ethylene glycol)
PFS	pentafluorostyrene
PMMA	poly(methyl methacrylate)
PNIPAM	poly(*N*-isopropylacrylamide)
PPFS	poly(pentafluorostyrene)
PS	polystyrene
RAFT	reversible addition fragmentation chain transfer
RDRP	reversible deactivation radical polymerization
ROP	ring opening polymerization
siRNA	small interfering RNA
SIV	simian immunodeficiency virus
SCNP	single-chain nanoparticle
SEC	size exclusion chromatography
SPR	surface plasmon resonance

TEM	transmission electron microscopy
TGA	thermogravimetric analysis
TMEDA	*N,N,N',N'*-tetramethylethylenediamine
THF	tetrahydrofuran
TNT	trinitrotoluene
UPy	2-ureidopyrimidinone
UV	ultraviolet
VR	vibrational relaxation
XPS	X-ray photoelectron spectroscopy
XRD	X-ray diffraction

Publications and conference contributions

Publications

(1) **Spatially Resolved Coding of λ-Orthogonal Hydrogels by Laser Lithography**

Batchelor, R. R.; Blasco, E.; Wuest, K. N. R.; Lu, H.; Wegener, M.; Barner-Kowollik, C; Stenzel, M. H., submitted.

(2) **Photo-induced ring-closure via a looped flow reactor**

Baeten, E.; Rubens, M.; Wuest, K. N. R.; Barner-Kowollik, C.; Junkers, T., *React. Chem. Eng.* **2017**, 2, 826-829.

(3) **Fluorescent Glyco Single-Chain Nanoparticle Decorated Nanodiamonds**[*]

Wuest, K. N. R.; Lu, H.; Thomas, D. S.; Goldmann, A. S.; Stenzel, M. H.; Barner-Kowollik, C. *ACS Macro Lett.* **2017**, 6, 1168-1174.

(4) **Direct Light-induced (Co-)Grafting of Photoactive Polymers to Graphitic Nanodiamonds**[*]

Wuest, K. N. R.; Trouillet, V.; Köppe, R.; Roesky, P. W.; Goldmann, A. S.; Stenzel, M. H.; Barner-Kowollik, C. *Polym. Chem.* **2017**, 8, 838-842.

(5) **Catalyst free visible light induced cycloaddition as an avenue for polymer ligation**

Lederhose, P.; Wuest, K. N. R.; Barner-Kowollik, C.; Blinco, J. P. *Chem. Commun.* **2016**, 5928-5931.

(6) **Polymer Functional Nanodiamonds by Light-Induced Ligation**[*]

Wuest, K. N. R.; Trouillet, V.; Goldmann, A. S.; Stenzel, M. H.; Barner-Kowollik, C. *Macromolecules* **2016**, 49 (5), 1712-1721.

---

[*]   Publications arising from the current thesis

(7) **Photochemical Design of Functional Fluorescent Single-Chain Nanoparticles**

Willenbacher, J.; Wuest, K. N. R.; Mueller, J. O.; Kaupp, M.; Wagenknecht; H.-A.; Barner-Kowollik, C. *ACS Macro Letters* **2014**, 3, 574-579.

(8) **A Mild and Efficient Approach to Functional Single-Chain Polymeric Nanoparticles via Photoinduced Diels-Alder Ligation**

Altintas, O.; Willenbacher, J.; Wuest, K. N. R.; Oehlenschlaeger, K. K.; Krolla-Sidenstein, P.; Gliemann, H.; Barner-Kowollik, C. *Macromolecules* **2013**, 46, 8092-8101.

Conference contributions

(1) **Fluorescent single-chain glycopolymer nanoparticles[‡]**

Wuest, K. N. R.; Lu, H.; Thomas, D. S.; Goldmann, A. S.; Stenzel, M. H.; Barner-Kowollik, C. *5th KIT PhD Symposium*, **September 2017**, Karlsruhe, Germany. Oral presentation.

(2) **Photochemical grafting of functional polymers to nanodiamonds[‡]**

Wuest, K. N. R.; Trouillet, V.; Köppe, R.; Roesky, P. W.; Goldmann, A. S.; Stenzel, M. H.; Barner-Kowollik, C. *Sydney Surfaces and Soft Stuff Meeting*, **June 2017**, Sydney, Australia. Oral presentation.

(3) **Light-induced grafting of functional polymers to nanodiamonds[‡]**

Wuest, K. N. R.; Trouillet, V.; Köppe, R.; Roesky, P. W.; Goldmann, A. S.; Stenzel, M. H.; Barner-Kowollik, C. *14th Annual UNESCO/IUPAC Workshop and Conference on Macromolecules and Materials*, **April 2017**, Stellenbosch, South Africa. Oral presentation.

(4) **Photochemical design of functional single-chain nanoparticles**

Wuest, K. N. R.; Willenbacher, J.; Mueller, J. O.; Kaupp, M.; Wagenknecht; H.-A.; Barner-Kowollik, C. *35th Australasian Polymer Symposium*, **July 2015**, Gold Coast, QLD, Australia. Oral presentation.

[‡]   Conference contributions arising from the current thesis.

List of Figures

196

List of Schemes

List of Tables

Acknowledgements

First of all, I would like to express my gratitude to my supervisors Prof. Dr. Christopher Barner-Kowollik and Prof. Dr. Martina Stenzel for their dedication and mentorship throughout the course of my doctoral studies as well as for providing an excellent research environment. The coordination of my project between two continents always ran smoothly and the opportunity to work on this project in an international collaboration was outstanding.

Furthermore, I would like to thank Dr. Anja Goldmann for her scientific guidance and organisational support during the last years of my doctoral studies.

Some of the work would not have been possible without my collaboration partners. I would like to thank Dr. Vanessa Trouillet for XPS measurements, Dr. Donald Thomas for assisting with DOSY experiments, Silvana Hurrle for XRD measurements, Dr. Ralf Köppe for helping with the annealing of nanodiamonds and Dr. Hongxu Lu for performing cell experiments.

Many thanks go to the entire macroarc team for the friendly working atmosphere, good team spirit and after-work activities. A special thanks goes to all my colleagues. It was always a pleasure to work with you. Furthermore, I would like to thank Dr. Maria Schneider, Evelyn Stühring, Vincent Schüler and Katharina Elies for their great help with laboratory-related and organizational issues.

Many thanks go to the Stenzel group and CAMD for making me feel at home as soon as I arrived. I would like to thank all my CAMD friends for the good working environment and for fun after work activities. Furthermore, I would like to thank Dr. Robert Chapman, Dr. Hongxu Lu and Eh Hau Pan for their great help with technical and organizational issues.

Many thanks go to Rhiannon Batchelor, Rouven Müller, Hannah Rothfuß, Alberto Piloni and Haiwang Lai for proofreading this thesis.

Furthermore, I would like to thank the students I have worked with. I would like to thank Sergej Baraban, Luca Filippi, Jordan Lovegrove and Zihao (Alvin) Li.

I would like to thank the German chemical industry association (Verband der Chemischen Industrie, VCI) for supporting me with a *Chemiefonds Fellowship*. Furthermore, I would like to thank the DFG for financial support of the project.

My deepest gratitude goes to my family and friends for their support and patience during my studies. Finally, I would like to thank Rhiannon for her support and the amazing time we have spent together. Without you this work would have not been possible.

Declaration

Hiermit erkläre ich, dass die vorliegende Arbeit im Rahmen der Betreuung durch Prof. Dr. Christopher Barner-Kowollik und Prof. Dr. Martina Stenzel selbstständig von mir verfasst wurde und keine anderen als die angegebenen Quellen und Hilfsmittel verwendet wurden. Die wörtlich oder inhaltlich übernommenen Stellen wurden als solche kenntlich gemacht. Die Regeln zur Sicherung guter wissenschaftlicher Praxis des Karlsruher Instituts für Technologie (KIT) wurden beachtet und die Abgabe und Archivierung der Primärdaten gemäß Abs. A (6) der Regeln zur Sicherung guter wissenschaftlicher Praxis des KIT beim Insitut ist gesichert. Die elektronische Version der Arbeit stimmt mit der schriftlichen überein. Des Weiteren erkläre ich, dass ich keine vorausgegangenen Promotionsversuche unternommen habe und mich derzeit auch nicht in einem weiteren, laufenden Promotionsverfahren befinde.

_____   _____

Ort, Datum   Unterschrift